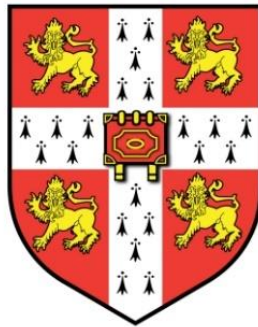# Long-Term Performance
# of a concrete-lined Tunnel
at CERN

Vanessa Di Murro

Department of Engineering

University of Cambridge

This dissertation is submitted for the degree of

Doctor of Philosophy

To my beloved parents and brother

Declaration

I hereby declare that, except where specific reference is made to the work of others, the contents of this dissertation are original and have not been submitted in whole or in part for consideration for any other degree or qualification in this, or any other University. This dissertation is the result of my own work and contains nothing which is the outcome of work done in collaboration with others, except as specified in the text and Acknowledgements. This dissertation contains less than 65,000 words including appendices, bibliography, footnotes, tables and equations and contains less than 150 figures.

Vanessa Di Murro

June 2019

Acknowledgements

I would like to express my deepest gratitude to my supervisor Professor Kenichi Soga, in providing not only invaluable advice and guidance throughout my PhD but also for being extremely careful and generous. Thank you for encouraging my research, you have been a tremendous mentor for me and it has been a privilege being one of your students.

My great appreciation also goes to my industrial supervisor Dr Luigi Scibile and to my section leader John Andrew Osborne, for their valuable assistance and great encouragement during my stay at CERN. My gratitude also goes to the Head of the SMB Group, Lluis Miralles, for allowing me the opportunity to join the successful engineering group at CERN. Having worked and being part of the SMB-SE-FAS group at CERN has enhanced me to grow professionally and personally. A big thanks should also go to Richard Morton, who has fed me with his practical experience in tunnelling and has also assisted me with care in many practical ways. I would also like to thank the CERN EN/SMM Group, in particular Patrick Bestmann for releasing the conventional monitoring data collected in the TT10 tunnel. I am also extremely grateful to my examiners, Professor Lord Robert Mair and Professor Neil Taylor, for their valuable suggestions and corrections.

Many other people I would like to thank you. My appreciation is also expressed to all my colleagues from the Cambridge Centre for Smart Infrastructure and Construction (CSIC) and CERN. I would especially like to thank Dr Jennifer Schooling and Professor Lord Robert Mair for their kindness and for giving me the opportunity to join the flourishing CSIC research Group in Cambridge.

There are many others I would like to thank for their great help. Dr Loizos Pelecanos, who dedicated a large amount of time to assist me in FO data analysis and gave me priceless advice on many occasions. I am also indebted to Dr Zili Li for his remarkable advice on ABAQUS and his great patience throughout the last years.

I would like to thank also Dr Elliot James Fern for his great contribution to the geotechnical characterization of the molasse rock and for dedicating his time to

Abstract

At the world's largest physics centre for nuclear research (CERN) under controlled laboratory conditions, two high-energy particle beams travel close to the speed of light around the most powerful particle accelerator ever built. The accelerator runs through a deep network of underground tunnels and caverns. To forefront the boundaries of experimental physics, CERN physicists rely on civil engineers to keep their systems running efficiently, performing repairs and upgrades when necessary. However, due to ageing of CERN underground infrastructure, certain amounts of cracking and swelling-induced heave have developed at certain sections along the tunnel linings, which could potentially result in structural damage of the existing infrastructure with consequent impact on the performance of physical experiments. Furthermore, the long-term groundwater seepage has caused the deterioration of the drainage system, inducing a change in the flow regime around the tunnel. This inevitably introduced a new loading condition to the lining, which may have affected the tunnel stability with time.

This thesis focuses on the long-term investigation of a horseshoe-shaped concrete-lined tunnel excavated at CERN, in Geneva, in a weak sedimentary rock called the *red molasse*, an irregular and heterogeneous rock mass comprising a sequence of marls and sandstones. Such complex ground conditions in addition to a change in groundwater and tunnel drainage conditions especially after the large seepage flow event in the year 2013 have contributed to additional loading to the tunnel lining and consequently led to cracks, water infiltration and other structural distress after tunnel construction.

To improve the understanding of the long-term tunnel lining performance, a detailed analysis of the field data measurements was undertaken. Both conventional and innovative monitoring technologies were deployed in order to assess the tunnel lining deformation mode with time and also to evaluate the feasibility of different monitoring instrumentation in CERN radioactive environments.

The observed data show that compressive and tensile strains develop at the tunnel crown and tunnel axis respectively, suggesting a vertical tunnel elongation with time as the tunnel lining mechanism of deformation. Yet slow development of strains with time was observed, albeit over a relatively short monitoring period of three years. Additionally, noteworthy peak strain values seem to be localised along the lining when the very weak marl units with swelling properties are encountered.

   In order to validate the field data and to assess the ground loading on the tunnel lining, a series of soil-fluid coupled 2D finite element analyses has been conducted with a particular interest in the effect of change of lining permeability into the lining response. The FE findings show that the tunnel lining permeability relative to the surrounding rock plays an important role on the tunnel deformation mode during the long-term. In particular, the layering divisions in the complex molasse region greatly affect the earth pressure distribution on the tunnel lining and hence results in critical tunnel damage (e.g. cracks and heaving at the tunnel invert). The consolidation-induced structural damage in addition to a reduced capacity of the drainage system with time, in turn, creates a new drainage tunnel lining condition around the tunnel circumference which exacerbates further tunnel distress with time.

Table of contents

List of figures

List of tables

Nomenclature

Roman symbols

c'	Effective cohesion
C_b	Soil model parameter controlling small strain stiffness
C_T	Temperature coefficient
C_ε	Strain coefficient
d, t	Tunnel lining thickness
C/D	Cover – Tunnel diameter ratio
D	Slope of swelling unloading line, Tunnel diameter
DS	Dimensionless settlement
e_0	In situ void ratio
E	Elastic modulus of beam element
E'	Effective stiffness
E'_d	Drained Young's modulus
E_u	Undrained stiffness
E_{50}	Secant undrained stiffness at 50 % of the
EI	Bending stiffness
k, k_s	Soil permeability
k_T	Tunnel lining permeability
K_T	Tunnel lining seepage coefficient
k_V	Vertical permeability of soil
k_h	Horizontal permeability of soil
K	Trough width parameter
K'	Soil bulk modulus
K_0	Coefficient of earth at rest
G	Shear stiffness modulus
G_s	Gravity density

I	Second moment of inertia of beam element
i	Settlement trough width
i_y	Transverse horizontal distance from the inflection point of total settlement trough and tunnel centre-line
L_c	Tunnel axis depth below water table
M	Gradient of critical state line in the q-p' space; Bending moment in tunnel lining
$N_{sc, max}$	Normalised maximum surface settlement
n	Refractive index; Shape function parameter
p'	Mean effective stress
p_0'	Mean effective preconsolidation pressure
q, t	Deviatoric stress
q_s, q_t	Volumetric flow rate through the soil and the lining per unit tunnel respectively
$S_{c\ max}$	Maximum consolidation settlement
S_v	Transverse vertical settlement
$S_{v, max}$	Maximum transverse vertical settlement
s'	Mean effective stress
t_T	Tunnel lining thickness
y	Distance from the neutral axis of the beam element
V_a	Acoustic velocity
v	Incident light
V_L	Volume loss
V_S	Volume of surface settlement trough per unit length of tunnel
y	Horizontal distance from the tunnel centre-line
z	Vertical distance below ground surface
z_0	Depth of tunnel axis below surface

Greek symbols

γ_{sat}	Saturated density
γ_w	Bulk unit weight of water

λ	Wavelength of light
σ'_t	Tensile strength
σ_{ci}	Compressive strength
ν'	Effective Poisson's ratio
ν_u	Undrained Poisson's ratio
τ	Pulse width
χ	Curvature of tunnel lining
G_{hh}	Shear modulus in the horizontal plane
G_{vh}	Shear modulus in the vertical plane
ε_a	Axial strain along the optical fiber
ε_{axial}	Axial strain along the beam element
$\varepsilon_{bending}$	Bending strain along the beam element
ψ	Soil dilatancy
φ'	Friction angle
μ	Parameter in the modified Gaussian curve to ensure that i remains as the horizontal distance to the inflection point

Abbreviations

ACSM	Advanced critical state model
API	American Petroleum Institute
BOTDA	Brillouin Optical Time-Domain Analysis
BOTDR	Brillouin Optical Time-Domain Reflectometry
CERN	European Centre for Nuclear research
CSIC	Cambridge Centre for Smart Infrastructure and Construction
CSL	Critical state line
DFOS	Distributed Fibre Optic Sensors
EN – SMM - RME	Engineering - Survey, Mechatronics and Measurements- Radiation Tolerant and Measurements Electronics
FE	Finite Element
FEA	Finite Element Analysis
FO	Fibre Optic
GPR	Ground-Penetrating radar

JLE	Jubilee Line Extension
LHC	Large Hadron Collider
LS1	Long Shutdown 1
MC	Mohr-Coulomb model
NATM	New Austrian tunnelling method
PEMAG	Magnitude of plastic strains evaluated with the MC model
POR	Pore pressure
PS	Proton Syncrotron
RIA	Radiation-induced attenuation
RI	Refractive index
ROC	Radius of Curvature
RP	Soil-lining relative permeability
RQD	Rock-quality designation
SCL	Sprayed concrete lining
SDV132	Plastic strains evaluated with the ACSM model
SMB – SE –FAS	Site Management and Buildings Department - Site Engineering – Future Accelerator Studies
SPS	Super Synchrotron Protons
TBM	Tunnel boring machine
2D	Two-dimensional
3D	Three-dimensional

Chapter 1

1 Introduction

1.1 Background of the study

At the European Centre of Nuclear Research (CERN), the well-known deep particle accelerator is hosted in a circular underground facility made of shafts, caverns and tunnels, excavated in a weak sedimentary rock mass in the Geneva basin. Through a long chain of injectors, physical particles are fed into the main Large Hadron Collider (LHC) to push the boundaries of physical knowledge.

Aged concrete tunnels commonly exhibit tunnel lining deterioration with time, resulting in a significant increase in maintenance costs and in the meanwhile compromising the success of physical experiments. Recent changes in the flow regime around the tunnel have brought new challenges to the operation of the horseshoe-shaped concrete-lined tunnel. Particularly, due to extreme weather conditions, large amounts of groundwater flowed towards the tunnel, resulting in long-term hydraulic deterioration of the drainage systems (i.e. clogging of drains). This, in turn, increased the magnitude of the external water pressures acting upon the lining. As a result, some part of the tunnel is experiencing a vertical elongation as a mechanism of deformation, with the development of structural distress. Therefore, it is hypothesised in this research that the influence of groundwater regime change on the tunnel lining response plays a crucial role when evaluating the long-term behaviour of the tunnels. The current status of the tunnel is assessed by analysing the data derived from conventional and novel monitoring systems. A series of numerical analyses is conducted to assess the long-term performance of the tunnel as it is subjected to an increase in the external water pressure.

1.2 Objective of the research

This research aims to investigate the long-term performance of an existing concrete-lined tunnel at CERN, called TT10 tunnel, entirely excavated in the molasse region, in Geneva. Particularly, the study aims to develop a good understanding of the long-term tunnel lining deformation mechanism when its tunnel drainage condition changes many years after construction. To this end, field monitoring and finite element analyses have been conducted. The present research work pursues the following specific objectives:

- Investigate the mechanism of tunnel lining deformation through a detailed observational study of crack development inside the tunnel.
- Characterize the weak layered sedimentary rock mass at CERN through the analysis of geotechnical data obtained from laboratory and field explorations.
- Deploy different monitoring technologies and interpret the data to assess the mechanism of tunnel lining deformation. Both conventional and novel monitoring systems are evaluated for their feasibility in the CERN radioactive environment with limited accessibility.
- Construct several finite element models of the tunnel and surrounding soil and develop a methodology to simulate the changes in the drainage conditions of the tunnel as the drainage system deteriorates.
- Perform a series of finite element analyses to examine the effect of soil layering in the molasse region on the lining response.

The outcome of the research provides a better understanding of the long-term performance of a concrete-lined tunnel at CERN when subjected to a change in the ground flow and drainage regimes around the tunnel. It is envisaged that this work may be referenced to improve the forthcoming underground works at CERN to realize the Future Circular Collider (FCC).

1.3 Structure of the thesis

The thesis is organised into eight chapters, with the first one being the introduction.

Chapter 2 presents the review of current research associated with the long-term behaviour of tunnels in clay. It examines both short and long-term ground movements due to tunnelling and the tunnel lining response.

Chapter 3 introduces the investigation carried out for a CERN concrete-lined tunnel (the TT10 tunnel) that underwent damage many years after construction. The possible causes and, hence, the mechanisms of tunnel lining deformation are identified and presented. The conventional total station monitoring instrumentation data at the affected tunnel cross-sections are discussed.

Chapter 4 discusses the instrumentation deployed to assess the lining behaviour using advanced distributed fibre optic strain sensing. The radiation effect on optical fibres is discussed along with the background of technology. The details of the fibre optic installations carried out at the site are given. The pattern of tunnel lining deformation derived from the DFOS data is presented.

Chapter 5 presents the results of the geotechnical investigation of the weak rock mass at this site through the analysis of laboratory and field tests.

Chapter 6 describes the results of two-dimensional soil deformation and pore fluid flow coupled finite element simulations of a tunnel cross-section that is found to be critical at the site. The simulations involve time-dependent changes in the drainage conditions of the tunnel lining and the computed results are validated against field measurements.

Chapter 7 examines the effect of soil layering observed within the molasse region on the tunnel lining behaviour.

Chapter 8 summaries the main findings and recommendations and future research for further studies are also presented.

Chapter 2

2 Review of the long-term behaviour of tunnels

2.1 Ground response induced by tunnelling

After tunnel construction, further ground movements occur, primarily due to the consolidation of the ground around the tunnel. In fact, the tunnel inevitably introduces new drainage boundary conditions, since at the inside face of the lining the pressure is by definition atmospheric (Harris, 2002). The pore pressure equilibrium immediately after construction is not guaranteed, resulting in water flow if the tunnel lining is not impermeable. As a result, pore pressures will reduce in the long-term, causing settlements at the ground surface and an increase of effective stresses, inducing then consolidation of the soil and, hence, consolidation settlements.

Settlements induced by the excavation of a tunnel can be divided into two components: short-term and long-term settlements. The former can be reasonably predicted for a given tunnel excavation process and ground conditions (Mair and Taylor, 1997). The latter, defined as the incremental settlements taking place after the short-term construction settlement, are also called consolidation settlements and their magnitude varies significantly according to where the tunnel is situated in the ground. Harris (2002) observed that consolidation settlements in the Jubilee Extension Line (JLE) tunnels have been considered to be effectively completed when movements were less than 2mm/year, which criterion was not met until 5 years. Addenbrooke (1996) noticed that for permeable linings settlements become negligible after 10-15 years whilst for impermeable lining approximately 20 years due to the longer drainage distance. Empirical methods for the prediction of the extent and the magnitude of long-term settlements are not available, therefore finite

element analysis (FEA) or other numerical methods are the only practical method to rely on.

By examining field data from post-construction tunnelling settlements, Mair and Taylor (1997) observed that the major factors influencing the development of post-construction settlements above tunnels are as follows:

- The magnitude and distribution of excess pore pressure Δu after the construction of the tunnel;
- The initial pore pressure distribution in the ground, before the tunnel construction;
- The permeability and the compressibility of the soil;
- The relative soil- tunnel lining permeability.

In order to evaluate the long-term effects, it is important to evaluate how excess pore pressures are generated and how they will dissipate with time.

The magnitude and the distribution of pore pressure play an important role in the long-term behaviour and have one of the greatest influences on it. Mair and Taylor (1997) noticed that excess pore pressure strongly depends on the construction process: whether the ground is unloaded during the construction of the tunnel or whether it is subject to an increase of loading. The former coincides with the open face tunnelling procedure, the latter (sometimes in soft clays) with closed face tunnelling, using EPB or slurry shields.

2.1.1 Short-term surface settlement

Many authors such as Martos (1958), Peck (1969) and Schmidt (1969) have shown that for a single tunnel in greenfield conditions the vertical transverse settlement trough immediately following tunnel construction can be well-described by a Gaussian distribution curve (Figure 2.1), as follows:

$$S_v = S_{v,max} \cdot e^{\frac{-y^2}{2 \cdot i_y^2}} \qquad\qquad (2.1)$$

where:
- S_v is the ground settlement
- $S_{v,max}$ is the maximum settlement on the tunnel centre-line
- y is the horizontal distance from the tunnel centre-line

- i_y is the horizontal distance from the tunnel centre-line to the point of inflexion of the settlement trough.
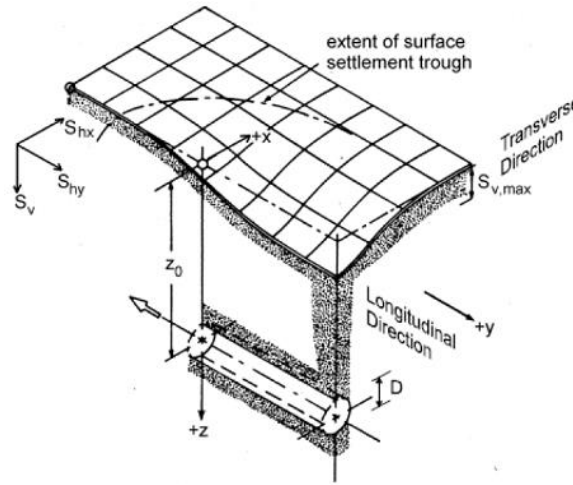
Figure 2.1. Ground settlement above advancing tunnel heading (Attewell et al., 1986).

Depending on the ground conditions, Peck (1969) firstly proposed a relationship between the parameter i_y, the tunnel depth and the tunnel diameter. Following the suggestion of O'Reilly and New (1982), Mair and Taylor (1997) proposed a linear relationship between the parameter i and tunnel depth z_o through validation against field data:

$$i = K \cdot z_o \tag{2.2}$$

With K being the trough width parameter, found to be equal to 0.5 for a tunnel in clays and 0.25 for a tunnel in sand and gravels.

By integrating Equation 2.1, the volume of the surface settlement trough Vs (per metre length of tunnel) may be expressed as follows:

$$V_s = \sqrt{2\pi}\, i\, S_{v,max} \tag{2.3}$$

For a circular tunnel, V_s can be expressed as a percentage fraction of the excavated area of the tunnel V_L, which is designated as the volume loss:

$$V_s = \frac{\pi D^2}{4} V_L \tag{2.4}$$

From the estimation of V_L, the maximum settlement $S_{v\,max}$ can be determined.

Wongsaroj et al. (2013) stated that a noticeable discrepancy was found when validating field data from the Heathrow Express tunnel and the St. James's Park tunnel

with the Gaussian curve of Eq. 2.1, which is often used to characterize short-term surface settlement. A modified Gaussian curve was proposed by Vorster et al. (2005) to gain a better fit of long-term transverse settlement profile:

$$S = S_{max} \frac{n}{(n-1) + e^{\mu \frac{y^2}{i_y^2}}} \tag{2.5}$$

$$n = e^\mu \left(\frac{2\mu - 1}{2\mu + 1} \right) + 1 \tag{2.6}$$

Where n is the parameter controlling the width of the settlement profile, and μ is a parameter introduced to keep i as the distance from the inflexion point and tunnel centreline. The Eq. 2.6 governs the relationship between n and μ. By decreasing the value of μ from 0.5 to 0.1, Wongsaroj et al. (2013) noticed a wider settlement profile compared to that in the short-term.

O'Reilly and New (1991) proposed a relation for determining the total settlement profile for twin tunnels, assuming them to be identical:

$$S_{(y)} = S_{max} \left[e^{\frac{-y^2}{2 \cdot i_y^2}} + e^{\frac{-(y-d')^2}{2 \cdot i_y^2}} \right] \tag{2.7}$$

Where d' is the distance between tunnel centreline. The long-term investigation of twin tunnels will be discussed in the following sections.

2.1.2 Subsurface settlement

From the analysis of subsurface data from tunnels in stiff and soft clays, Mair et al. (1993) showed that the shape of subsurface settlement profiles developed during tunnel construction can be approximated to the Gaussian distribution, in the same approach as surface settlements. Therefore, at a certain depth z below the surface the width trough parameter can be evaluated as follows:

$$i = K \cdot (z_o - z) \tag{2.8}$$

With the parameter K increasing with depth, showing considerably wider subsurface settlement profiles. Mair et al. (1993) suggested the following expression for evaluating the parameter K:

$$K = \frac{0.175 + 0.325 \, (1 - z/z_o)}{(1 - z/z_o)} \tag{2.9}$$

2.2 Influence on long-term ground movements: single tunnel

Many studies have been conducted to predict long-term tunnel consolidation deformation in soft and clay soils.

A method to predict long-term surface settlements for single tunnels in London clay was devised by Wongsaroj (2005). The results obtained from the FE parametric study revealed the importance of the permeability of tunnel lining relative to the one of the surrounding soil. It has been observed that in heavily consolidated clay when the tunnel lining is fully permeable, the pore water pressure would flow towards the tunnel causing the pore pressure around the tunnel to reduce. This reduction in pore water pressure causes the soil to consolidate. Hence, further surface settlement is expected in the long-term until a steady-state flow condition is reached. When the tunnel lining is fully impermeable, the pore pressure around the tunnel tends to recover, causing the soil to swell and the dissipation of negative excess pore water pressures. Therefore, heave can be expected in the long-term (Wongsaroj, 2005).

Whether the tunnel lining is acting as a permeable or an impermeable boundary relative to its surrounding depends not only on the permeability of the soil and the tunnel lining but also on the thickness of the clay above the tunnel as well as the thickness of the tunnel lining.

Following the work of Wongsaroj et al. (2007) and Wongsaroj et al. (2013), a new non-dimensional displacement $NS_{c \, max}$ parameter was proposed to evaluate the consolidation vertical surface settlement, assuming a radial flow hydraulic field condition around the tunnel (Laver 2010):

$$NS_{c \, max} = \frac{E'_d}{5 D_T L_c \gamma_w} S_{c \, max} \tag{2.10}$$

where E'_d is the equivalent drained 1D elastic modulus, D_T is the tunnel diameter, L_c is the tunnel axis depth below the water table, γ_w is the bulk unit weight of water

and $S_{c\,max}$ is the maximum consolidation settlement. The thickness of the consolidation layer is taken at ± 2.5 D_T from tunnel axis and E'_d is taken at axis depth.

Wongsaroj (2005) and Wongsaroj et al. (2013) analysed the consolidation settlement characteristics through numerical analyses and field tests for a tunnel located in London clay strata, into a parametric study. Long-term ground response and tunnel lining behaviour in London clay depend on a combination of several factors, which are considered to have a major influence, as reported by Wongsaroj (2005):

- Drainage condition of the tunnel lining

- Distribution and profile of the soil permeability (k_h/k_v ratios)

- Depth and diameter of the tunnel (C/D ratio)

- Volume loss in the long-term

It was found that the width and the rate of the consolidation settlement profile were much more sensitive to the permeability anisotropy (k_h/k_v) and soil-lining permeability than the volume loss and cover-diameter (C/D) ratio. Wongsaroj (2005) also observed small magnitudes of long-term surface settlement with large values of volume loss and with a permeable tunnel lining, whilst the magnitude of the long-term heave increases with greater values of volume loss. In addition, for values of C/D = 5 and C/D = 7 the magnitude of long-term displacement reduces with an increase of C/D ratio (Wongsaroj, 2005).

For a permeable tunnel lining, the magnitude of ground movement in the long-term becomes greater with larger k_h/k_v ratio, from k_h/k_v = 1 to k_h/k_v = 10. As the horizontal permeability increases, the decrease in the pore pressure is larger and the decrease extends more laterally from the tunnel, causing then more consolidation settlements. For an impermeable lining the extent of consolidation settlements does not depend on the ration of k_h/k_v (Wongsaroj et al., 2013).
In addition, for a permeable lining larger ratio of the horizontal permeability to the vertical (i.e. k_h/k_v = 10) will lead to a greater magnitude of change in the horizontal diameter and, hence, in the tunnel squatting deformation.

The coefficient of earth pressure at rest K_0 also plays an important role, as a reduction in K_0 causes greater settlement, inducing more squatting deformation of the tunnel lining in the long-term. This is due to the soil providing less horizontal stress upon the lining.

The applicability of the mentioned method was validated against two case studies: St. James's Park and Heathrow Express Tunnels. The prediction method reproduced a realistic trough shape, however, it might be restricted by the knowledge of soil and lining in-situ permeability as the prediction can drastically change by varying the mentioned parameters.
Both vertical and horizontal surface displacements distributions were also provided by the application of different equations.

Further studies conducted by Wang et al. (2012) highlighted the influence of soil creep and flow boundary condition on the long-term ground settlement behaviour above a shallow tunnel in soft ground.

Shen et al. (2014) also studied the long-term settlement behaviour of Shanghai metro tunnels. By examining field observations and employing numerical modelling, Shen et al. (2014) observed significant long-term settlement and differential settlement, leading to longitudinal deformation.

The hydraulic performance and the influence of a cross passage in London underground tunnels on the ground response were also investigated (Li, 2014). From the results of a series of 3D soil-fluid coupled finite element analyses, Li (2014) found out that for closely-spaced twin tunnels the effect of a cross passage on the long-term surface ground settlement is relatively negligible. Indeed, the soil consolidation due to drainage into twin tunnels is much greater than the additional drainage effect by the cross passage. In addition, the hydraulic performance of a cross passage behaves more like a bigger tunnel rather than a small single tunnel in the middle.

Recently, Qiu et al. (2018) employed three-dimensional FE analysis to investigate the long-term settlement performance of a loess section tunnel in China, using jet grouting reinforcement to improve tunnel stability. The results showed that nearly 90 % of long-term settlement occurred within the first 60 days after tunnel

construction, with a significantly lower consolidation settlement rate when the reinforcement technique is adopted.

2.2.1 Role of tunnel lining and soil permeability

The effectiveness on how a tunnel acts as a drain depends on the permeability of the tunnel lining and the immediately surrounding soil. In the Jubilee Extension Line (JLE) Contract 102, data showed that most of the tunnels were visibly wet to varying degrees, supporting the concept that tunnels in London clay act as a drain, introducing then a new drainage boundary condition and, hence, leading to long-term reduction in pore pressures with associated consolidation settlements (Shin et al., 2002; Wongsaroj et al., 2007; Mair, 2008).

Recent measurements of pore pressures taken around five bolted cast iron tunnels in London clay also confirmed that tunnels act as a drain. A clear trend of decreasing pore pressure close to the tunnel was observed (Mair, 2008) (Figure 2.2).
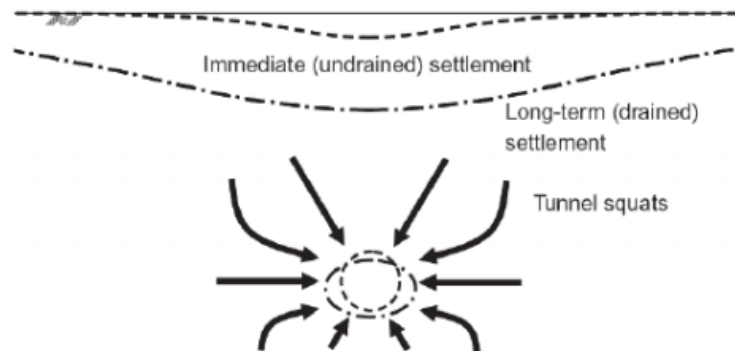
Figure 2.2. Tunnel acting as a drain in London clay (Mair, 2008).

As the long-term settlements occur with time, the surface settlement profile changes over the period and usually the normal Gaussian curve cannot be used to fit the consolidation settlement profile. This is mainly due to the widening of the settlement trough; O'Reilly et al. (1991) reported a settlement trough widening by two-three times. Bowers et al. (1996) showed that for the Heathrow Express trial tunnel case, over a period of three years after tunnel construction, great differences were found between the Gaussian settlement profile and the data. In particular, it was observed that in the long-term the Gaussian troughs were three times wider than the ones in the short term. Reporting on measurements from St. James's Park,

Nyren (1998) also noted a widening in the post-construction settlement trough. Results from numerical analyses conducted by Harris (2002) showed surface settlement extended to a wider zone than volume loss movements.

In the Jubilee Line Extension project Contract 102 in St. James's park and Heathrow Express trial tunnel, Wongsaroj et al. (2013) showed that the rate of consolidation settlement is very sensitive to the permeability of the soil. Mair (2008) stated that in situ measurements of horizontal permeability from head-tests in the piezometers confirmed that the permeability of London clay may vary significantly, and its variation can reach two orders of magnitude (from about 5×10^{-11} m/s to 5×10^{-9} m/s). This may be due to layering within London clay, as the units on the east part of London clay basin showed lower permeability than the one in the western and central parts (Hight et al., 2007). Significant deepening and widening of the settlement trough with the increase of the permeability anisotropy (for values of k_h/k_v from 1 to 4) were also observed by Mair (2008), whereas the value of the maximum settlement S_{max} at tunnel axis doubled. Harris (2002) highlighted that both the magnitude and the rate of settlement were greatly influenced by the soil permeability profile.

Wongsaroj (2005) also investigated the influence of soil permeability within the layering divisions of London clay on the long-term behaviour, by simulating different permeability profiles. This allowed simulating more accurately the long-term ground movements. Therefore, choosing appropriate values of k_t and k_s (lining and soil permeability respectively) is very important in order to make better predictions of the long-term settlements (Wongsaroj et al., 2013). Specific leakage associated with segmental lining joints should also be considered in the FE analysis (Mair, 2008).

The initial pore pressure distribution prior to tunnelling also influences the magnitude and rate of long-term settlement (Mair, 2008). This was confirmed by piezometers measurements taken at two different sites: St. James's Park and Elizabeth House, where a hydrostatic regime and an underdrained profile due to deep-level pumping were found respectively in the London clay. From long-term settlement monitoring, it has been noted that for St. James's Park site considerable consolidation settlements occurred, reaching 80 mm after 11 years of which only the 20% were observed at Elizabeth House site. This may be due to differences between

the two sites such as relative soil-lining permeability and the initial pore pressure distribution in the ground before tunnel construction.

Results show that long-term surface movements due to the construction of a single tunnel in London clay mainly depend on the permeability of the lining relative to the one of the surrounding soil (Wongsaroj et al., 2013).

Upon the effort of Wongsaroj et al. (2013), Laver et al. (2016) extended his work by proposing a new definition of relative soil-lining permeability index RP, in order to describe the dependence of ground movements upon permeability, which governs many aspects of consolidation behaviour. The new derivation of RP considers a more realistic flow regime in the tunnel such as a radial seepage flow, which is assumed to be uniform around the tunnel (Figure 2.3b).

By equating the volumetric flow rate through the soil per unit tunnel length q_s with the one through the lining q_t and by applying Darcy's law, a new expression of RP was derived (Laver et al., 2016):

$$RP = \frac{D_T \gamma_w \, K_T}{2k_S} \ln\left(\frac{2C_{clay}}{D_T} + 1\right) \tag{2.11}$$

where:

- D_T is the tunnel diameter

- k_S is the soil permeability that for anisotropic soil can be evaluated as $k_S = \sqrt{k_v k_h}$

- C_{clay} is the clay cover above the tunnel crown

- K_T is the lining seepage coefficient ($k_t/\gamma_w t_T$)

- t_T is the lining thickness

- k_T is the lining permeability

The relative soil-lining permeability index RP aforementioned is plotted against a dimensionless surface settlement DS, which equation was firstly developed by Wongsaroj (2005) as follows:

$$DS = \frac{NS_{cmax(SS)} - NS_{cmax(SSI)}}{NS_{cmax(SSI)} - NS_{cmax(SSP)}} \tag{2.12}$$

$NS_{cmax(SSI)}$ is the normalised long-term maximum surface settlement for the case with an impermeable tunnel lining whereas $NS_{cmax(SSP)}$ is the normalised long-term maximum surface for the case with a fully permeable lining, and $NS_{cmax(SS)}$ is the normalised long-term maximum surface settlement for a particular case.

Based on the results of numerical FE analysis on long-term ground settlement due to a single tunnel, Laver (2010) developed an empirical equation of $DS = 1/(1 + 1.4RP^{-1})$ and a distinctive S-shaped curve was observed when plotting RP versus DS. Data from numerical FE analysis conducted by Laver (2010) for different values of volume loss, lining permeability and cover-diameter ratios (C/D) fall within a thinner band compared to the one noted by Wongsaroj (2005) (Figure 2.4). Mair (2008) also conducted a parametric study and the results fall in the same range proposed by Wongsaroj (2005). The Figure 2.4 shows that the tunnel lining is defined to be fully impermeable for a value of RP less than 0.1 with DS = 0 whereas is said to be permeable when the value RP is greater than 100 with DS = 1. Between values of RP that go from 0.1 to 100, the tunnel lining is expected to be partially drained. Therefore, these ranges allow to determine whether a lining-soil system is likely to act as a permeable or an impermeable one.
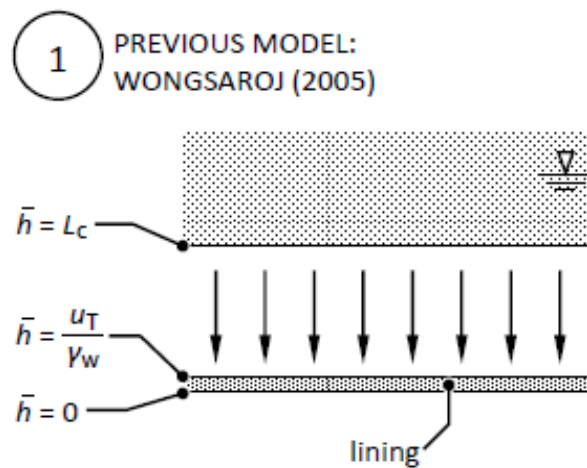
(a)
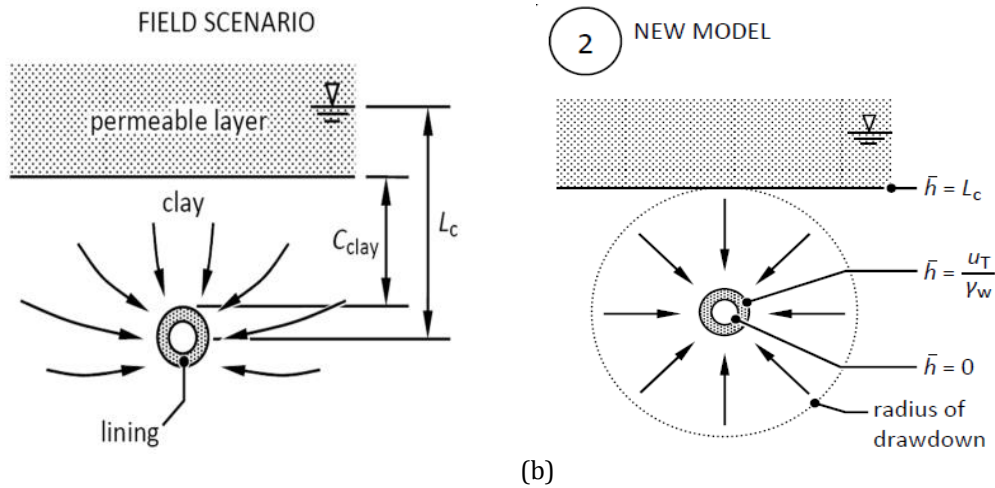
Figure 2.3. Mathematical models for deriving relative soil-lining permeability: (a) Wongsaroj (2005) and (b) Laver e al. (2016).
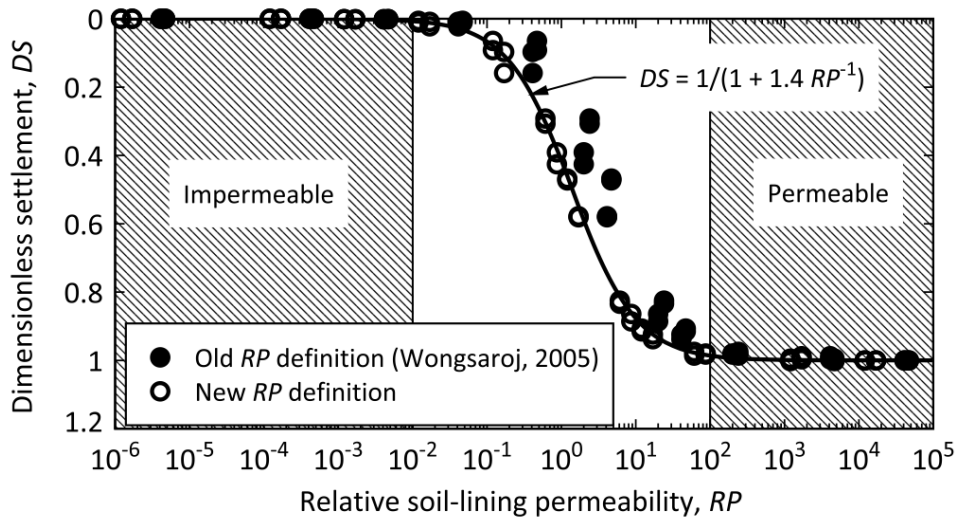
Figure 2.4. Relative soil-lining permeability (RP) against dimensionless settlements DS (Laver et al., 2016).

2.3 Twin-tunnel interaction and cross-passage

Frequently tunnels are constructed in pairs. The presence of twin tunnels alters the original soil arching generated by a single tunnel, introducing then further drainage boundaries during consolidation if the lining is permeable. The long-term response of twin tunnels was investigated by Laver (2010), who conducted finite element analyses of twin tunnels. Laver (2010) reported that the long-term

behaviour of twin tunnels excavated simultaneously side by side is influenced by the volume loss, cover-diameter ratio (C/D) and separation to depth ratio (d'/z_0).

Laver (2010) also identified three possible key twin tunnels interaction mechanisms during consolidation, listed as follows.

Mechanism A: strain field interaction. Twin tunnel interaction causes larger strains than those of a single-tunnel. As a result, since soil stiffness behaviour is usually non-linear, larger soil strain induced by twin tunnel during tunnel excavation and consolidation may lead to softening of the soil, which is due to different causes. Hence, three different mechanisms are distinguished:

- **Mechanism Ai**: **new drainage boundary.** The new drainage condition introduced by the second tunnel may cause further settlements when the lining is permeable and without volume loss.

- **Mechanism Aii: excavation interaction with a permeable lining.** The interaction due to the excavation of two tunnels generates softening of the soil and hence would augment the consolidation strain of Mechanism Ai.

- **Mechanism Aiii**: **excavation interaction with an impermeable lining.** As the lining is impermeable, the interaction during excavation allows further swelling in the long-term.

Mechanism B: flow supply restriction. The ability to supply water flow by the soil surrounded two tunnels which are closely-spaced with a permeable lining is restricted by the finite permeability of the soil itself. Hence, reduced drainage effects result in fewer consolidation effects.

Mechanism C: lateral soil compression. As the consolidation takes place, a fully permeable lining tends to squat. For two tunnels closely-spaced the soil column in between is compressed, inducing a vertical extension of the soil column and reducing surface settlement.

Results from a parametric study showed that the influence of each interaction mechanism depended upon the twin-tunnel geometry and lining permeability. Furthermore, the interaction amplifies surface settlements and has different effects on horizontal and vertical movements: the former can double whereas the latter can increase considerably. Therefore, twin side-by-side tunnels interaction should be accounted for in the long-term behaviour.

Further study to examine the long-term behaviour of a cross passage between closely spaced twin tunnels was carried out by Li (2014). Significant structural deformation and groundwater infiltrations were observed near cross passage of Shanghai metro (Shen et al., 2014).

Li et al. (2015) reported minor influence on surface settlement when a cross passage is excavated, compared to the magnitude of ground settlement due to twin tunnels construction, suggesting that the ground consolidation due to the drainage into twin tunnels is much greater than the additional drainage effect by the cross passage. Also, results from the hydraulic performance of a cross passage showed that the mechanism of a cross passage with twin tunnels may behave like a big circular tunnel circumscribing the twin tunnels (Figure 2.5a), providing a curve which well fit the equation proposed by Laver (2010) (Figure 2.5b).

(a)

(b)
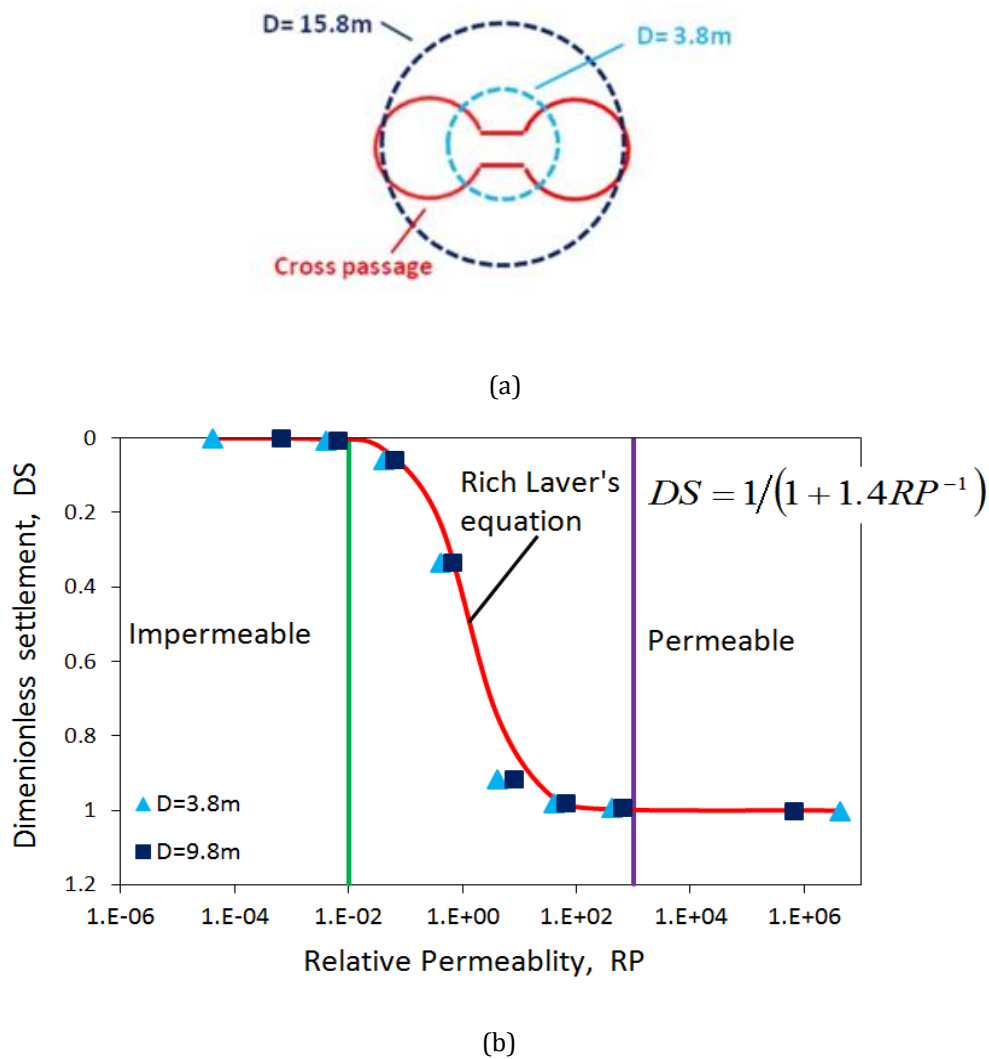
Figure 2.5. (a) Equivalent tunnel diameter (Soga et al., 2017) and (b) Dimensionless settlement against the relative permeability (Li et al., 2015).

2.4 Long-term tunnel lining behaviour

2.4.1 Lining loads for a single tunnel

Many field observations agree that tunnel lining load builds up after tunnel excavation until a steady-state drainage condition is reached (Soga et al., 2017). Groves (1943) firstly stated that a cast-iron tunnel lining in London clay reached the full overburden within two weeks. Ward and Thomas (1965) also observed that for cast iron large tunnels, diametric changes were still measured after six years, reaching the 75 % of full overburden. Peck (1969) observed a logarithmic increase of the lining load with time for tunnels in London Clay, reaching larger loads than the full overburden. For the Jubilee Line Extension tunnel, Bowers and Redgers (1996) reported lining loads of 40 % and 50 % of full overburden after 100 days at tunnel spring line and at tunnel crown respectively.

Most of the tunnels excavated in clays exhibit squatting deformation after construction, as the vertical diameter decreases and the horizontal diameter increases (Nyren, 1998). Further observations on lining loads were reported by Mair (1994), observing larger vertical loads compared to the horizontal loads. Additionally, Mair and Taylor (1997) noted that the horizontal load was about 70 % of the vertical load at Regent's Park. A similar observation was also reported by Dimmock (2003), reporting an increase in both vertical and horizontal load as the soil consolidates, but recording much larger vertical loads than the horizontal.

Shen et al. (2014) also observed that most of the shield metro tunnels in the soft deposits of Shanghai deform into the shape of a horizontal ellipse in the long-term, with the greatest diametrical distortion recorded at the ring adjacent to the cross passage.

Li et al. (2015) reported that after tunnel excavation in stiff London clay, the lining develops further squatting as the soil consolidates, and most of the tunnel squatting builds up within 2000 days after construction. Less tunnel squatting was instead observed for a cross passage opening, as it's pushed horizontally by soil loading and due to a reduction in its stiffness tends to deform back to the original shape (Li, 2014).

Wongsaroj (2005) found similar trends of tunnel lining deformation when analysing the long-term tunnel lining response in London clay through parametric

studies for a combination of the cover-diameter ratio (C/D), tunnel lining permeability, volume loss in the long-term and different values of permeability anisotropy.

The variation in the hoop force-bending moment was observed from the end of the construction phase until a steady state condition. In particular, for an impermeable tunnel lining, a small change in the magnitude of bending moment from the end of construction until the long-term steady-state condition was observed.

The distribution of load in the lining was found to be highly influenced by relative tunnel lining permeability, with an impermeable lining bearing load during consolidation up to 60 % of full overburden, compared to the 45% of full overburden of permeable linings (Shin et al., 2002). As soil consolidates, Wongsaroj (2005) detected a larger change in the horizontal diameter for a permeable lining (i.e. K_T= 1e-11) compared to a less permeable lining (i.e. K_T= 1e-13), but smaller hoop force at both the tunnel crown and the tunnel axis level, leading to more squatting in the long-term.

Mair (2008) stated that permeable linings tend to squat, whereas impermeable linings do not exhibit this deformation mode. However, the assumption of a uniform permeability at tunnel lining may not predict accurately tunnel lining loads, due to the presence of leaks and joints (Mair, 2008). In Shanghai metro tunnels, structural deformation has led to significant opening of the joints, resulting in groundwater infiltration, especially at the cross passage sections (Shen et al., 2014).

Leakage from tunnel joints, cracks and grouting holes will lead to an increase of ground loading and tunnel lining deformation (Shin et al., 2012).

To this end, Wongsaroj (2005) endeavoured to replicate a non-uniform tunnel lining permeability when simulating the behaviour of St. James's Park, resulting in a better match with field observational data.

As the tunnel lining becomes more permeable, the bending moment at the tunnel crown decreases during consolidation while it increases at the tunnel spring line, resulting in a squatting deformation of the tunnel lining in the long-term. There is a small reduction in the hoop force at the crown but a significant increase in hoop force at the spring line. Additionally, with an increase of permeability anisotropy (k_h/k_v), the change in bending moment and hoop force becomes larger. More significant horizontal diameter change and, therefore, a squatting deformation was also

observed for a permeable lining, as the permeability anisotropy increases (Wongsaroj, 2005).

However, simulations carried out with smaller values of volume loss gave a larger hoop force in tunnel lining, with positive bending moment at the tunnel crown and negative at the spring line level. This suggests that the tunnel may elongate in the vertical direction. Moreover, Wongsaroj (2005) observed that when the tunnel lining is impermeable the hoop force increases more at the tunnel crown than at the spring line, which can lead to a further elongation in the long-term. For a permeable tunnel lining, instead, tunnel squatting deformation of the tunnel lining is observed, as the bending moment decreases at the crown and increases at the tunnel axis level. In conclusion, although the magnitude in the hoop force in tunnel lining decreases with an increase of volume loss in the long-term, the deformation of tunnel lining is greater with also a bigger change in the magnitude of bending moment.

2.4.2 Effect of groundwater condition

Aged tunnels are commonly subjected to tunnel maintenance due to leakage problems and specifically long-term hydraulic deterioration of the drainage systems (Shin, 2010; Shin et al., 2012). This would develop pore water pressures on tunnel lining with time, resulting in further tunnel lining deformations. However, the evaluation of pore water pressure behind the lining is often difficult to assess. Additionally, there are no well-known tunnel design guidelines for evaluating the water pressures behind the lining (Yoon et al., 2014). Analytical solutions for fully permeable circular tunnels in homogeneous ground conditions were proposed by Shin (2010). Further, numerical investigations were also performed for non-circular tunnel shape by Yoo et al. (2005), by proposing characteristics relationship between relative permeability of lining and ground (k_l/k_s) for evaluating the residual water pressure p_l on the lining from the hydrostatic water pressure p_0 (Figure 2.6).
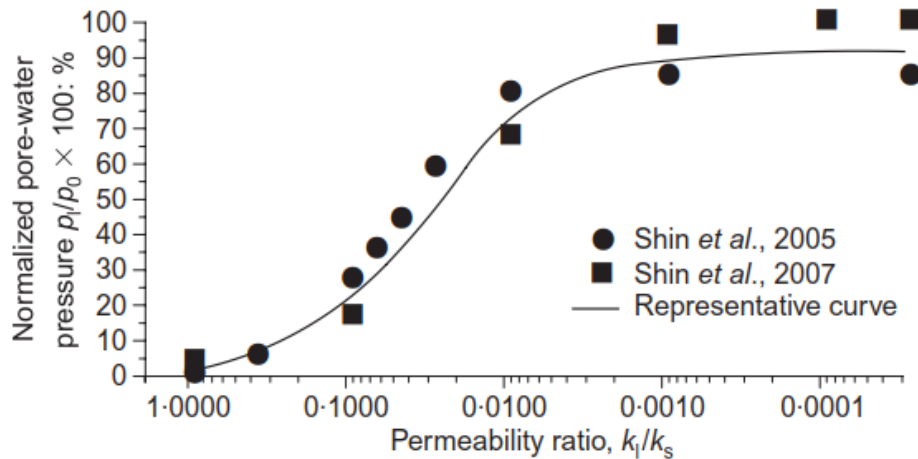
Figure 2.6. The characteristic curve of pore pressure distribution (Shin, 2010).

The progress of the hydraulic deterioration of the tunnel drainage system and the consequent change in the pore water pressure for segmental linings was also investigated using FE analysis (Shin et al., 2012). The results showed that the hydraulic deterioration of the tunnel causes a small increase in the ground loading and lining deformation of joints, with an increase of tunnel leakage.

More recent studies include those of Yoon et al. (2014), in which the effect of water pressure development on long-term tunnel performance was investigated through coupled numerical analysis, and the hydraulic deterioration was modelled by decreasing the permeability of solid elements representing the drainage filter.

Fang et al. (2016) also investigated the effect of external pore pressure on the tunnel lining behaviour, on a laboratory scale, due to a reduced drainage capacity with time. The external pore pressure was applied behind the liner of large cross-section tunnels, through a developed apparatus. The obtained results showed that the application of the external pore pressure caused the increase of bending moment and hoop thrust along the lining, with the development of cracks which first appeared at the tunnel knee, tunnel invert and lastly at the tunnel crown.

2.4.3 Effect of tunnel shape

The tunnel lining deformation and the development of water pressure on the lining strongly depend on the tunnel shape and hydraulic boundary conditions (Yoon

et al. 2014). Tunnel shape plays an important role when evaluating tunnel structural behaviour as the drainage system deteriorates (Yoon et al., 2014).

Numerical analyses of three different tunnel cross sections (circular, egg and horseshoe-shaped) located in one ground layer showed a significant increase in lining load when the hydraulic deterioration of drainage system progressed, which was simulated by decreasing the lining permeability. The pore water pressure distribution on a circular tunnel was observed to change smoothly from the tunnel crown to invert for a circular tunnel, whereas for non-circular tunnels the water pressure slightly increased at the tunnel corners due to seepage concentrations (Yoon et al., 2014).

Yoon et al. (2014) observed that the maximum ground load for non-circular tunnels increased more than double compared to the load on circular tunnels. Additionally, horseshoe-shaped tunnels exhibit the largest vertical displacement at tunnel invert (i.e. at the middle point) and significant tensile stress around tunnel corners.

2.4.4 Effect of swelling ground

Swelling phenomena are commonly observed in tunnels in central Europe crossing anhydrite, marls and clays, swelling rocks and gypsum formations (Gysel, 1977; Alonso et al., 2013). Tunnelling in swelling ground often leads to structural damage and the consequent increase of time and costs (Wittke, 2006).

The swelling of the rock, which is usually attributed to both physical and chemical processes, contributing to strength degradation, is due to the increase in volume of some clay minerals (for instance clays like smectite, montmorillonites) and anhydrite when in contact with water (Lombardi 1984; Alonso et al., 2013; Ramon et al., 2017). This can result in the development of tremendous swelling pressures if not prevented (Wittke, 2006). Particularly, the swelling was found to occur in the tunnel floor area, which is associated with tunnel heave during tunnel construction (Lombardi, 1984; Kovari et al., 1988; Einstein, 1996; Alonso et al., 2013), as shown in Figure 2.7.
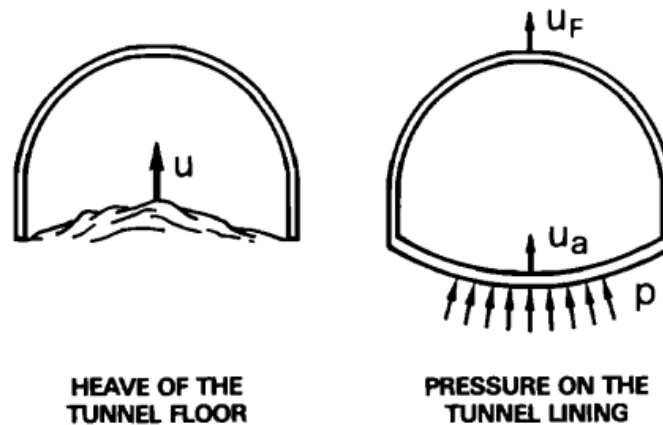
Figure 2.7. Effect of swelling in tunnelling (Kovari et al., 1988).

Lombardi (1984) stated that the horseshoe cross-section tunnels at CERN experienced tunnel floor heave due to the swelling potential of certain marl bands, whereas circular tunnels do not. The tunnel floor started to heave during the construction of the Pfaender tunnel in Austria (Kovari et al., 1988). Wittke (2006) reported the behaviour of various tunnels for the construction of a project in the area of Stuttgart (Germany), located in the swelling Gypsum Keuper. No tunnel heave due to swelling was encountered during tunnel excavation. Yet, many years after construction levelling measures showed heaving of tunnel invert.

Alonso et al. (2013) also observed swelling-induced tunnel damage associated with the precipitation of the gypsum crystals from clayey rock in presence of water for the Lilla tunnel, in Tarragona (Spain).

2.5 Summary

This chapter presents the review of the long-term investigation of the mechanisms observed on ground surface and the tunnel lining performance after tunnel excavation in clayey soil.

Particularly, the review has shown the importance of relative soil-lining permeability on the long-term tunnel performance. In fact, whether the lining is fully permeable or impermeable, different mechanisms occur after tunnel construction. In the case of tunnel being fully permeable, analyses show that significant tunnel squatting is observed whereas the tunnel develops minor lining forces compared to the impermeable lining, which causes heave on ground surface and the development of more important lining forces.

However, in aged tunnels long-term effects such as the change in the groundwater condition behind tunnel lining due to the deterioration of the tunnel drainage system are of paramount importance, as water pressure may develop on the tunnel lining, resulting in further tunnel loading in the long-term. To this end, also the tunnel geometry (i.e. circular, horseshoe and egg shape) was found to have an influence on the tunnel performance, leading to the development of lining load when analyzing the long-term behaviour.

References

Addenbrooke, T.I. (1996). Numerical analysis of tunnelling in stiff clay. PhD thesis, University of London, UK.

Alonso, E.E. & Ramon, A. (2013). Heave of a railway bridge induced by gypsum crystal growth: field observations. *Géotechnique*, **63**, No. 9, 707-719.

Barratt, D.A., O'Reilly, M.P., Temporal, J., (1994). Long term measurement of loads on tunnel linings in overconsolidated clay. Tunnelling '94, London, pp. 469-481.

Bowers, K. H., & Redgers, J.D. (1996). Discussion: Observations of lining load in a London clay tunnel. *Proceedings of the international symposium on geotechnical aspects of underground construction in soft ground*, London, pp. 335.

Bowers, K. H., Hiller, M.D. and New, B. M. (1996). Ground movement over three years at Heathrow Express trial *tunnel. Proceedings of the international symposium on geotechnical aspects of underground construction in soft ground*, London, pp. 557-562.

Dimmock, D.A., O'Reilly, M.P., Temporal, J. (1994). Long-term measurement of loads on tunnel linings in overconsolidated clay. *Tunnelling '94,* 469-481, London.

Fang, Q., Zhang, D.L., Li, Q., Wong, L.N.Y., (2016). Effects of twin tunnels construction beneath existing shield-driven twin tunnels. Tunnelling Underground Space Technology 45, 128-137.

Gysel, M. (1977). A contribution to the design of a tunnel lining in swelling rock. *Rock Mech.* **10**, No. 1-2, 55-71.

Groves, B.L. (1943). Tunnel lining with special reference to a new form of reinforced concrete. *J. Instn. Civ. Engrs*, 20, 29-64.

Harris, D.I. (2002). Long-term settlement following Tunnelling in overconsolidated London clay. *Proc. 3rd* International *Symposium on Geotechnical Aspects of Underground Construction in Soft Ground*, Toulouse, France, October 2002.

Hight, D.W., Gasparre, A., Nishimura, S., Minh, N.A., Jardine, R.J. and Coop, M.R. (2007). Characteristics of the London Clay from the Terminal 5 Site at Heathrow Airport. *Géotechnique,* **57**, 3-18.

Kovari, K., Amstad, C., Anagnostou, G. (1988). Design/construction methods: tunnelling in swelling rocks. In *Key* questions *in rock mechanics: proceedings of the 29th US symposium* (eds P. A. Cundall, R. L. Sterling and A. M. Starfield), pp. 17-32. Rotterdam, the Netherlands: Balkema.

Laver, R. (2010). Long-term behaviour of twin tunnels in London clay. PhD thesis, University of Cambridge, UK.

Laver, R.G., Li, Z., & Soga, K. (2016). Method to evaluate the long-term surface movements by tunnelling in *London clay. Journal of Geotechnical and Geoenvironmental Engineering.*

Li, Z. (2014). Long-term behaviour of cast-iron tunnel cross passage in London clay. PhD thesis, University of Cambridge, UK.

Li, Z., Soga, K., & Wright, P. (2015). Long-term performance of cast-iron tunnel cross passage in London clay. Tunnelling *and Underground Space Technology, 50,* 152-170.

Li, Z., Soga, K., & Wright, P. (2016). Behaviour of cast-iron tunnel cross passage in structures and their 3D FE analyses. *Canadian Geotechnical Journal, 53,* 930-945.

Lombardi, G. (1979). Rock mechanics at the CERN proton-antiproton facilities. In: International Society for Rock Mechanics (Ed.), 4th ISRM Congress. International Society for Rock Mechanics, Montreux. Balkema, pp. 433-436.

Lombardi, G. (1984). Underground openings in swelling rock. National Conference on Case Histories in Geotechnical Engineering. Pakistan, Lahore.

Mair, R.J., Gunn, M.J., and O'Reilly, M.P. (1981). Ground movements around shallow tunnels in soft clay. *Proceedings of 10th International Conference on Soil Mechanics and Foundation Engineering*, Stockholm, Vol.1, pp 323-328.

Mair, R.J., Taylor, R.N. and Bracegirdle, A. (1993). Subsurface settlement profiles above tunnels in clays, *Géotechnique*, Vol. 43, No. 2, pp. 315-320.

Mair, R.J. (1994). Discussion on paper 'Long-term movements of loads on tunnel linings in overconsolidated clay' by Barratt et al. (in Proceedings of Conference Tunnelling '94, London Institution of Mining and Metallurgy, Chapman and Hall). *Transaction of the Institution of Mining and Metallurgy (Section A: Mining Industry),* Vol. 103, pp. A188-189.

Mair, R.J., Taylor, R.N. and Burland, J.B. (1996). Prediction of ground movements and assessment of risk of building damage due to bored tunnelling. *Proc. International Symposium on Geotechnical Aspects of Underground Construction in Soft Ground*, London, Balkema, pp. 713-718.

Mair, R.J. and Taylor, R.N. (1997). Bored tunnelling in the urban environment: state-of-the-art report and theme lecture. *Proceedings of14[th] International Conference on soil mechanics and foundation engineering, Hamburg*, Vol. 4, 2353-2385.

Mair, R.J. (2008). Tunnelling and geotechnics: new horizons. *Géotechnique* **58**, No. 9, 695-736.

Martos, F. (1958). Concerning an approximate equation of the subsidence trough and its time factor. *In international Strata Control Congress, Leipzig, 1958 (Berlin: Deutsche Akadamie der Wissenschaften zu Berlin, Sektion fur Berfbau,1958).* Pp. 191-205.

Martinez, R., Schroeder, F. and Potts, D. (2015). Numerical study of long-term settlement following twin tunnel construction. Obras y Proyectos **17**, 23-29.

Nyren, R. (1998). Field Measurements above Twin Tunnels in London clay. PhD thesis, Imperial College, University of London, UK.

O'Reilly, M.P., Mair, R.J. and Alderman, G.H. (1991). Long-term settlements over tunnels: an eleven-year study at Grimsby. *Tunnelling'91*, London, pp. 55-64.

Peck, R.B. (1969). Deep excavations and tunnelling in soft ground. Proceeding of the 7th international conference on soil mechanics and foundation engineering, Mexico City, SOA, Volume pp. 225-290.

Ramon, A., Alonso, E. E., Olivella, S. (2017). Hydro-chemo-mechanical modelling of tunnel in sulphated rocks. *Géotechnique*, **67**, No. 11, 968-982.

Schmidt, B. (1969). Settlements and ground movements associated with tunnelling in soils, PhD thesis, University of Illinois, Urbana.

Shen, S., Wu, H., Cui, Y., and Yin, Z. (2014). Long-term settlement behaviour of metro tunnels in the soft deposits of Shanghai. *Tunnelling Underground Space Technology,* 40, 309-323.

Shin, J. H., Potts, D. M. (2003). Time-Based Two Dimensional Modelling of NATM *Tunnelling Canadian Geotechnical Journal*, 39 (3), 710-724.

Shin, J. H., Addenbrooke, T.I., Potts, D. M. (2002). A numerical study of the effect of ground water movement on long-term tunnel behaviour. *Géotechnique,* **52**, No. 6, 391-403.

Shin, J. H. (2010). Analytical and combined numerical methods evaluating pore water pressure on tunnels. *Géotechnique,* **60**, No. 2, 141-145.

Shin, J. H., Kim, S.H., Shin, Y.S. (2012). Long-term mechanical and hydraulic interaction and leakage evaluation of segmented tunnels. Soils and Foundations, 52(1): 38-48.

Soga, K, Laver, R. G. and Li, Z. (2017). Long-term tunnel behaviour and ground movements after tunnelling in clayey soils. Underground Space Vol. 2, 149–167.

Vorster, T. E. B., Klar, A., Soga, K., and Mair, R. J. (2005). Estimating the effect of tunnelling on existing pipelines. *ASCE Journal of Geotechnical and Geoenvironmental Engineering,* 131, 1399-1410.

Wongsaroj, J. (2005). Three-dimensional finite element analysis of short and long term tunnelling induced settlement in stiff clay. PhD thesis, University of Cambridge, UK.

Wongsaroj, J., Soga, K. & Mair, R.J. (2007). Modelling of long-term ground response to tunnelling under St James' Park, London. *Géotechnique* **57**, No. 1, 75-90.

Wongsaroj, J., Soga, K. & Mair, R.J. (2013). Tunnelling-induced consolidation settlements in London clay. *Géotechnique,* **63**, No. 13, 1103-1115.

Yoo, C., Kim, S.B., Shin, H.C., Baek, S.C. (2005). Effect of tunnelling and groundwater interaction on ground and lining responses. Underground Space Use: Analysis of the Past and Lessons for the Future, London.

Yoon, J.U., Han, J.W., Joo, E. J., Shin, J.H. (2014). Effects of tunnel shapes in structural and hydraulic interaction. *KSCE Journal of Civil Engineering*, 18(3): 735-741.

Chapter 3

3 CERN TT10 tunnel: investigation and instrumentation

3.1 Introduction

The large and world-famous underground particle accelerators network of the Large Hadron Collider (LHC) is housed at the European Centre for Nuclear Research (CERN) through miles of deep tunnels at around 50 to 175 m below ground. In this large underground framework, the TT10 tunnel, which is the subject of interest in this dissertation, is an inclined beam tunnel located at the French-Swiss border, on the outskirts of Geneva (Figure 3.1).
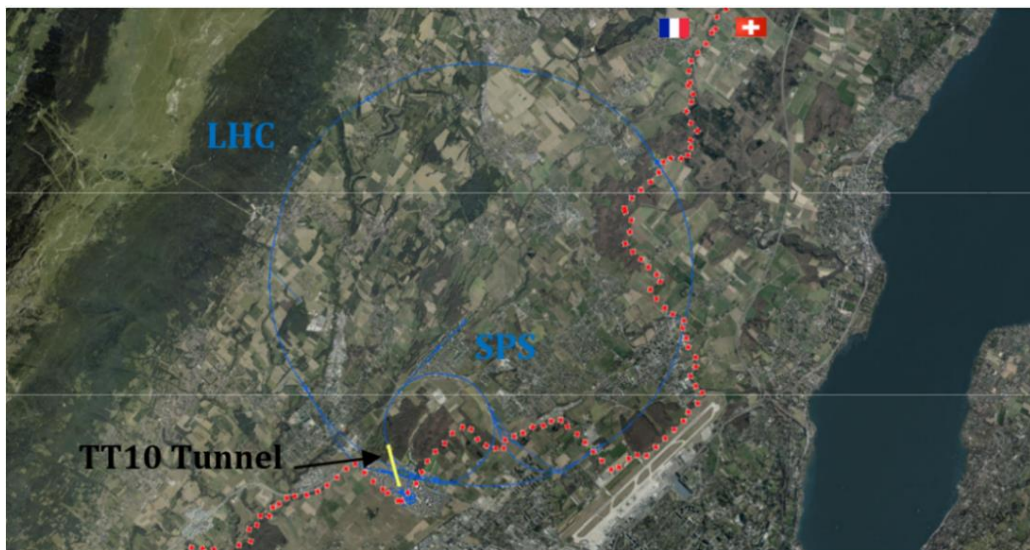
Figure 3.1. CERN underground network plan view: location of the TT10 tunnel (Photo credit: CERN GIS Portal).

This transfer tunnel connects the beam accelerator of the Proton Synchrotron (PS) circular tunnel to the 7 kilometres in circumference of the Super Synchrotron Protons (SPS), the second-largest machine in CERN's accelerator complex (Figure 3.2).
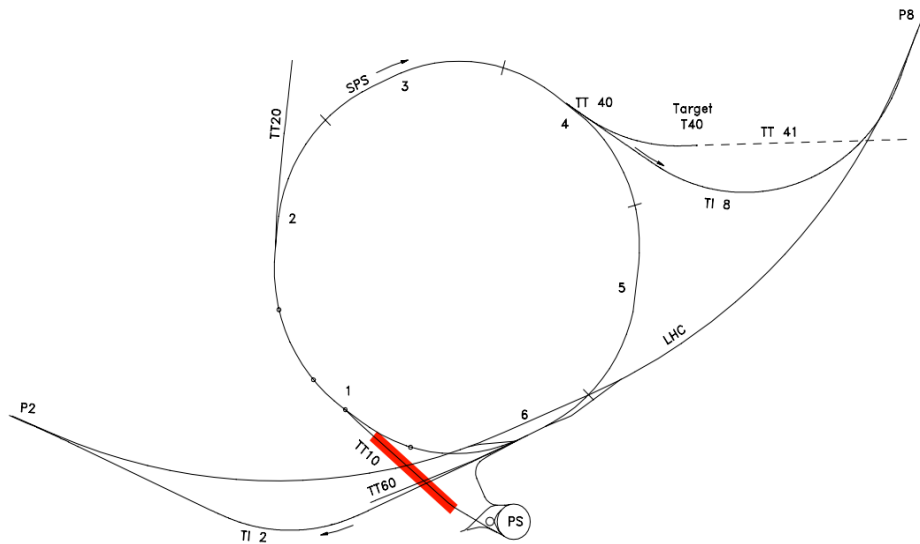
Figure 3.2. PS and SPS plan view: the TT10 transfer tunnel (Photo Credit: CERN).

3.2 Tunnel background

The main injection beamline TT10 tunnel was constructed in the 1970s in a horseshoe shape. Figure 3.3 shows the TT10 tunnel cross-section. In particular, the horseshoe cross-section consists of four parts: one circular arc in the top roof with a radius of 2.25 m, two side circular arcs of a radius of 1.25 m and a flat bottom of a length of 4 m. The tunnel presents a diameter of 4.5 m at the intrados and 5.1 m at the extrados.
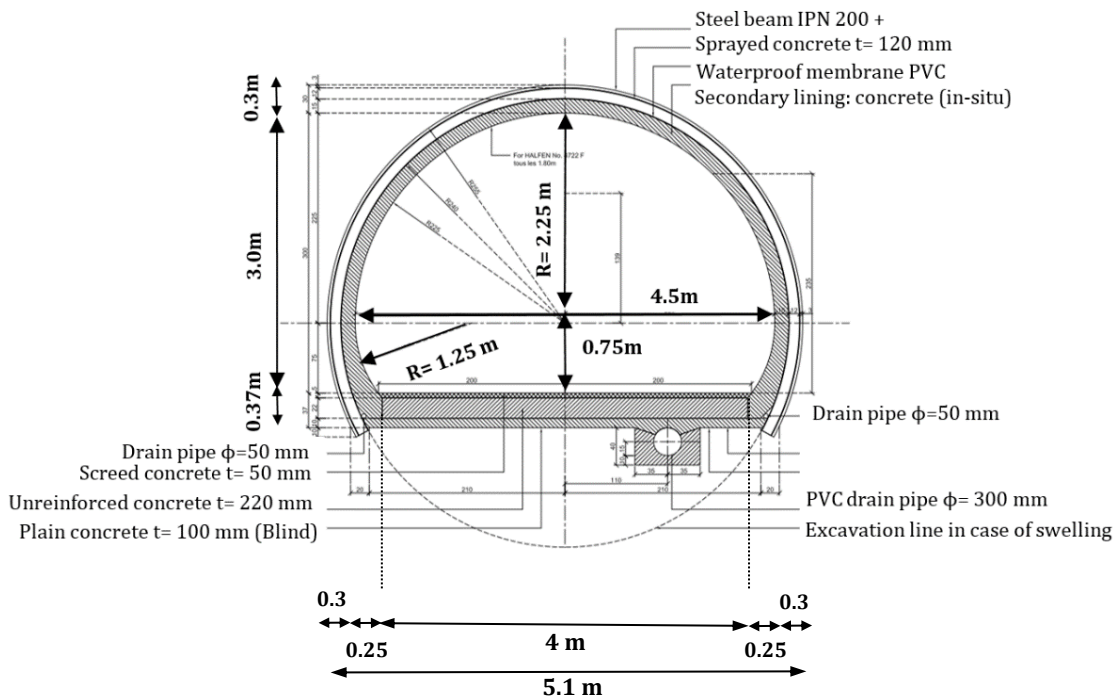
Figure 3.3. TT10 tunnel cross-section.

The tunnel excavation started in December 1972 and was performed by means of mechanical excavation method. Figure 3.4 presents each excavation stage accomplished in the multiple construction steps. The tunnel was constructed using an alpine road-header machine, with excavation span of around 1.2 m length as shown in Figure 3.4a. The initial tunnel excavation face stability immediately after the excavation was supported with the installation of a thin layer of sprayed shotcrete. Further lining support was then installed as early as required, to stabilize the excavation and prevent eventually excessive deformation with steel beam (IPN 120) and steel mesh, when the very weak rock was encountered (Figure 3.4b).

The waterproofing of the excavated tunnel was done by installing a PVC sheet membrane between the primary temporary support and the secondary permanent inner lining, avoiding possible water infiltrating from the moraine levels. The secondary lining was then poured in-situ with a thickness of 180 mm. In the floor section, a concrete slab of 370 mm in depth was placed after installing a drainage complex made of two small drainage pipes of 50 mm diameter at both sides of tunnel invert, which collects the groundwater and convey it to the main drainage pipe (ϕ= 300 mm) located below tunnel floor, 1.10 m away from tunnel axis. Therefore, the drainage conditions of the tunnel can be considered to be fully drained.

(a)

(b)   (c)
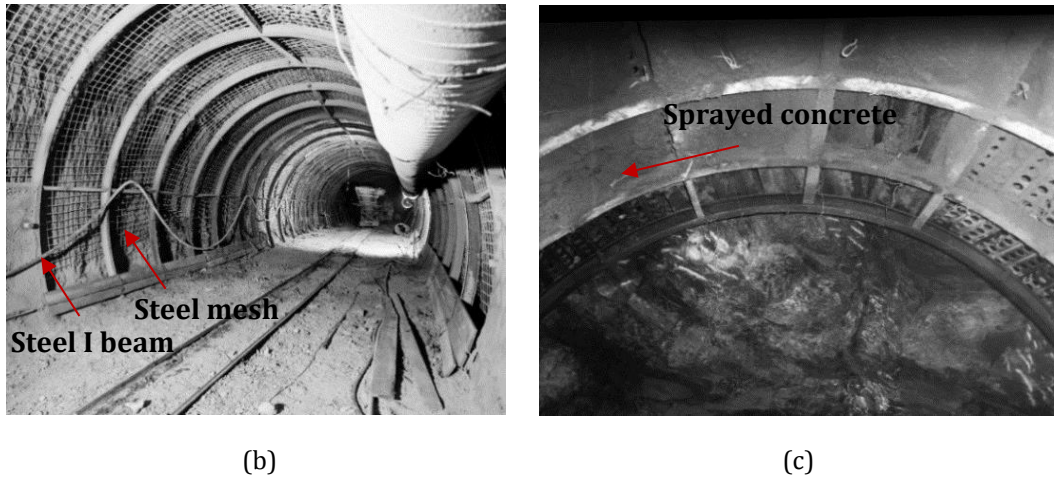
Figure 3.4. Excavation of TT10 tunnel: (a) tunnel excavation stage using an alpine road-header machine, (b) installation of the primary lining with steel I beams and steel mesh (c) Installation of sprayed concrete (Photo credit: CERN).

Table 3.1 shows a summary of TT10 tunnel lining properties, such as its materials and size. The tunnel lining of a total thickness of 300 mm is composed of: (i) the primary lining, which consists of steel beams of IPN profile sections of 120 mm height embedded in a layer of sprayed concrete of 120 mm of thickness, (ii) a cast in-situ concrete layer of 180 mm thickness and (iii) a flat bottom floor of a total thickness of 370 mm, composed of a top layer of screed concrete of 50 mm thickness, an unreinforced slab of 220 thickness and a final thin layer of 100 mm thickness made of plain concrete, after the installation of the tunnel main drainage system.

Table 3.1. Tunnel lining properties.

Member	Support Property	Size[mm]
Crown- Axis	Primary Lining (sprayed)	t= 120
Crown-Axis	Steel Beam IPN 120	h= 120
Crown-Axis	Secondary Lining (cast in-situ)	t= 180
Floor	Screed Concrete	t= 50
Floor	Unreinforced Basement	t= 220
Floor	Plain concrete	t= 100

Figure 3.5 shows the longitudinal section of the TT10 tunnel. The tunnel for the first 50 m runs with a flat gradient, after which it inclines at around 6 % (Figure 3.5).

The tunnel was entirely excavated in the molasse region, the so-called *red molasse*, an extremely heterogeneous sedimentary rock which consists of an alternate sequence of interbedded rock layers characterized by different mechanical proprieties (i.e. stiffness, strength etc). The geotechnical characterization of the molasse region will be presented in more detail in Chapter 5.
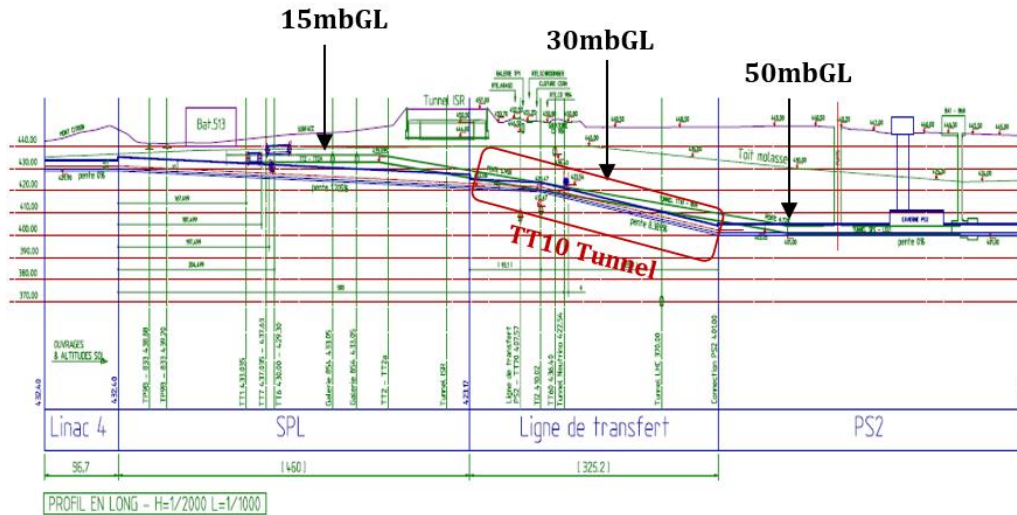
Figure 3.5. Longitudinal section of TT10 tunnel.

3.3 Tunnel lining issue: development of cracks

3.3.1 Introduction

With the aim and the need of protecting the integrity of CERN accelerator's beamline, the bulk of site investigations takes place during "long shutdown" periods, for inspecting the underground facilities and installing any potential mitigation measure.

At the beginning of the 2-year "Long shutdown 1" called LS1 that started in February 2013, strong evidence of ongoing movement was observed in several areas of the TT10 tunnel, in addition to water leakage through tunnel lining cracking.

To understand the fissures pattern, their origins and consequences on the tunnel stability, a detailed survey of the crack development was held in June 2013, with the help of a specialized team from ARUP firm.

Based on the resulting observations, the TT10 tunnel was divided into different zones as shown in Figure 3.6: the *work zone* (green area), assessed to be the least critical area, the *critical zone* (orange area), where the majority of the tunnel lining

damage occurred and the _secondary zone_ (blue area), a less damaged area but to be monitored in the longer term. The magnet ID numbers (QID) placed with an interval of around 30 m between each other, were used as a reference, with the _work zones_ located between QID 10100 – QID 101200 and QID 101500- QID 101700, the _critical zone_ assessed to be between QID 101200 – QID 101500 and the _secondary zone_ between QID 100700 and QID 100900. Figure 3.6 also shows the zoning divisions along the TT10 tunnel.

The resulting survey of the observed cracks showed that the most significant area of tunnel lining damage occurred between the magnets QID 101300 – QID 101500, with cracks between 1-5 mm of thickness, covering a horizontal tunnel distance of around 60m. Therefore, the area of interest for tunnel investigation in this study runs from the location of the ventilation shaft (QID 100700) where the tunnel cover is about 25.7 m from the ground surface, in the North-East direction (downstream direction) for about 241 m (QID 101500), as shown in Figure 3.7.
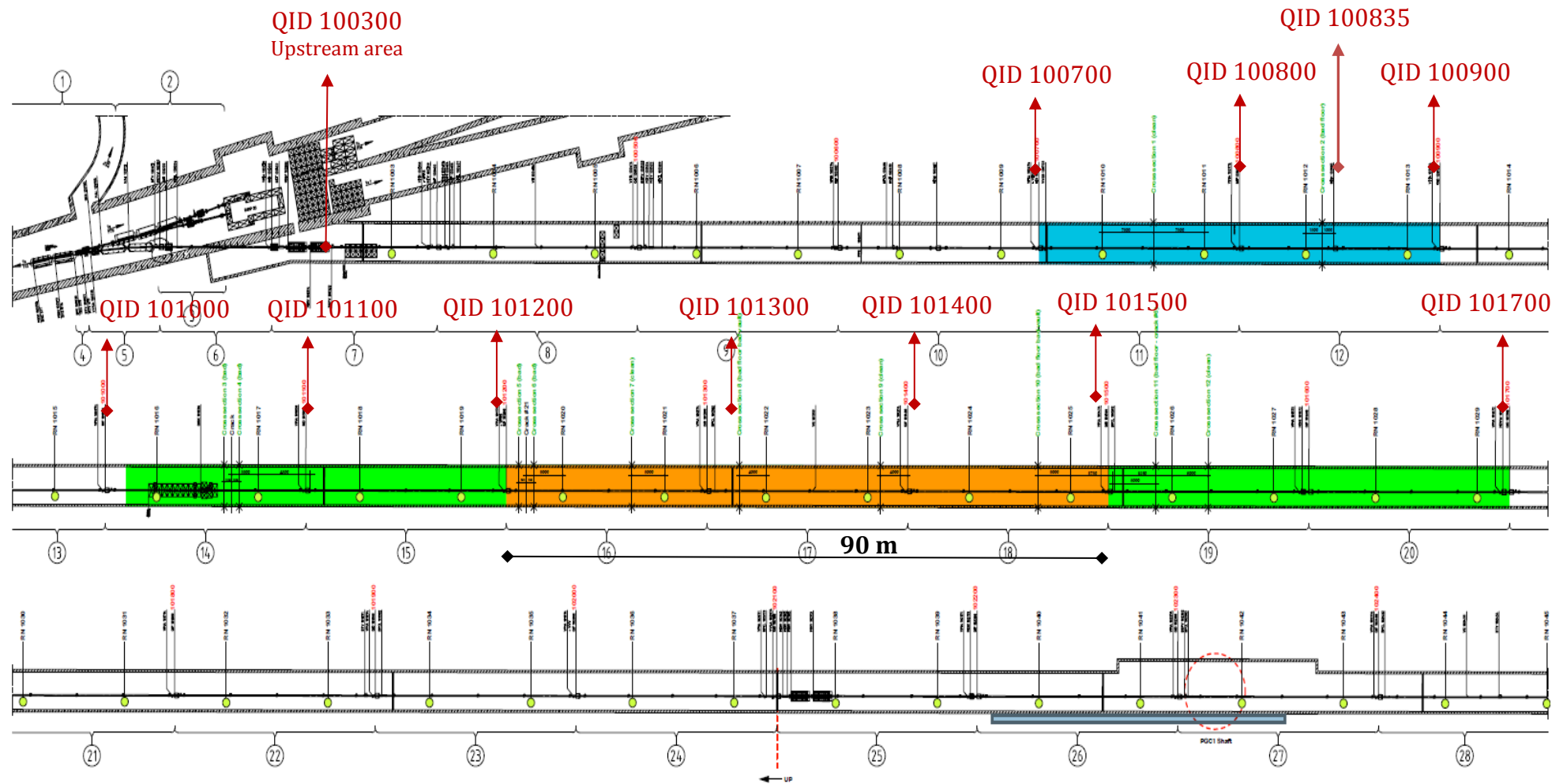
Figure 3.6. TT10 tunnel plan view with the location of the three zones: the secondary blue zone, the work green zone and the critical orange zone.
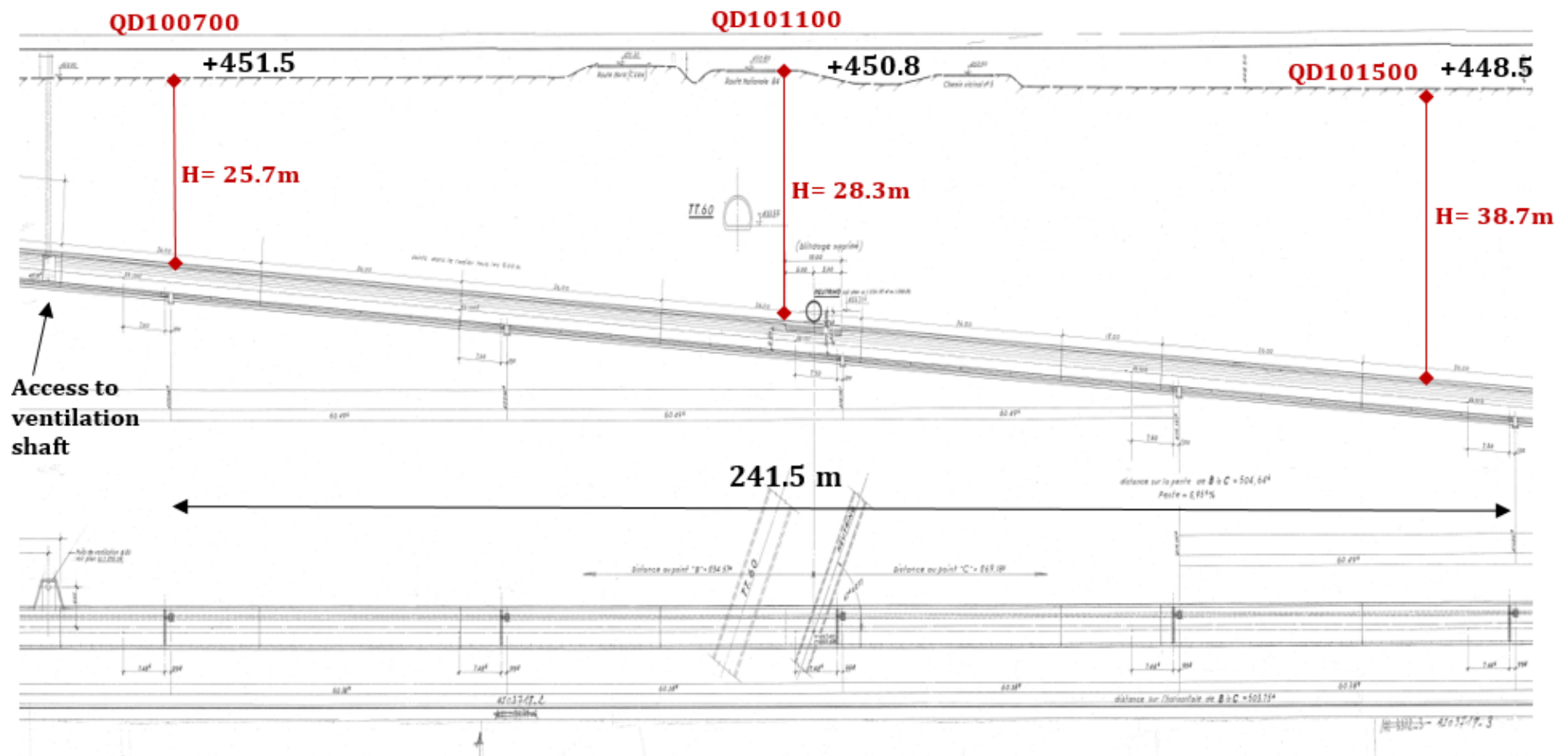
Figure 3.7. Longitudinal and plan view section of TT10 tunnel of the interested area.

3.3.2 Geology

The geology surrounding the tunnel has an impact on the above-mentioned development of cracks on the tunnel lining.

The formation in the area of the TT10 tunnel consists of highly weathered and extremely heterogeneous sedimentary rock called the *red molasse*.
The geomechanical characteristics of the sub-horizontal interbedded rocks vary significantly, going from relatively very stiff sandstones to weak marls with considerable swelling potential of the very weak lumpy marl layers (Parkin et al. 2002).

Figure 3.8 illustrates the tunnel face loggings recorded during the tunnel excavation, providing a geotechnical cross-section every 15 m along the tunnel. Variable sequences of weak marls, medium marls and sandstones are observed.

The dominant rock strata intersected within the geological section at the location of major cracks (QID 101400) are mainly weak-medium marl and very weak marl. This type of marl, called "*lie-de-vin*" *grumeleuse marl* or *lumpy marl* (highlighted in green in Figure 3.8), alters quickly in presence of air and humidity, causing a loss of strength and lastly complete disintegration (Parkin et al. 2002). These marls may show a reddish colour due to oxidation of ferric minerals caused by the increase of permeability. These lumpy marl beds have proved to be the most active movement horizons during the excavation works of the LHC underground (Parkin et al. 2002).
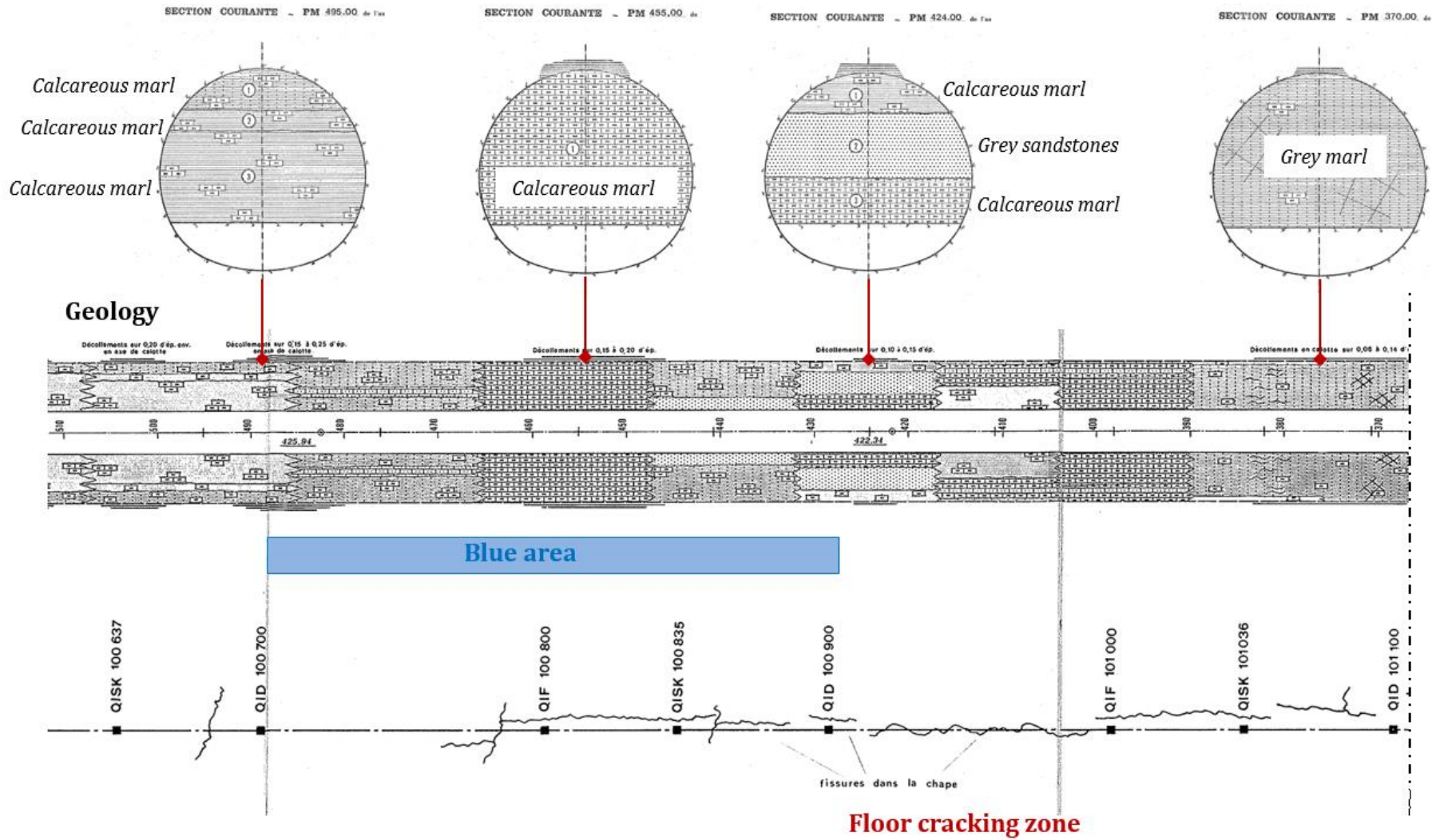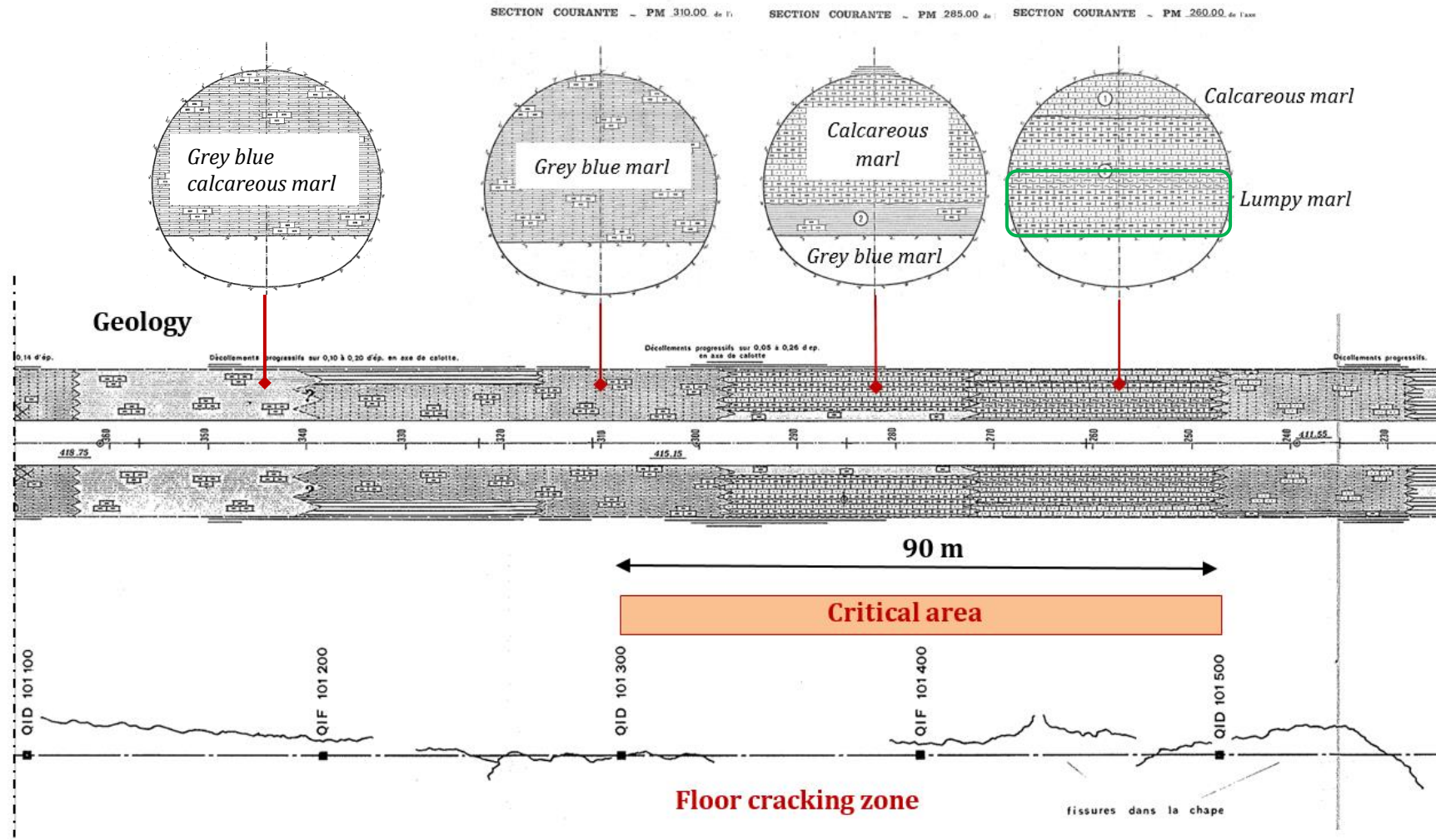
Figure 3.8. Archive records of the tunnel face loggings and tunnel floor cracking after tunnel construction (CERN).

A series of boreholes was drilled from ground surface in great depth to determine the nature of the rock strata during the SPS project. A plan view of the boreholes is provided in Figure 3.9. Yet, only one main investigation (borehole F9) was performed in the area surrounding the TT10 tunnel, carried out in 1970 (CERN, 1972).
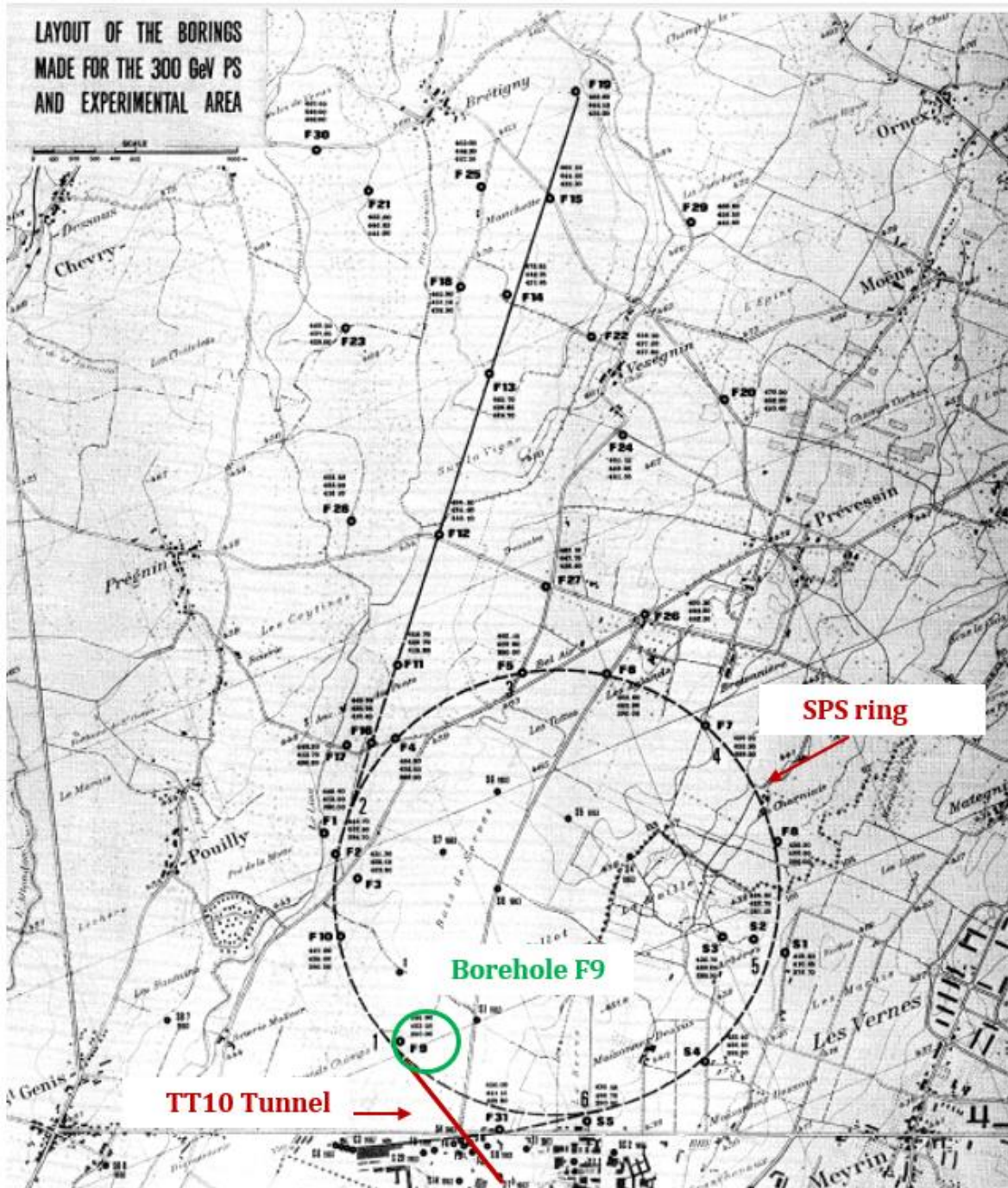
Figure 3.9. Layout of the boreholes made for the SPS project (CERN, 1972).

The topography of the top of the molasse bedrock of varying depth (Figure 3.10) is mainly the signature of glacial erosion in the molasse during the Quaternary

period. Additionally, the stratigraphy encountered is shown in Figure 3.11a, with the moraine layer (from altitude 445.20 m to 423.5 m) and the molasse region from an altitude of 423.50 m to 390 m.
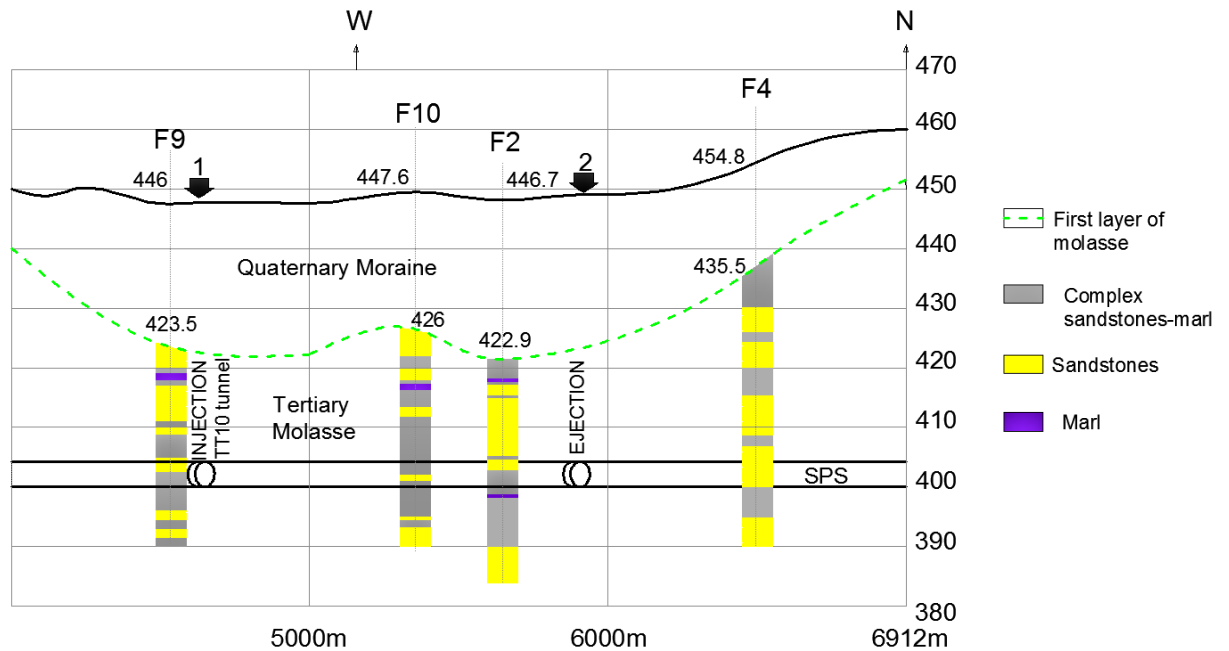
Figure 3.10. Cross-section: detection of the first layer of molasse and position of TT10 tunnel (CERN, 1972).

By knowing the geometry of the tunnel, its position within the molasse region and the geology found during tunnel excavation, the stratigraphy of the ground was traced, as shown in Figure 3.11b. In order to determine the ground stratigraphy which could represent both the ground conditions encountered during tunnel construction and during site investigation, an accurate comparison was made as shown in Figure 3.11. It is noted that the geological conditions met during the excavation phase slightly differed from those assessed from site investigation, especially in the molasse layer. For example, a layer of 6 m thickness of *hard and compact grey sandstones with some weak marl* is found from the borehole F9 from the altitude of 416 m to 410 m, which was not detected during the excavation progress, where *red-brown* and *grey-blue marls* are instead observed. However, compatibility in the findings of the subsequent layers of marls was found, principally for the weak problematic layer of lumpy marl. Particularly, from the borehole F9 a layer of *grey-blue marl a bit lumpy* is located between altitudes 400.70 m – 399.60 m

and 398.60 m – 397.10 m, which is also observed from the tunnel face logs survey between the altitudes 402.2 m – 399.5 m and 398.5 – 397 m.

Finally, the assumption of the existence of horizontally bedded layers of sandstones, weak and strong marls, in addition to some engineering judgement, will lead to the final geotechnical strata division used in this study.

		SURVEY F9					
		Geological Section			Start date 18.11.1970 End date 27.11.1970		
Stratigraphy	Altitude 448.00	Depth 0.00		N° of levels	Type of soil		
RECENT	445.20	0.80		1	Topsoil red-brown, not grainy, a bit slimy		
Quaternary	440.90	5.10		2			
					Massive clay, silty-gravelly, a bit plastic and greasy, oxidised, in sedimentary metamorphic and crystalline pebbles of 2-3 cm, 6-7 cm, and more than 13 cm.		
Moraine Wurmienne				3	Very massive clay, silty-gravelly, homogeneous and compact, dry, a bit humid and plastic, in sedimentary metamorphic and crystalline pebbles of 2-3 cm, 6-7 cm, and more than 13 cm Ømax.		
	423.50	22.50					
TERTIARY				4	Gray-beige molassic marl, weathered and oxidized.		
	421.00	25.00			Gray sandstones, with micaceous marl, homogeneous, hard and compact.		
	420.20	25.80		5			
				6	Gray-blue marl, green and 'lie-de-vin', very fine sandstones, dry and lumpy.		
	418.30	27.70		7	Variegated marl, gray-blue marl, green and 'lie-de-vin', not sandstones, shiny and tender.		
	417.60	28.40		8	Gray-blue marl, green and 'lie-de-vin', very fine sandstones, dry and lumpy, a bit friable.		
Molasse Oligocéne	416.00	30.00					
		30.90		9	Gray sandstones, marly, micaceous, hard, compact and homogeneous, with weak marls at levels 30.90 and 34.45.		
		34.45					
	410.00	36.00		10	Gray-blue marl, green and 'lie-de-vin', very fine sandstones, dry and hard.		
	409.40	36.60		11	Gray sandstones, marly, micaceous, hard, compact and homogeneous.		
	409.00	37.00		12			
	407.10	38.90		13	Gray-green marl, very fine sandstones, dry hard and compact.		
	406.70	39.30		14	Gray sandstones, cement marl, hard, homogeneous and compact.		
	406.20	39.80		15	Gray-blue marl, green and 'lie-de-vin', very fine sandstones, friable.		
	405.10	40.90		16	Gray marl, very fine sandstones, with regular small marl levels.		
					Gray sandstones, marly, micaceous, hard, homogeneous and compact with soft marl between levels 43.00 - 43.40.		
	402.60	43.40		17	Gray marl, very fine sandstones, hard, compact, homogeneous.		
	400.70	45.30		18	Gray-blue marl, green and 'lie-de-vin', very fine sandstones, a bit lumpy, relatively homogeneous.		
	399.60	46.40		19	Gray marl, fine sandstones, hard, compact, homogeneous.		
	398.60	47.40		20	Gray-blue marl, green and 'lie-de-vin', very fine sandstones, a bit lumpy, with dry cracks.		
	397.10	48.90		21	Gray marl, fine sandstones, hard, compact, homogeneous.		
	396.40	49.60		22	Gray-blue marl, green and 'lie-de-vin', very fine sandstones, a bit lumpy, with dry cracks.		
	395.10	50.90		23	Gray marl, fine sandstones, hard, compact, homogeneous.		
	394.10	51.90		24	Gray sandstones, marly, micaceous, hard, homogeneous and compact.		
	393.20	52.80		25	Gray marl, fine sandstones, hard, compact, homogeneous.		
	392.00	54.00		26	Gray marl, fine sandstones, hard, compact, homogeneous.		
	391.50	54.50		27	Gray sandstones, marly, micaceous, hard, homogeneous and compact.		
	390.50	55.50		28	Gray-green marl, very fine sandstones.		
	390.00	56.00					

		Face logs Survey	
		Geological Section	
Stratigraphy	Altitude		Type of soil
Quaternary Moraine Wurmienne			
	431.2		Gray-blue marl, green and calcareus sandstones, compact, homogeneous a bit dump but indurated
	430.2		
	427.7		Gray-blue marl, green and calcareus sandstones, compact, homogeneous a bit dump but indurated
			Dark brown-red and gray-blue marl calcareous compact, homogeneous
	425.5		
	424.7		Marly-limestone gray, compact, homogeneous, hard and dry
TERTIARY			Marly-limestone red-brown with some patches gray-blue and green, compact, homogeneous, hard
	421		Gray sandstones, homogeneous, hard and compact.
	419.45		Gray marl, very fine sandstones, dry, homogeneous, and indurated
	418.35		Green calcareous marl and a bit green, compact, homogeneous, very hard and dry
	415.6		
Molasse Oligocéne			Red-brown and gray-blue marl, and green coarsely lumpy, dry
	411.2		Dark brown-red marl and a little gray-blue, not silty, a bit dump, weak and brittle
	408.4		Gray-green marl, very fine sandstones, dry hard, homogeneous and compact
	405		Gray sandstones, marly, compact, homogeneous with marl
	402.9		Gray-blue marl, green, compact, a bit dump, homogeneous, calcareous
	402.2		Gray-blue marl, green and 'lie-de-vin', very fine sandstones, a bit lumpy, homogeneous, hard
	399.5		Gray-blue marl, green, compact, tender, homogeneous, dry
	398.5		Gray brown-red marl and green, not silty, a bit lumpy, humid, not silty, homogeneous, indurated, compact
	397		

(a)   (b)

Figure 3.11. (a) Survey F9: geological section (CERN, 1972); (b) Stratigraphy carried out from tunnel face loggings.

The large differences in the rock strata can lead to problems for the stability of the infrastructure (Laughton 1988). The molasse is overlain by glacial moraine deposits, which comprise essentially sands and gravel with varying amounts of clay and silt. In addition, due to its compact structure, the molasse shows a really low permeability. The molasse encountered during the excavation of the SPS ring and the transfer tunnel was found to be dry, and the permeability values measured are extremely low, of the order of 10^{-10} to 10^{-11} m/s, sometimes less than 10^{-11} m/s, after which they become impossible to measure (CERN, 1972). Little water ingress was also noted during the excavation of the LEP tunnel (Laughton 1988).

In the frame of the LHC Project and future underground constructions, Lugeon tests were carried out. The tests were conducted in a portion of a borehole where the water was injected and put under pressure and the volume of water absorbed was measured. The test results suggest a low permeability of the rock mass of 0.01 Lugeon ($10^{-8} \div 10^{-9}$ m/s), based upon a very low water loss (GADZ 1996a, GADZ 1996b).

Immediately after completing tunnel construction in 1972, records show the development of tunnel floor cracking along the tunnel due to heave of the flat slab (Figure 3.8), particularly from the starting of the blue zone (magnet QID 100700) to the end of the critical zone (magnet QID 101500), indicating that both ground consolidation and presence of swelling rock layers may have induced the detected damage. The abovementioned cracking pattern identified along the TT10 tunnel floor after tunnel excavation is shown in Figure 3.8.

Lombardi (1984) also noted that the CERN inclined transfer tunnels (TT10, TT20 and TT60) with a horseshoe shape section experienced a lifting of the flat tunnel floor where the swelling marl layers were crossed. Furthermore, during the excavation of the 2.5 km TI8 tunnel in 2001, the tunnel invert heaving reaction of certain bands was observed when in contact with the water introduced by the excavation process. The invert heave recorded was as large as 300 mm (CERN Tunneltalk, 2001).

Severe heave of the slab was also recorded for the high-speed railway Lilla tunnel in Spain, built with a horseshoe cross-section and excavated in the anhydrite formations of the Keuper rocks, a frequent geological rock mass in central Europe known to induce swelling strains as a result of gypsum crystal growth (Ramon et al. 2017). The mentioned phenomena are well documented in the literature, especially

for tunnels excavated through the Jura Mountains (Switzerland) and the GipsKeuper in Germany (Alonso & Ramon, 2013).

Conversely, no problems have arisen during the construction of the main SPS ring tunnel, with a circular cross-section and whose lining seems to be stiff enough to support any possible swelling pressure (Lombardi, 1984).

3.3.3 Tunnel lining issues

One of the damage patterns detected in the secondary lining of the tunnel was a compression failure at the tunnel crown and additional longitudinal tensile cracking on the shoulders (Figure 3.12). The mentioned crack development was identified in the *critical zone*, between the magnets QID 101300 - QID 101400 and the magnets QID 101400 - QID 101500, highlighted in Figure 3.6.
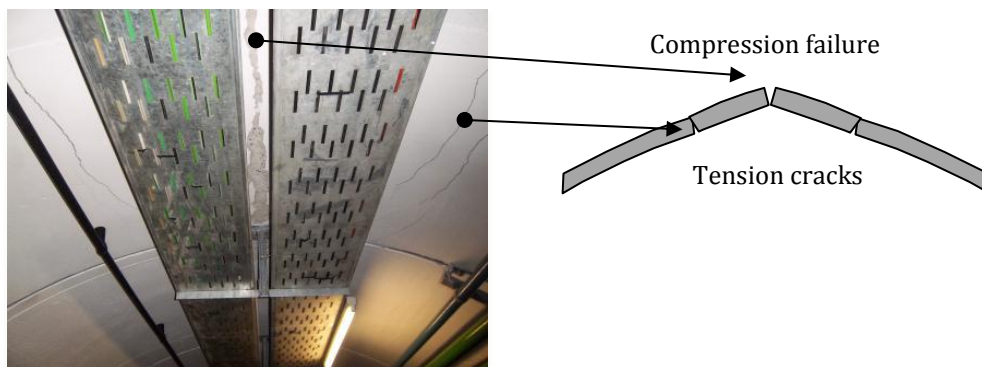
Figure 3.12. Compression failure at tunnel crown and tension cracks on shoulders (between magnets QID 101400 and QID 101500).

Due to the compression spalling at the tunnel crown section, pieces of concrete were flaking on the floor of the critical zone, between the magnets QID 101400 and QID 101500, approximately 11 m away from QID 101500, towards the upstream tunnel area (Figure 3.13).

Figure 3.13. Concrete flaking from tunnel crown.

Additionally, a compression failure at the tunnel foot was also detected, which might have occurred due to a concentration of compression stress at the tunnel intrados exceeding the compression strength of concrete (Figure 3.14a). Further, some concrete panels were found to move transversally, weakening the whole structure (Figure 3.14b).

(a)   (b)
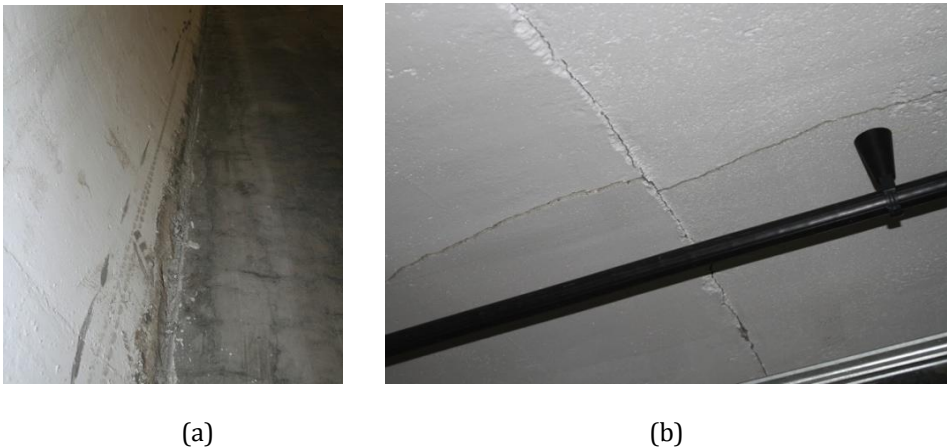
Figure 3.14. Observed cracks: (a) compression failure at tunnel foot (invert) and (b) radial movement.

Moreover, a detailed survey showed the development of cracks on the floor. The movement observed on the tunnel floor is due to heave (Figure 3.15a), which can occur when the heaving pressure caused by the swelling of the rock mass in presence of water exceeds the structural capacity of the invert. The swelling-induced cracking consisted of fine crazing of the concrete (Figure 3.15c) and a distinct longitudinal crack that follows some features, such as the central drain or bolt holes (Figure 3.15b).

(a)   (b)   (c)
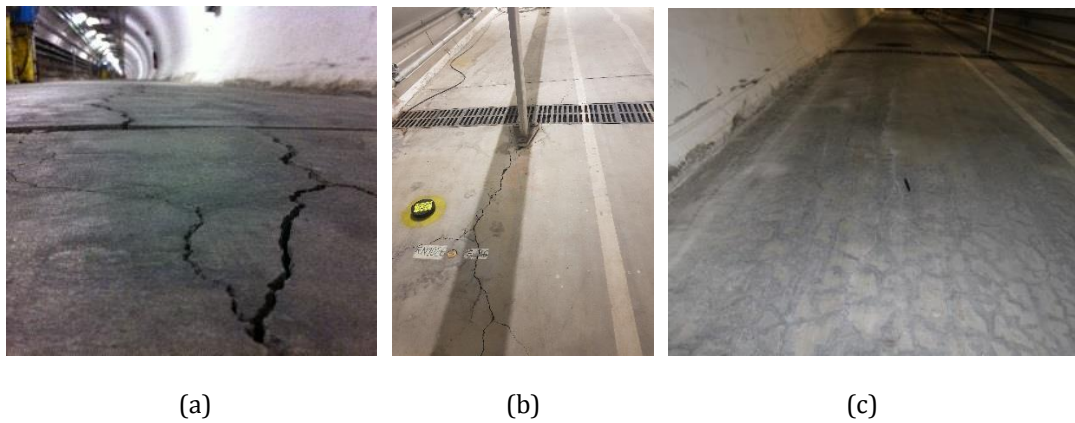
Figure 3.15. Cracking on the tunnel floor: (a) heave at the tunnel floor, (b) longitudinal crack and (c) crazy patterns crack.

To assess the tunnel invert thickness in the critical area, some concrete samples were drilled from the tunnel floor by the company *Gruppo Dimensione* based in Turin, Italy (Figure 3.16). From the taken samples, the invert slab was found to be thinner than the designed value and unreinforced, suggesting that there is a small resistance to the swelling potential of certain bands. The concrete strength of the floor was found to be class C30.
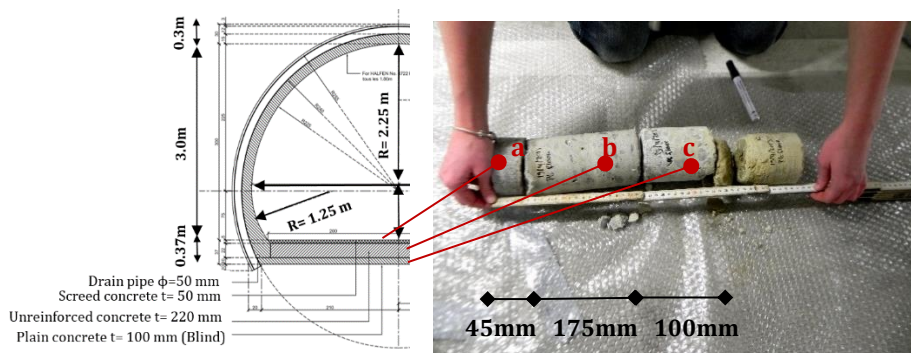
Figure 3.16. Concrete samples taken at tunnel invert: a) screed concrete, b) unreinforced concrete, c) Plain concrete (Gruppo Dimensione).

Further tunnel lining inspection was commissioned by CERN to gain more information on the tunnel lining geometry and materials. This included the performance of ground-penetrating radar (GPR) investigation along the TT10 tunnel floor, for mapping eventual cavities and for detecting any reinforcement mesh and/or steel components in the concrete slab. In fact, at any distinct abrupt material change, the pulses propagated by the GPR system returns differently. The radar data were taken and processed by the Suisse Company *GeoTest*, in November 2013.

Figure 3.17 displays the GPR measurements recorded, where the horizontal x-axis corresponds to the distance along the tunnel invert and the y-axis relates to the tunnel invert depth. Particularly, the presence of eight metallic objects in the surveyed materials was observed, with dimensions of 40 cm x 40 cm between the magnet QID 101100 and QID 101200, in the *green area*, with the last metallic profile being almost 10 m away from the magnet QID 101200. A number of nine metallic objects were also found beside the magnet QID 101300 of the *critical area*, by covering a distance of approximately 12 m along the tunnel, suggesting the existence of potential steel reinforcement (Figure 3.17). Although the construction record is not available, the observed steel element profiles imply that, due to the weak ground conditions met during tunnel excavation, it was decided to reinforce the concrete slab to counter-act swelling pressures at these sections. The type of weak rock encountered at the mentioned locations was analysed from the geological face loggings taken along the tunnel during the excavation, shown in Figure 3.8. This highlighted the presence of the *"lie-de-vin"* (lumpy) *calcareous red lumpy marl* with swelling properties between the magnets QID 101100 – QID 101200, whereas *grey-blue* and *calcareous green marls* were found in the formations around the magnet QID 100300 (Figure 3.8).

The weak ground conditions associated with the very weak marl layers were also noted during the excavation of both the UX15 cavern and the USA15 cavern at Point 1 adjacent to this site (Parkin et al. 2002). A certain amount of cracking of the shotcrete was noticed along the vault, with the majority of displacements localised on the very weak marl. Although the overall stability of the cavern was not compromised, steel mesh was installed for safety purposes.
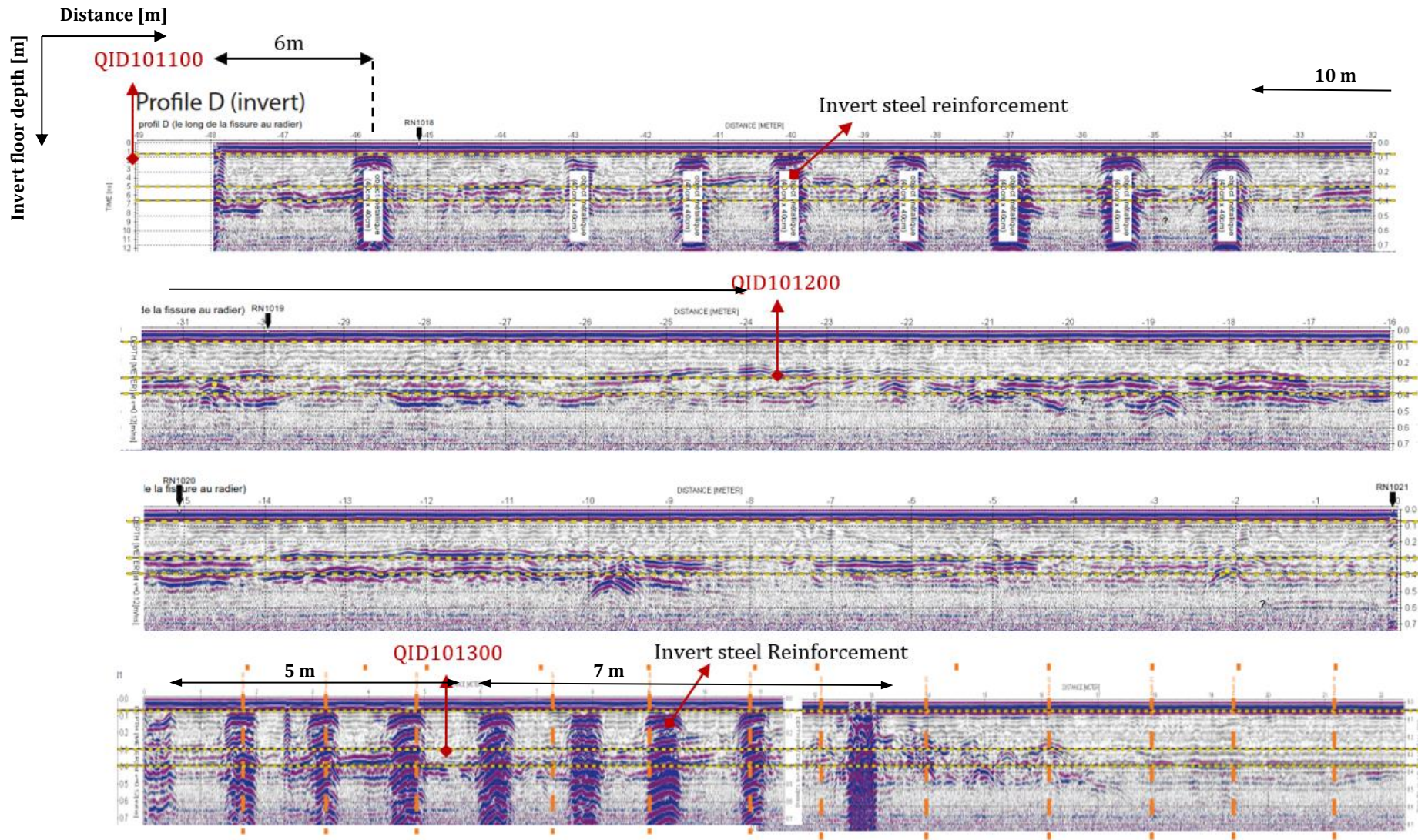
Figure 3.17. Ground-penetrating radar (GPR) investigation along the TT10 tunnel floor (GeoTest).

In the *secondary blue zone* between the magnets QID 100700 – QID 100800, significantly less damage was caused by the longitudinal tensile cracking observed at the tunnel axis level and usually interrupted by construction joints (Figure 3.18a, Figure 3.19b and c), in addition to circumferential cracking (Figure 3.18b, Figure 3.19a). The possible causes behind the observed radial lining cracks may be related to the shrinkage of the cast concrete after tunnel construction, as the concrete hardens with time. Also, the unreinforced secondary lining of 18 cm may have developed longitudinal cracking at tunnel axis level due to the high horizontal load applied on the lining, exceeding the tensile strength of concrete, which is known to be very small. The tunnel floor in this area was also found damaged, with a remarkable longitudinal crack developed around the magnet QID 100835 (Figure 3.19d) and less significant floor cracks between the magnets QID 100835 and QID 100900, around 9 m away from the magnet QID 100835, towards the downstream area of the tunnel (Figure 3.19e, f). However, no compression failure was observed at the tunnel crown in this zone.

(a)   (b)
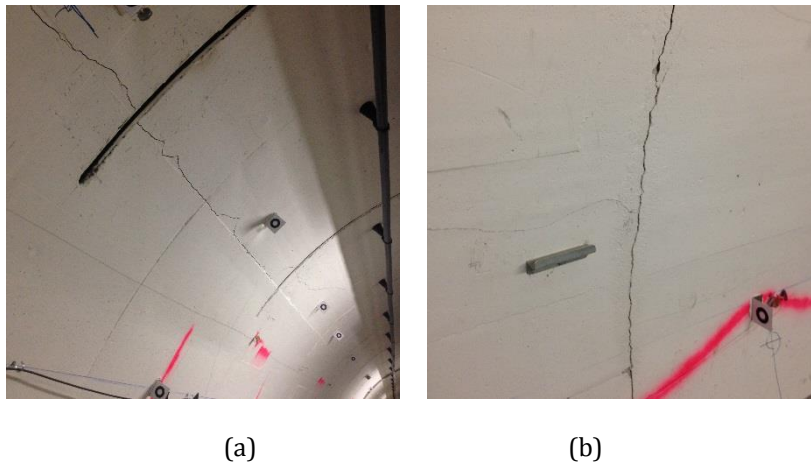
Figure 3.18. (a) Longitudinal cracking observed at tunnel axis level (QID 100700) and (b) radial crack.

(a)   (b)   (c)

(d)   (e)
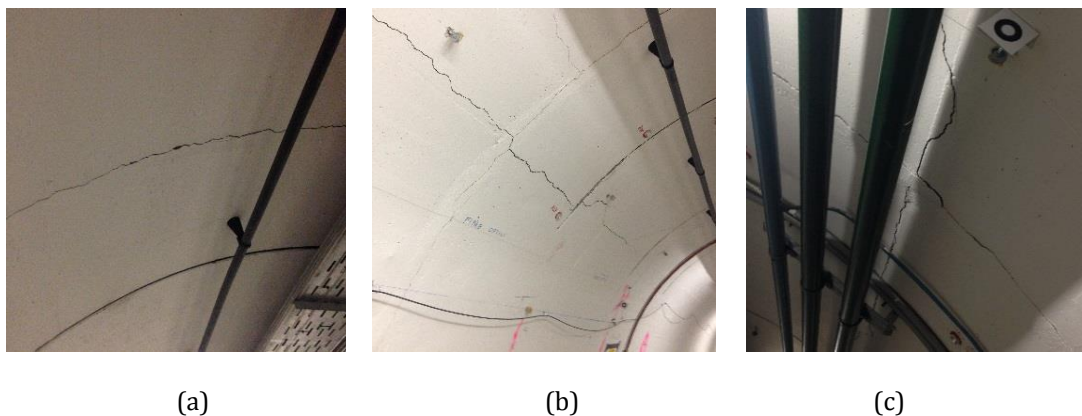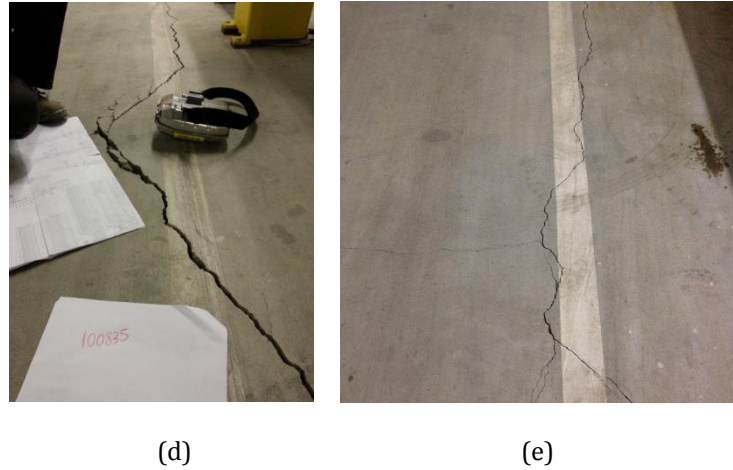
Figure 3.19. (a) Circumferential cracks (QID 100800), (b) Longitudinal cracking on the left side and (c) on the right side of tunnel axis level (QID 100800), (d) Longitudinal floor cracking around magnet QID 100835 (CERN), (e) Longitudinal floor cracking between magnets QID 100835 and QID 100900.

3.3.4 Cause and mechanism of tunnel deformation

In 2008, in the upstream area of the TT10 tunnel, close to the magnet QID 100300 (Figure 3.6), at the interface between the molasse region and the moraine deposits, a first sign of groundwater ingress with calcite deposits was detected during one of the maintenance technical stops. To prevent the water infiltration through the crack openings, a short-term attempt was made by a Swiss company called *Vacca Résines & Batiment S.A.* based in Meyrin, Switzerland. The adopted method involved the injection of a polyurethane resin into boreholes previously drilled into the crack. By reacting with the water, the system then results in a waterproof repair (Morton, R., 2018, personal communication). However, the implemented approach seemed to be successful only for a short period of time (between 12-18 months), after which the material was washed off by water leaks, suggesting the presence of an active pore pressure behind the tunnel lining, at the interface with the permeable moraine layer.

Some years later, a tunnel inspection occurred during the beginning of the LS1 has identified water leakage with calcite deposits on the TT10 tunnel floor, at the location of the magnet QID 101100 of the green zone (Figure 3.20).

Figure 3.20. Water leakage with calcite deposits (close to magnet QID 101100).

Since the moraine layer is found to be a more permeable deposit compared to the molasse unit, the water table tends to oscillate due to the change of groundwater conditions. In particular, extreme weather conditions with heavy rainfall may cause large amounts of groundwater to flow towards the tunnel, exceeding the tunnel drainage system capacity (Figure 3.21a). This water ingress, in addition to the transported calcite deposits, may lead to calcification and may reduce the tunnel drainage capacity, resulting in a build-up of water pressure on the outer edge of the tunnel lining (Figure 3.21b).

The accumulated pressure, acting as a tunnel boundary load, in combination with poor concrete integrity is expected to lead to a reduced lining capacity, especially in the areas of weaker ground conditions. Moreover, the groundwater collected by the two small drainage pipes located at both tunnel invert sides flows into the main drainage system through white PVC pipes (Figure 3.22b), whose connection is placed every 60.38 m along the tunnel (horizontal distance) with a visible drainage grid in the tunnel floor (Figure 3.22c). A camera inspection revealed that the drainage pipes were found to be damaged (Figure 3.22b). As a result, it is possible that the tunnel was not in fully drained conditions and, therefore, the water pressure was accumulating around the tunnel. This can potentially lead to the swelling-induced damage at the location of weaker ground conditions and resulting in a heave of the tunnel floor.

(a)   (b)
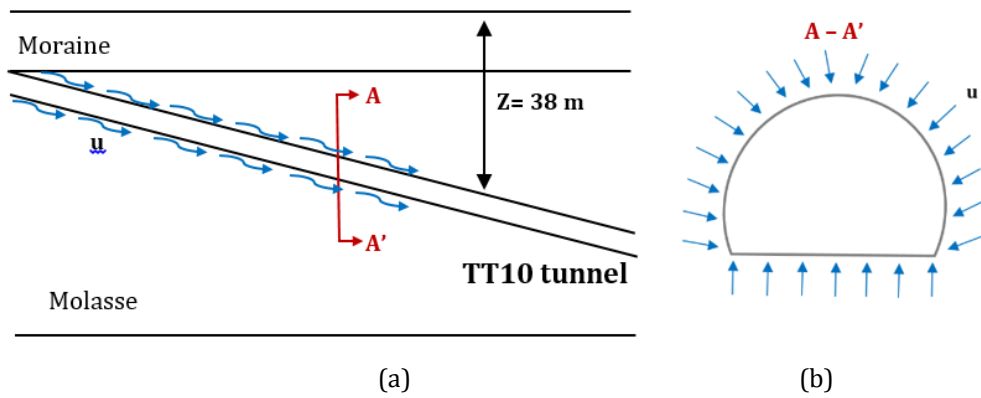
Figure 3.21. (a) Longitudinal section of the TT10 tunnel, (b) cross-section with the application of the external water pressure u on the outer edge of tunnel lining.

(a)   (b)

(c)
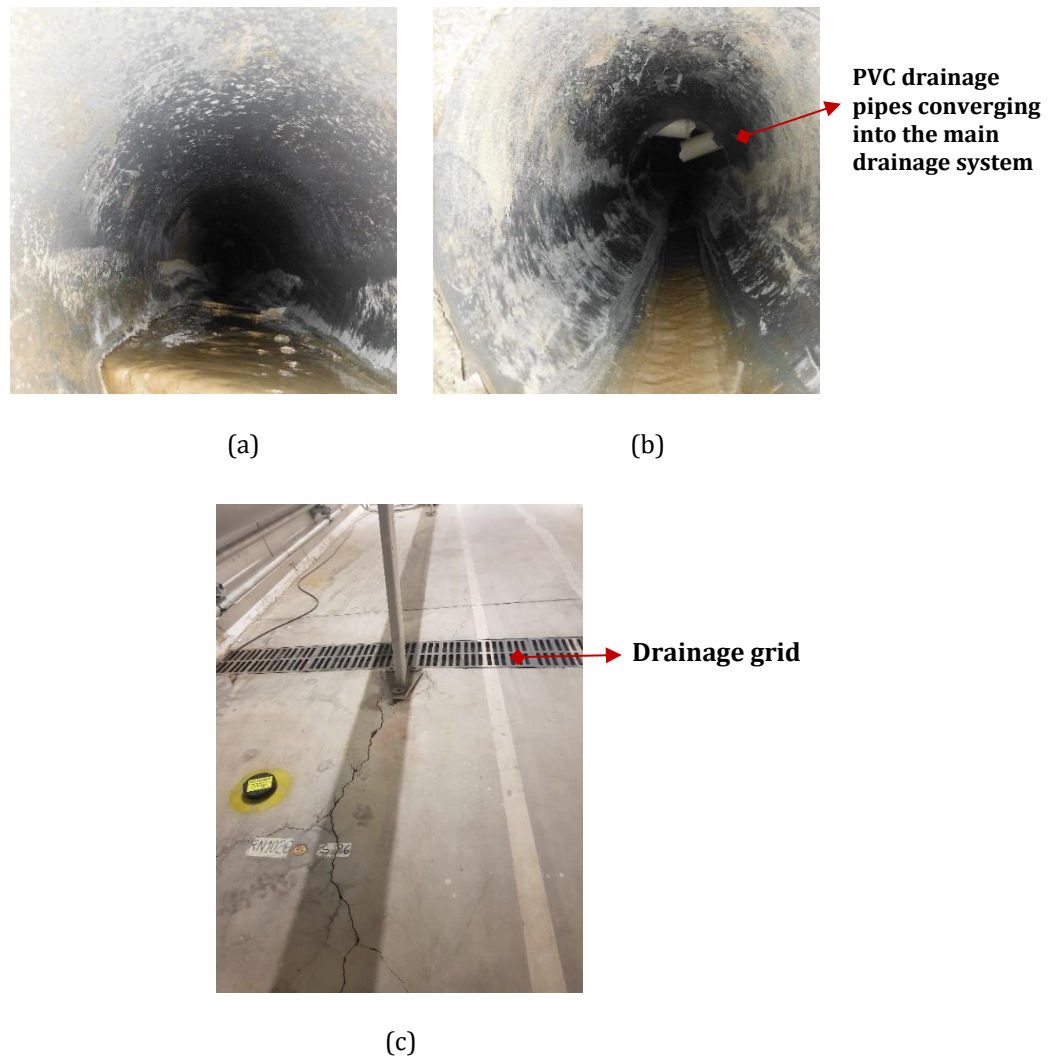
Figure 3.22. Tunnel drainage system: (a) calcite deposits and (b) PVC drainage pipes converging into the main drainage system and (c) drainage grid placed on the tunnel floor.

With this in mind, two potential tunnel lining mechanisms of deformation have been identified in this study: *mechanism A* and *mechanism B*. The former shows the development of compressive stress and tensile stress at the tunnel crown and tunnel shoulder respectively (Figure 3.23a), which might have generated due to high horizontal in-situ load pattern and aggravated by an unreinforced tunnel invert. Two hypothetical scenarios may be drawn for *mechanism A*:

- The compression failure at the tunnel crown may be caused by the failure of both primary and secondary lining, due to a possible void above the lining or due to the presence of weak ground conditions (Figure 3.23b).
- The secondary lining may fail due to potential poor concrete conditions at the tunnel crown.

The latter *mechanism B* implies the swelling-induced damage resulted in severe heave of the floor slab, which was triggered by a change in hydrologic conditions (Figure 3.23c).
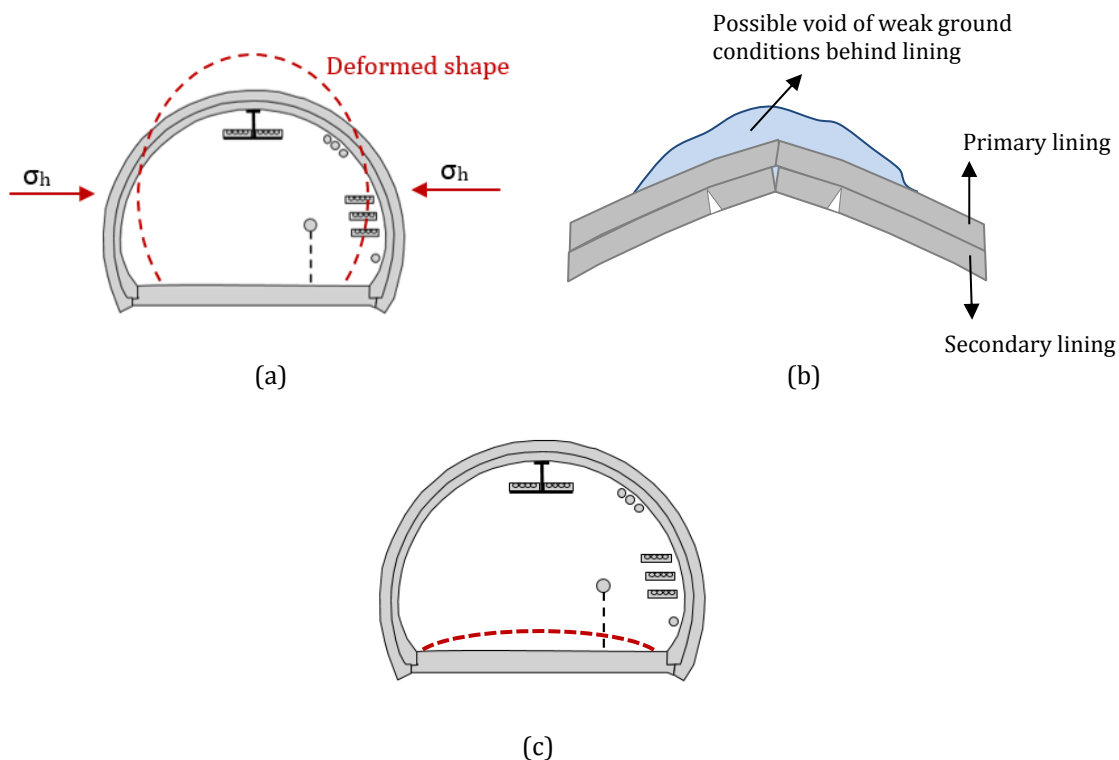
Figure 3.23. Potential tunnel lining deformation mechanisms: (a) Compressive stress at tunnel crown and tension stress on tunnel shoulder; (b) Failure mechanism of both primary and secondary lining at tunnel crown due to possible void or weak ground conditions behind the lining; (c) Heave at tunnel floor.

In summary, the observed behaviour would suggest that the combination of the swelling properties of the very weak marl and the deterioration of the concrete lining may have compromised the mechanical strength of the lining, resulting in the above-mentioned mechanism of deformation. Therefore, a remedial short-term solution was suggested by consulting engineers contracted by CERN.

The mitigation measure involved the deployment of a number of steel I-beams, in order to absorb the horizontal load and the design was carried out by ARUP engineers. The mentioned installation took place in the critical area along the TT10 tunnel, by placing eight I-beams between the magnets QID 101400 - QID 101500 and fifteen I-beams in the area between the magnets QID 101300 - QID 101400 (Figure 3.24). Simultaneously, in order to assess the tunnel lining performance in the long-term, it was decided to monitor not only the critical area but also the secondary zone, where the cracks start to develop (blue area of Figure 3.8). For this purpose, both conventional and advanced monitoring technologies were adopted.

Figure 3.24. Installation of steel I beams in the critical area along the TT10 tunnel between magnets QID 101300 and QID 101400.

3.3.5 Conventional monitoring

The development of cracks along the TT10 tunnel has triggered the need for a monitoring plan in order to understand the tunnel lining behaviour and control its deformation with time. The primary monitoring technology adopted in 2013 for capturing lining displacements involved conventional automatic total stations

within the affected area. The two-year CERN shutdown occurring in 2013 enabled access to all CERN underground facilities and, therefore, allowed the implementation of geodetic surveying in order to measure structural movements in the long-term. Six geodetic cross-sections were installed on the tunnel lining of the critical zone. Each monitoring section comprised a total of six reference targets bolted on the tunnel lining and positioned at tunnel axis, tunnel invert and tunnel shoulder as shown in Figure 3.25, with the optical targets 1, 2 and 3 installed on the right side of the tunnel lining whereas the targets 6, 7 and 8 are positioned on the left side, looking from the downstream tunnel area. Figure 3.26 shows a detail of the geodetic target installed on the TT10 tunnel lining.
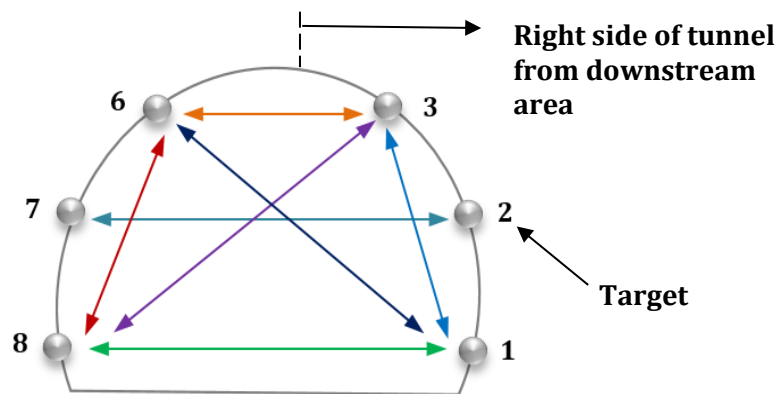
Figure 3.25. Schematic tunnel cross-section: six geodetic targets.

Figure 3.26. Geodetic bolt installed on tunnel lining.

The overall layout of the monitoring sections is shown in Figure 3.27. The measurement of the targets inside the tunnel was obtained by placing the total station on predefined brackets and successively moving the instrument forward to cover all the profiles by measuring the coordinates of each target for all the instrumented cross-sections. The installation and the data collection were carried

out by CERN surveyors, working with the SMM group (Survey, Mechatronics and Measurements) of the Engineering department (CERN EN/SMM).
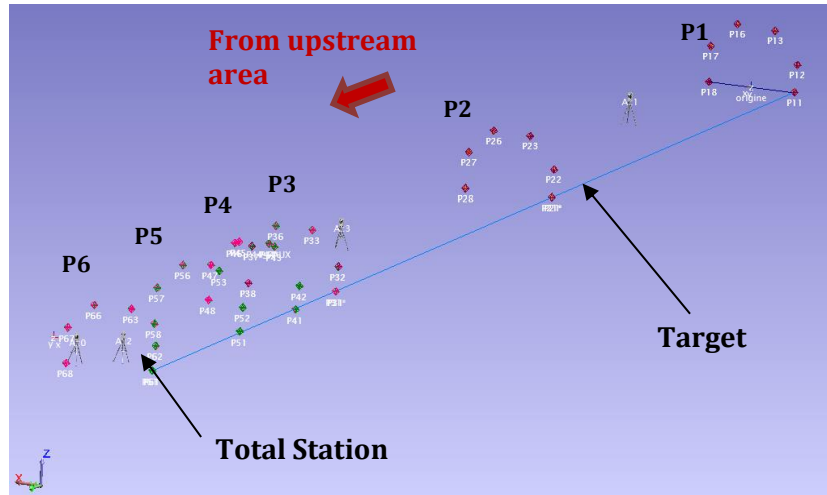
Figure 3.27. Layout of targets and the measuring total station (Courtesy of CERN EN/SMM).

The amount of geodetic data gathered enables the estimation of the 3D displacements of the targets and the final deformation profile for the different sections along the TT10 tunnel.

A reference measurement was taken in March 2013 for profiles P1, P2, P3, P4, P5, P6 and further measurements were gathered periodically during the first year of monitoring (2013), by collecting around one measurement per month. However, in the subsequent three years of monitoring (2014-2017), three measurements were taken, one per year. Only in 2015, an additional geodetic profile P0 was installed, yet only two monitoring measurements were taken as the CERN accelerator's shutdown drew to a close in February 2015.

The location of the geodetic profiles along the TT10 tunnel is shown in Figure 3.28. The profiles were numbered by starting from the cross-section P1 located in the *critical zone* (orange zone) of the upstream area of the tunnel and proceeding to the downstream side of the TT10 tunnel, as shown in Figure 3.28.
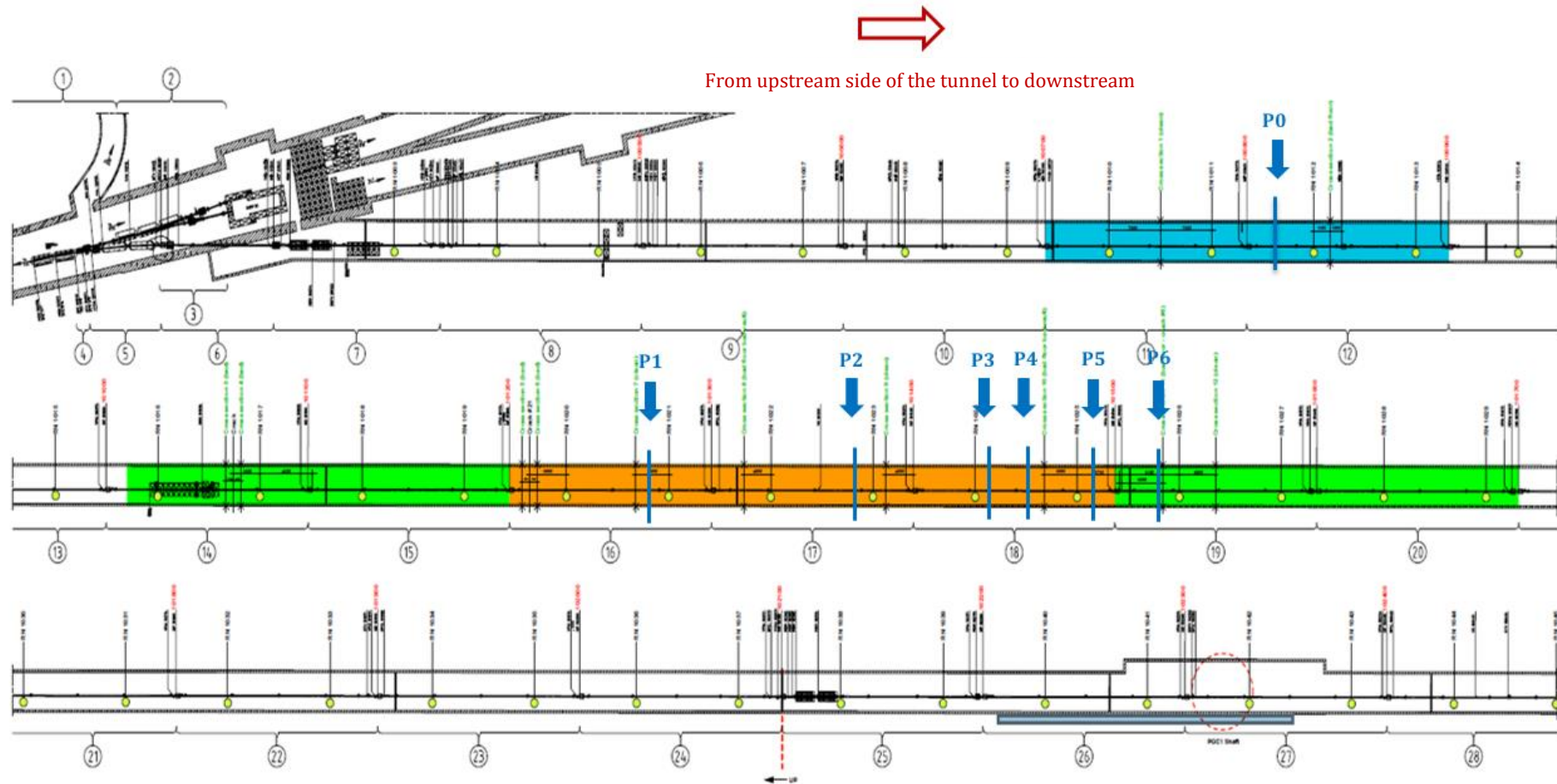
Figure 3.28. Location of the geodetic profiles along the TT0 tunnel: P0, P1, P2, P3, P4, P5 and P6.

Table 3.2 shows a summary of the geodetic measurements collected.

Table 3.2. Geodetic measurements taken for the monitored profiles.

Geodetic Profile	Measurements
P1	March 2013
	April 2013
P2	May 2013
	June 2013
P3	August 2013
	September 2013
P4	December 2013
	August 2014
P5	January 2015
	January 2016
P6	February 2017
P0	January 2016
	February 2017

Figure 3.29 shows the change in the vertical, horizontal and diagonal distances between the optical targets between 2013 and 2017 for the monitored cross-sections.

During the first year of monitoring, minor changes in tunnel distances were recorded. However, since August 2014 the horizontal distance between targets seems to rise with time at both tunnel axis level and tunnel shoulder for all the measured cross-sections, throughout the monitoring period. Therefore, this decrease in the horizontal tunnel distances suggests that the tunnel lining is horizontally moving inwards.

Conversely, the vertical change in distances on both the left and right side of the tunnel lining seems to develop with a smaller rate, by increasing with time. Profile P4 is identified as exhibiting the maximum convergence of approximately -0.88 mm and -1.05 mm at the tunnel shoulder and tunnel axis level respectively, as shown in Figure 3.29d. This deformation profile seems to be in agreement with the cracking pattern observed at this tunnel cross-section, placed in the critical area where the deformation *mechanism A* was identified. Additionally, the change in the horizontal diameter of both profile P5 and profile P6 increased to about -0.87 mm and -0.77 mm respectively within the three monitoring years (Figure 3.29e and Figure 3.29f). Moreover, no measurements were taken in August 2014 for profile P6 (Figure 3.29f).

Figure 3.29g shows the results for profile P0, which was installed in the *secondary area*, in 2015, hence only two measurements are available (2016 and 2017). The horizontal change in distance decreases more at tunnel axis level than tunnel shoulder and tunnel invert. The vertical geodetic targets seem to experience a small decrease as well. However, only two measurements were taken, and therefore it might be difficult at this stage to outline a deformation mode for this cross-section (Figure 3.29g).

Overall, the tunnel lining deformation mode observed for the monitored geodetic profiles suggests that the tunnel is experiencing a vertical ovalisation, as the horizontal distance between targets is decreasing with time whereas the vertical distance seems to increase. Nevertheless, the change in tunnel diameter seems to develop slowly with time, reaching maximum values of 1 mm within the monitoring period of 4 years.
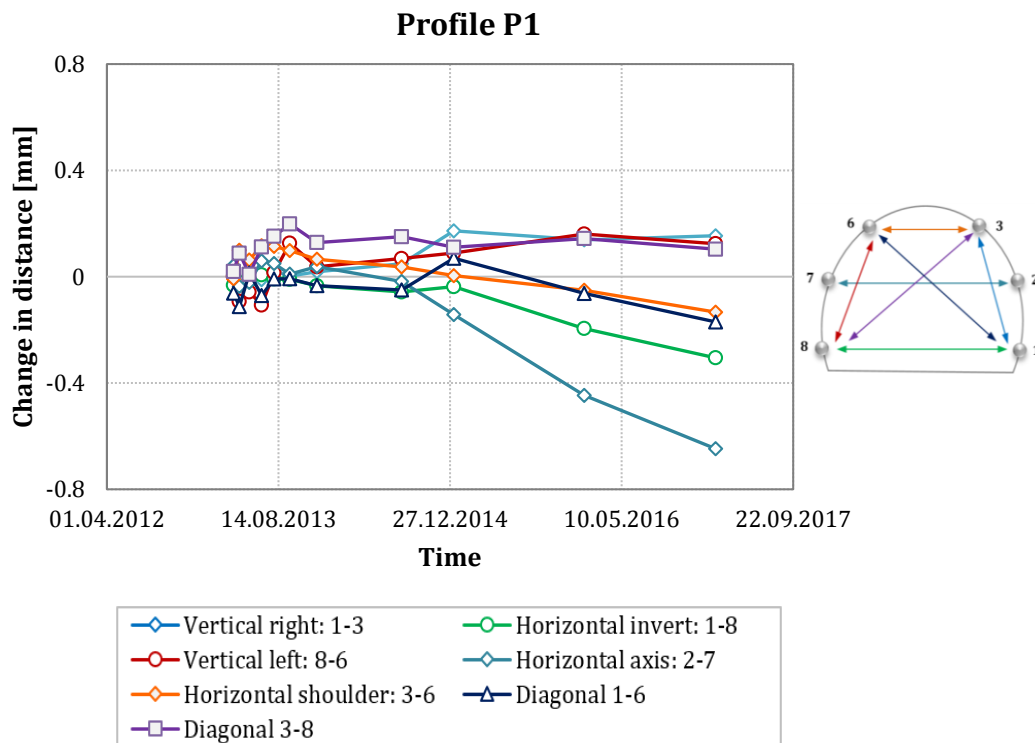
(a)
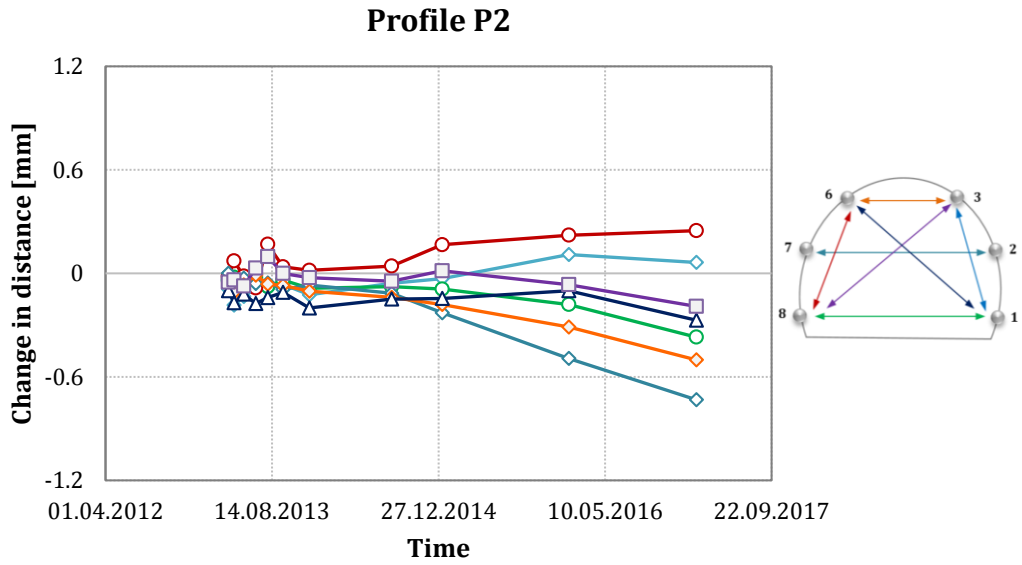
(b)
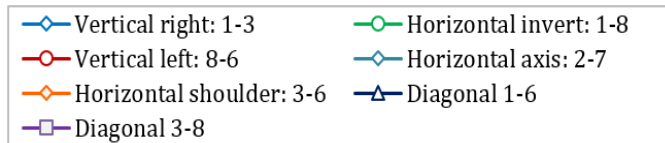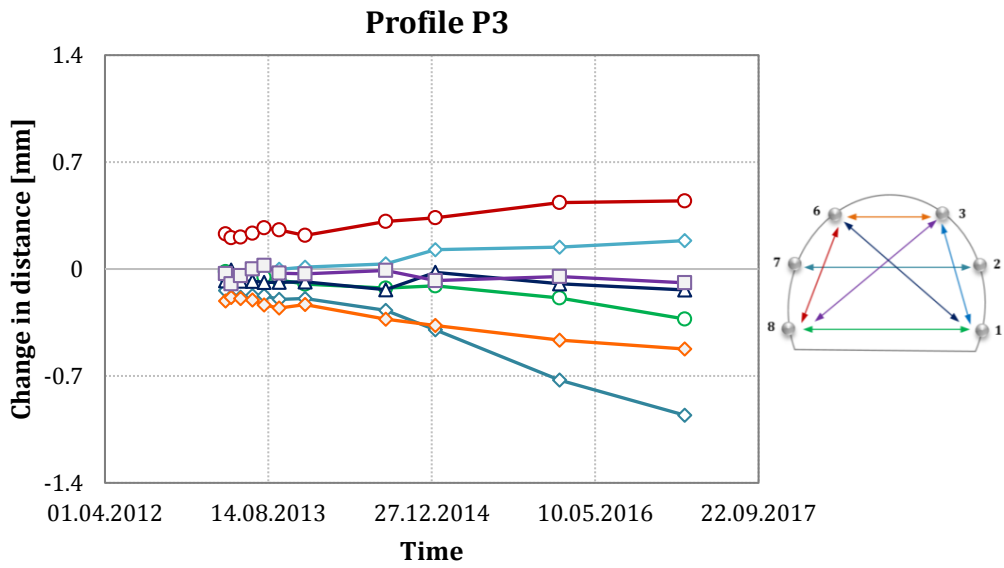
(c)
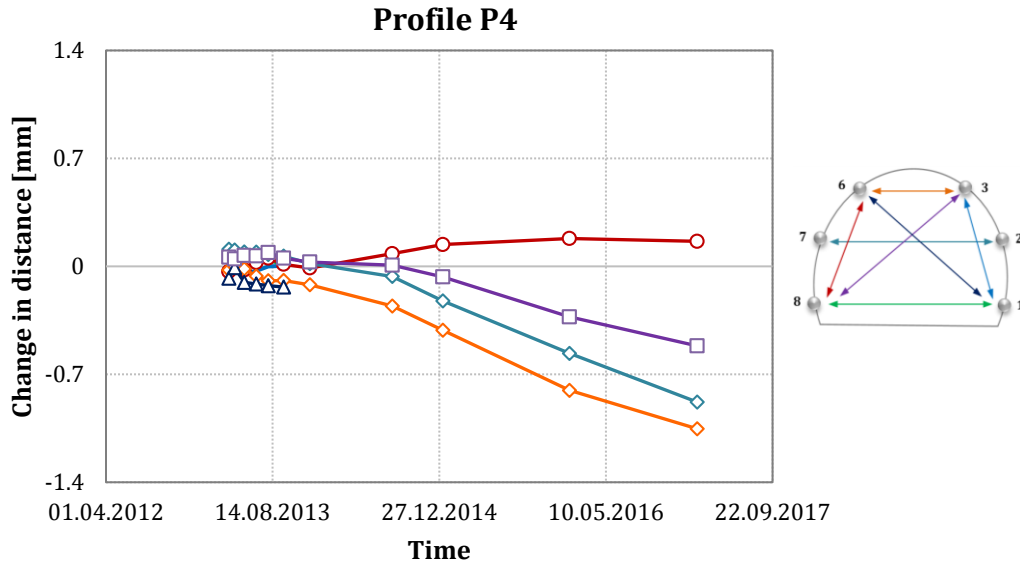
(d)
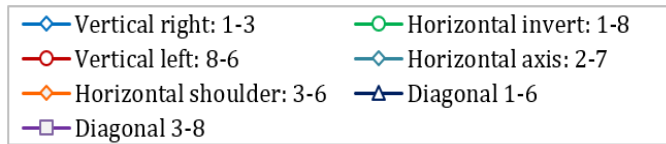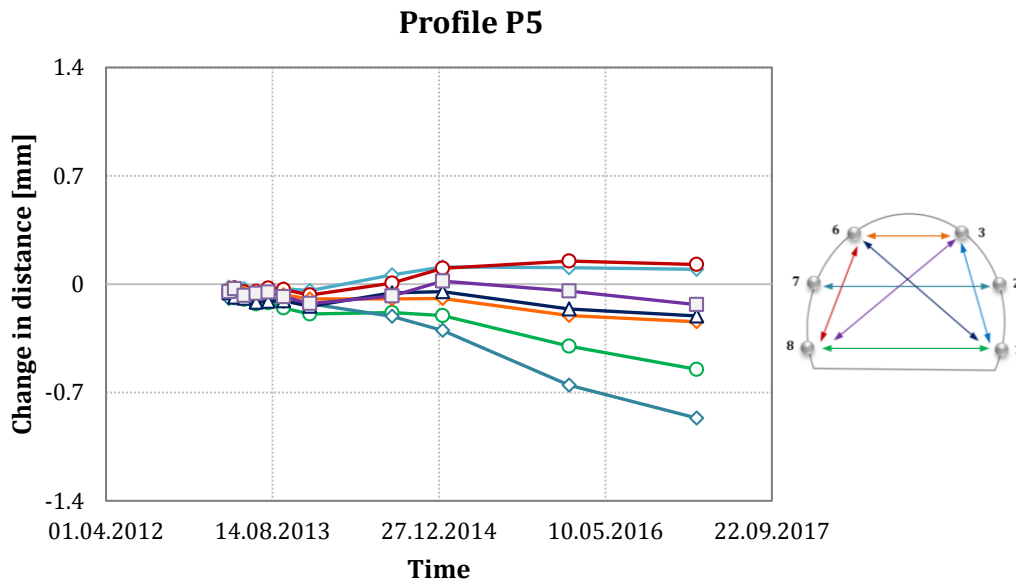
(e)
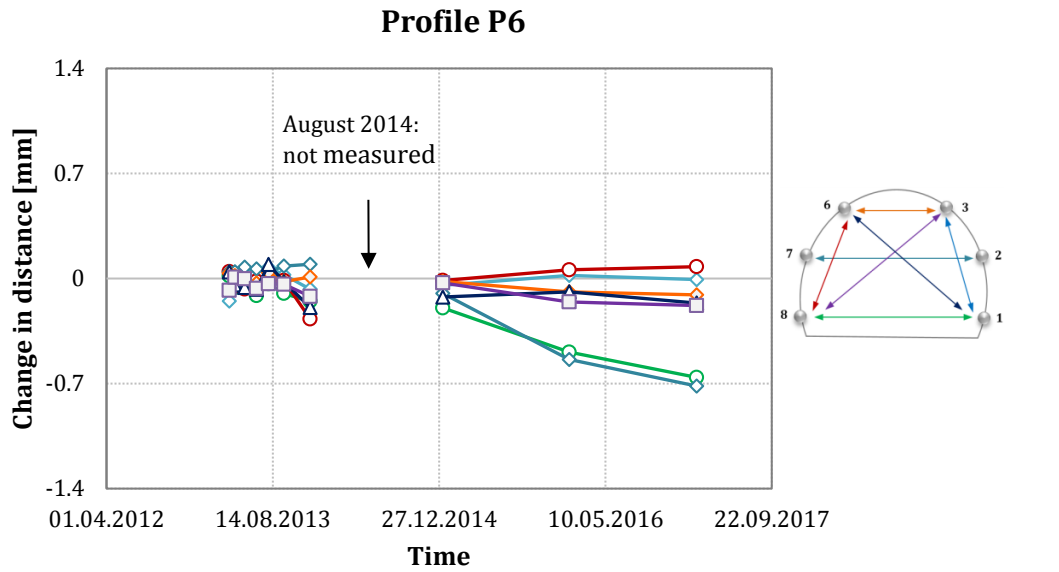
(f)
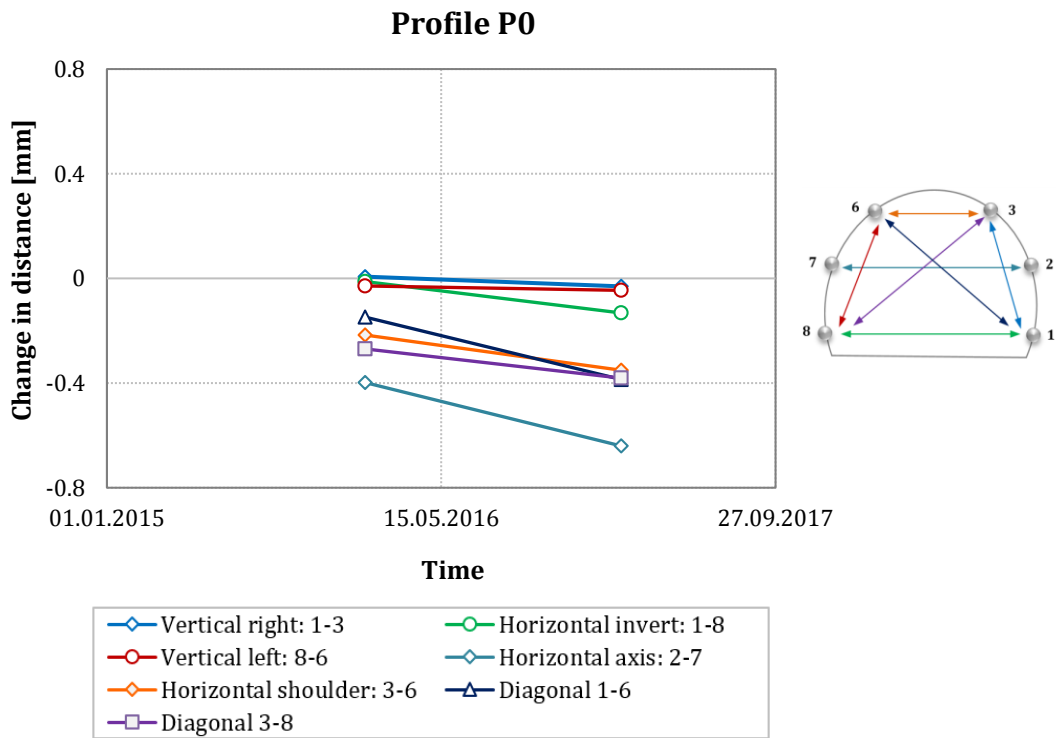
(g)

Figure 3.29. Change in tunnel distance for the geodetic profiles: (a) Profile P1, (b) Profile P2, (c) Profile P3, (d) Profile P4, (e) Profile P5, (f) Profile P6 and (g) Profile P0 (Credit: CERN EN/SMM).

3.4 Summary of key findings

This chapter presented the investigation of a CERN concrete-lined tunnel that underwent displacements and lining damage many years after construction. An extensive suite of site investigations, geological characterization and a successful total station monitoring instrumentation have contributed to the identification of tunnel lining deformation mode and, therefore, to gain a better understanding of lining response.

Two main tunnel lining deformation mechanisms were identified: the first one implies a compressive failure at the tunnel crown with tension cracks on the tunnel shoulder whereas the second one involves heave at the tunnel floor.

The key observations are as follows:

- The tunnel lining investigation highlighted the presence of a very thin floor slab without any reinforcement. However, some GPR tests detected anomalous reflectance along the tunnel floor at certain locations, suggesting that the tunnel invert was reinforced due to the swelling potential of certain marl layers met during tunnel construction.

- Further geological investigation revealed the most critical tunnel lining damage to be localised in the tunnel area where the very weak marl bands are localised, suggesting that the geology surrounding the tunnel has a great impact on the observed lining behaviour.

- Conventional monitoring targets have successfully measured the displacements of seven cross-sections. Data results were taken for a monitoring period that goes from 2013 to 2017. Data was collected only during daily tunnel shut-downs, providing a limited dataset to look at in the context of the long-term monitoring.

- The tunnel lining converges horizontally by a maximum of -1.05 mm and -0.88 mm at the tunnel shoulder and tunnel axis level respectively for the Profile P4, installed in the damage affected area. Conversely, the lining is experiencing an increase in the vertical tunnel diameter, with peak values of approximately +0.44 mm on the right side of the tunnel and +0.19 mm at the left tunnel side.

To conduct the long-term monitoring strategy due to restricted tunnel access (limited to daily technical stops), a remote and radiation resistant monitoring technique is required. Ideally, it should provide continuous measurements, regardless of underground accessibility. In this study, the tunnel lining mechanism of deformation was further explored by adopting advanced monitoring instruments (i.e. DFOS, distributed fibre optic sensors) in Chapter 4, and through two-dimensional FE modelling in Chapter 6 and Chapter 7.

References

Alonso, E.E. & Ramon, A. (2013). Heave of a railway bridge induced by gypsum crystal growth: field observations. *Géotechnique*, **63**, No. 9, 707-719.

CERN, (1972). The 300 GeV Programme. CERN, Geneva.

GADZ, 2016a. Reconnaissances géotechnique Point 1 – No 7222/2. Technical report, Géotechnique Appliquée Dériaz SA (in French).

GADZ, 2016b. Reconnaissances géotechnique Point 1 – No 7223/2. Technical report, Géotechnique Appliquée Dériaz SA (in French).

Laughton, C. (1988). CERN Accelerator Project. World Tunnelling Project Report.

Lombardi, G. (1979). Rock mechanics at the CERN proton-antiproton facilities. In: International Society for Rock Mechanics (Ed.), 4th ISRM Congress. International Society for Rock Mechanics, Montreux. Balkema, pp/433-436.

Lombardi, G. (1984). Underground openings in swelling rock. National Conference on Case Histories in Geotechnical Engineering. Pakistan, Lahore.

Parkin, R.J.H, Varley, P.M. and Laigle, F. (2002). The CERN LHC Project – Design and Construction of large caverns in tight spaces. *Geotechnical Aspects of Underground Construction in Soft Ground*, Lyon.

Ramon, A., Alonso, E. E., Olivella, S. (2017). Hydro-chemo-mechanical modelling of tunnel in sulphated rocks. *Géotechnique*, **67**, No. 11, 968-982.

Shani Wallis, (2001). Spectacular excavations for physics research. CERN *TunnelTalk*, www.tunneltalk.com.

Chapter 4

4 Distributed Fibre Optic Sensing (DFOS) instrumentation

4.1 Introduction

For assessing the structural performance and the deformation mechanism of CERN TT10 tunnel, innovative distributed fibre optic strain sensors (DFOS) based on Brillouin Optical Time-domain Analysis (BOTDA) were also deployed, as they are found to be one of the most promising monitoring tools in the civil engineering field (Soga and Luo, 2018). The purpose of supplementary monitoring instrumentation is that fibre optic strain sensors can operate remotely, overcoming the limitations of conventional technologies, whose information is restricted to short CERN operational shutdowns, and hence a better understanding of the lining behaviour can be assessed.

Despite the radiative environment and the limited accessibility to CERN facilities, optical fibres provide data continuously over the entire structure. Therefore, the use of a robust and reliable technology to monitor CERN infrastructure provides continuous strain measurements of several tunnel cross-sections, enabling to understand the tunnel lining deformation mechanism in the context of a long-term monitoring plan. The DFOS instrumentation included multiple installations along the tunnel and was successfully conducted under the guidance of Cambridge Centre for Smart Infrastructure and Construction (CSIC).

This Chapter provides a review of the DFOS applications in the engineering field and a brief description of the distributed strain sensing technology. The field monitoring instrumentation carried out in the TT10 tunnel are presented in detail followed by an overview of the basic steps taken in the data analysis. The monitoring results obtained are also shown and discussed.

4.2 Review of the DFOS applications

Distributed fibre optic sensors are widely known to be excellent tools in different fields such as geotechnical and civil engineering, hydropower, oil & gas etc., as they enable continuous strain and temperature measurements, thus providing data over a long distance. Recent improvements in the area of smart technology have significantly contributed to the deployment of a number of recent field trials for health monitoring purposes using Distributed fibre optic sensors (DFOS), demonstrating the suitability and the measurement capability of this technology for a wide range of geotechnical applications. Conventional measurements, which usually involve the use of tape extensometers for diameter changes, strain gauges, total stations and visual inspections, present the limit of providing discrete values of measurement at the sensor location. Therefore, the overall performance of a certain structure cannot be easily detected.

A variety of DFOS sensor applications has been implemented for measuring the deformations in structures. The concrete-lined tunnel in an existing London Underground tunnel was monitored by adopting Brillouin optical time domain reflectometry (BOTDR) technology (Cheung et al., 2010), showing a flexural tunnel behaviour comparable with the one obtained by conventional measurements. Another use of DFOS has included the implementation of BOTDR system to monitor the performance of a masonry tunnel during the construction of a new one at King's Cross in London (Mohamad et al., 2010). By attaching the optical fibres at five circumferential sections along the intrados of the tunnel lining, the brick-lined tunnel deformation was examined, and the results were compared with conventional total station data. The performance of a circular pre-cast concrete segmental lining while an adjacent second bored tunnel was constructed was investigated by deploying a number of optical fibre sensors, showing an ellipsoidal tunnel lining distortion (Mohamad et al., 2012).

To assess the performance of the existing Royal Mail tunnel due to the construction very close beneath of the Crossrail tunnel in London, several cross-sections were recently instrumented with fibre optic sensors (Gue et al. 2015; 2017). The FO data results showed the development of tensile and compressive strains at tunnel spring line and tunnel crown respectively, indicating a vertical tunnel ovalisation as a mechanism of deformation.

Fibre optic sensors were also installed for the monitoring of a deep circular shaft in London for capturing continuous hoop and bending strain profiles using the BOTDR system (Schwamb et al., 2014). The capability of optical sensors to measure the strain regime was also demonstrated by monitoring and instrumenting piles (Klar et al., 2006; Mohamad et al., 2007; Pelecanos et al. 2017; 2018) and masonry arches (Acikgoz et al., 2017) and many other geotechnical infrastructure.

Overall, optical fibres have shown the advantage of being small in size and, hence, not invasive as well as being corrosion-resistant, essentially explosion-proof and immune to electromagnetic influence, therefore suitable for many severe environments in civil applications.

4.2.1 Radiation effect on optical fibres

Unlike remote monitoring electronic devices, which would require not only maintenance but also measurements limited to short shutdowns of CERN underground infrastructure, DFOS sensors offer the remarkable advantage of being immune to the electromagnetic field associated with the high energy of the facilities of the Large Hadron Collider (LHC). In fact, fibre optic (FO) sensors are a promising technology adopted also by the nuclear industry for monitoring purpose. Despite many advantages, the properties of optical fibres change when exposed to radiation (Alasia et al., 2006; Girard et al., 2013). Although the fibre response is not fully predictable and it depends strictly on the specific environment, radiation absorption in silica optical fibre has been investigated in great detail over the last decade (Wijnands et al., 2008; Girard et al., 2013).

A change in the Brillouin characteristic parameters with the radiation dose was noticed by Alasia et al. (2006). In silica-based glasses, radiation mainly leads to a phenomenon called Radiation-Induced Attenuation (RIA), which is a wavelength dependent effect and causes a reduction of the Brillouin amplitude (Girard et al., 2013). The RIA mechanism strongly affects the sensor's distance range (Phéron et al., 2012). Under radiation, a change in the refractive index RI is observed, which is related to a variation in the silica density (Girard et al., 2013).

During the irradiation, a change in the silica density occurs and the density is correlated to the acoustic velocity (Alasia et al., 2006). Since the Brillouin

frequency v_b is related to the acoustic velocity V by the following relation, a variation of the density induces a variation of the Brillouin frequency v_b:

$$v_b = \frac{2 \cdot n \cdot V}{\lambda} \qquad\qquad (4.1)$$

where n is the refractive index of fibre, V is the acoustic velocity and λ is the light wavelength.

The effects of ionising radiations on the characteristics of the Brillouin gain spectrum in standard Ge-doped telecom single-mode fibres have been widely investigated up to very high gamma dose by Alasia et al. (2006). The samples were gamma-irradiated at the Brigitte facility of SCK-CEN in Belgium at room temperature up to 10 MGy. The results show a clear dependence of the Brillouin scattering on the ionising radiation due to a silica compaction phenomenon, modifying the Brillouin scattering properties.

The results also show that the frequency variation is about 5 MHz for the most irradiated fibre sample, which would correspond to around 5 °C error in the temperature measurement. Therefore, the radiation-induced shift of the Brillouin frequency can be essentially negligible.

Phéron et al. (2012) also investigated the performance of strain in Brillouin-scattering based optical fibre sensors by irradiating various fibre types. Their results show that the amplitudes and kinetics of the RIA response strongly depend on the composition of fibre core and cladding. After 10 MGy dose, the He-doped fibre presented the largest levels of RIA (400 dB/km), whereas a single mode fibre (SMF28) exhibited a strong RIA of about 230 dB/km. Limited losses were instead induced in F-doped fibres (50 dB/km). Their results also show that under radiation conditions some compositions have to be avoided, implying the use of radiation-hardened optical fibres (e.g. fluorine-doped fibres) in radiation environments. A single mode fibre (SM28) exhibited a shift of 4 MHz under 10 MGy radiation dose, an acceptable response for the radiation levels.

At the Large Hadron Collider (LHC) project, CERN is hosting one of the largest existing optical fibre installation exposed to ionising radiations for the transmission of large amounts of data, with maximum dose rate registered of 10 kGy/year (Girard et al., 2013). Several fibre samples from different manufacturers were exposed to gamma rays at the radiation test facility of the SPS tunnel at CERN, up to a total dose

of 10 kGy. The results show that pure silica fibres exhibit significantly lower losses than the Ge-doped fibre at the same dose (Wijnands et al., 2008).

The vulnerability of optical fibres to the radiative environment of the TT10 tunnel has been analysed to evaluate their response to the measured radiation dose and, hence, to adopt potential radiation hardening. In fact, the radiation tolerance of the fibre and its response during gamma-ray exposition in the TT10 tunnel were considered to ensure that the radiation dose remains consistently well below the radiation acceptance level (Di Murro et al. 2019).

Appropriate remote radiation monitoring systems were installed for measuring the gamma-ray dose in the TT10 tunnel. Figure 4.1 shows the radiation dosimeters attached at the tunnel crown. Two gamma-ray dose measurements were collected by the *Radiation Tolerant and Measurements Electronics* Section of CERN *Survey, Mechatronics and Measurements* Group (CERN EN-SMM-RME): the first one in June 2015 and the second one in July 2017. Both readings show minor gamma-ray dose (Table 4.1), reaching a maximum radiation dose of 30 Gy in 2017, confirming that the value is well below the tolerance radiation level of 100 kGy for a single mode fibre (Alasia et al., 2006).

Yet, radiation testing remains necessary as the optical fibre composition should be carefully chosen in order to minimize its vulnerability to the specific environment.

Figure 4.1. Radiation dosimeters installed on the TT10 tunnel crown (Di Murro et al. 2019).

Table 4.1.Gamma-ray dose measurements taken in the TT10 tunnel (Credit: CERN EN-SMM-RME).

Date of measurement	Gamma-ray dose [Gy]
15/06/2015	1.5 - 3.3
15/06/2017	25- 30

4.3 Principles of Brillouin Optical Time-Domain Analysis

The Brillouin optical time domain analysis (BOTDA) technology provides spatially continuous distributed strain measurements over long distances using standard optical fibre. As a light is launched in the optical fibre from a fibre optic interrogator with a pulse of around 1550 nm, a small amount is backscattered at every point toward the launch due to local impurities. A spectrum of the backscattered light generated along the fibre is shown in Figure 4.2. The backscattering process, which allows the light to propagate back to where it was originally sent, initiates from material impurities and its light signal appears in three frequency spectra (Figure 4.2). Conversely from the Rayleigh and Raman scattering, originated from material impurities and thermal excited acoustic waves respectively, the Brillouin scattering is generated from fluctuations of density induced by the propagation of acoustic waves. It is considered to be a diffusion of light radiation induced by acoustic phonons (Kechavarzi et al. 2016).

The peak of the Brillouin frequency of the fibre is proportional to the acoustic velocity (Eq. 4.1), which is strictly affected by the strain and temperature applied to the fibre (Horiguchi et al. 1995). The Brillouin frequency shift is in the range of 9-13 GHz for a light wavelength of 1300 – 1600 nm in standard single mode fibres.
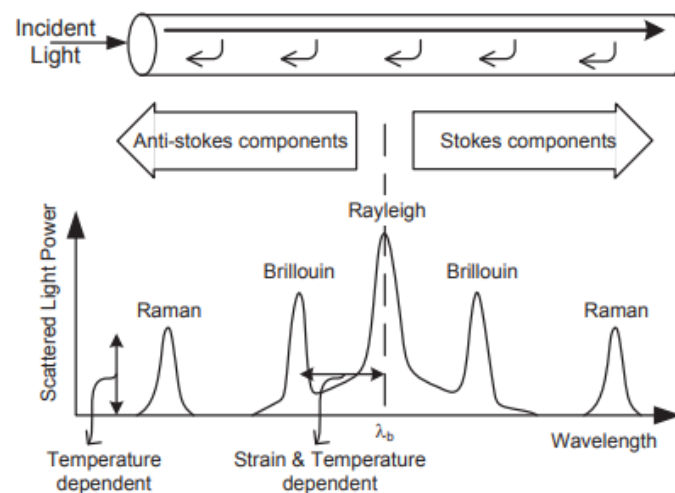
Figure 4.2. Launched light propagation and backscattered light components (Soga, 2014).

By measuring the time required for the backscattered light to return to the FO interrogator and by knowing that the speed of light is constant, the distance at which

the Brillouin frequency shift occurs can be precisely evaluated, as shown in Figure 4.3.
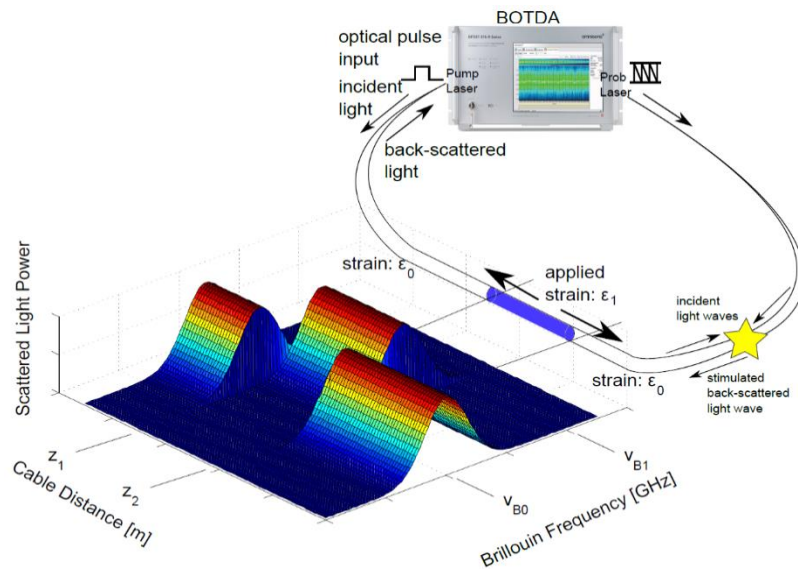
Figure 4.3. Distributed Fibre Optic Sensors: principles.

Due to any change in temperature or strain of the fibre, the acoustic velocity V of the light will change and the frequency of backscattered light obtained from the analyser is shifted by an amount that is linearly proportional to the applied strain $\Delta\varepsilon_{m(t,z)}$ and temperature $\Delta T_{(t,z)}$, as shown below:

$$\Delta v_{b(t,z)} = C_\varepsilon \Delta\varepsilon_{m(t,z)} + C_T \Delta T_{(t,z)} \tag{4.2}$$

where $\Delta v_{b(t,z)}$ is the change in frequency and C_ε and C_T are the coefficients for strain and temperature change respectively. Therefore, both strain and temperature profiles can be detected by the Brillouin scattering along the whole fibre length (Mohamad, 2008).

For the purpose of the monitoring of the TT10 tunnel, stimulated Brillouin scattering was adopted (Omnisens 2008), which enhances scattering in a Brillouin optical time domain analysis (BOTDA) with a better spatial resolution compared to the Brillouin Optical time domain reflectometry BOTDR (Bao and Chen, 2011). In fact, the BOTDA system provides a strain resolution of ±4 με compared to ±30 με of the BOTDR system, but it requires a closed continuous loop. Therefore, if any fibre breakage occurs, no data can be obtained if the environment is not reachable.

The BOTDA interrogator used in this study provides a minimal spatial resolution of 0.5 m and a readout resolution of 0.1 m (Table 2). The former is determined by the velocity of incident light v and the pulse width τ, according to the Eq. 4.3:

$$S = \frac{v \cdot \tau}{2} \qquad (4.3)$$

The sampling or readout resolution is determined by the distance between two measured data points.
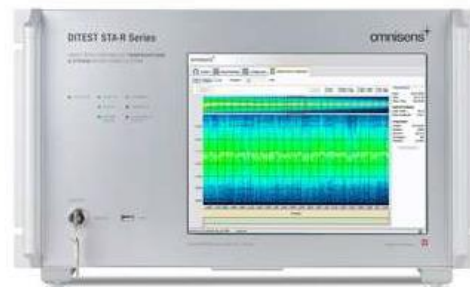
Figure 4.4. Omnisens DiTest STA-R BOTDA analyzer (Omnisens 2008).

Table 4.2. Characteristics of Omnisens BOTDA interrogator.

Parameters	BOTDA
Strain accuracy [με]	4
Temperature accuracy [°C]	0.2
Minimal spatial resolution [m]	0.5
Readout resolution [m]	0.1

4.4 Fibre Optic instrumentation of TT10 tunnel

4.4.1 Introduction to the monitoring area

Recent tunnel inspections highlighted the development of a number of cracks in different sections of the TT10 tunnel lining (Di Murro et al. 2016; 2018; 2019). In order to gain a better understanding of the tunnel lining mechanism of deformation as part of a long-term monitoring strategy, innovative instrumentation which makes use of optical sensors was adopted.

Two different zones of the TT10 tunnel were involved in the FO installations: 1) the *orange zone*, assessed to be the most critical area in terms of stability, as it appeared to be involved by the majority of the cracks on the tunnel lining and 2) the

blue zone, where cracks started to develop. A plan view of the zones involved in the FO installations is provided in Figure 4.5. To cover the cracked zones, several cross-sections along the tunnel were instrumented with both novel FO sensors and conventional geodetic profiles, mounted almost at the same locations in order to compare different technologies in the assessment of the tunnel lining response.

The limited tunnel access to CERN underground facilities gave the possibility to complete the first FO installation, named *CERN 1*, which took place in early 2014 and involved the deployment of eight circumferential FO loops in the *blue area*, as shown in Figure 4.5. The successful completion of CERN 1 installation enabled the plan of a second installation, named *CERN 2*, commenced in May 2014, with the placement of six FO tunnel loops in the *orange area* shown in Figure 4.5. Between the first FO tunnel loop (Loop 1) of CERN 2 installation and the last tunnel loop of CERN 1 (Loop 8), there is a section of 138 m length which is unmonitored.
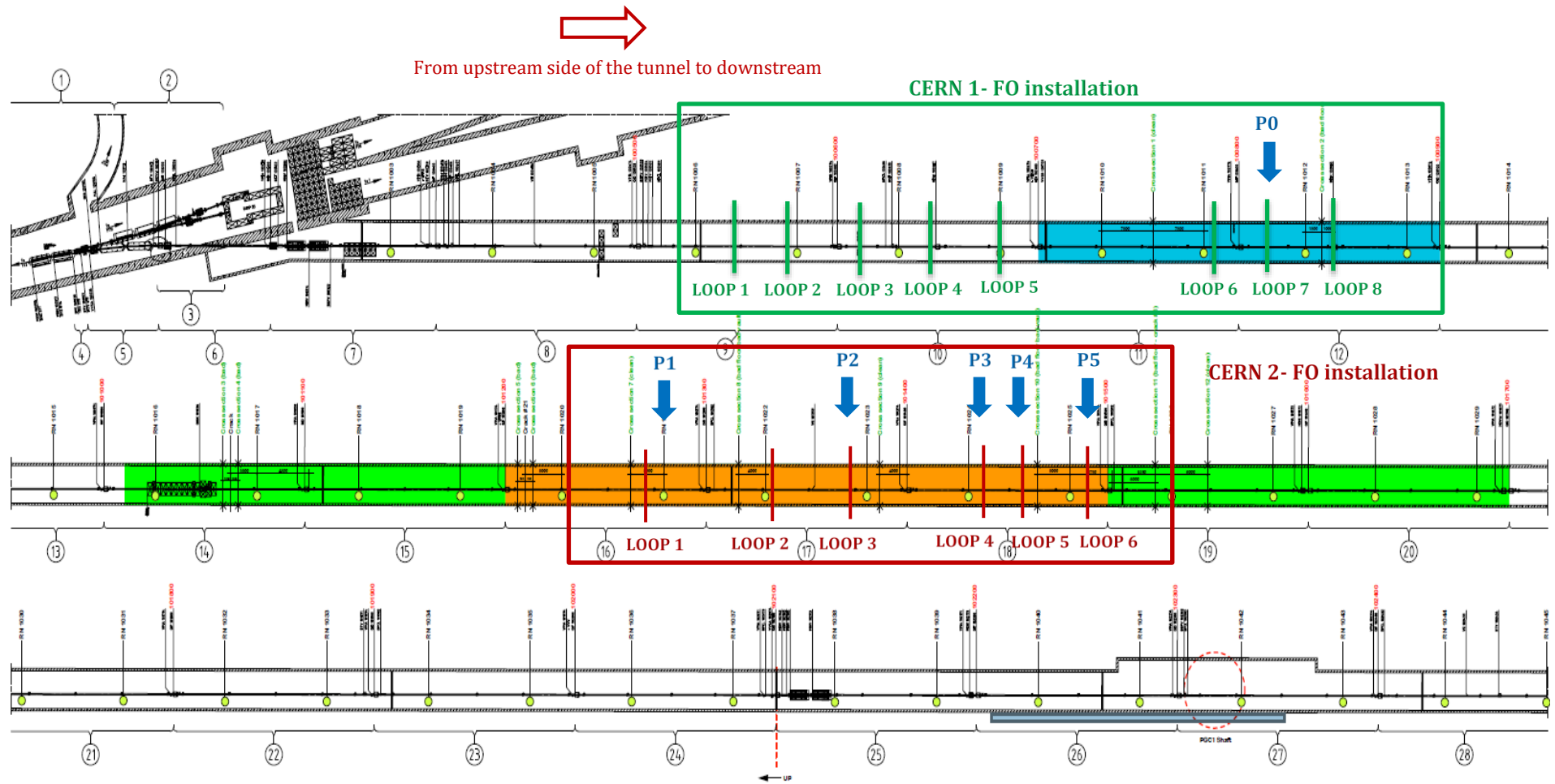
Figure 4.5. TT10 tunnel plan view: location of the blue, green and orange area; location of the FO loops for _CERN 1_ and _CERN 2_ installations; location of the geodetic profiles.

Due to tunnel access restrictions, the long-term monitoring was planned to be carried out from outside of the tunnel, using an Omnisens BOTDA analyser (Omnisens 2008), where both ends of the FO cables are connected. The installation of the FO sensors took place in March 2014 and was completed in May 2014. As in the deep CERN underground infrastructure the temperature was assessed to remain constant, no fibre optic temperature cable was needed, requiring then only the installation of a strain sensing cable. The FO strain cable runs in both the longitudinal and cross-section directions of the tunnel, forming several circumferential loops and one straight cable section in the longitudinal direction, with the cable sections of interest pre-strained, as shown in Figure 4.6, where the solid line refers to the pre-strained cable section whereas the dashed line refers to loose/slack cable section.

The application of a tension strain allows for accommodation of any compressive strain, read as a relaxation of the tensile strains without cable buckling. As the primary interest is to measure the relative change in strain, it was not essential to record the exact value of strain applied. The slack FO cable sections (i.e. zero mechanical strain) placed between consecutive strained sections served as a thermal strain reference during data analysis.

At the end of the monitored circuit, the two ends of the cable were joined together in a connection box (Figure 4.7a), located in the upstream area of the tunnel beside a red access door (Figure 4.7b). The optical fibre was then spliced to a standard extension cable and then routed out of the tunnel section via a 50 m vertical shaft into a secure monitoring area where the BOTDA unit was located (Figure 4.7c). No further access in the tunnel section was then required, as long as there was no cable breakage and resulting required cable fixing. Consequently, the monitoring and the data collection were planned to be carried out in a controlled area (Building 806), a strategic point as it is located very closely to the CERN *SMB-SE-FAS* Group's office building (Figure 4.7d).

To minimize any risk of the equipment damage due to potential tunnel inspection, appropriate warning signs were placed in a number of different places close to the instruments. Since no major construction activity was taking place nearby and the aim was the long-term structural health monitoring of the tunnel, the BOTDA analyser was not required to stay on site on a permanent basis and thus it was rented monthly.
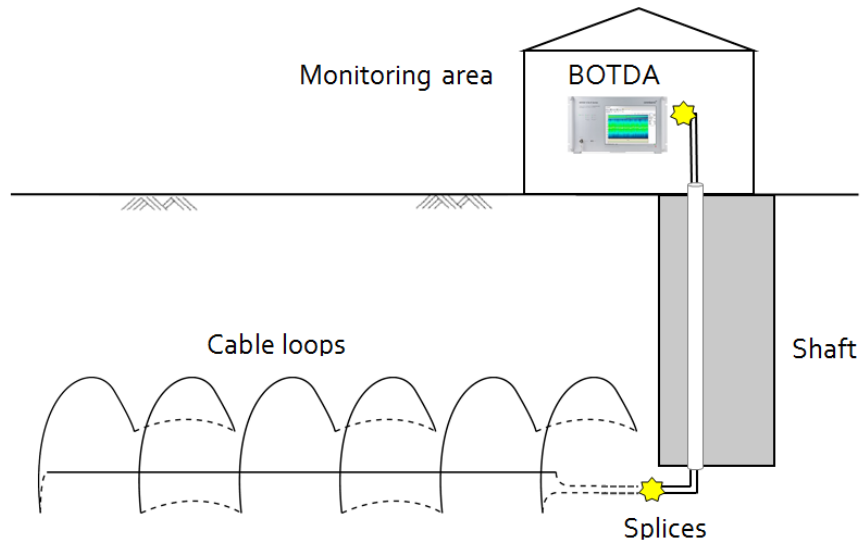
Figure 4.6. Fibre optic installation layout in TT10 tunnel (Kechavarzi et al. 2016, Di Murro et al. 2019).

(a)
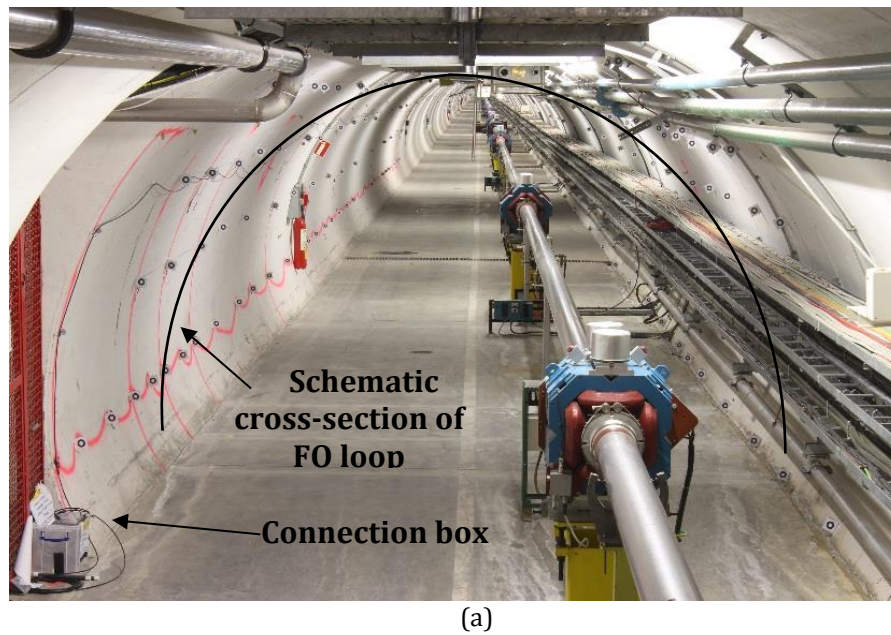
(b)

(c)
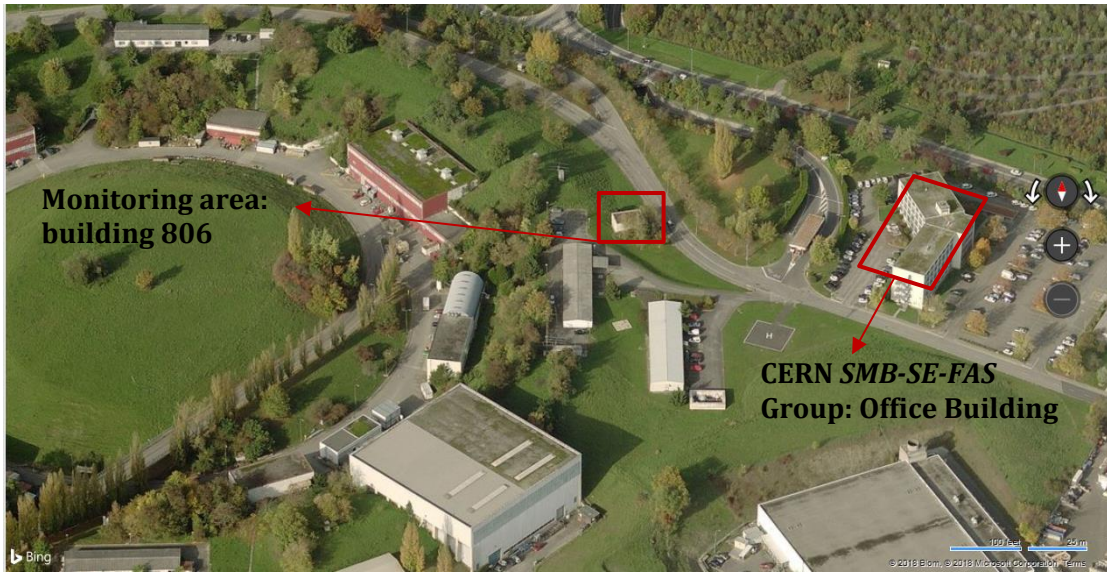
(d)

Figure 4.7. (a) View of TT10 tunnel from the upstream part with highlighted the instrumented cross-section FO loop, (b) Access door to the 50 m vertical shaft, (c) BOTDA analyser placed in the monitoring control room on the surface (CERN Building 806), (d) Top view of the location of CERN SMB-SE-FAS Group's Office and the controlled monitoring building 806 (Photo credit: CERN GIS Portal).

4.4.1.1 Type of optical fibres

Two types of standard optical fibre were used in the TT10 tunnel monitoring: (i) a tight buffered single mode strain sensing cable, manufactured by Nanjing University, in China (Figure 4.8a), and (ii) an extension cable (Figure 4.8b), a more robust cable used to bring the sensing cable to the monitoring area based on ground surface.

The FO strain sensing cable is a single mode cable, which consists of a core of 9 μm usually made from glass, surrounded with two outer layers: a glass layer of cladding of 125 μm diameter and a plastic buffer of 250 μm of diameter, used to protect the glass, as shown in Figure 4.8a.

Unlike the strain sensing cables, the fibres in the standard loose tube telecommunication cable are placed loosely inside a plastic or steel tube, filled with a water-blocking gel (Kechavarzi et al. 2016). This prevents any external mechanical strain to be transferred to the optical fibre located inside. Also, this cable comprises an additional polyethylene coating layer (Figure 4.8b).

(a)

(b)
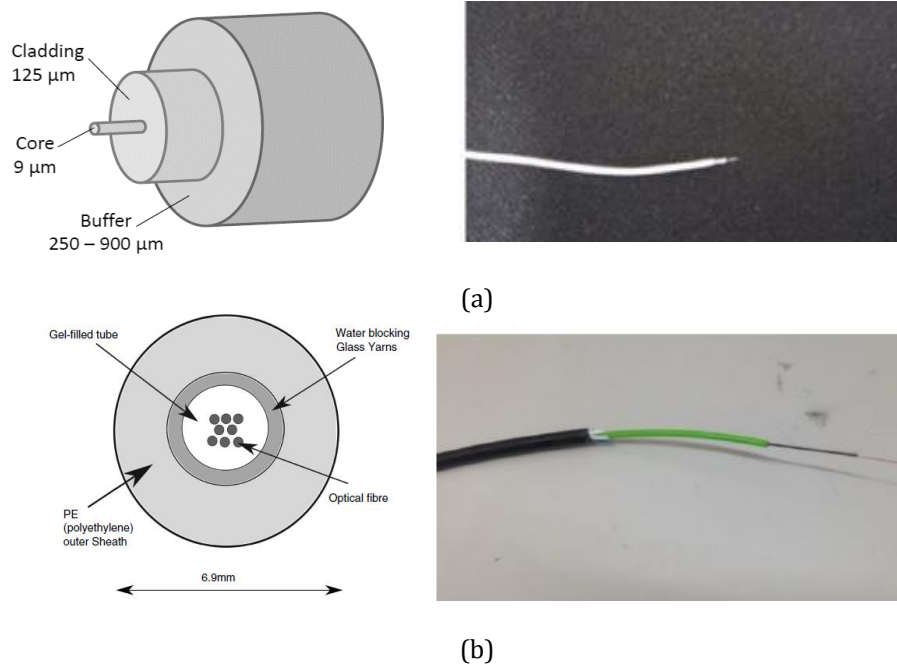
Figure 4.8. Fibre optic strain cables: (a) single fiber tight buffer strain sensing cable manufactured at Nanjing University; (b) extension gel-filled loose cable (Soga and Luo, 2018).

4.4.1.2   *Method of attachment of optical fibres*

The accuracy and reliability of a fibre optic installation involve an adequate method of attachment of fibre to the structure that needs to be monitored. Optical fibres can be either embedded or glued within the structure or can be anchored at fixed points. In the former case, the optical fibre is fully bonded and the fibre strain profile coincides with the one experienced by the structure. In the latter case, the strain sensing cable is attached to the structure only at discrete points through a gauge length installation (Kechavarzi et al. 2016). In the TT10 tunnel, the latter gauge length method was adopted. The cable was attached to the tunnel lining at discrete locations by using a serious of hook-and-pulley systems, with the hook screwed into the tunnel lining's surface and the FO cable passing along the pulley (Figure 4.9b). The gauge length method requires that strain can only be measured if the optical fibre is properly pre-tensioned, without leaving any slack sections. Therefore, each strain cable section between two discrete points was tightened before gluing it to each pulley wheel. The pretension strain applied to the fibre was induced by pulling the optical fibre from both ends of the cable in addition to the application of some weights until the glue became dry.
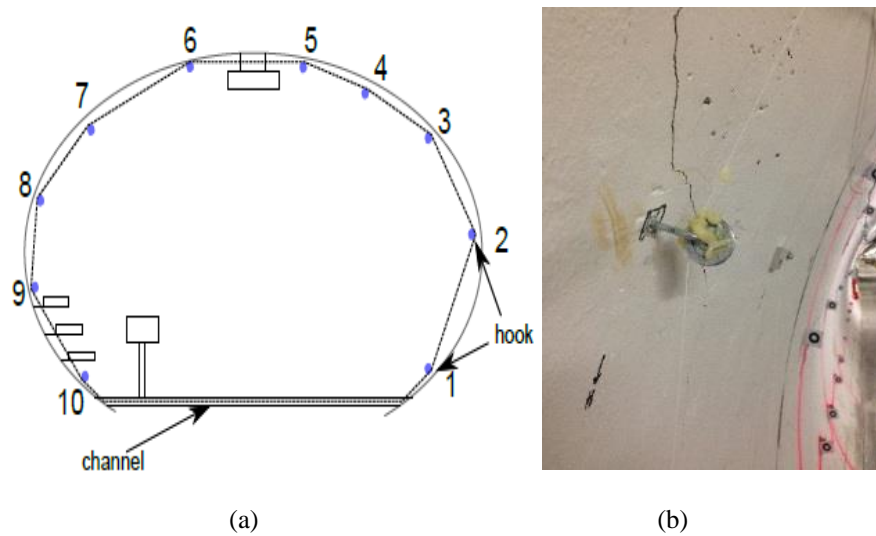
Figure 4.9. FO field installations: (a) Cross-section of the circumferential strain cable loop (Kechavarzi et al. 2016); (b) Method of attachment of optical fibre: pulley wheels.

4.4.2 Data analysis

The Brillouin frequency peak shift is linearly dependent on the mechanical strain experienced by the fibre and temperature. If at any point a strain-sensing fibre is experiencing some strain ε_0, the value of Brillouin frequency, for which the peak amplitude occurs, changes ($\Delta \nu_b$). It is assumed that the change in the Brillouin frequency experienced by a strain-sensing cable is linearly dependent not only on the mechanical strain that the fibre is experiencing but also on temperature. Therefore, the temperature effect needs to be compensated in order to obtain pure strain measurements.

One solution for compensating the temperature is to install a temperature cable along with the strain cable, which is only sensitive to temperature change. The optical fibre of the temperature cable is surrounded by a gel liquid, therefore eventual external strain applied on the tube will not be directly transferred to the fibre inside (Figure 4.8b).

Under isothermal conditions, the linear relationship between the frequency shift and the axial strain is as follows:

$$\nu_b = \nu_{b0} + C_\varepsilon(\varepsilon - \varepsilon_0) \tag{4.4}$$

where $(v_b - v_{b0})$ is the change in frequency, and $(\varepsilon - \varepsilon_0)$ is the change in axial strain.

However, under non-isothermal conditions the Brillouin frequency shift varies with the longitudinal strain and temperature, according to the Eq.4.5:

$$\Delta v_{b_{(t,z)}} = C_\varepsilon \Delta \varepsilon_m + C_T \Delta T = C_\varepsilon (\Delta \varepsilon_s + \Delta \varepsilon_T) + C_T \Delta T \tag{4.5}$$

where $\Delta v_{b_{(t,z)}}$ is the Brillouin change in frequency due to mechanical strain $\Delta \varepsilon_{m_{(t,z)}}$ and temperature $\Delta T_{(t,z)}$ due to a change in the refractive index and acoustic wave velocity. The coefficients C_ε and C_T depend on fibre properties and do not depend on the type of fibre cable used. The coefficient C_ε is the value of the rate of change of frequency with applied strain in a strain cable and for a given fibre it can be obtained from calibrating a strain cable under constant temperature. The value assumed for Nanjing's strain cable is around 493 MHz/µε. The coefficient C_T is the value of the rate of change of frequency with applied temperature in a temperature cable and a common value is around 1 MHz/°C (Kechavarzi et al. 2016). Both strains $\Delta \varepsilon_s$ and $\Delta \varepsilon_T$ are caused by the thermal expansion of the structure and the FO cable components respectively through a thermal coefficient α (Equation 4.6):

$$\Delta v_{b_{(t,z)}} = C_\varepsilon \Delta \varepsilon_s + (C_\varepsilon \alpha + C_T) \Delta T \tag{4.6}$$

It can be assumed that the thermal coefficient is only due to the structure (Mohamad, 2008), which is usually assumed to be around 10 µε/°C for concrete.

The temperature change ΔT can be calculated from the temperature loose cable, according to Eq.4.7:

$$\Delta T(t,z) = \frac{\Delta v_t(t,z)}{C_{T_t}} \tag{4.7}$$

where C_{T_t} is the thermal coefficient calibrated from a temperature cable and its value is slightly larger than C_T.

The total mechanical strain $\Delta \varepsilon_{mech}$ can then be evaluated as follows:

$$\Delta \varepsilon_{mech}(t,z) = \left(\frac{\Delta v_s(t,z)}{C_\varepsilon} \right) - \left(C_T \frac{\Delta v_t(t,z)}{C_{T_t}} \right) \tag{4.8}$$

4.4.2.1 Basic steps for the FO data analysis

Several basic steps are required to process the primary raw data provided by the BOTDA unit into the final engineering information desired. The general steps in addition to several unexpected issues taken for analysing the FO data are summarized in Figure 4.10.

Each circumferential fibre optic loop allows the measurement of a strain profile along the fibre through a series of steps listed below.

a. **Obtain the raw data** (Brillouin frequency values). Repeated automatic measurements were taken with at least ten measurements per installation in order to minimise the measurement error. The readings were then averaged so that each Brillouin frequency profile per dataset is obtained:

$$v_{raw}(t, z)$$

b. **Filtering phase.** The Brillouin frequency values obtained from the BOTDA can be noisy, determining unrealistic fluctuation of data, which may occur due to either potential bend of the cable or fibre splices not completed carefully with consequent signal loss. A second-order smoothing of the data was performed using a Savitzky-Golay filter. By fitting a polynomial to a frame of data points, the filter minimises the least-squares errors (Savitzky and Golay, 1964).

c. **Differential Brillouin Frequency response.** Each dataset reading was subtracted from a baseline reading taken at the end of the FO installation in order to obtain the accumulated strain response.

$$\Delta v(t, x) = v_{raw}(t, x) - v_{raw}(t = t_0, x) \tag{4.9}$$

d. **Calculation of the mechanical strain profile.** As no temperature cable was installed, no temperature compensation was needed. According to Equation (4.4), the axial strain profile was obtained for all the circumferential loops.

Moreover, unexpected issues can occur during the data analysis and, therefore, further steps may need to be taken. The mentioned issues are listed below.

- The strain cable may show some unpredicted residual displacements in the free/slack sections, which have to be shifted vertically.

- The fibre cable length can change throughout the monitoring period due to the eventual use of extension cables or splices, resulting in a distance difference between different datasets. To overcome this issue, a distance (horizontal) shift can be done.
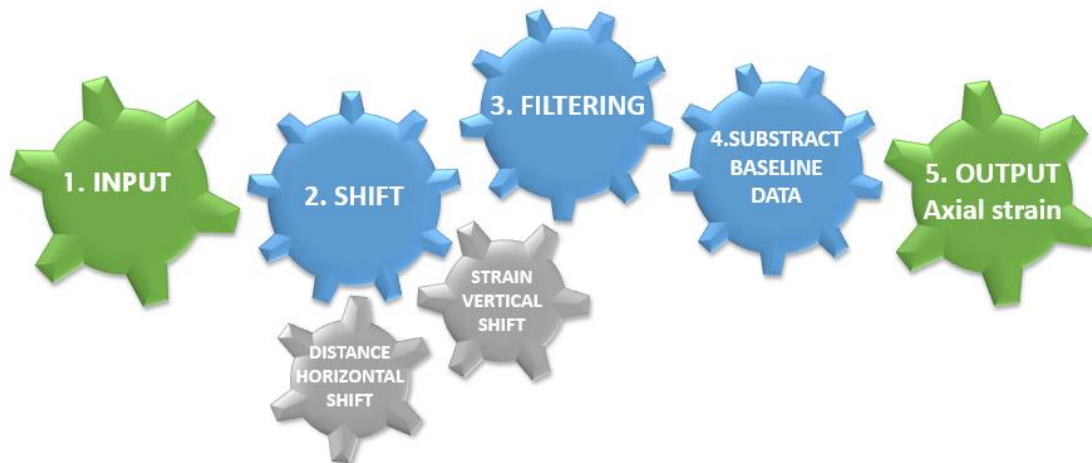
Figure 4.10. Basic steps for FO data analysis.

4.4.2.2 *Data collection*

The FO data was collected by attaching both ends of each FO installation to the BOTDA interrogator. A spatial resolution and a sampling interval of 1 m and 0.10 m were adopted respectively for this project. The raw Brillouin frequency profiles were subtracted from a baseline measurement to obtain the incremental strain changes. The baseline reading, which shows the initial applied strain, confirmed a good signal and clear repeatable trends among the instrumented FO cross-sections (Soga et al. 2017). Progress monitoring readings were initially planned to be taken every two-three months; however, based on the FO strain results collected, the long-term monitoring plan was adapted to the need. As no real movement was observed during the first monitoring year, measurements were taken almost every three-four months, depending also on the availability of the BOTDA unit, rented directly from the manufacturer Omnisens based in Lausanne, Switzerland. A total of twelve measurements was collected within a monitoring period of three years (July 2014 – October 2017). Table 4.3 shows the FO datasets taken for the installations CERN 1, CERN 2 and CERN 3.

Table 4.3. FO datasets for CERN 1, CERN 2 and CERN 3 installations: baseline and progress readings.

Monitoring Section	Date	Reading
CERN 1: eight circumferential loops	July 2014	Baseline
	August 2014	Progress
	May 2015	
	June 2015	
	October 2015	
	March 2016	
	April 2016	
	July 2016	
	November 2016	
	February 2017	
	April 2017	
	July 2017	
	October 2017	
CERN 2: six circumferential loops	July 2014	Baseline
	August 2014	Progress
	October 2015	
	March 2016	
	April 2016	
	July 2016	
	November 2016	
	February 2017	
	April 2017	
	July 2017	
	October 2017	
CERN 3: two circumferential loops	February 2016	Baseline
	July 2016	Progress
	November 2016	
	February 2017	
	April 2017	
	July 2017	
	October 2017	

4.4.3 FO data results: circumferential sections

4.4.3.1 CERN 1

The first fibre optic monitoring setup comprised the deployment of eight cross-sections to measure circumferential strains. Figure 4.11 shows the FO instrumentation layout of CERN 1 installation, with the first loop located in the upstream tunnel area. The first tunnel loop was placed almost 3 m away from the access red door, located in the upstream area of the tunnel. The distance between each tunnel loop is shown in Figure 4.11. Overall, the instrumented FO tunnel loops cover a monitoring area of around 45 m, with a section in between of 28 m unmonitored (Figure 4.11). Both ends of the optical fibre return to the connection box, where the fibres are spliced to an extension cable and then brought to the surface.
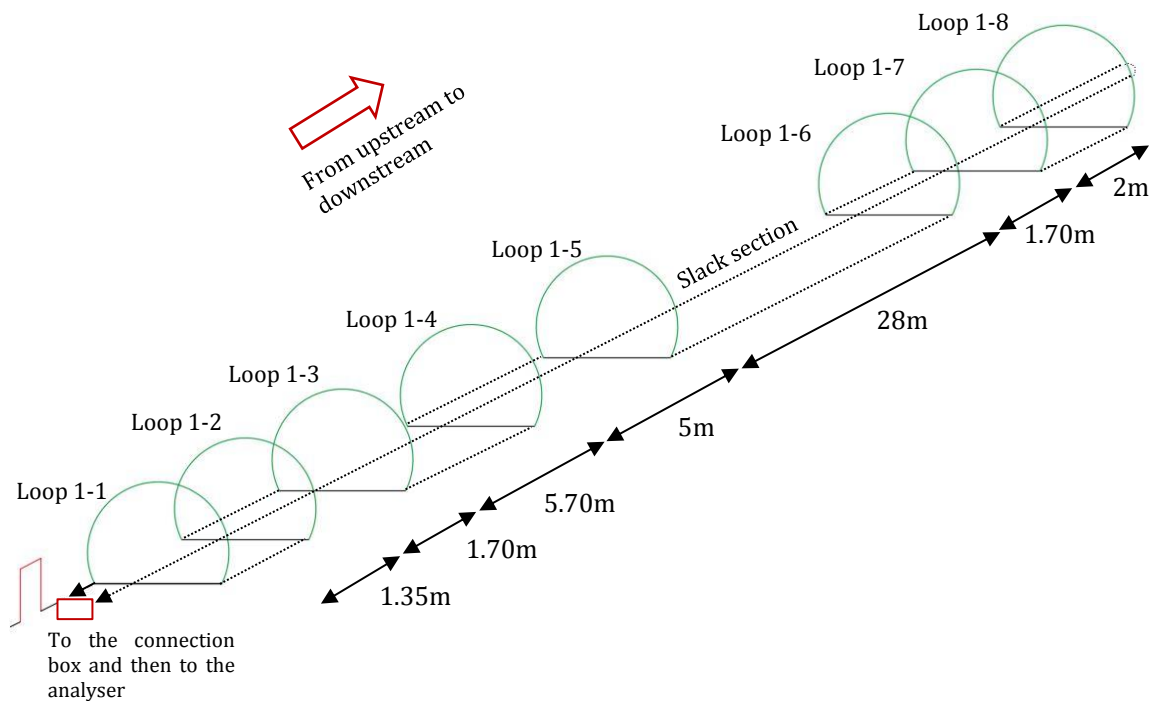
Figure 4.11. CERN 1: Fibre optic instrumentation layout of tunnel loops.

The primary data obtained is the measured peak Brillouin frequency shift experienced by the optical fibre caused by the application of a strain along the whole length for the instrumented loops. The measurements were taken by considering a spatial resolution and a sampling interval of 1 m and 0.1 m respectively. Figure 4.12 shows the raw Brillouin frequency FO data obtained from the BOTDA interrogator. Due to the applied strain, eight discrete sections and a longitudinal long section exhibit high

frequency (Di Murro et al. 2019). As mentioned previously, a baseline reading was taken in July 2014, and subsequent monitoring readings were taken with an interval of two-three months, providing a total of twelve measurements and a dataset of three years of monitoring. By subtracting the baseline reading from the dataset of the progress readings, the accumulated response in terms of Brillouin frequency was obtained.
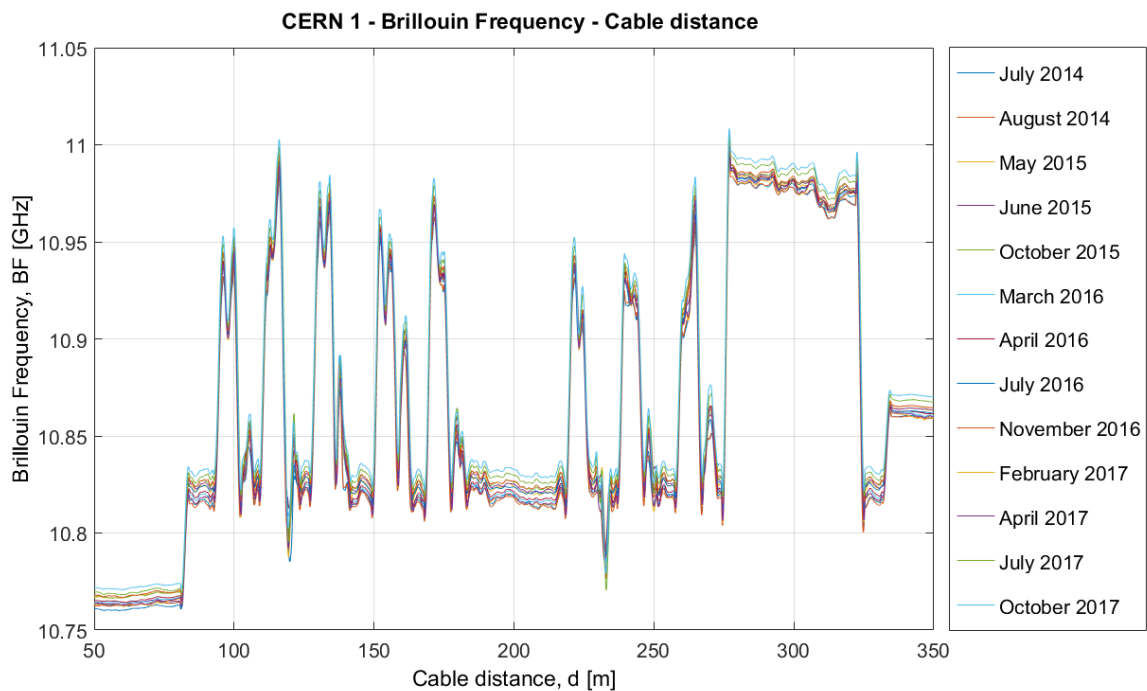
Figure 4.12. CERN 1: Brillouin frequency shift along cable distance.

Figure 4.13 displays the cumulative strain increments recorded for the circumferential loops: loop 1-1, loop 1-2, loop 1-3, loop 1-4, loop 1-5, loop 1-6, loop 1-7 and loop 1-8. The computed axial strain was plotted against the optical cable distance in Figure 4.13, looking from the upstream tunnel area for all the tunnel loops. Positive tensile strains were computed at the lateral sides of the tunnel lining, being the start and the end of the horizontal axis. Conversely, negative (compressive) strains developed at the crown of the tunnel, represented by the central section of the x-axis (Figure 4.13).

   Insignificant strains occurred after one month of monitoring (July 2014 – August 2014) for all the monitored cross-sections. A big change in the axial strain occurs within the first nine months (July 2014 – May 2015) for all the circumferential loops. Unlike loop 1-4 and loop 1-8, a consistent development of positive (i.e. tensile) and negative (i.e. compressive) strains is recorded at the tunnel axis level and the tunnel

crown respectively for the loop 1-1, loop 1-2, loop 1-3, loop 1-5, loop 1-6 and loop 1-7. Also, within one loop the peak strain value seems not to occur at the same location along the fibre for all the measurements taken throughout the monitoring period.

The axial strain experienced by the loop 1-1 is shown in Figure 4.13a. A small increase in the axial strain with time can be observed. In particular, after the measurement taken in April 2016 where peak strain values of around 150 με are recorded, the axial strain slightly decreases in July 2016, followed by a further drop in the strain in November 2016. A similar trend in the development of the axial strain is observed for the loop 1-3, with peak strain values of around 100 με at the tunnel crown and almost 200 με at the tunnel axis level (Figure 4.13c). The axial strains developed by the loop 1-4 shown in Figure 4.13d differ from the other loops as a distinct shape of positive and negative strains at the tunnel axis and the tunnel crown respectively cannot be detected, apart from some measurements (i.e. May 2015, June 2015, and October 2015). However, strain values smaller than 100 με are observed, except for the measurement collected in April 2016, which shows maximum strain values of 200 με.

Figure 4.13f illustrates the axial strain recorded by the loop 1-6, which shows a slow development of strain with time, reaching a compressive and tensile peak strain value in October 2017. Further, the measurement taken in April 2016 displays large strains of almost 200 με at both the tunnel axis and the tunnel crown, more significant strain values compared to those detected for the following months (i.e. November 2016, February 2017, April 2017), indicating a seasonal fluctuation in the data. The axial strain computed by the loop 1-7 shows a strong change between July 2014 and May 2015, after which the strain exhibits a slight increase until October 2017, as shown in Figure 4.13g.

Similarly to the loop 1-4, the FO axial strain of the loop 1-8 does not show a clear strain pattern of tensile and compressive strains, except for some measurements. Also, peak strain magnitudes of 100 με are observed at the tunnel crown, whereas the tunnel axis level experiences maximum strain values of 300 με at one side (Figure 4.13h).

Overall, the tensile strain values occurred at the lateral sides of the tunnel lining seem not to exceed 200 με for the loop 1-1, loop 1-2, loop 1-3, loop 1-4, loop 1-5, loop 1-6 and loop 1-7. However, loop 1-8 shows large tensile strains of approximately 300 με at one tunnel lateral side in April 2017. The crown shows compressive negative

peak strain values of around 120 με for loop 1-2 and loop 1-3, 200 με for loop 1-5 and loop 1-7 and almost 300 με for loop 1-6.

(a)

(b)
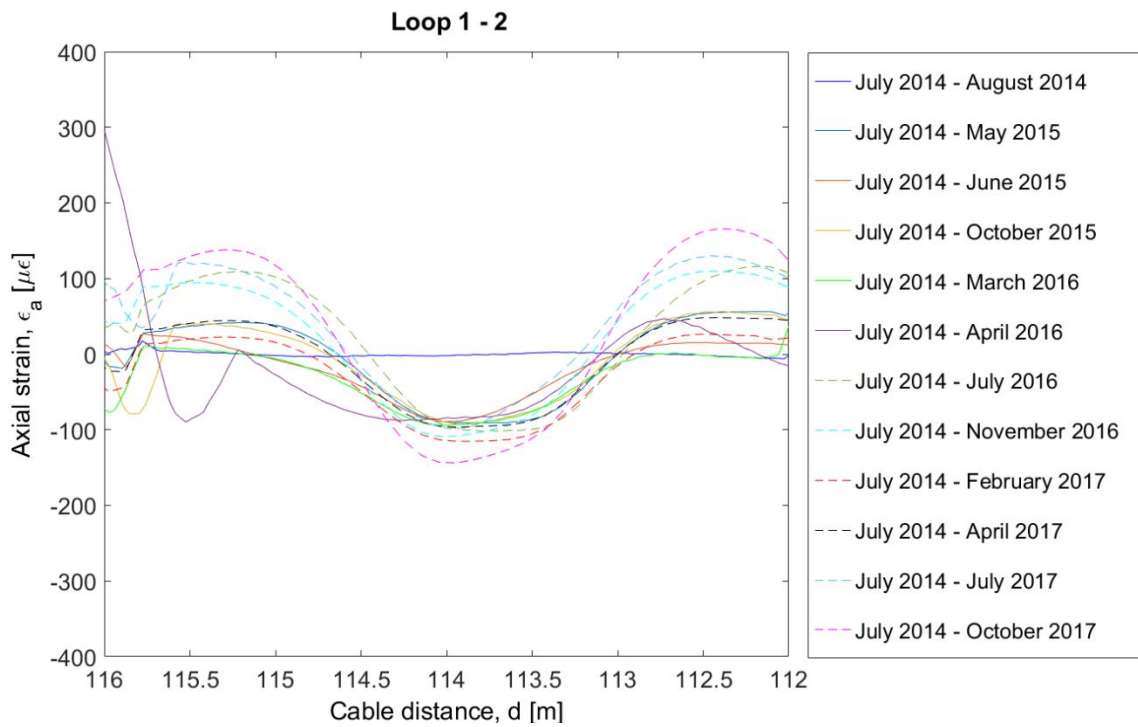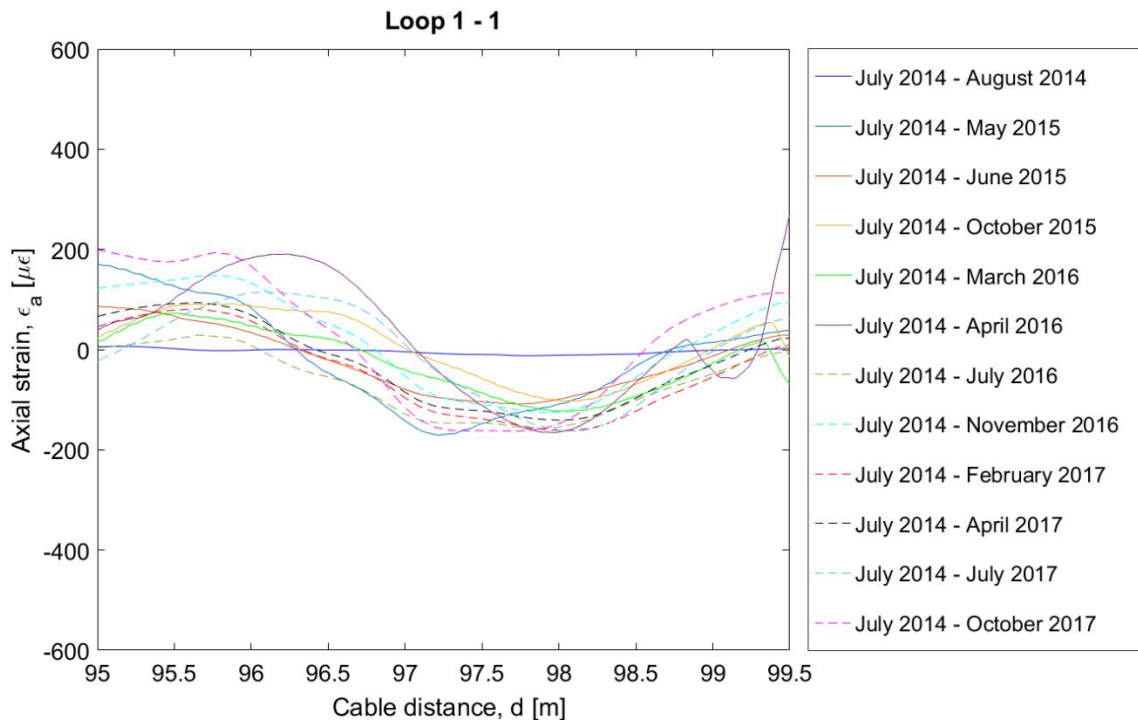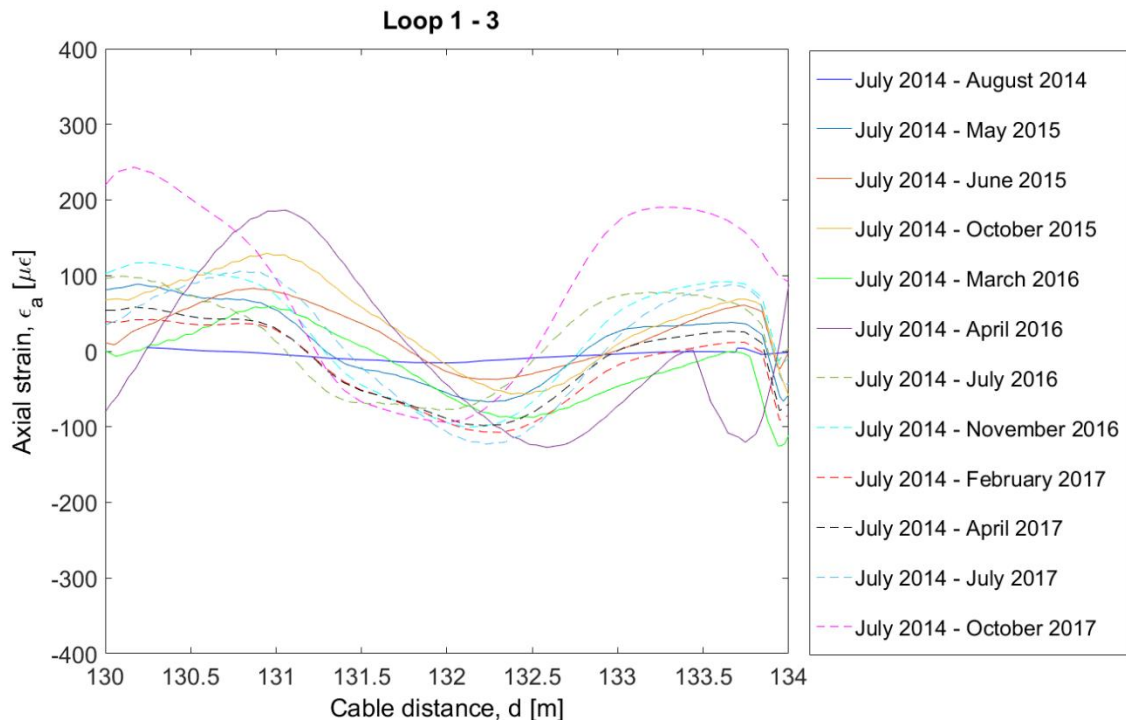
(c)
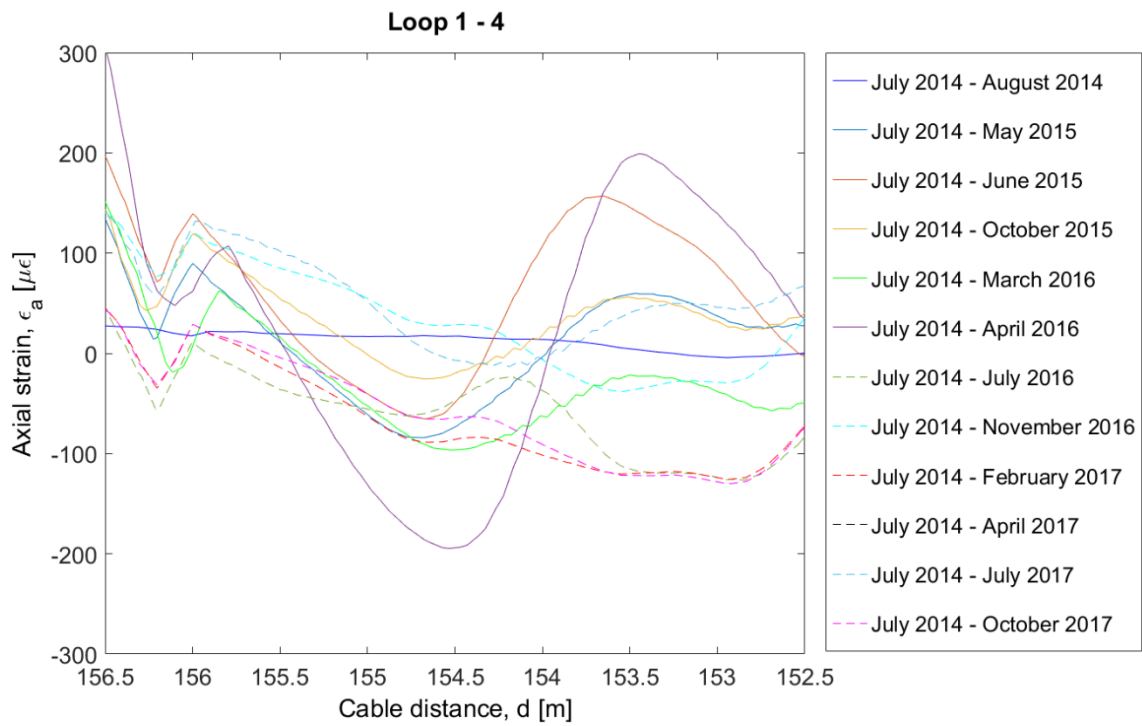
(d)
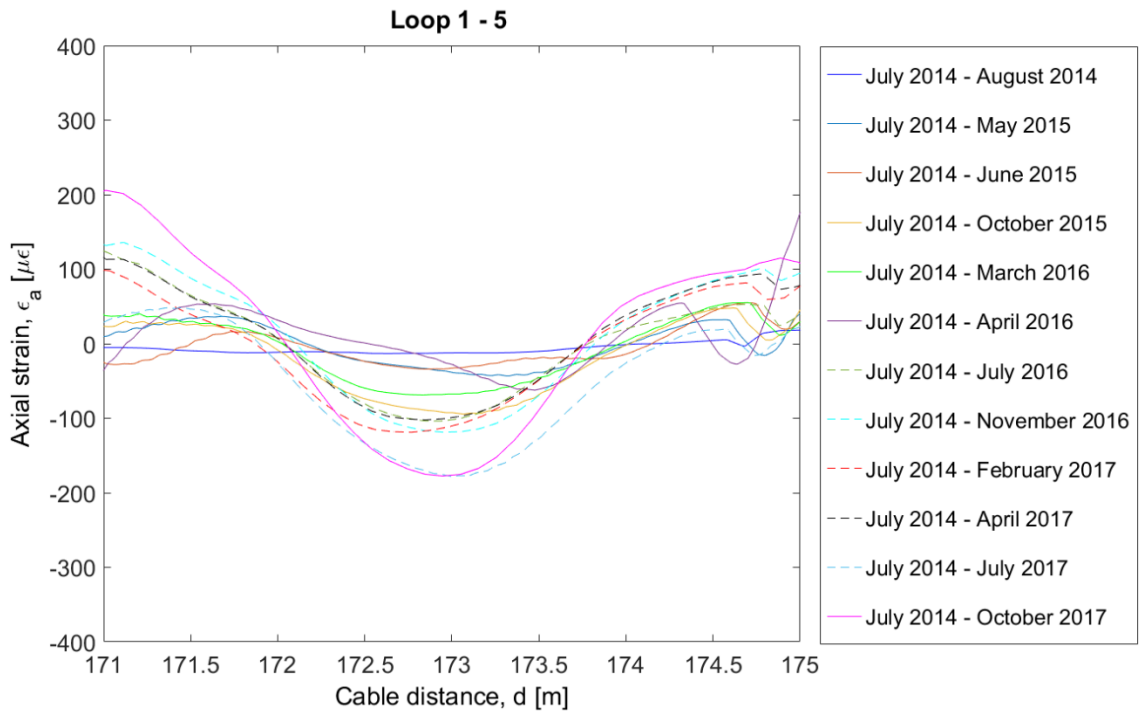
(e)
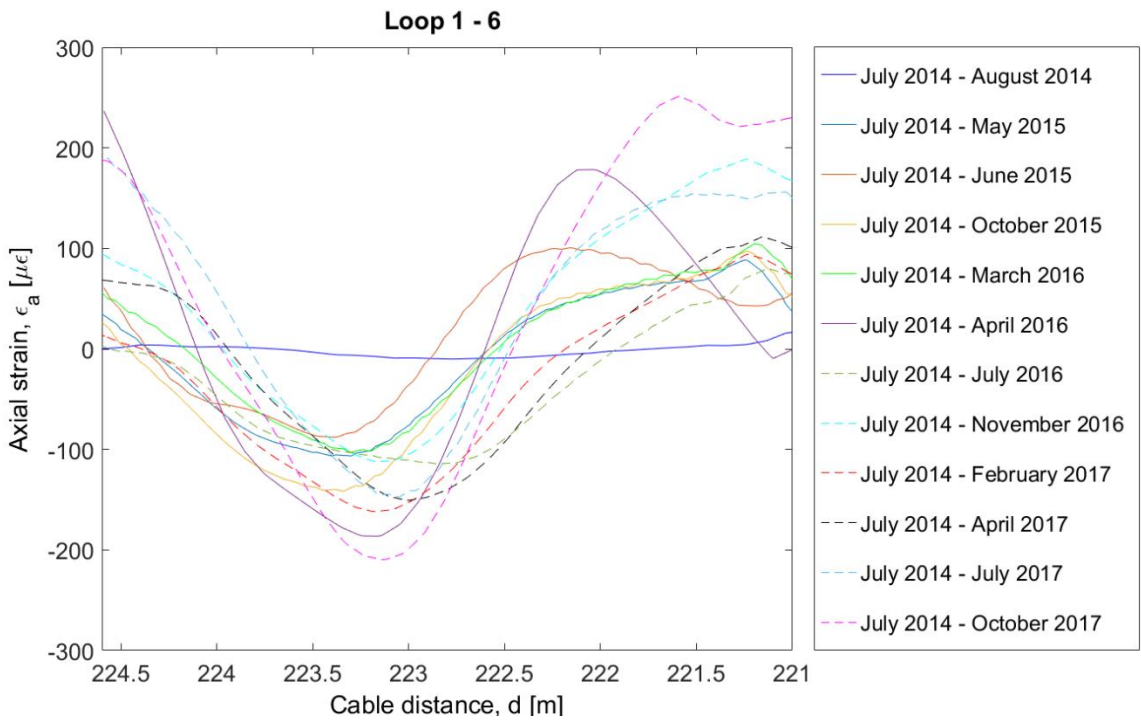
(f)
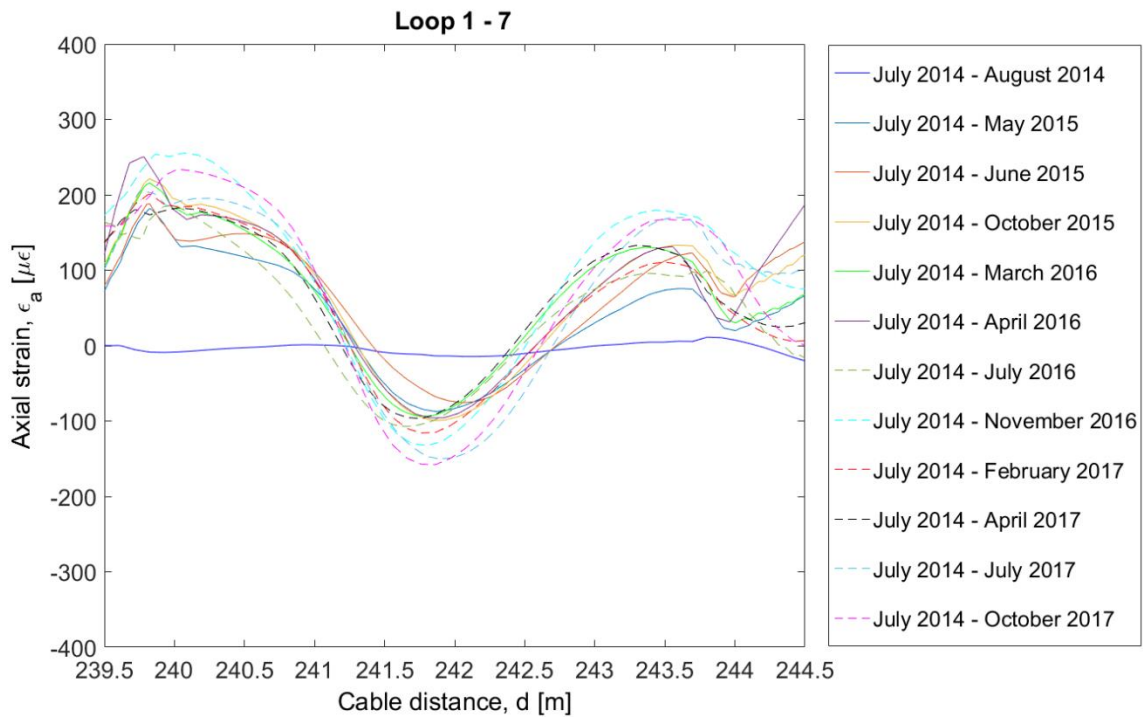
(g)
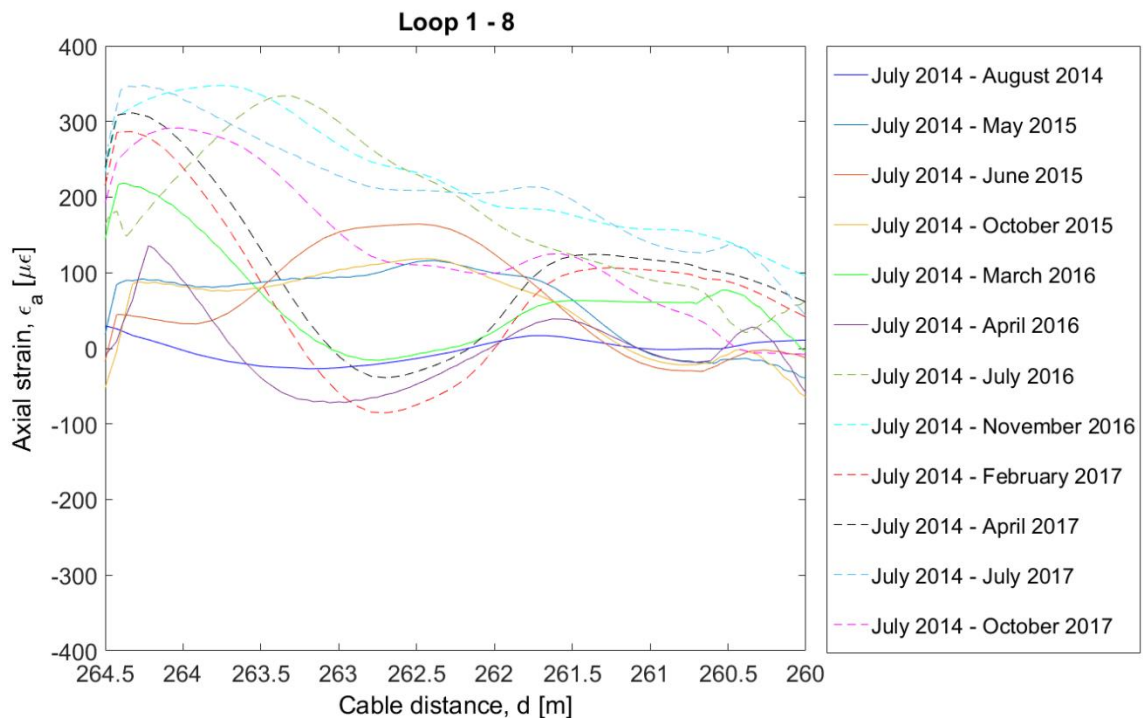
(h)

Figure 4.13. Fibre optic axial strain for cross-sectional loops of CERN 1: (a) Loop 1-1, (b) Loop 1-2, (c) Loop 1-3, (d) Loop 1-4, (e) Loop 1-5, (f) Loop 1-6, (g) Loop 1-7 and (h) Loop 1-8.

Throughout the monitoring period, the strain profiles recorded for _CERN 1_ installation show the development of tensile and compressive strain at the lateral sides of the tunnel lining and the crown respectively for most of the tunnel loops. This behaviour suggests that the TT10 tunnel lining seems to experience a vertical tunnel ovalisation (Di Murro et al. 2016; 2019). It can be concluded that the FO cumulative results show a slow small development of strains, within the range of ±200 με over the considered time periods, which is relatively short and, therefore, it may indicate a tunnel deformation development over the longer term.

4.4.3.2   CERN 2

The second fibre optic installation in the TT10 tunnel took place in May 2014. It consists of six cross-sections, as shown in Figure 4.14. The FO tunnel loops were numbered from the upstream to the downstream side of the tunnel. The first three tunnel loops (loop 2-1, loop 2-2 and loop 2-3) were approximately 16.5 m and 13 m apart from each other, whereas loop 2-4, loop 2-5 and loop 2-6 were 4 m and 6 m away respectively.
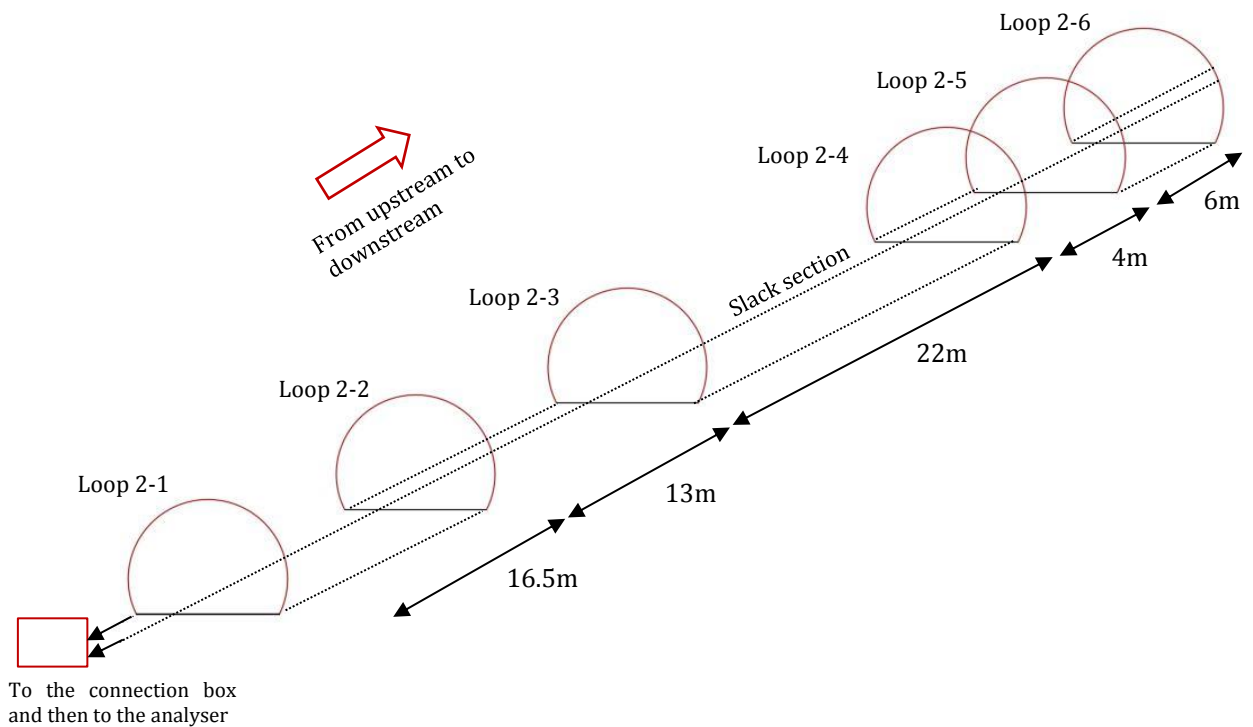
Figure 4.14. CERN 2: Fibre optic instrumentation layout.

Due to a fibre breakage occurred in early 2015, no measurements were taken for CERN 2 installation between August 2014 and October 2015, as no tunnel access was permitted. The earliest daily shutdown of CERN accelerators happened in September 2015, during which the fibre was fixed.

Figure 4.15 shows the raw Brillouin frequency FO data along the cable distance for the monitored sections since July 2014.
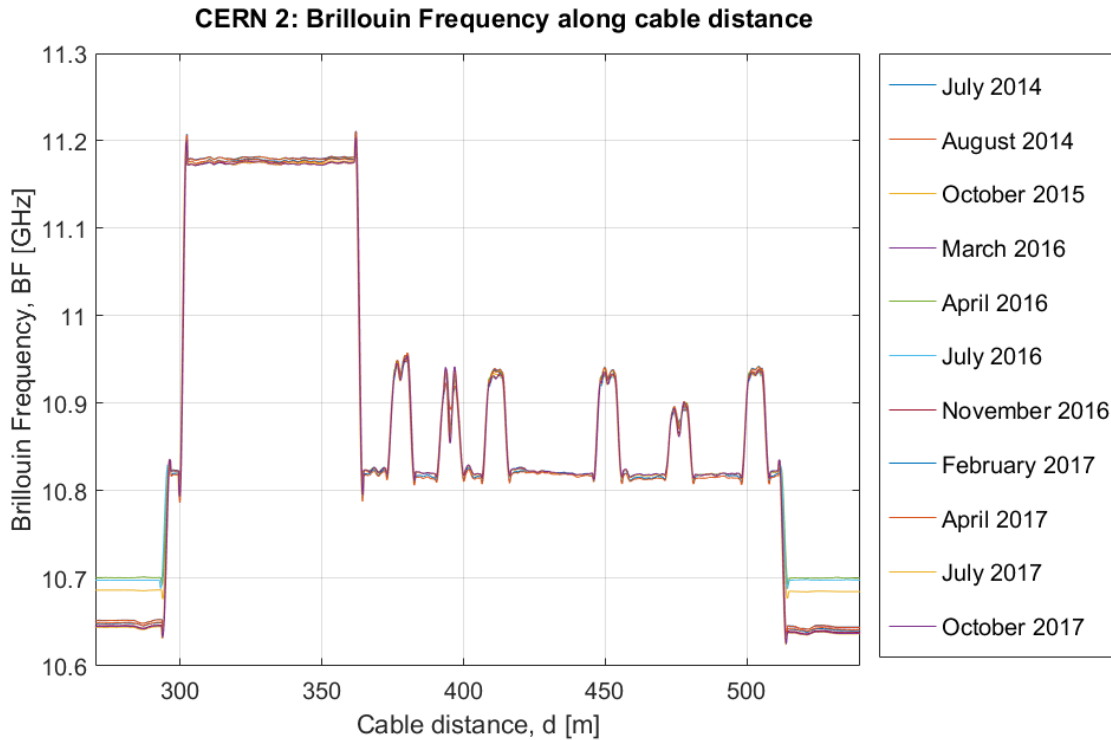
Figure 4.15. CERN 2: Brillouin frequency shift along cable distance.

Figure 4.16 shows the FO results in terms of accumulated axial strain for 6 tunnel loops. Minor strain values were observed within the first month of monitoring (July 2014 – August 2014) for all the instrumented tunnel loops. A small increase of axial strains with time is observed for the loop 2-1, which seems not to exceed strain magnitudes of 50 με at the tunnel axis level and around 40 με at the tunnel crown, as shown in Figure 4.16a.

Slightly larger strain values were recorded for the loop 2-2, as shown in Figure 4.16b. A sudden increase in the axial strain is observed within the first twelve months of monitoring (July 2014 – October 2015), after which the strain further rises with time, reaching around 300 με and 200 με at the tunnel crown and at the tunnel axis level respectively in October 2017.

The tensile and compressive strain values seem not to exceed 100 µε at both the tunnel crown and the tunnel axis level for the loop 2-3, as shown in Figure 4.16c. The axial strains developed by the loop 2-4 also show a small increase with time, reaching maximum strain values of around 150 µε and 100 µε at the tunnel axis and the tunnel crown respectively (Figure 4.16d).

Loop 2-6 also experiences minor axial strain with time, recording around 50 µε in October 2015, followed by a further small increase of axial strain with time (Figure 4.16f). Although the strain magnitudes are within the range of 100 µε, the measurement of July 2017 shows larger strains than the one collected in October 2017.

Noticeably bigger strain values were detected instead for the loop 2-5, which seems to develop axial strain continuously with time, reaching peak values of around 700 µε and 400 µε at the crown and the tunnel sides respectively, as shown in Figure 4.16e. A significant increase of 400 µε is observed at the tunnel crown between August 2014 and October 2015, whereas the tunnel axis level exhibits strain values in the range of 200-300 µε. After two further years of monitoring (October 2017), the magnitudes of axial strain almost doubled at both the tunnel crown and the tunnel axis level.

The soil profile surrounding the tunnel at the tunnel depth of the loop 2-5 seems to have an influence on the recorded tunnel lining strains. An alternate sequence of *very weak* lumpy marl and *medium-weak* marl layers was found in the geology surrounding the tunnel at the location of the FO circumferential loop 2-5, with particular attention to the weaker marls, which exhibit swelling behaviour when in contact with water, inducing additional loads on the tunnel lining. The severe strain distribution of the loop 2-5 is obviously considered to be the most critical section of the TT10 tunnel and its correlation with the soil stratigraphy will be discussed later in this chapter.

Generally, the FO monitoring results gathered for CERN 2 installation suggest a vertical tunnel elongation mechanism of deformation, as well as CERN 1 data results.

(a)

(b)

(c)


(d)

(e)

(f)
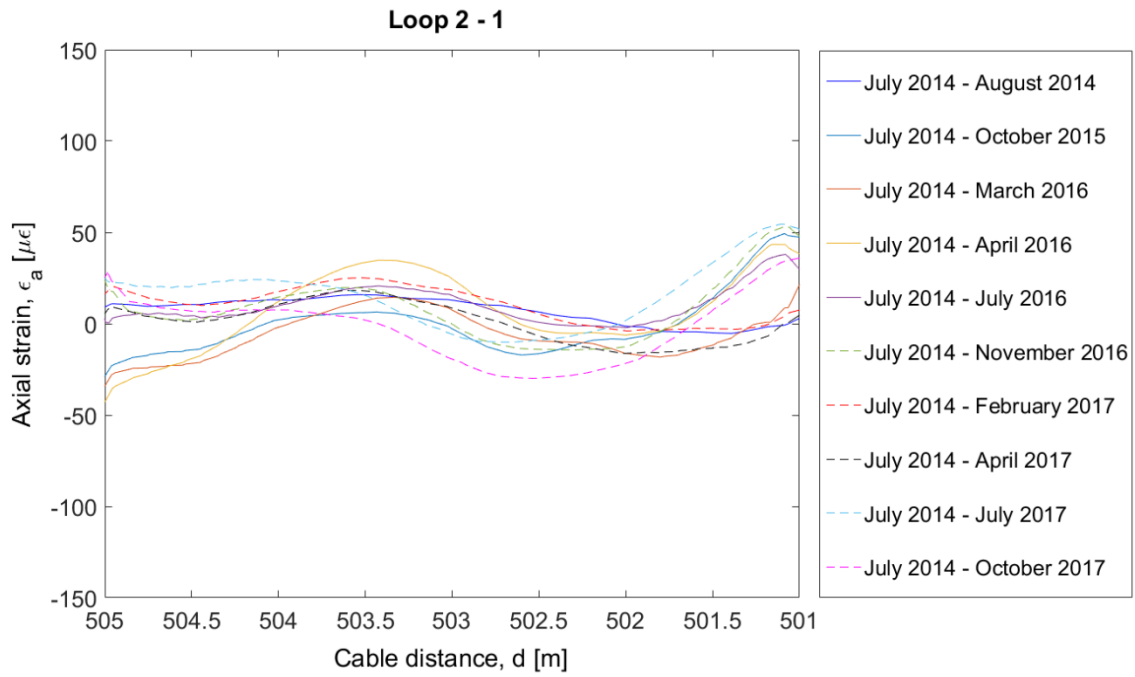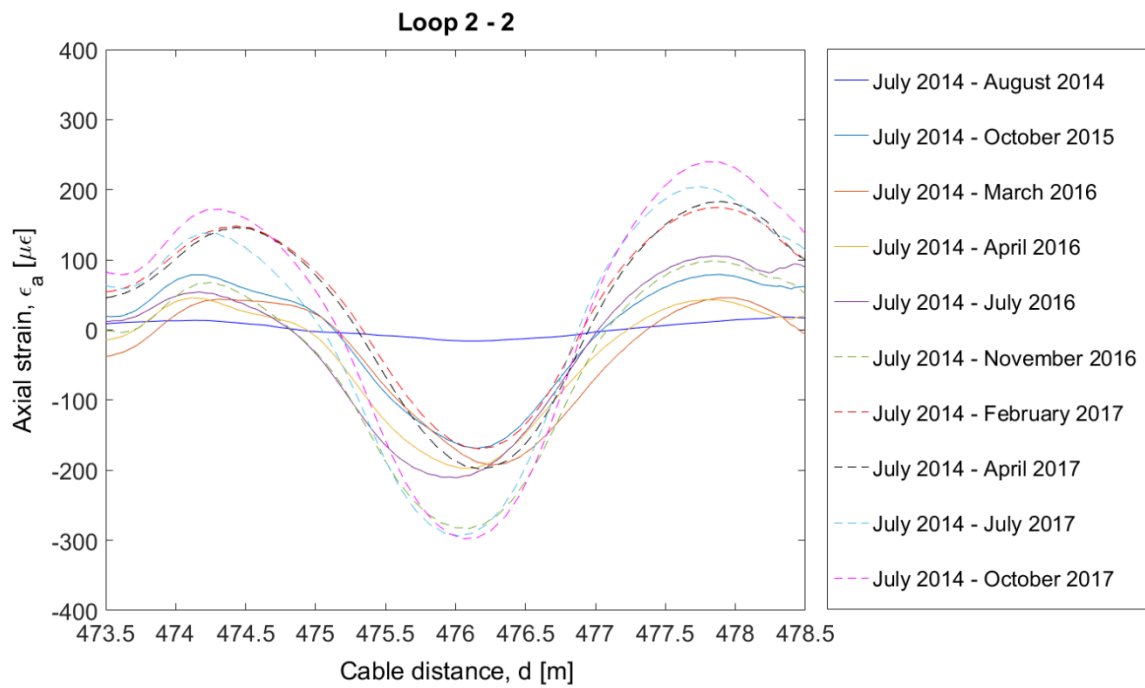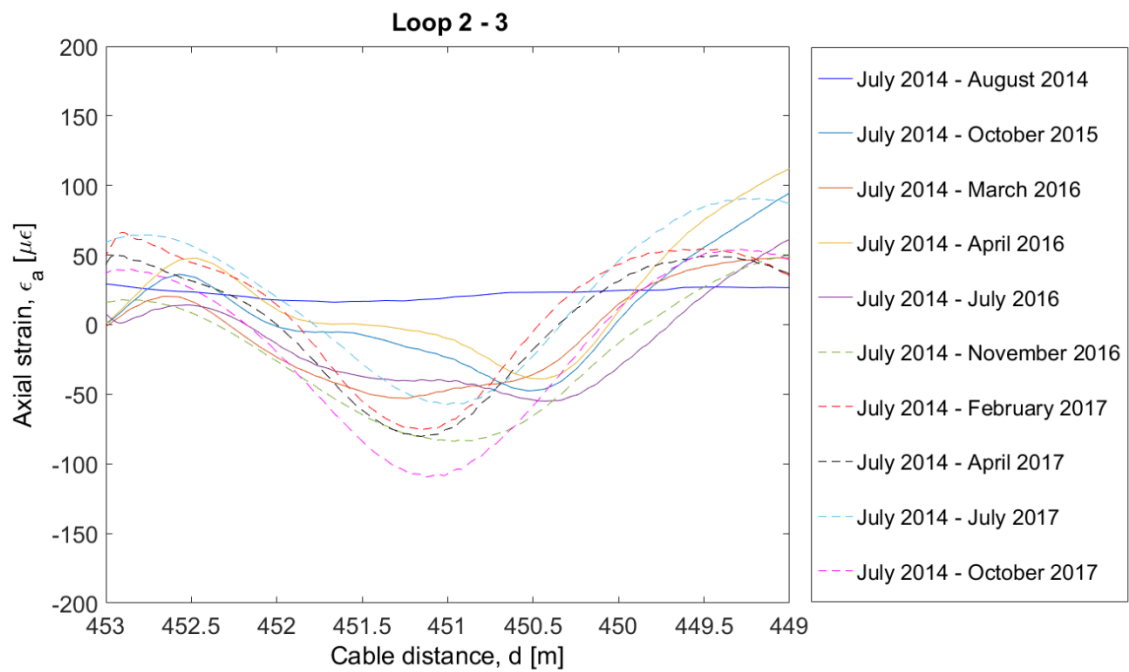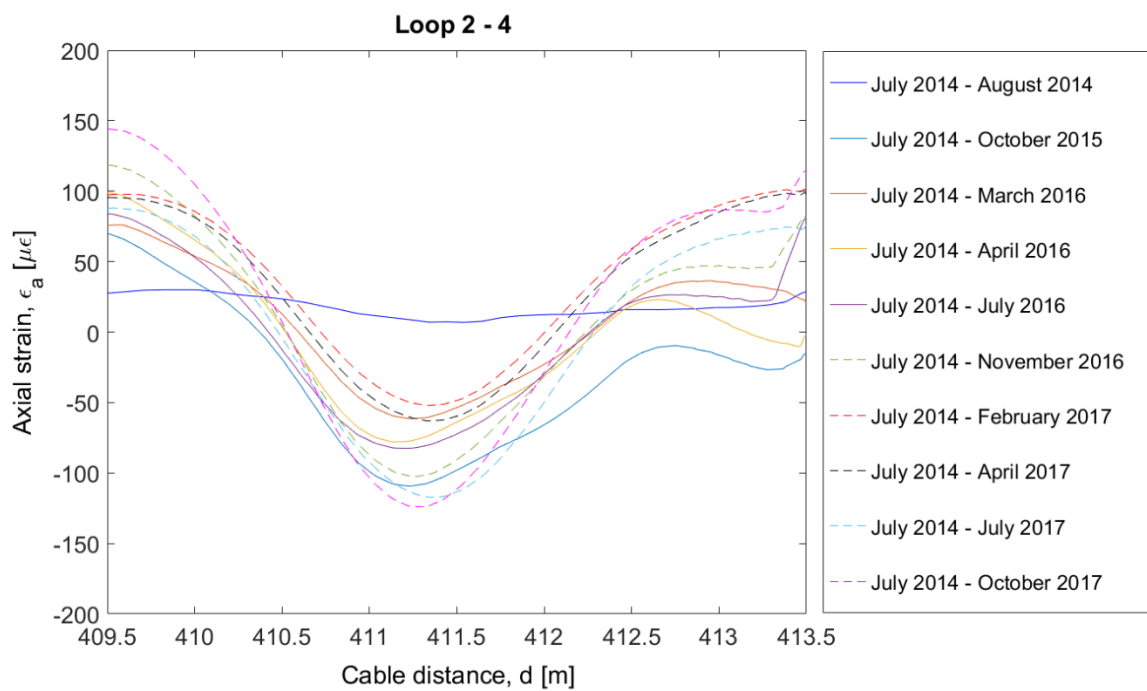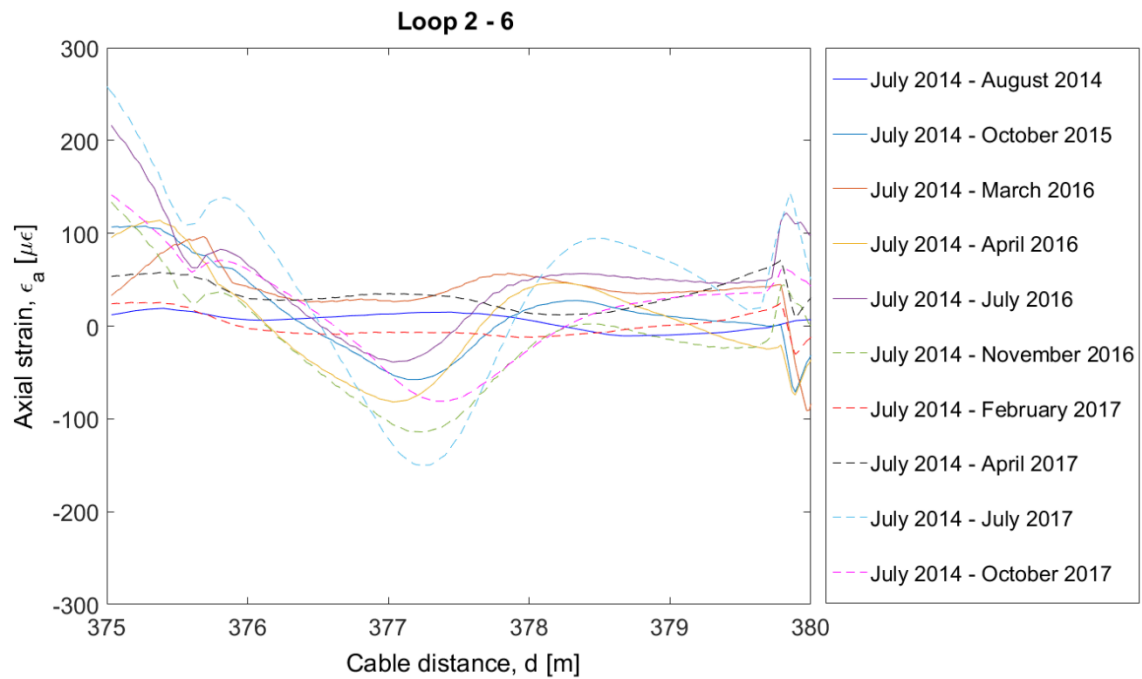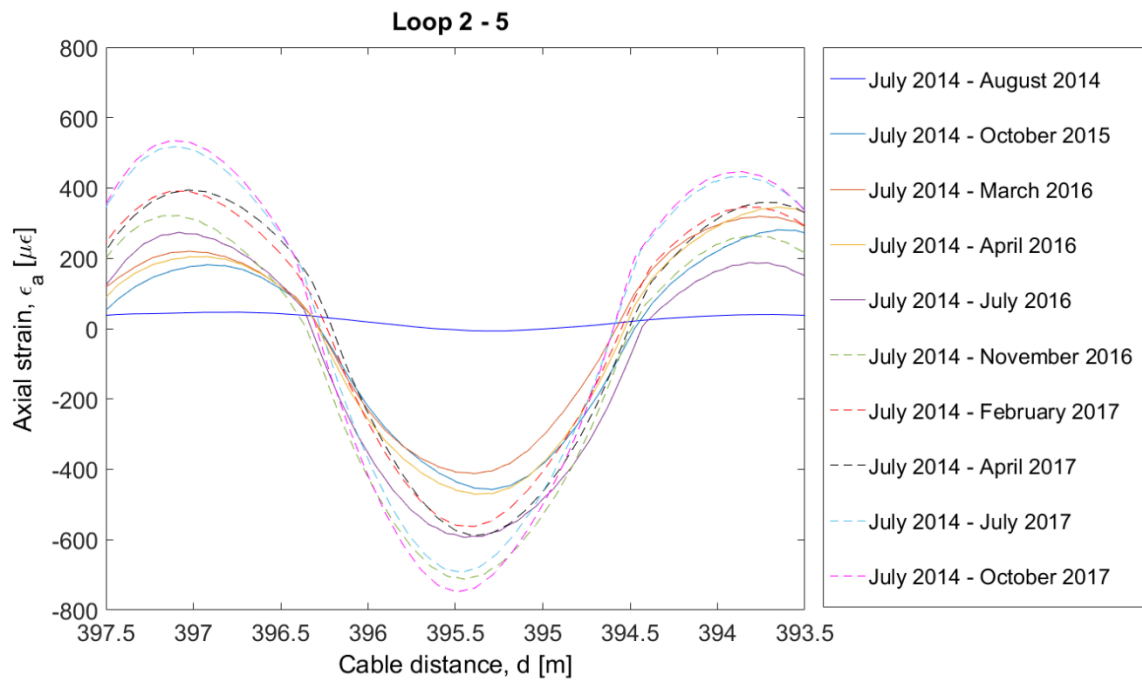
Figure 4.16. Fibre optic axial strain for cross-sectional loops of CERN 2: (a) Loop 2-1, (b) Loop 2-2, (c) Loop 2-3, (d) Loop 2-4, (e) Loop 2-5 and (f) Loop 2-6.

4.4.3.3 CERN 3

Long-term FO attachments which make use of pulley wheels require the use of the glue, showing a creep behaviour with time. An alternative solution is to adopt metal clamps, which have been designed and manufactured by CSIC (Kechavarzi et al. 2016). This technique consists of two metal plates joined by a clamping bolt. Both plates are designed to accommodate precisely the temperature as well as the strain cable (Figure 4.17).

A trial FO installation was deployed in the TT10 tunnel by installing two circumferential loops besides the existing one (CERN1), by adopting the standard hook-pulley-glue attachment system for one loop and metallic clamps for the second loop. The two new FO loops were set up next to each other near the shaft access door and before the first FO loop of CERN 1 installation (Figure 4.18). This will allow to compare the two different systems and to improve future fibre optic installations.

Figure 4.17. Metallic clamps for attaching the FO cable to the tunnel lining.

CERN 1: 8 FO tunnel loops

FO loop 2: hook & pulley & glue

FO loop 1: metallic clamps
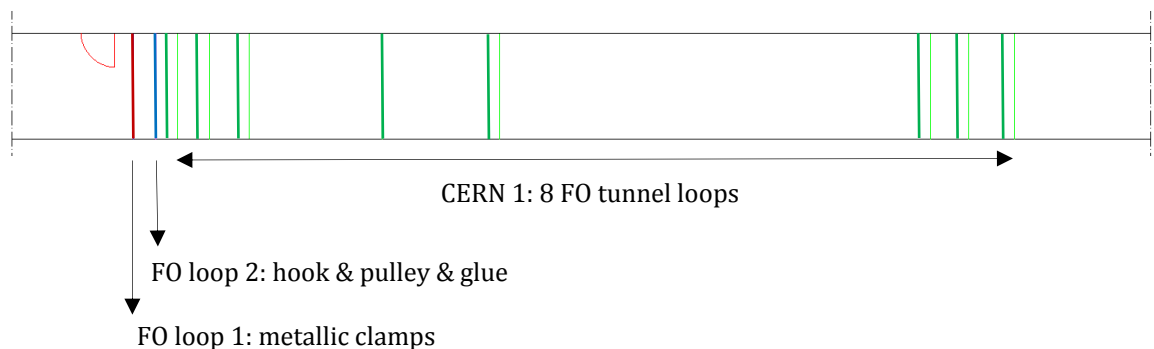
Figure 4.18. TT10 tunnel plan view: FO tunnel loop attached by using metallic clamps beside the FO loop attached with the hook & pulley system.

The installation was executed and completed in February 2016. The baseline reading showed a successful signal transfer and six measurements were collected throughout the monitoring period (Table 4.3). The raw Brillouin Frequency along the cable distance for the baseline reading taken in February 2016 is shown in Figure 4.19a. In particular, the Brillouin frequency within the section of Loop 1 decreases and then rises again, which might be due to the pre-tensioning of the optical fibre, applied not uniformly between the metallic clamps (Figure 4.19a).

Figure 4.19b and Figure 4.19c show the axial strain for the two FO circumferential loops: loop 1 and loop 2. It was observed that the single mode fibre optic clamped gave considerably higher strains than fibres glued on pulley wheels. Clamped fibres recorded larger strain values at both lateral sides and the crown of the tunnel lining than those developed by the glued fibres. A smooth distribution of axial strain is experienced by the loop 2, whereas the loop 1 shows localised peak strain values at the location of the clamps, probably due to the design of metallic clamp which induces localized strain. For this reason, the method of gluing the optical fibres on circular wheels provides more reliable axial strain values and it remains, at this moment, the most adopted methodology for the deployment of fibre optic sensors.

(a)

(b)

(c)
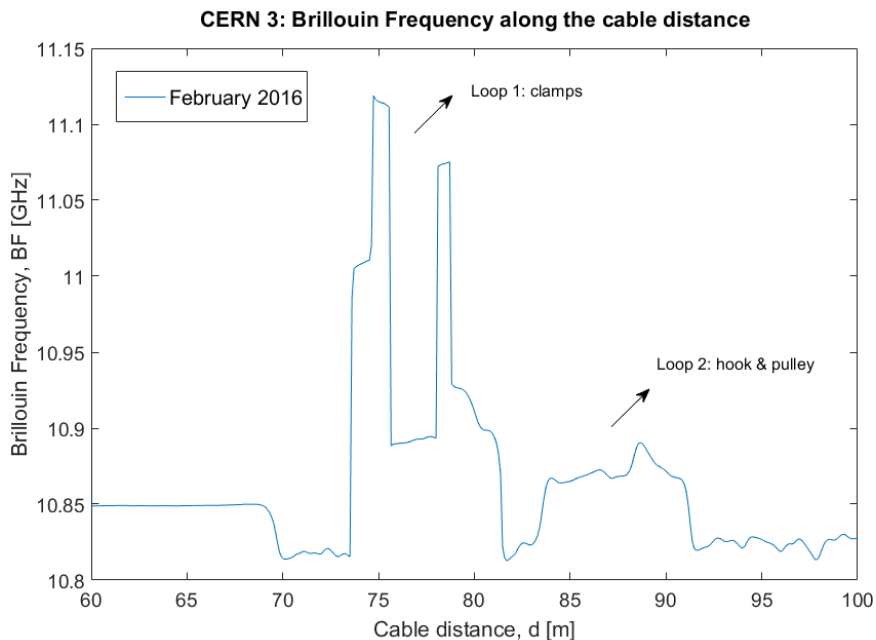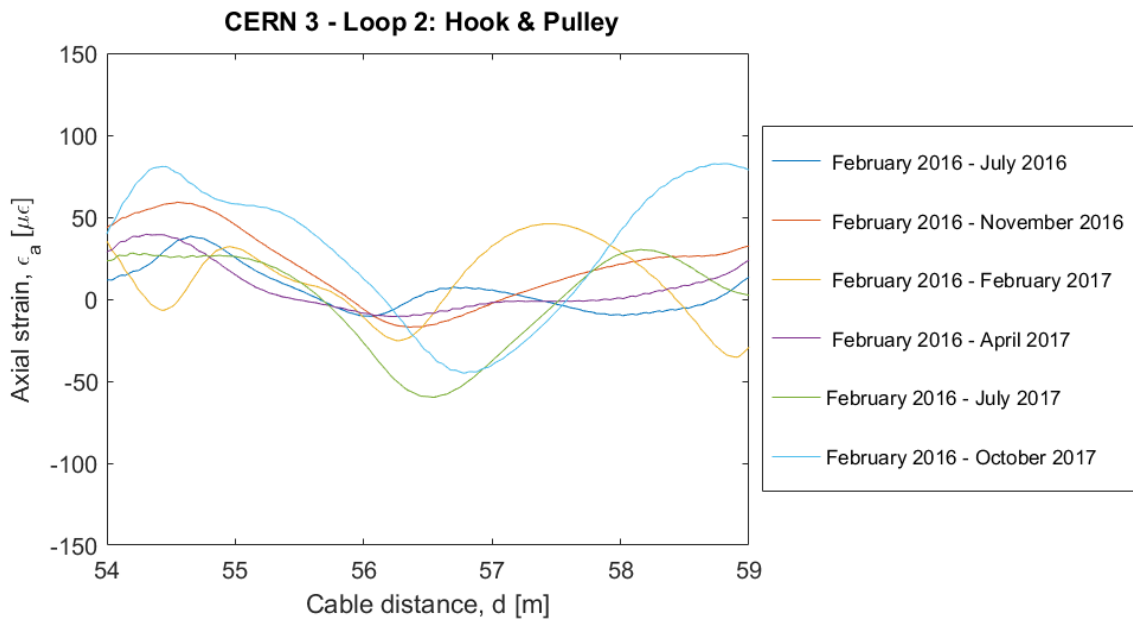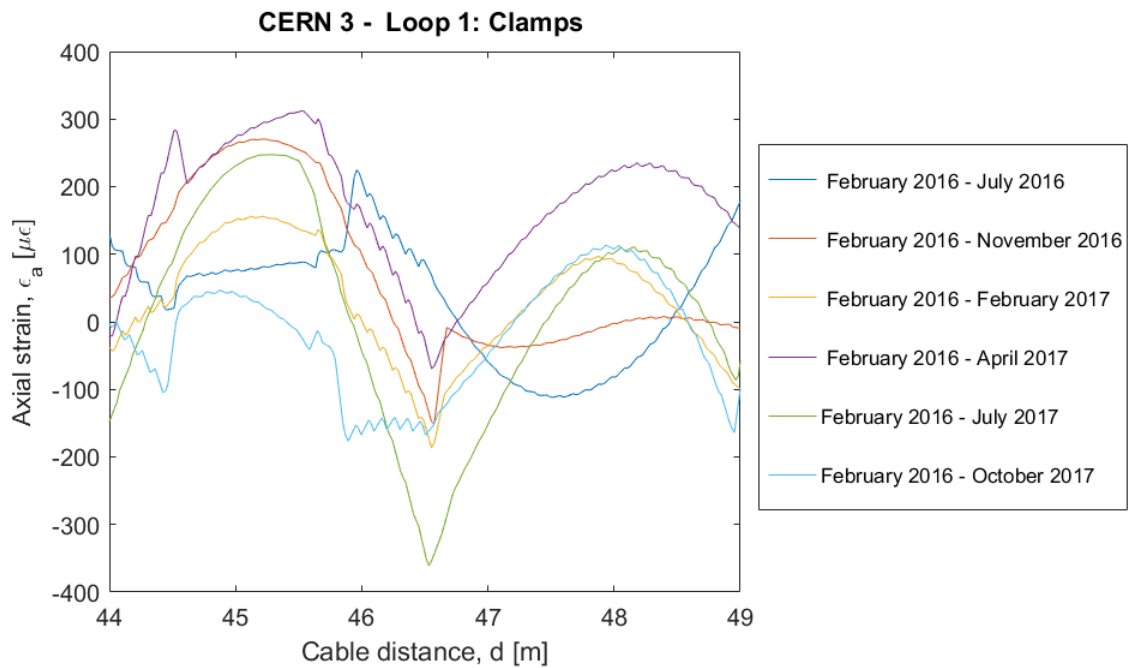
Figure 4.19. CERN 3 installation: (a) Brillouin Frequency along cable distance, (b) Fibre optic axial strain for cross-sectional Loop 1 and (c) Loop 2.

4.4.3.4 Tunnel lining mechanism of deformation: CERN 1 and CERN 2

The strain distribution profiles evaluated for the instrumented tunnel cross-sections of both CERN 1 and CERN 2 installations show the development of a similar axial strain pattern of tensile (positive) and compressive (negative) strains at the tunnel lateral sides and the tunnel crown respectively.

Figure 4.20 (a) and (b) provide information on the development of the peak tensile and compressive strains at the tunnel lining for the selected FO tunnel loops of CERN 1 installation, throughout the monitoring period. Both tensile and compressive strains seem to slightly increase with time, with notable peaks and troughs values at certain periods of the year (Figure 4.20a, b). For all the selected loops, the tensile strain values gradually increased between August 2014 and May 2015, after which the loops 1-1, 1-2 and 1-5 reached a lower strain value in June 2015, whereas the loop 1-3 and the loop 1-7 slightly increased until October 2015. Interestingly, all the loops experienced a tensile peak in the months of October 2015 and November 2016 and a trough in March 2016 and February 2017.

The tensile strains recorded for the loop 1-1 and the loop 1-6 sharply increased in April 2016, reaching around 200 µε and then suddenly dropped to 30 µε and 80 µε in July 2016 for the loop 1-1 and the loop 1-6 respectively.

At the tunnel crown (Figure 4.20b), an initial rise in the strain pattern is observed between August 2014 and May 2015 for all the instrumented loops, followed by a remarkable decrease in the strain in June 2015. On the other hand, a sudden decrease in the compressive strain is recorded in April 2016 for the loop 1-2, loop 1-3, loop 1-5 and in April 2017 for the loop 1-1, loop 1-3, loop 1-5 and loop 1-7 (Figure 4.20b). While the negative strains at the tunnel crown for the loop 1-1 and the loop 1-7 levelled off after July 2017, the strains experienced by the loop 1-3 and loop 1-5 decreased. The strains of the loop 1-2, instead, slightly increased. Also, the largest compressive strain is developed by the loop 1-6 in October 2017.

Overall, the peak tensile and compressive strains rose gradually over the years, reaching a maximum strain value in October 2017, without exceeding values of 300 µε at the tunnel lateral sides and 200 µε at the tunnel crown.

Tension development

(a)

Compression development
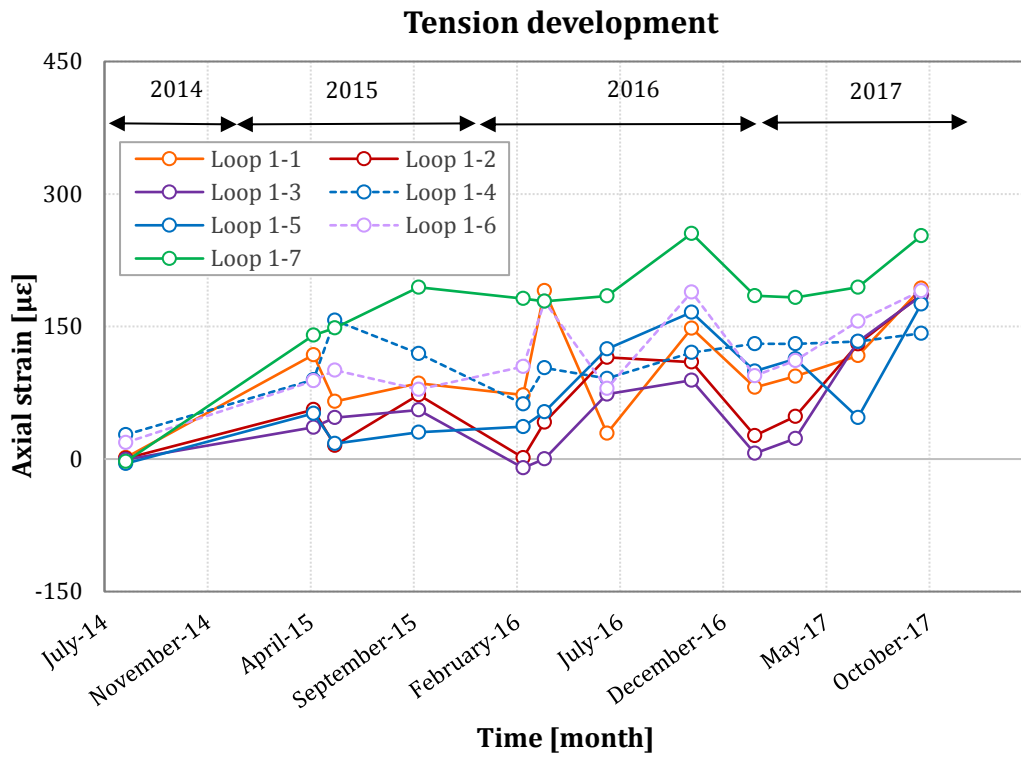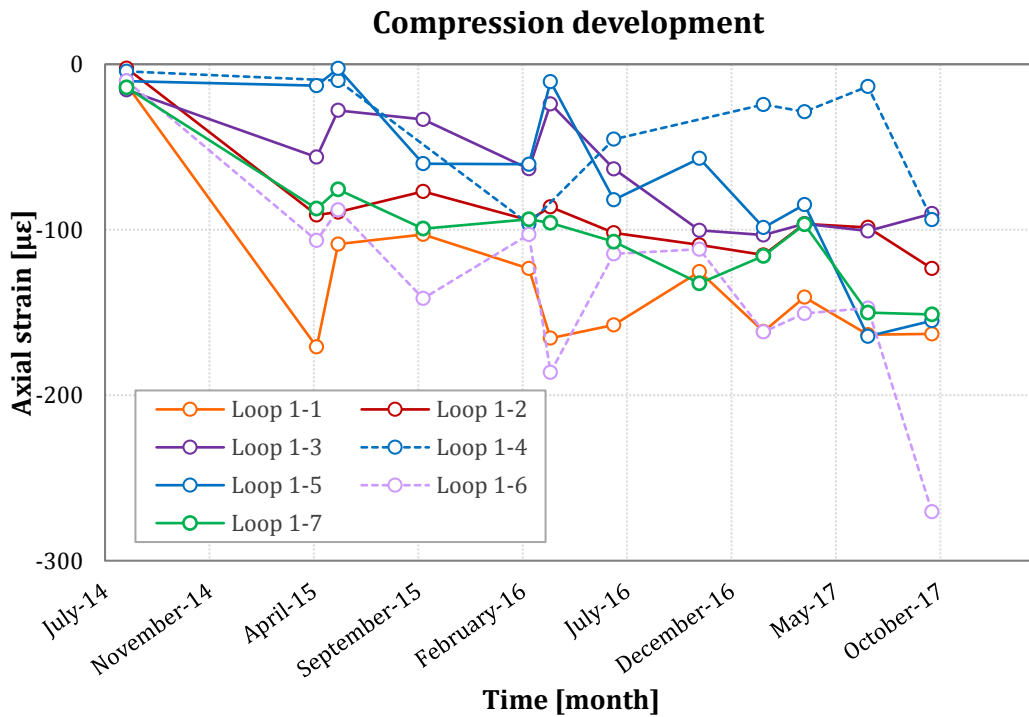
(b)

Figure 4.20. Peak axial strain development with time for CERN 1 installation: (a) Tension and (b) Compression development.

Figure 4.21 (a) and (b) compare the tensile and compressive axial strain detected with time for the monitored loops of CERN 2 installation. It can be seen that since July 2014 the axial strain increased gradually with time for the loop 2-1, loop 2-2, loop 2-3, loop 2-4 and loop 2-6, while for the loop 2-5 tensile and compressive strains steeply reached significant magnitudes.

Small axial strains were recorded for the loop 2-1, loop 2-3 and loop 2-4 and they do not exceed values of 200 με for both tension and compression sides. Conversely, the loop 2-2 and the loop 2-5 develop higher strain, with peak values registered in October 2017. Whilst the loop 2-2 shows peak strain values within the range of 300 με at both the tunnel crown and the lateral sides, the loop 2-5 experiences by far the largest strain magnitudes. In fact, peak tensile and compressive strain values of 534 με and 580 με are observed respectively for the loop 2-5 (Figure 4.21a, b). Moreover, all the loops experience a peak compressive strain at the tunnel crown in November 2016 and a trough in February 2017, after which the strain values remained constant until April 2017, for both the tension and compression sides.
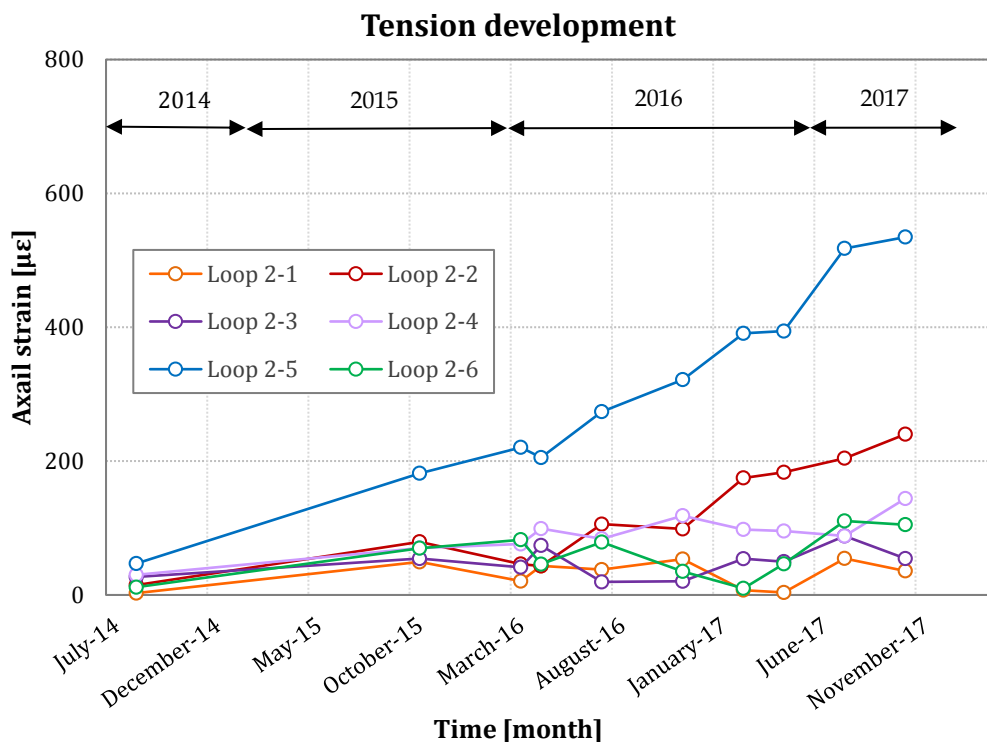
(a)
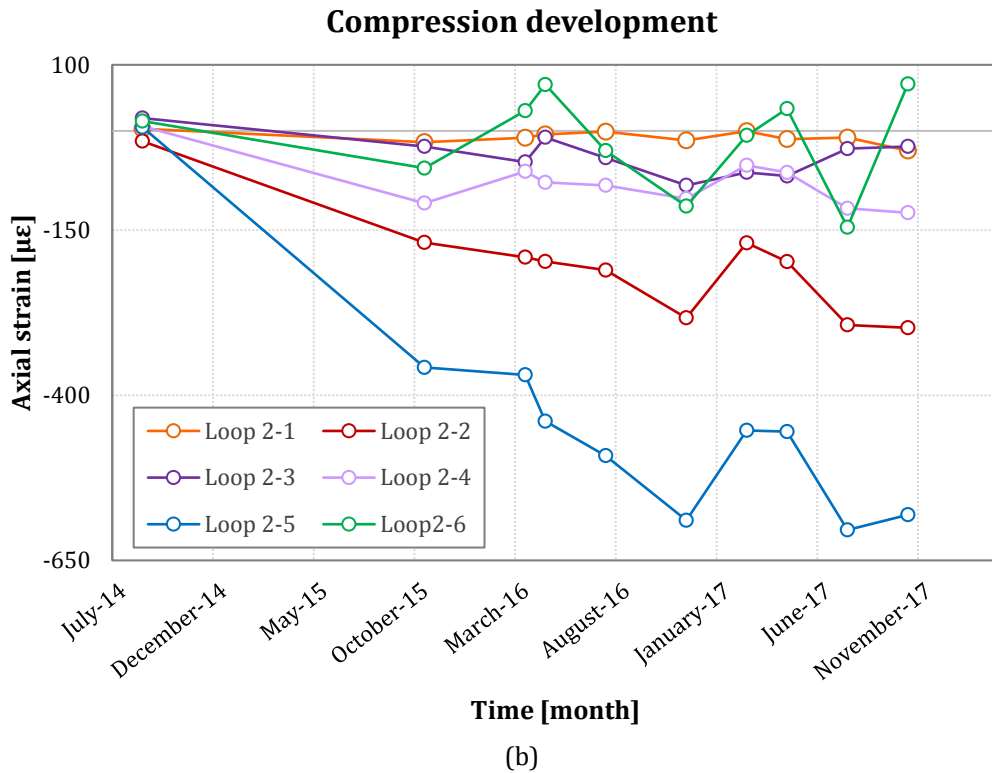
Figure 4.21. Peak axial strain development with time for CERN 2 installation: (a) Tension and (b) Compression development.

It can be highlighted that, similarly to the CERN 1 installation, the strain distribution pattern seems to experience some peaks and troughs at certain months of the year (i.e. peak strain values in October-November and a trough in February-March), suggesting that there might be a seasonal effect on the recorded FO data. To this end, records on the amount of rainfall measured by the pluviometers located in the French region have been examined for the period that goes from August 2014 to October 2017. In particular, the TT10 tunnel is located on the French-Swiss border, crossing both St Genis Pouilly and Prevéssin cities in the downstream and upstream tunnel area respectively, in the Rhône-Alpes region of eastern France, as shown in Figure 4.22. Therefore, the average rainfall amount related to the abovementioned locations was inspected (*World Weatheronline*). However, the records showed similar precipitation data for both cities, hence, only the data related to the city of Prevéssin will be presented.

Figure 4.23 provides information about the average amount of rainfall measured in Prevéssin between 2015 and 2017. Peak rainfall amounts are observed in August 2015, June 2016, and June 2017, as shown in Figure 4.23a, Figure 4,23b and Figure 4.23c respectively, by recording over +75 mm of rainfall. The Figure also shows a

notable and consistent trough in the amount of rainfall over the period in the following months: April 2015, October 2015, April 2016, April 2017 and October 2017 (Figure 4.23). Additionally, a decrease in the amount of precipitation is also observed in February 2015 (Figure 4.23a) and December 2016 (Figure 4,23b).

Overall, the analysis of the amount of rainfall measured in the area where the TT10 tunnel is located allows a better understanding of the seasonal effect on the detected cross-sectional FO strains. Some correlations between the peak and trough FO strain values and the rainfall amount were found. In particular, for CERN 2 installation, a trough in the strain can be observed in April 2016 and April 2017, as shown in Figure 4.21, which corresponds to a decrease in the amount of rainfall measured (Figure 4.23b and Figure 4.23c). Also, a peak strain value was detected in November 2016 for CERN 1 and CERN 2 installations, as shown in Figure 4.20 and Figure 4.21, which corresponds to a peak in the amount of rainfall measured (Figure 4.23b).

Overall, the peak strain values observed from the FO strain profiles were detected during the most rainfall months (i.e. June 2016, November 2016 and June 2017), whereas a trough in the strain development can be observed when smaller amounts of precipitation are measured (i.e. April 2016 and April 2017). This would suggest that during heavy rainfall periods, the more permeable moraine deposits would saturate and, in the hypothesis of a reduced capacity of the tunnel drainage system, the groundwater pressure would accumulate behind the lining acting as a boundary load, resulting in the development of tunnel lining movements with time.
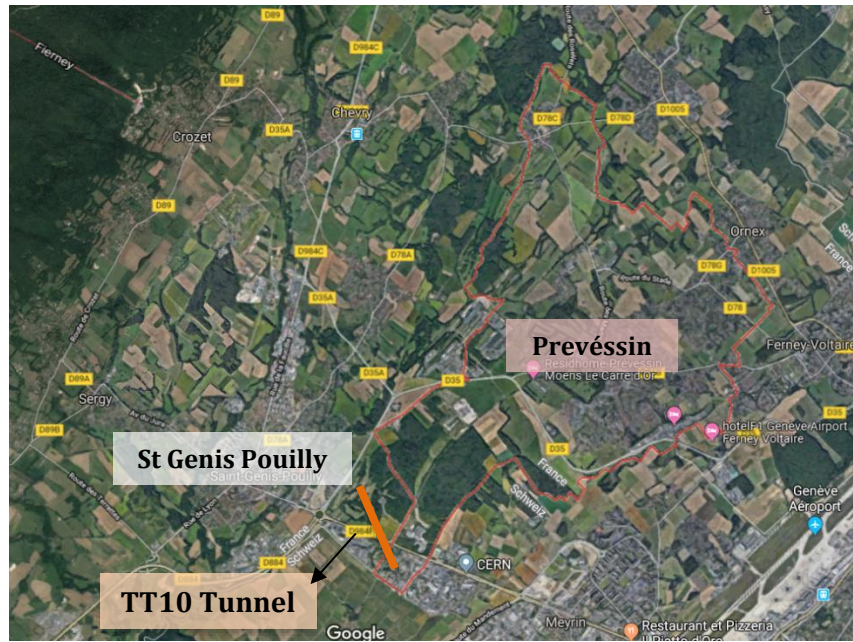
Figure 4.22. Location of the TT10 tunnel in the French-Swiss border (Google Map).
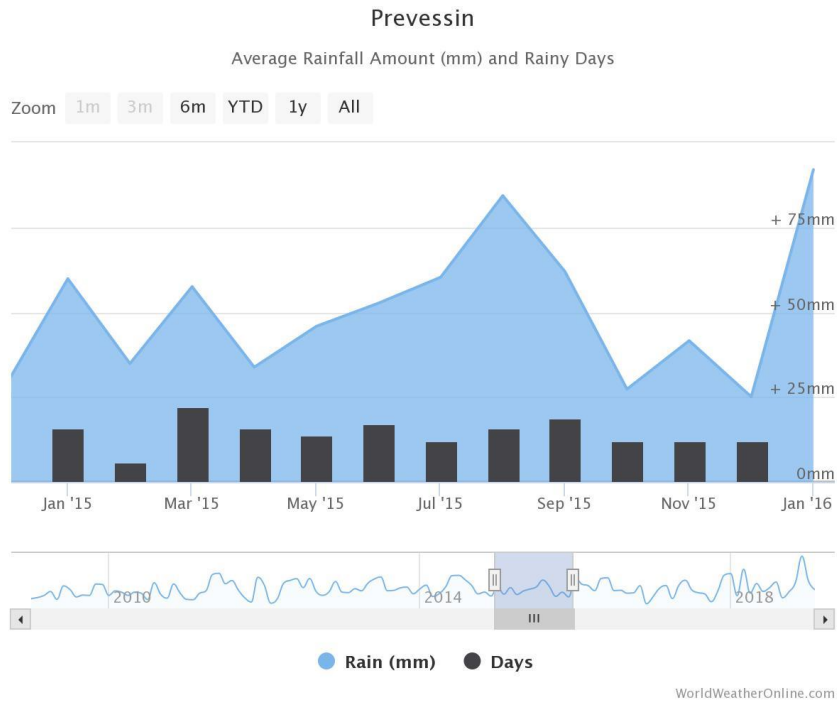
(a)
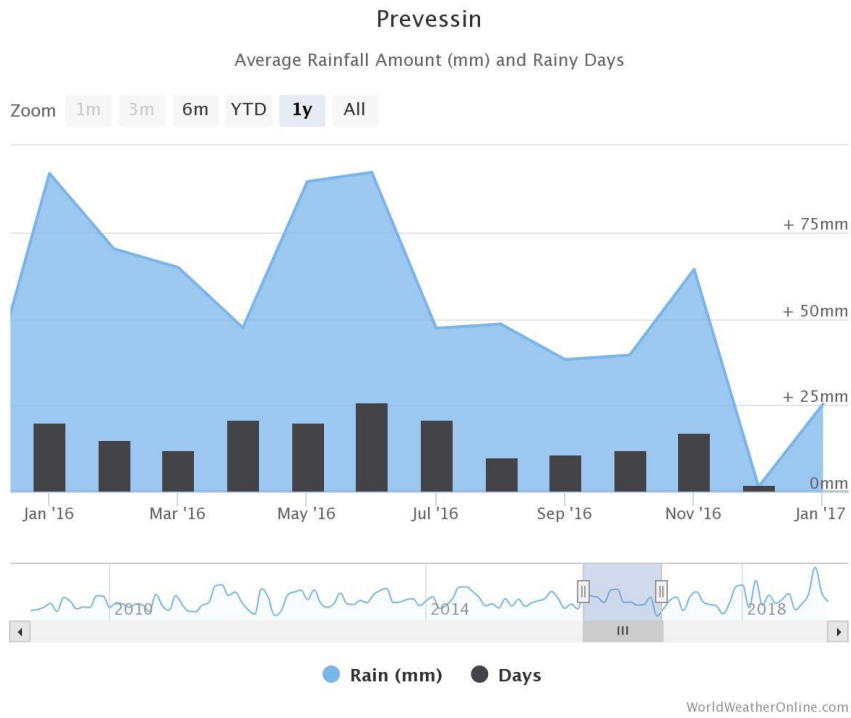
(b)
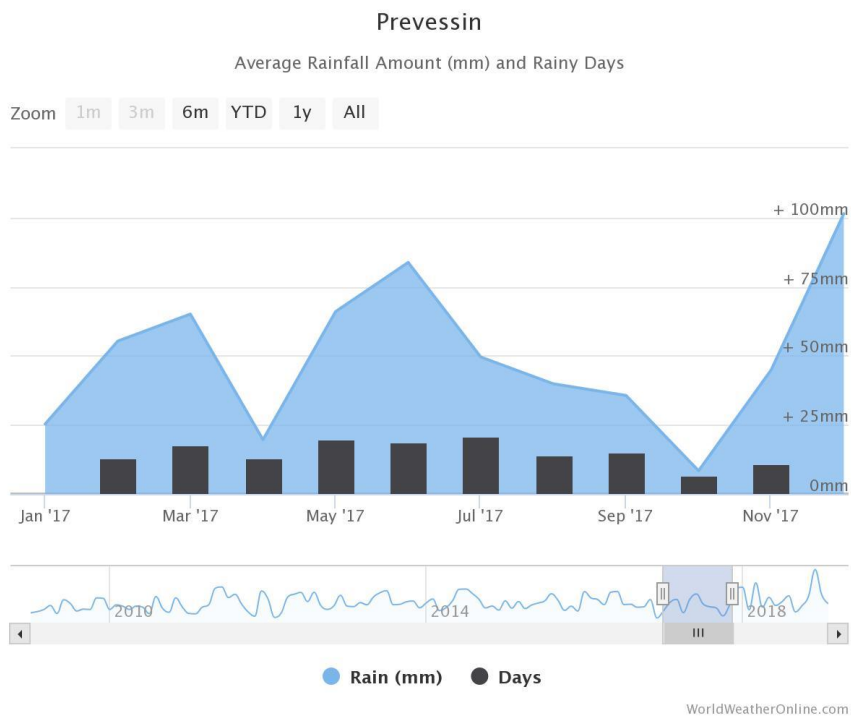
(c)

Figure 4.23. Average rainfall amount for Prevéssin city for the years (a) 2015, (b) 2016 and (c) 2017 (WorldweatherOnline.com).

In addition to the innovative fibre optic strain sensors, conventional geodetic measurements of optical targets using total stations give further information on the long-term tunnel structure response in selected cross-sections.

As discussed in Chapter 3, six targets were mounted on the tunnel lining in each monitoring section, with a total of 6 cross-sections along the tunnel, closely installed beside the FO tunnel loops (Figure 4.5). The five geodetic profiles P1, P2, P3, P4 and P5 were installed beside the loop 2-1, loop 2-3, loop 2-4, loop 2-5 and the loop 2-6 respectively, whereas the profile P0 was placed close to loop 1-7.

Figure 4. 22 displays the change in the horizontal and vertical tunnel distances taken for the cross-section P4, close to the loop 2-5. The horizontal distance changes between the targets for the sections at tunnel shoulder (3-6), at tunnel axis (2-7) and at tunnel invert (8-3) are constantly increasing since 2013, reaching maximum values of -1 mm, -0.88 mm and -0.5 mm respectively in May 2017, suggesting that the tunnel circumference is converging inwards. The vertical distance change, instead, seems to increase for the section on the left side of the tunnel (8-6), whereas the right one (1-3) doesn't seem to change with time (Figure 4.24).

The vertical change in distances increases with a smaller rate compared to the horizontal one throughout the monitoring period, as shown in Figure 4.24.
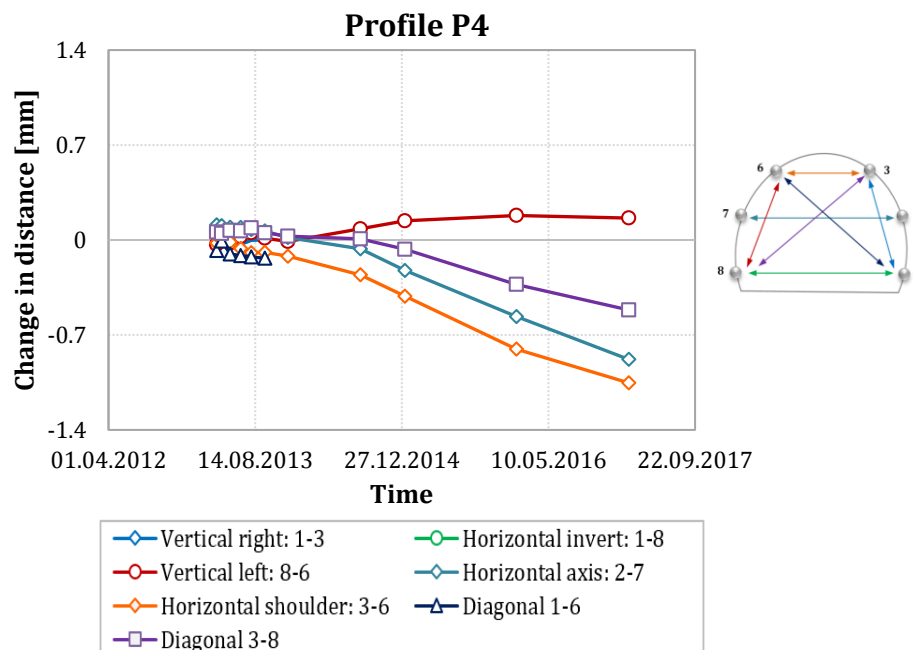
Figure 4.24. Change in the horizontal and vertical tunnel distances for the geodetic profile P4.

The geology surrounding the tunnel seems to have an impact on the above strain development. The strain profile observed for the loop 2-5 was expected, as the most

significant area of tunnel lining damage occurred in the *critical area*, where the geological conditions were considerably worse than those observed in the *blue* area. Variable sequences of weak and strong marl are observed in the dominant geological conditions encountered, as shown in Figure 4.25a. The geological cross-section consists of a layer of a *very weak* and sensitive type of marl called *"lie-de-vin grumeleuse"* or *lumpy marl* which can alter quickly when exposed to air and humidity (Figure 4.25b). Therefore, the combination of poor ground conditions with the external water pressure acting behind the tunnel lining is expected to lead to a reduced lining capacity and, hence, facilitate the development of strain with time.

(a) (b)
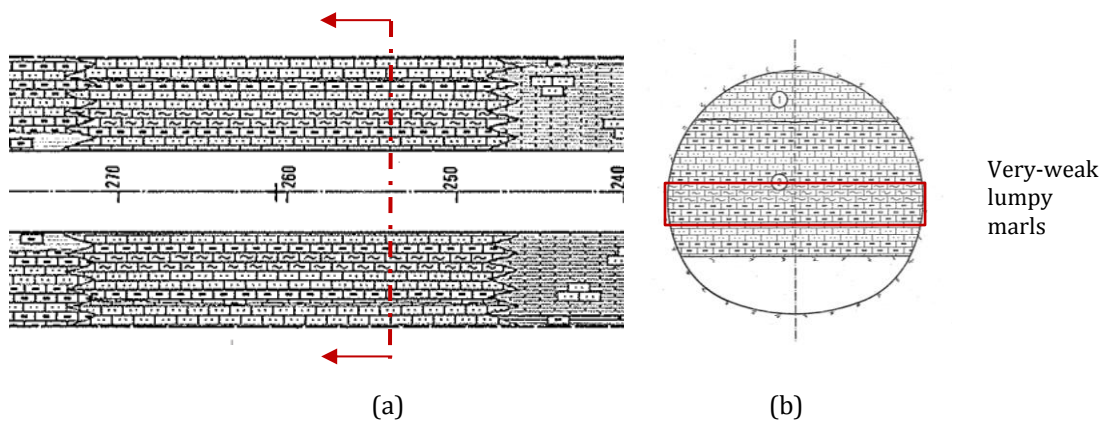
Figure 4.25. (a) Geological plan view of a section of TT10 tunnel at the location of loop 2-5, (b) Geological face-log cross-section.

Overall, the fibre optic profiles gathered for both CERN 1 (Figure 4.13) and CERN 2 (Figure 4.16) show a consistent and illustrative sinusoidal strain response along cable distance, with positive (tensile) strains at the tunnel axis level and negative (compressive) strains at the tunnel crown. Yet, the conventional lining displacements recorded by total station system as well as the geology correlation, showed agreement with the FO data results, meaning that the final tunnel lining deformation mode may be confidently associated with a vertical tunnel ovalisation at certain tunnel locations, albeit for the circumferential tunnel loops of CERN 2 installation.

4.5 Summary of key findings

The deployment of distributed fibre optic strain measurement technology was presented for the monitoring of a section of CERN TT10 tunnel. The use of a novel

monitoring system has enabled the measurement of continuous strain profiles to assess the actual tunnel mode of deformation. Three FO installations were carried out: 1) Eight tunnel cross-sections in *CERN 1* installation; 2) Six tunnel loops in *CERN 2* installation and 3) further two tunnel loops were also installed to compare different methodologies for attaching the optical fibre to the structure (*CERN 3*). The first two installations took place in March 2014 and May 2014 respectively, with a baseline reading collected in July 2014, whereas *CERN 3* installation was carried out in February 2016.

The strain distributions recorded for the examined sections for CERN 1 and CERN 2 show slow development of strain continuously with time over the monitored period of three years. For all the instrumented cross-sections, a sinusoidal-shaped strain profile with tension (positive strains) at tunnel spring line and compression (negative strains) developed along the tunnel lining, suggesting a vertical tunnel ovalisation. Two different approaches of attaching the optical fibre to the structure were implemented. The system which makes use of metallic plates showed peak axial strains at the location of the attachment, therefore, making the hook & pulley system more reliable for evaluating the tunnel strain profile.

Distinctive peaks and troughs strain values were noticed in the tension and compression development in certain periods of the year, indicating that there might be a seasonal effect in the FO data. To this end, the analysis on the amount of rainfall measured in the region nearby to the TT10 tunnel has enabled the evaluation of the potential seasonal fluctuation on the monitored axial strains. This study identified some correlations between the peak strain values with the heaviest rainfall months of the year (i.e. November 2016, July 2017), whilst a trough strain value was observed when a smaller amount of precipitation occurred. The observed behaviour suggests that the tunnel lining may experience larger strains with time in the occurrence of heavy rainfall periods, due to the groundwater flowing towards the tunnel. In the hypothesis of a reduced capacity of the tunnel drainage system many years after construction, the water pressure would act as a hydrostatic load behind the tunnel lining, leading to tunnel lining distress with time. Severe strain values were recorded for the loop 2-5, which seems to experience an increase in axial strains over the years at the tunnel lining. The soil profile surrounding the tunnel at the location of the loop 2-5 is weak layers of marl, which in contact with water tend to swell. The poor ground conditions in addition to the change in the groundwater

conditions may have triggered the development of further cracks at both the tunnel floor and the tunnel crown in that area and, therefore, caused the development of axial strain with time.

Additionally, the FO strain results and the geodetic convergence measurements seem to be in agreement, as both monitoring technologies suggest that the tunnel may be deforming with a vertical elongation deformation mode. On the basis of the performed measurements, it is concluded that a slow development of strains has been recorded for several instrumented tunnel cross-sections.

References

Acikgoz, M. S., Pelecanos, L., Giardina, G., Aitken, J. and Soga, K., (2017). Distributed sensing of a masonry vault due to nearby piling. Structural Control and Health Monitoring, 24 (3), e1872.

Alasia D., Fernandez-Fernandez A., Abrardi L., Brichard B., and Thèvenaz L. (2006). The effects of gamma-radiation on the properties of Brillouin scattering in standard Ge-doped optical fibres. Measurement Science and Technology 17 (5): 1091–94.

Bao, Xiaoyi, and Liang Chen. (2011). Recent Progress in Brillouin Scattering Based Fiber Sensors. Sensors 11 (4): 4152–87.

Cheung, L.L.K., Soga, K., Bennett, P.J., Kobayashi, Y., Amatya, B., Wright, P. (2010). Optical fibre strain measurement for tunnel lining monitoring. Geotechnical Engineering 163. ICE Publishing.

Di Murro, V., Li, Z., Soga, K., Scibile, L. (2018). Long-Term Behaviour of CERN Tunnel in the Molasse Region. Proceedings of GeoShanghai 2018 International Conference: Fundamentals of Soil Behaviours, pp 671-678. GSIC 2018. Springer, Singapore.

Di Murro, V., Pelecanos, L., Soga, K., Kechavarzi, C., Morton, R., Scibile, L. (2016). Distributed fibre optic long-term monitoring of concrete-lined tunnel section TT10 at CERN. International Conference on Smart Infrastructure and Construction, pp. 27–32. ICE Publishing, Cambridge, U.K.

Di Murro, V., Pelecanos, L., Soga, K., Kechavarzi, C., Morton, R., Scibile, L. (2019). Long-term deformation monitoring of CERN concrete-lined tunnels using distributed fibre-optic sensing. Geotechnical Engineering Journal of the SEAGS & AGSSEA, 50 (1) (Accepted).

Girard, S., Kuhnhenn, J., Gusarov, A., Brichard, B., Van Uffelen, M., Ouerdane, Y., Boukenter, A., Marcandella, C. (2013). "Radiation Effects on Silica-Based Optical Fibers: Recent Advances and Future Challenges". IEEE Trans. Nucl. Sci. 2013, 60, 2015-2036.

Gue, C.Y., Wilcock, M., Alhaddad, M.M., Elshafie, M.Z.E.B., Soga, K. and Mair, R.J., (2015). The monitoring of an existing cast iron tunnel with distributed fibre optic sensing (DFOS). Journal of Civil Structural Health Monitoring, 5(5), pp.573-586.

Gue, C.Y., Wilcock, M.J., Alhaddad, M.M., Elshafie, M.Z.E.B., Soga, K. and Mair, R.J., (2017). Tunnelling close beneath an existing tunnel in clay–perpendicular undercrossing. *Géotechnique*, **67**(9), pp.795-807.

Kechavarzi, C., Soga, K., de Battista, N., Pelecanos, L., Elshafie, M. Z.E.B., and Mair, R.J. (2016). Distributed fibre optic strain sensing for monitoring civil infrastructure – A Practical Guide. ICE Publishing, London, UK. ISBN 9780727760555.

Klar, A., et al. (2006). Distributed Strain Measurement for Pile Foundations. Proc. ICE Geotech. Eng., 159 (3), 135-144.

Mohamad, H., Bennett, P.J., Soga, K., Mair, R.J., and Bowers, K. (2010). Behaviour of an old masonry tunnel due to tunnelling-induced ground settlement. *Géotechnique*, 60(12), 927-938.

Mohamad, H. (2008). Distributed Optical Fibre Strain Sensing of Geotechnical Structures. PhD thesis, Department of Engineering, Cambridge University, UK.

Mohamad, H., Soga, K., Bennett, P.J., Mair, R.J. and Lim, C.S. (2012). Monitoring Twin Tunnel Interactions Using Distributed Optical Fiber Strain Measurements. Journal of Geotechnical and Geoenvironmental Engineering, American Society of Civil Engineers, Vol. 138, No.8, pp. 957-967.

Omnisens. 2008. "User Manual DITEST STA-R™."

Pelecanos, L., K. Soga, M. P. M. Chunge, Y. Ouyang, V. Kwan, C. Kechavarzi, and D. Nicholson. (2017). Distributed Fibre-Optic Monitoring of an Osterberg-Cell Pile Test in London. Géotechnique Letters 7 (2): 152–60.

Pelecanos, L., Soga, K., Elshafie, M.Z., de Battista, N., Kechavarzi, C., Gue, C.Y., Ouyang, Y. and Seo, H.J., (2018). Distributed Fiber Optic Sensing of Axially Loaded Bored Piles. Journal of Geotechnical and Geoenvironmental Engineering, 144(3), p.04017122.

Pheron, X., Girard, S., Boukenter, A., Brichard, B., Delepine- Lesoille, S. et al. (2012). High γ-ray dose radiation effects on the performance of brillouin scattering based optical fibre sensors. Opt. Express. 2012, 26978-2685.

Savitzky, A., and Golay, M.J.E. (1964). Smoothing and Differentiation of data by simplified least squares procedures. Anal. Chem., 36 (8): 1627–39.

Soga, K. (2014). Understanding the real performance of geotechnical structures using an innovative fibre optic distributed strain measurement technology. Rivista Italiana di Geotecnica, 48, 7-48.

Soga, K., et al. (2017). Distributed fibre optic strain sensing for monitoring underground structures—Tunnels case studies. Underground sensing, S. Pamukcu and L. Cheng, eds., 1st Ed., Elsevier, Amsterdam, Netherlands.

Soga, K., & Luo, L. (2018). Distributed fiber optics sensors for civil engineering infrastructure sensing. Journal of Structural Integrity and Maintenance, 3 (1): 1–21.

Wijnands, T., De Jonge, L.K., Kuhnhenn, J., Hoeffgen, S.K., and Weinand, U. (2008). Optical Absorption in Commercial Single Mode Optical Fibers in a High Energy Physics Radiation Field. IEEE Transactions on Nuclear Science 55 (4): 2216–22.

Chapter 5

5 Geotechnical characterization of the weak rock mass

5.1 Introduction

Over the past 70 years, CERN has progressively expanded its underground facilities in order to meet nuclear physicists' demands for increasing the energy levels of particle accelerators. In the early '80s, CERN launched the construction of the Large Electron Positron (LEP) ring, to accommodate the particle accelerators. Some years later, additional experimental points with associated structures were constructed, forming the actual LHC circular ring. The design of new structures required additional site investigations as well as laboratory testing to be carried out. More recently, for the *High Luminosity* project, further geotechnical explorations have been implemented, particularly at Point 1 (ATLAS experiment) where the largest cavern is housed and Point 5 (CMS experiment).

This chapter presents some laboratory data results for the *molasse* region collected during the past years, in order to determine the geotechnical parameters of the rock mass and to evaluate its mechanical behaviour.

5.2 Geology

CERN laboratory sits across the French-Swiss border, between the Alps and the Jura Mountains, in the Molassic Plateau (Figure 5.1). Most of the underground tunnels were built in the molasse region, called the *red molasse,* which comprises irregular sub horizontal bedded sequences of marls and sandstones (Parkin et al. 2002).
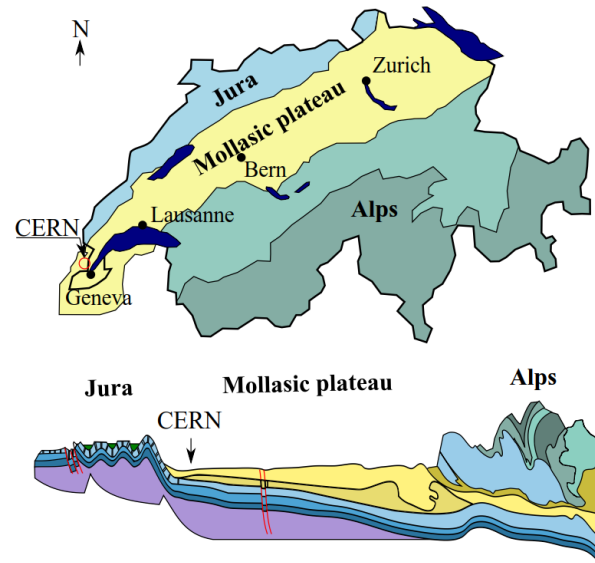
Figure 5.1. Swiss geology: CERN location (Fern et al. 2018).

5.2.1 Rock divisions

Within the molasse region, two types of rock can be distinguished: the marls and the sandstones, which can be further divided into three sub-units for each rock type. Figure 5.2 shows the mineralogy analysis of the marls, composed of varying amount of clay minerals, approximately 50 % of illite, 20-25 % of chlorite and calcite and quartz (Fern et al. 2018). Also, the marls alter quickly with air and humidity and tend to swell in presence of water.

The marls can be divided into the following sub-units, according to the international rock classification (ISRM, 1981).

1. _Very weak marl:_ is a type of marl made from the diagenesis of high-plasticity clay (Figure 5.2a and Figure 5.2b), characterized by discontinuous and multi-directional micro-fissures, with low stiffness and ductile behaviour. This rock unit falls in the R1 rock classification (ISRM, 1981).

2. _Medium-weak marl:_ is composed of 20-45% of clay minerals, calcite (20-30%) and around 30% of quartz (Figure 5.2a). From the Atterberg limits, Figure 5.2b shows that this rock unit has low-plasticity clays.

3. _Weak marl_: is mainly composed of around 50 % of clay, 15-30 % of quartz and 20-30 % of calcareous minerals (Figure 5.2a), with medium-high plasticity clay, mainly illite minerals, whereas smectite and chlorite are present in a lower

percentage. As the very-weak unit, the weak marl is also susceptible to swelling and slaking.

The sandstones unit is presented as a homogenous rock mass and consists of well-cemented silts and sands, with a limited number of widely-spaced joints. The sandstones can be divided into three sub-units:

4. _Weak sandstone_: is mainly made of poorly-cemented granular materials with some clay minerals.

5. _Medium-strong sandstone_: presents well-cemented coarse-grained materials with good mechanical properties and rare discontinuities.

6. _Strong sandstone_: presents very well-cemented grains with few discontinuities. Its mineralogy composition is similar to the medium-strong sandstone, with RQD values close to 100.
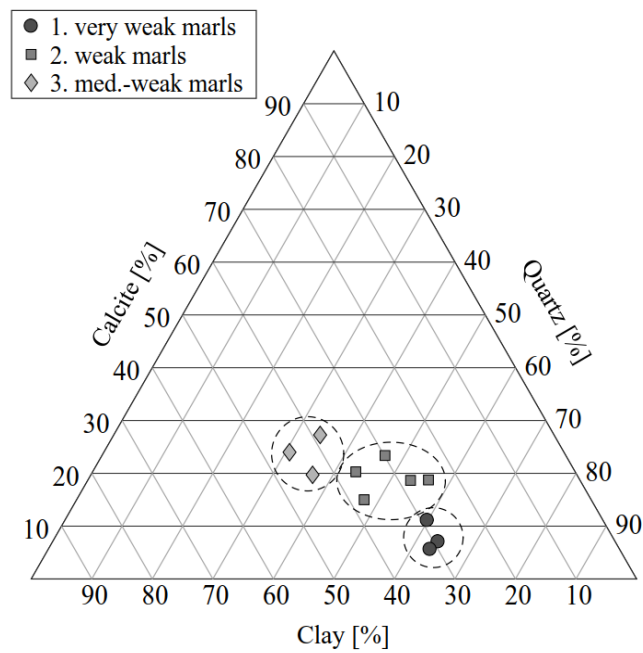
(a)
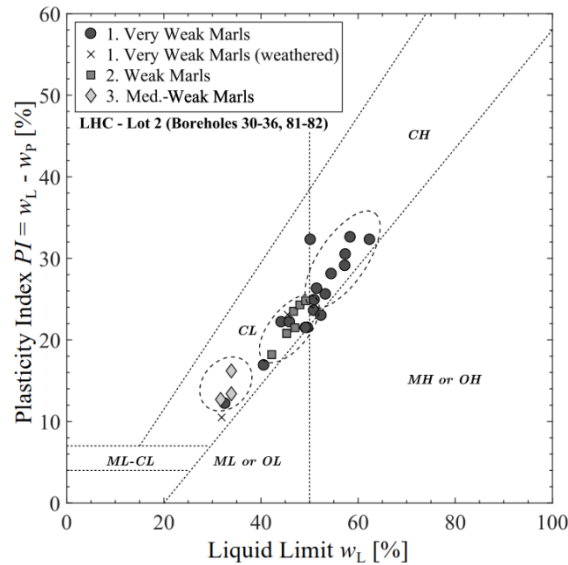
(b)

Figure 5.2. (a) Mineralogy of the marls and (b) Plasticity index and Liquid Limit (Fern et al. 2018)

A photograph of a borehole core taken in 2015 at Point 1 shows the transitions from sandstones to marls (Figure 5.3). Particularly, it is notable that after 18 months of storage, at 90 m depth, a certain weak type of marl identified as *very weak marl* in reddish colour is subjected to slaking (Figure 5.3b).
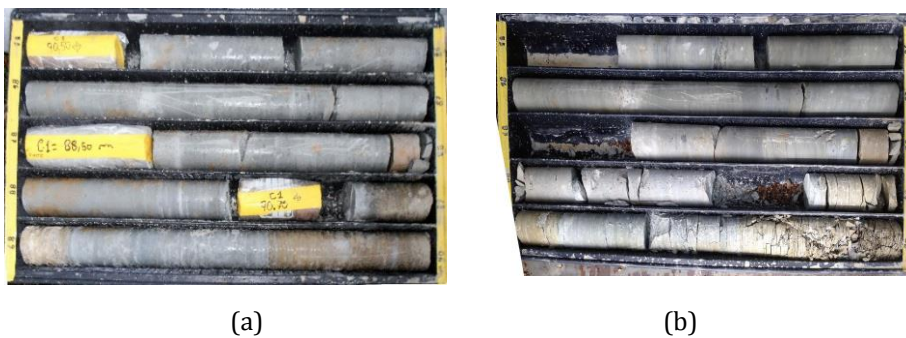
(a) (b)

Figure 5.3. Photograph of the borehole at Point 1 at a depth of 85 m to 90 m with the transition from sandstones to marls: (a) after extraction in October 2015 (Photo credit: CERN-GADZ), (b) after 18 months storage in March 2017 (Fern et al. 2018).

5.3 Borehole investigation

This section presents the results of a series of tests implemented for the High-Luminosity project for borehole C1 at Point 1 (ATLAS). The tests consist of Caliper

tests, sonic wave velocity tests, dilatometer tests and γ-ray tests, which were carried out by the Contractor *Terratec Geophysical Services* in October 2015 (GADZ, 2016a) and the data interpretation is reported in Fern et al. 2018.

Caliper tests

Through a series of Caliper logs, the diameter and the shape of the borehole C1 (ATLAS) was investigated. Figure 5.4 shows an increase of the borehole radius when the *very weak* and *weak* marls were encountered through the borehole, as a measure of the borehole wall collapse.

γ-ray tests

Results from γ-ray tests from borehole C1 are shown in Figure 5.4. It can be seen that a value of API equals to 90 divides the sandstones (API < 90) from the marls (API > 90). Additionally, while the *very weak* and *weak* marls experience the largest magnitudes of API, for the sandstones the smallest values are recorded (*medium strong* and *strong* sandstones).

Figure 5.4. Borehole tests: Caliper, sonic wave velocity and γ-ray tests (Fern et al. 2018).

Sonic wave velocity tests

The sonic P-wave velocity results shown in Figure 5.4 indicate that higher velocity values were recorded for the stronger rock units (i.e. sandstones) with v_p = 3000 - 3500 m/s, against those observed for the marls (v_p = 2500 -3000 m/s). Yet, a precise transition between the rock units is difficult to achieve, as the measurements were taken at small depth intervals of around 50 cm.

Dilatometer tests

The calculation of the coefficients of earth pressure for Point 1 and Point 5 was carried out from the results of some dilatometer tests carried out at 92 m depth, as reported by GADZ (2016a, 2016b). The data confirmed the anisotropic stress field (Table 5.1).

Table 5.1. Earth pressure coefficients reported by GADZ (2016a, 2016b).

CERN Location	K_0 max	K_0 min
Point 1	2.0 ± 0.3	1.5 ± 0.1
Point 5	1.75 ± 0.5	1.29 ±0.1

5.4 Laboratory testing

The extensive laboratory reports gathered from the sampling of borehole cores for the various construction works at CERN have enabled the characterization of the rock units. The mechanical parameters for the six rock units were obtained by GADZ (2016a, 2016b) and are presented in Table 5.2.

Table 5.2. Mechanical properties for intact rock (GADZ 2016a, b).

Variable	Units	Marls			Sandstones		
		1. Very weak	2. Weak	3. Med.-weak	4. Weak	5. Med.-strong	6. Strong[a]
w	[%]	8.6 ± 1.2	6.7 ± 1.2	5.0 ± 1.21	7.8 ± 1.8	4.1 ± 1.02	3.0 ± 1.09
ρ	[t/m³]	2.44 ± 0.04	2.5 ± 0.04	2.55 ± 0.04	2.38 ± 0.06	2.56 ± 0.04	2.60 ± 0.03
w_L	[%]	51.4 ± 6.7	48 ± 5.5	(34.8 ± 3.7)	–	–	–
w_P	[%]	25 ± 2.6	23 ± 1.7	(20.7 ± 1.9)	–	–	–
σ_{ci}	[MPa]	3.7 ± 1.5	8.0 ± 2.87	15 ± 4.9	10.8 ± 3.2	22.9 ± 5.5	46.1 ± 14.2
E_s	[MPa]	340 ± 241	690 ± 534	1960 ± 1508	1230 ± 624	3420 ± 1490	9417 ± 4750
$\sigma_{ti,b}$	[MPa]	0.58 ± 0.31	1 ± 0.43	1.76 ± 0.7	0.8 ± 3.5	2.11 ± 0.77	3.3 ± 1.5
I_s	[MPa]	0.22 ± 0.13	0.33 ± 0.17	0.57 ± 0.27	0.26 ± 0.13	0.7 ± 0.27	1.59 ± 0.6
V_{pl}	[m/s]	2240 ± 425	2500 ± 444	3040 ± 536	2455 ± 456	3340 ± 547	3955 ± 524
RQD	[–]	71 ± 27	91 ± 13	97 ± 8	96 ± 8	98 ± 4	99 ± 2
ISRM grade		R1	R2	R2	R2	R2–R3	R3

Where w is the water content, ρ the unit density, w_L the liquid limit, w_P the plastic limit, σ_{ci} the intact rock unconfined compression strength, E_s the secant Young's modulus $\sigma_{ti,b}$ the Brazilian test tensile strength, I_s the point load test index and V_{pl} the longitudinal P-wave velocity. The ISRM grade (ISRM, 1981) are R1 for very weak rock (1 MPa $< \sigma_{ci} <$ 5 MPa), R2 for weak rock (5 MPa $< \sigma_{ci} <$ 25 MPa), and R3 for medium-strong (25 MPa $< \sigma_{ci} <$ 50 MPa).
[a] Inclusive of specimens containing limestone.

Particularly, since the samples were saturated, the void ratio was determined from the water content w listed in Table 5.2 and from the specific gravity G_s, assumed equal to 2.70 for both marls and sandstones ($e = w \cdot G_s$). Therefore, the following

range of void ratio values was obtained: e = 0.14 – 0.23 for the marls and e = 0.08 – 0.21 for the sandstones.

Compression tests: confined and unconfined

Figure 5.5 shows the results of some compression tests carried out for the rock units: unconfined and confined tests. The results obtained from the unconfined tests (UCT) in undrained conditions suggest that the sandstones exhibit a more brittle behaviour than the marl units (Figure 5.5a). Additionally, the compression strength σ_{ci} increases from the *very weak* to the *medium weak* marl, with the latter rock unit behaving stronger than the soft sandstones. A good correlation between the strength and the secant stiffness E_{50} is shown in Figure 5.5b, where E_{50} can be evaluated through the following Equation (Hoek et al. 2005):

$$E_{50} = \alpha \cdot \sigma_{ci} \qquad (5.1)$$

where α is the stiffness coefficient, which shows a value of 90, 140 and 240 for the marls, *weak* and *medium weak* sandstones and *strong* sandstones respectively.

Moreover, confined compression tests (CCT) results are presented in Figure 5.5c and Figure 5.5d. Both marls and sandstones exhibit a similar mechanical behaviour than the one observed in UCT, with the sandstones being stiffer and more brittle than the marls. A peak strength state followed by a softening is reached by all rock units, with the exception of the *very weak marl*. The relation between strength and stiffness is presented in Figure 5.5d and it is defined as follows:

$$E_{50} = \beta \cdot q_f \qquad (5.2)$$

where β is the stiffness coefficient in the range of 40 and 100 for the marls and sandstones respectively, and q_f is the deviatoric strength.

Further, the stiffness is plotted against the initial void ratio (Figure 5.5e). The Figure shows an increase in the stiffness as the void ratio decreases. Hoek et al. (2005) observed similar mechanical behaviour when characterizing the molasse rock in Greece.

(a)

(b)

(c)

(d)

(e)
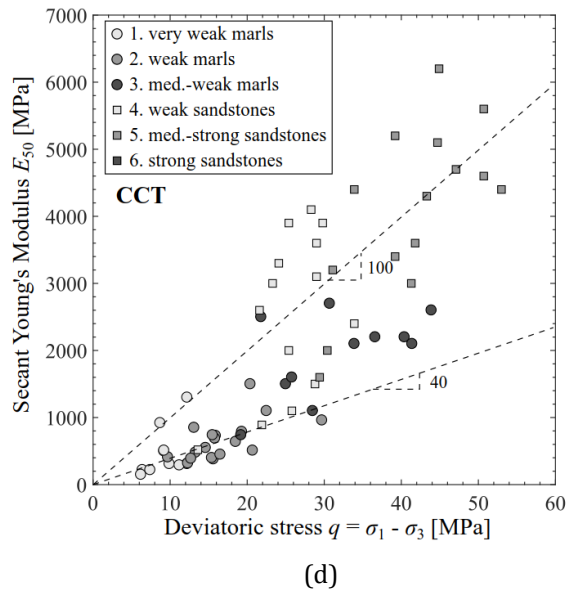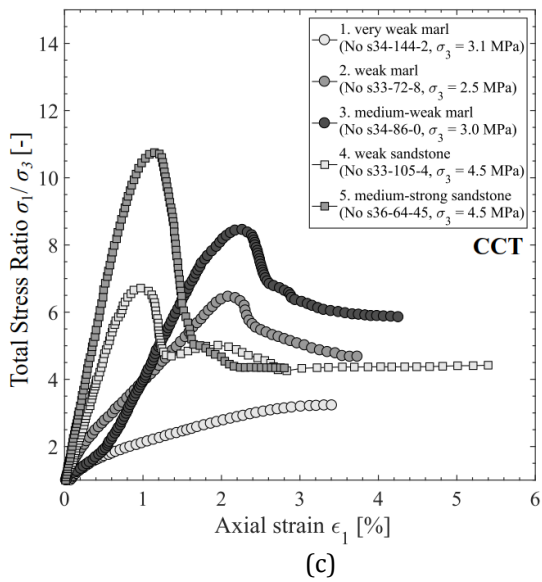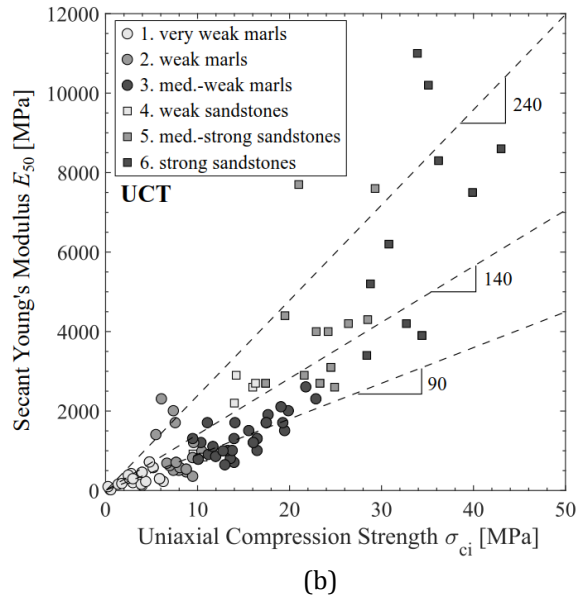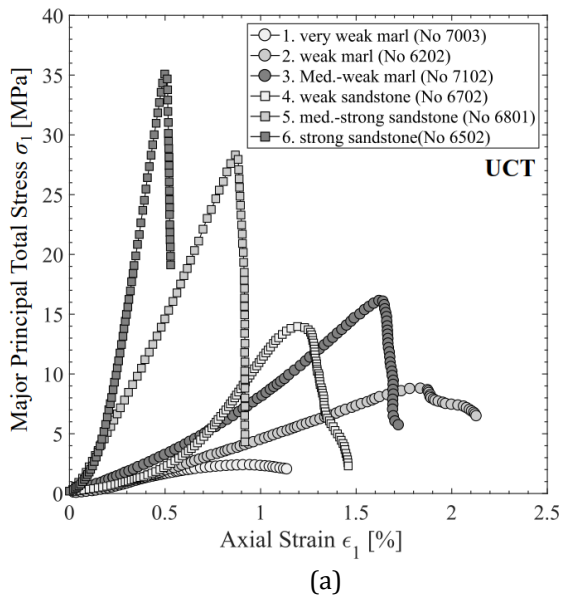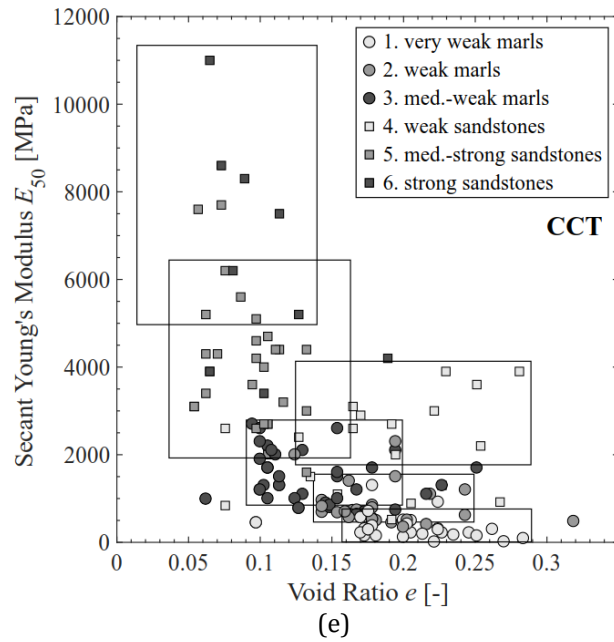
Figure 5.5. Compression tests: (a) unconfined tests, (b) strength and stiffness of unconfined tests, (c) confined tests, (d) strength and stiffness of confined tests and (e) void ratio and stiffness of confined tests (Fern et al. 2018).

Indirect tensile (Brazilian) tests were also carried out to measure the tensile strength of the rock units. In Figure 5.6 the void ratio is plotted against the tensile strength σ_t. Larger values of tensile strength were observed for the sandstones compared to those of the marl units, with the exception of the *weak* sandstones. Overall, the tensile strength for the rock units ranges between $\sigma_t = 0 \div 3$ MPa.
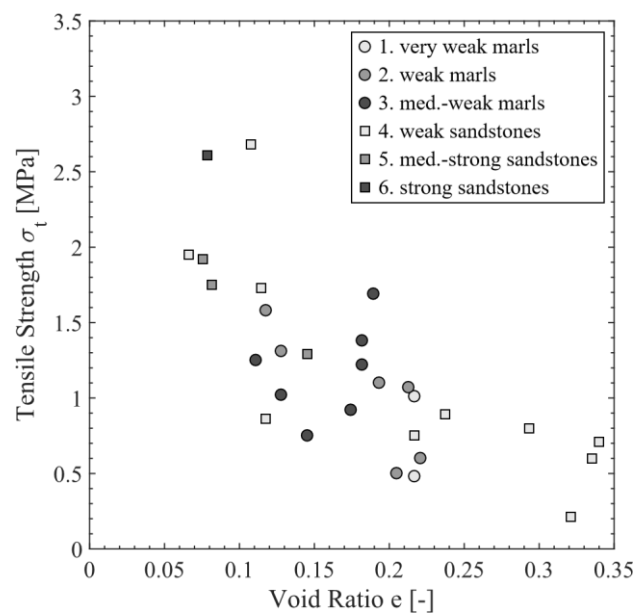
Figure 5.6. Tensile test results: tensile strength and void ratio (Fern et al. 2018).

Swelling and Permeability tests

Due to the swelling potential of certain layers within the marl units, swelling tests were carried out on intact rock: swell pressure tests and Huder-Amberg tests. The former tests were carried out in an oedometer cell where the vertical swell of the specimen is measured for the *very weak* and the *weak* marl as a function of the applied pressure (Figure 5.7). Particularly, the magnitude of swelling for the *very weak* marl seems to be larger than that of the *weak* marl (Fern et al. 2018). Figure 5.8 illustrates the results of some Huder-Amberg tests gathered for the marl units, through which the swelling pressure can be obtained, with the *very weak* marl exhibiting higher swelling pressures than the *weak* marl.
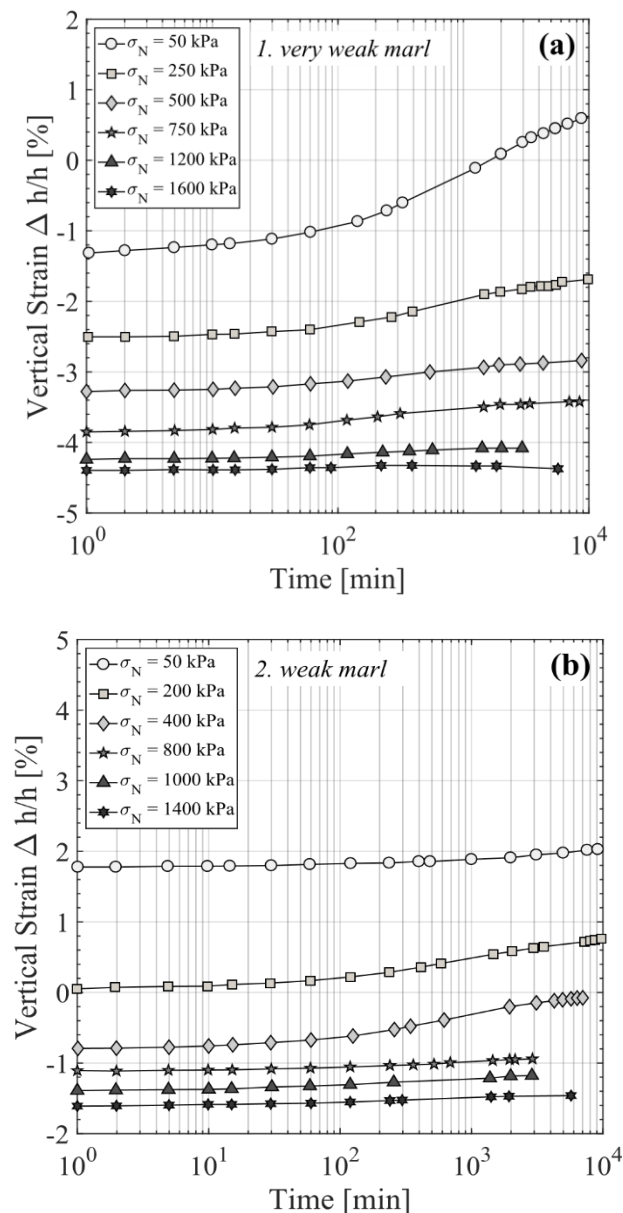
Figure 5.7. Swelling tests for: (a) very weak marl and (b) weak marl (Fern et al. 2018).
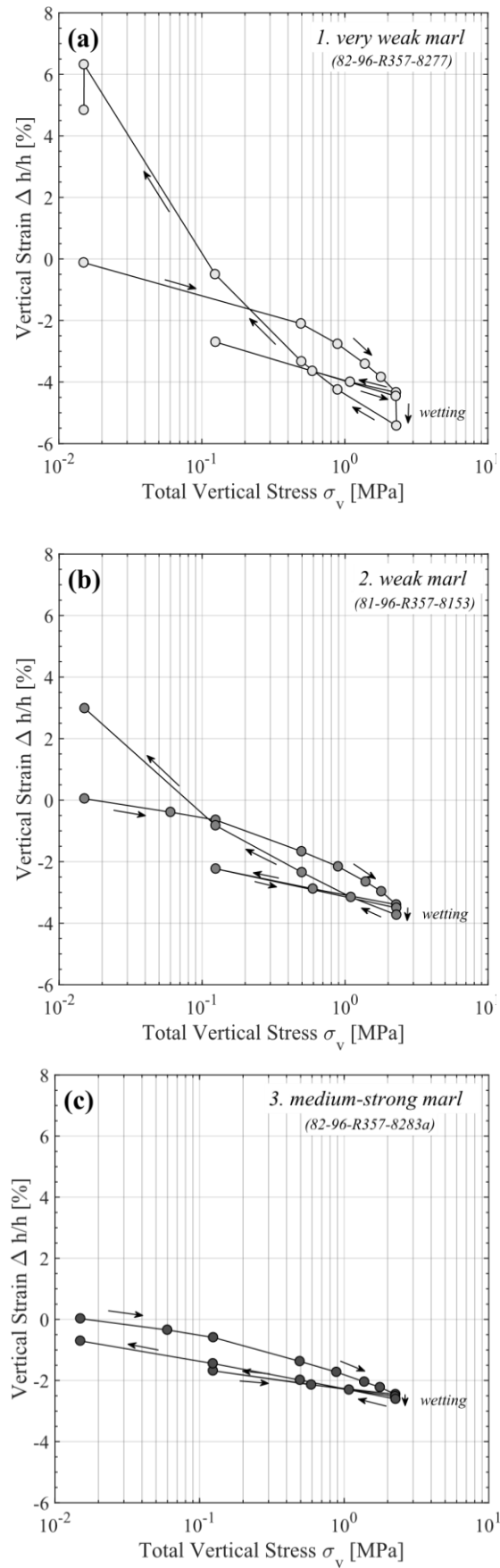
Figure 5.8. Huder-Amberg swelling tests: (a) very weak marl, (b) weak marl and (c) medium strong marls (Fern et al. 2018).

In the frame of the LHC project, some Lugeon tests were carried out in boreholes at Point 1 (Atlas) and Point 5 (CMS). The test consisted of putting the water in the borehole under a pressure of 1 MPa and 0.75 MPa at Point 1 and Point 5 respectively and to monitor the loss of water. GADZ (2016a, 2016b) reports that little water loss was found, suggesting a very low permeability of the molasse; also, the loss of water was lower than the accuracy of the instruments. Moreover, various water ingresses were observed during the 27 km excavation of the LEP/LHC tunnel, with a maximum inflow of 120 litres/min (6 l/min/km). These water ingresses were located between Point 7 and Point 8 and suggest a permeability as low as 10^{-9} to 10^{-10} m/s (0.01 Lugeon) (GADZ, 2016a).

5.5 Ground condition: material properties

The characterization of the molasse through the analysis of laboratory and in-situ data results has enabled the definition of the mechanical properties for all the rock units, as shown in the previous Section (Table 5.2). However, the data presented in the Table refer to the undrained conditions (i.e. total stress conditions), as no pore pressure measurements were recorded. Therefore, with the aim of simulating the long-term tunnel lining response during and after the consolidation through a coupled fluid-soil analysis following the tunnel excavation, the effective stress parameters are required. Since water does not resist any shearing stress, the effective shear stiffness modulus G' is equal to the undrained shearing modulus G_u, enabling the evaluation of the effective Young's modulus E' through the following Equation:

$$E' = E_u \frac{(1 + \nu') \cdot 2}{(1 + \nu_u) \cdot 2} \tag{5.3}$$

where E_u is the undrained elasticity modulus, ν' is the effective Poisson's ratio and ν_u is the undrained Poisson's ratio assumed to be equal to 0.49.

Figure 5.9 shows the result of the triaxial compression tests carried out for all the rock units, where the confining pressure σ_3 is plotted against the deviatoric stress q (GADZ 2016a, 2016b).

The graph σ_3 – q is presented in total stress. In order to convert it into the q – p' plane, two main assumptions were adhered to: (i) the pore pressure at the beginning of the shearing phase is nil (i.e. u= 0) and (ii) the specimen behaves elastically until failure. The Figure shows that the very weak marl unit exhibits a shear failure whereas the other rock units (i.e. weak marl, medium weak marl, weak sandstone and medium strong sandstone) show a tension failure, which can be described by assuming the Tresca yield criterion, which states that the maximum shear stress τ in the material equals to the maximum shear stress (σ_1 – σ_3) at failure, as follows:

$$(\sigma_1 - \sigma_3) = 2\,c' \tag{5.4}$$

where $(\sigma_1 - \sigma_3)$ is the deviatoric stress and c' the effective cohesion.

The tension failure line was traced by fitting the data with a line of inclination 1:3 in the q-p' space, with the tensile strengths values σ'_t estimated by extending the tension failure line towards the negative x-axis, as shown in Figure 5.9. The value obtained from the intersection of the tension failure line and the horizontal axis corresponds to the tensile strength of the rock layers.
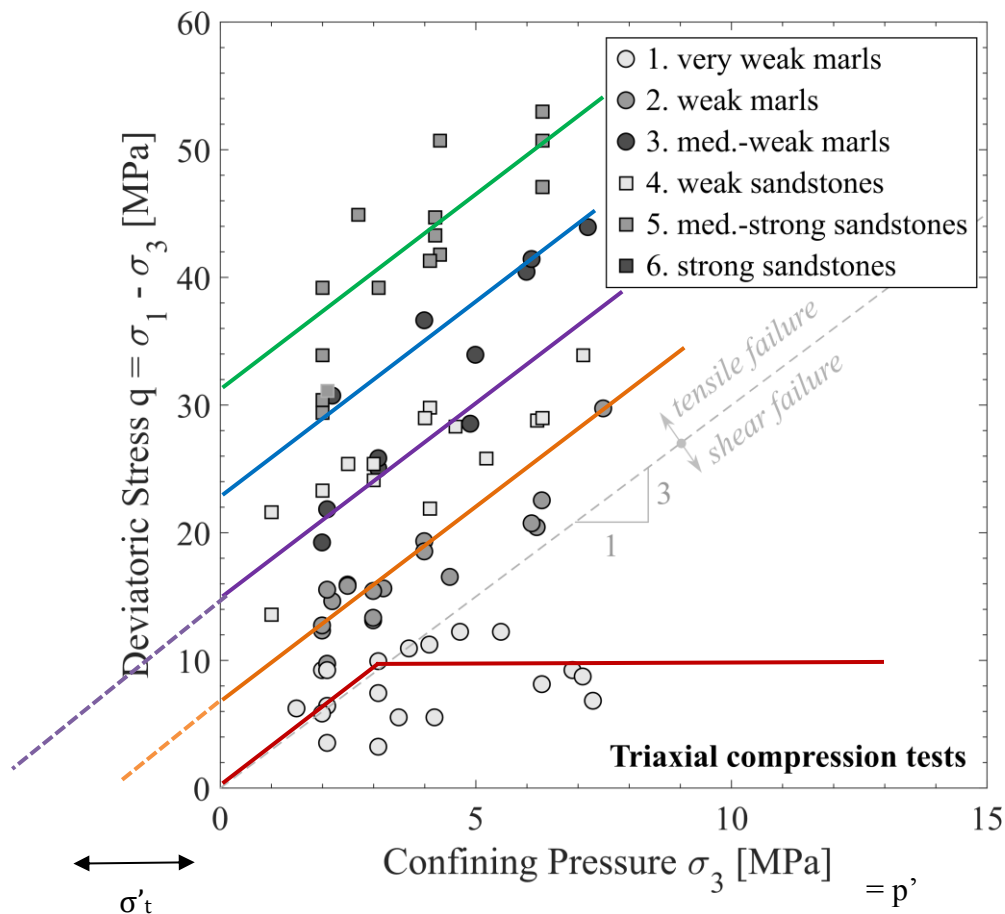
Figure 5.9. Triaxial compression tests for all the rock units (E.J. Fern, 2018).

For the *very weak marl* unit, instead, the data obtained from the triaxial compression test was fitted by assuming a shear failure line, which is described by the following Equation:

$$q = 2\,c' + Mp' \tag{5.5}$$

where M is the gradient of the critical state line in the q-p' space and c' is the effective cohesion, assumed to be equal to 1 and zero respectively (Figure 5.9).

By considering the parameter M = 1, the effective friction angle φ' for shearing resistance can be evaluated from the relation between the gradient M and φ' for a compression triaxial test (Eq. 5.6):

$$M = \frac{6\sin\varphi'}{3 - \sin\varphi'} \qquad \longrightarrow \qquad \varphi' = \arcsin\frac{3M}{M+6} \tag{5.6}$$

To simulate the ground response, the following constitutive models will be employed: the linear elastic model, the linear elastic-perfectly plastic Mohr-Coulomb model and the advanced non-linear elasto-plastic critical state soil model developed by Wongsaroj (2005). The latter constitutive model assembles some major mechanical features, such as: (i) elastic anisotropy, (ii) small-strain stiffness and its non-linearity, (iii) recent stress history and (iv) elasto-plastic behaviour within the yield surface. Further details of the proposed model can be found in Wongsaroj (2005).

In particular, the advanced critical state model will be employed for modelling only the *very weak marl* unit, since it exhibits a shear failure and shows a soil-like behaviour with high plasticity clay, whereas the other rock units within the molasse region will be modelled by adopting the linear-elastic behaviour.

Table 5.3. Summary of parameters for the *very weak marl* unit (Wongsaroj 2005).

Rock unit parameters	Very weak marl
M	1
e_0	0.2
D	0.10 - 0.18
u_1	300
m	0.2
ω_s	3
ρ_c	0.3
C_b	200
r	2
v'_{vh}	0.07
v'_{hv}	0.16
v'_{hh}	0.12
G_{hh}/G_{vh}	1.5
$p`_0$ [kPa]	3000

Table 5.3 shows the mechanical properties defined for the *very weak* marl unit in the advanced critical state model. Among the parameters listed in the Table, only the three variables highlighted were evaluated from the laboratory tests retrieved for very weak rock marl unit: (i) the gradient M assumed to be equal to 1, (ii) the initial void ratio e_0 determined from the water content and the gravity density, which was assumed equal to 0.2, a value in the range of e = 0.14 – 0.23 determined for the marls and (iii) the parameter *D* which represents the slope of the unloading swelling line in the *log_{10} p'– log of void ratio e* plane, where p' is assumed as σ'_v. The data suggest that the range of values for D lies between 0.10 – 0.18, as shown in Figure 5.10.
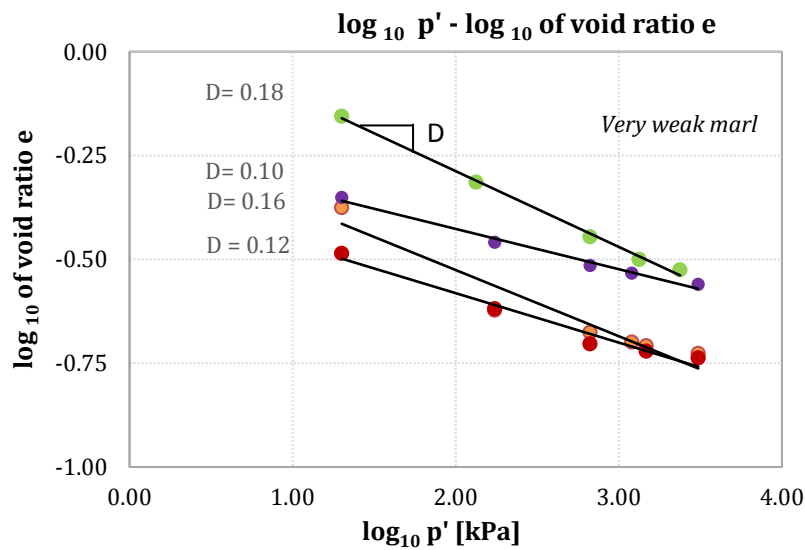
Figure 5.10. D parameter evaluation for the very weak marl unit in the log_{10} p'–log_{10} of void ratio e.

Except the three soil parameters aforementioned, the mechanical properties defining the advanced critical state model for the very weak marl layer were assumed according to Wongsaroj (2005) for the stiff London Clay due to the lack of laboratory and site investigation (Table 5.3).

A summary of the mechanical properties assumed for the molasse rock (i.e. marls and sandstones) and for the moraine deposits is presented in Table 5.4.

The Table comprises the following values: effective and undrained Young's modulus, effective and undrained Poisson's ratio, the initial void ratio e_0, the parameters defining the Mohr-Coulomb constitutive model such as the effective cohesion c', the effective friction angle φ', the dilatancy angle ψ assumed equal to a value of 2 and a tensile strength σ_t'. Moreover, the permeability of each rock layer is defined after GADZ (2016a, 2016b), by considering the moraine deposits more permeable than the molasse region. The saturated density γ_{sat} and the coefficient of earth pressure at rest K_0 were also defined according to GADZ (2016a, 2016b).

Table 5.4. Mechanical properties for intact rock.

Variable	Marls			Sandstones			Moraine
	1. Very weak	2.Weak	3. Med.-weak	4. Weak	5. Med. - strong	6.Strong	
E_u [MPa]	340	690	1960	1230	3420	9417	-
ν_u	0.49	0.49	0.49	0.49	0.49	0.49	-
ν'	0.2	0.2	0.2	0.2	0.2	0.2	0.3
e	0.2	0.2	0.2	0.2	0.2	0.2	0.6
E' [MPa]	273.8	555.7	1578.5	990.6	2754.4	7584.2	50
c' [MPa]	0	3	11	8	15	0	0.1
ψ [°]	0	2	2	2	2	2	2
φ' [°]	25	-	-	-	-	-	31
σ'_t [MPa]	0	2	7.8	5.2	10.1	-	1
k [m/s]	10e-10	10e-9	10e-9	10e-08	10e-08	10e-08	10e-7
γ_{sat} [kN/m³]		24			24		22.5
K_0	1.2	1.5	1.5		1.5		1.5

*where E_u is the undrained stiffness, ν_u the undrained Poisson's ratio, ν' the effective Poisson's ratio, e the void ratio, E' the effective Young's modulus, c' the effective cohesion, φ' the critical friction angle for shearing resistance, ψ the dilatancy, σ'_t the tensile strength, k is the permeability, γ_{sat} the saturated density, K_0 the coefficient of earth pressure at rest.

5.6 Summary

This chapter presented the geotechnical investigation of the *red molasse* through laboratory and field tests. This comprised the analysis of a wide data set collected in the past years thanks to the various underground constructions taken place at CERN. The results show that the weak rock unit is composed of a sequence of sandstones and marl layers, with different mechanical properties. Also, the transition between the different layers is often difficult to assess. However, a division into 6 sub-units for each rock type is proposed. The marls were characterized based on their strength, ranging from very weak (R1) to medium weak (R2), whereas the sandstones were ranged from weak (R2) to strong (R3). Particularly, one marl unit identified as *very weak* marl was found to have soil-like properties, with high plasticity clay and swelling potential. Additionally, the results from laboratory compression tests showed that the marls exhibit a more ductile behaviour compared to the sandstones. Overall, the molasse mass was found to be quite impermeable.

It should be noted that all the tests presented were carried out in undrained total stress conditions. Yet, in order to simulate the long-term consolidation after tunnel excavation through coupled fluid-soil analysis, the evaluation of the effective stress parameters for the rock units was also presented and discussed. Moreover, the results obtained from the triaxial compression tests carried out for both marls and sandstones showed that a shear failure is observed for the very weak marl layer whereas the other rock units exhibit a tensile failure. This enabled the calculation of the mechanical properties required for defining the constitutive soil models implemented in the finite element analysis presented in Chapter 6.

References

Fern, E.J., Di Murro, V., Soga, K., Li, Z., Scibile, L., and Osborne, J.A. (2018). Geotechnical Characterisation of a Weak Sedimentary Rock Mass at CERN, Geneva. *Tunnelling and Underground Space Technology* 77 (July): 249–60.

GADZ, 1996. Reconnaissances géologiques et géotechniques –rapport d'interprétation No 3545/91. Technical report, Géotechnique Appliquée Dériaz SA (in French).

GADZ, 1997. Reconnaissances de la Molasse – Rapport de Synthèse – No 3545/97. Technical report, Géotechnique Appliquée Dériaz SA (in French).

GADZ, 2016a. Reconnaissances géotechnique Point 1 – No 7222/2. Technical report, Géotechnique Appliquée Dériaz SA (in French).

GADZ, 2016b. Reconnaissances géotechnique Point 5 – No 7223/2. Technical report, Géotechnique Appliquée Dériaz SA (in French).

Hoek, E., Marinos, P.G., Marinos, V.P., (2005). Characterisation and engineering properties of tectonically undisturbed but lithologically varied sedimentary rock masses. *Int. J. Rock Mech. Min. Sci.*, 42(2), 277–285.

ISRM. Rock characterisation, testing and monitoring. Technical report, International Society of Rock Mechanics, Oxford, 1981.

Laughton, C. (1988). CERN Accelerator Project. World Tunnelling Project Report.

Lombardi, G. (1979). Rock mechanics at the CERN proton-antiproton facilities. In: International Society for Rock Mechanics (Ed.), 4th ISRM Congress. International Society for Rock Mechanics, Montreux. Balkema, pp/433-436.

Lombardi, G. (1984). Underground openings in swelling rock. National Conference on Case Histories in Geotechnical Engineering. Pakistan, Lahore.

Parkin, R.J.H, Varley, P.M. and Laigle, F. (2002). The CERN LHC Project – Design and Construction of large caverns in tight spaces. *Geotechnical Aspects of Underground Construction in Soft Ground*, Lyon.

Chapter 6

6 Two-dimensional finite element modelling of CERN TT10 tunnel

6.1 Introduction

The long-term behaviour of CERN concrete-lined tunnel in the molasse region was investigated through a series of soil-fluid coupled finite element (FE) numerical analyses in 2D plane strain conditions.

This chapter describes the FE simulations of tunnel lining performance and presents the results obtained during the ground consolidation after the TT10 tunnel construction and during the long-term, for a chosen representative cross-section. Particularly, the effect of groundwater changes around the tunnel with consequent alteration of the hydraulic regime in the ground is examined on the numerical predictions of tunnel lining response. The importance of tunnel lining permeability as well as the hydraulic regime in the ground are also highlighted.

The results in terms of tunnel lining diameter changes and total strains are compared against the field measurement data to validate the numerical analyses and to assess the status of the tunnel at CERN. Further, the mechanism of tunnel lining deformation is also identified.

6.2 Short-term analysis

The two-dimensional finite element model was constructed based on the in-situ conditions, with the tunnel size and its structures (primary lining, secondary lining, tunnel drainage conditions etc.) totally referenced to the design drawings. The analyses were conducted using the software package ABAQUS 6.14 (ABAQUS, 2014).

The following sections describe each step involved in the definition of the numerical method, such as the description of the model geometry and boundary conditions, discretization of the model and tunnel construction method.

6.3 Model geometry and ground condition

The soil profile adopted for the FE analysis is presented in Figure 6.1 and is based on the face-logs collected during tunnel excavation and the nearest borehole log available. The adopted profile comprises a 19 m thick layer of Moraine deposits overlaying different lithotypes disposed in interbedded layers rather than continuous layers within the Molasse region (73 m). It is obviously difficult to identify a single layer between boreholes. Yet, two types of rock were identified, marls and sandstones, and were divided into six sub-units, three for each rock type (Fern et al. 2018). The following main layers were identified for the presented model:

- Medium-strong sandstones;
- Medium-weak marl;
- Very weak marl or called "lumpy marl;
- Sandy marl.
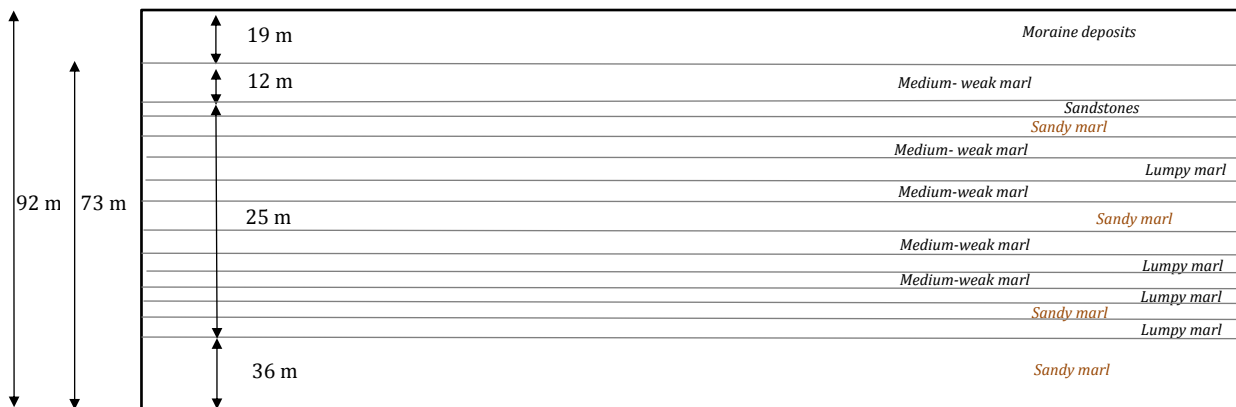
Figure 6.1. Soil profile and general geometry adopted for the 2D analysis.

The mechanical parameters of the mentioned rock units were determined based upon the geotechnical investigation carried out and discussed in Chapter 5.

6.3.1 Boundary conditions

Figure 6.2 shows the displacement boundary conditions fixed for the numerical model. No vertical displacements (u_2=0) and horizontal displacements (u_1= 0) were permitted along the bottom boundary and along the lateral vertical sides respectively (Figure 6.2). The top boundary was set to be free at ground surface.

The initial pore water pressure distribution profile was considered to be hydrostatic, and the water table sits in the moraine layer, with the moraine depth varying between different sites (i.e. Point 1 and Point 5) (Parkin et al. 2002). However, in this case study, the water table was located at ground surface (z= 0), as shown in Figure 6.3.
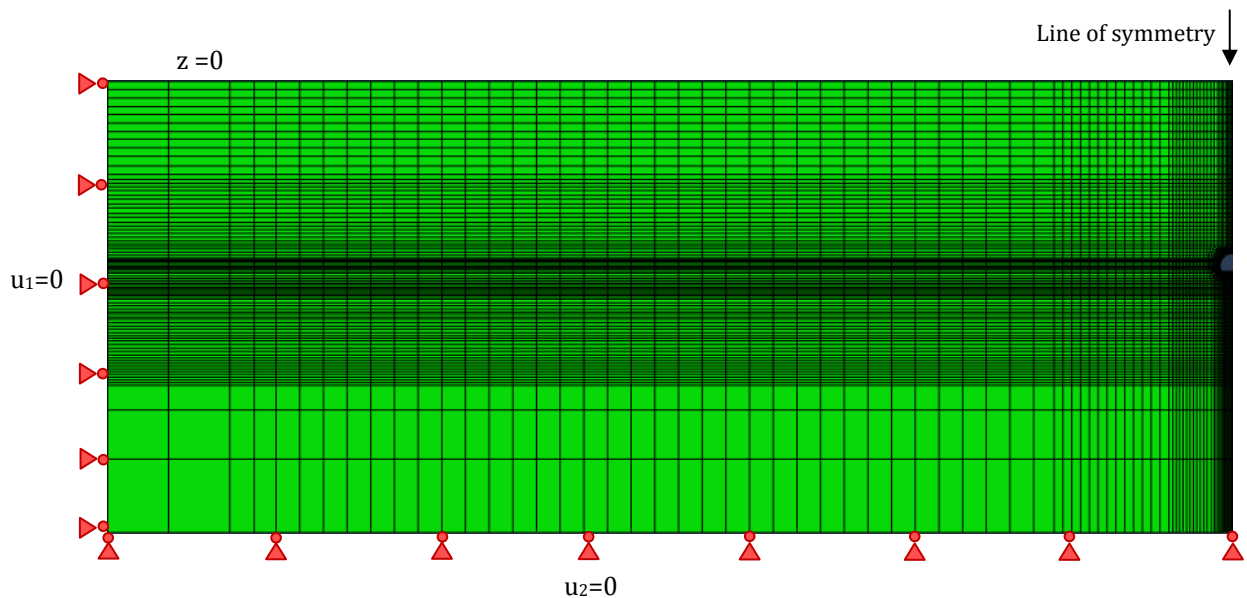
Figure 6.2. Boundary conditions fixed for the 2D model.
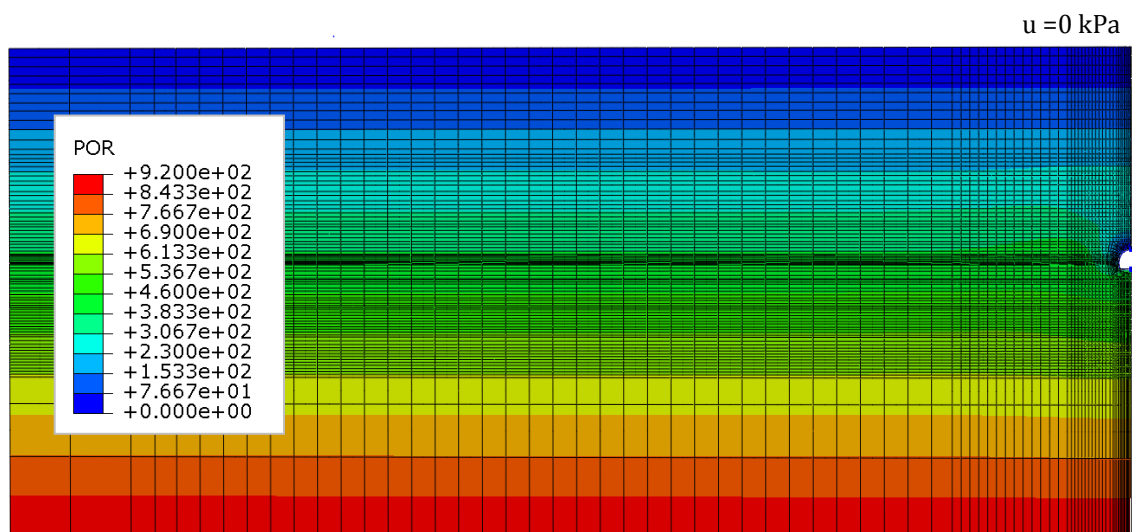
Figure 6.3. Pore pressure profile for the 2D model.

6.3.2 Mesh generation

To complete the numerical analysis by using the software ABAQUS 6.14, the entire model has to be discretized into finite elements by meshing the geometry. ABAQUS allows the mesh generation process to be automatic by choosing within a range of different element geometries. However, a difficult task is placing a mesh around the tunnel geometry.

Since the generation of unstructured meshes may cause convergence problems and/or compromise the accuracy of the results and, therefore, generate numerical errors, the approach adopted was to manually discretize the whole model. The desired mesh was achieved by adopting the software Altair HyperMesh, a multi-disciplinary finite element tool capable of supporting complex geometries. Its meshing capabilities enabled the development of a 2D customized mesh, with local mesh refinement applied at key sections, such as the tunnel opening. Coarser elements were adopted at the far boundaries. The approach required a large amount of time by the user, as the desired geometry was initially created in CAD, considering the constraints imposed by horizontally bedded layers of different thicknesses.

Once the desired level of refinement was reached, the geometry was imported into HyperMesh and the mesh was then generated. An exported file was then supported by ABAQUS, where the meshed model was successfully validated.

The whole domain was discretized into a set of quadrilateral elements. The soil was modelled with eight-node quadratic displacement and linear pore pressure elements, with the nodes placed at the corners of the elements with the additional four nodes being located at the midpoint of each side. In second-order elements, each node has two degrees of freedom, one for each component of displacement (u_1, u_2), whereas the pore pressure degrees of freedom are active only at the corner nodes. The tunnel lining was modelled with beam elements defined by three nodes at the tunnel boundary, which are shared by the surrounding soil.

The 2D FE mesh used in the analysis for a tunnel depth of $z = 38.75$ m from ground surface is shown in Figure 6.4. It consists of 14590 quadrilateral solid elements for modelling the soil and 45047 nodes. The FE mesh dimensions were carefully designated in order to ensure that the boundary sides of the model are sufficiently distant for any boundary effect to be insignificant (Franzius and Potts 2005). For this reason, the total length of the 2D model was around $5 \cdot z$ (400 m), with z being

the tunnel depth, a reasonable boundary distance for negligible boundary influence, as recommended by previous works (Wongsaroj 2005; Laver 2010).

The meshed model is perfectly symmetric and presents a total width of 400 m and a height of 92 m (Figure 6.4).
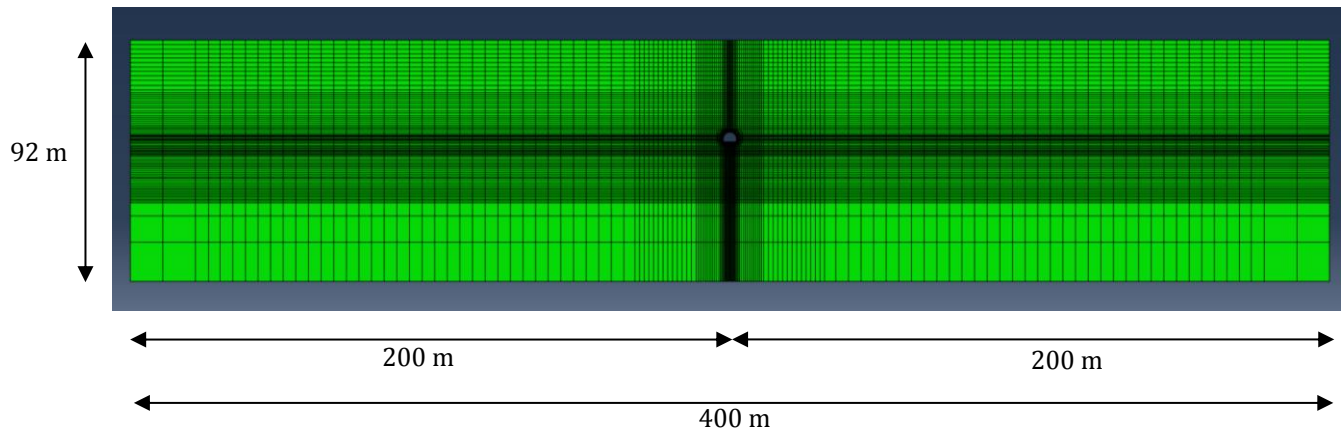
Figure 6.4. Finite element mesh for the 2D analysis.

6.3.3 Tunnel excavation modelling

Two basic approaches can be used for excavating a tunnel: the NATM, the New Austrian tunnelling method, more commonly referred to as the sprayed concrete lining SCL method, and tunnel boring machines (TBM). The former method is characterized by a sequence of small excavations before the application of primary support, which consists of sprayed concrete (shotcrete) and rock bolting. The latter excavation method makes use of open-face or full-face mechanised shields and can be grouped into earth pressure balance (EPB) and slurry machines.

It is widely known that tunnel construction is a three-dimensional process with stress redistributions near the tunnel face and ground movements occurring in both radial and longitudinal direction. Preferably, a full 3D numerical analysis is desired, but it requires enormous computational resources. Additionally, due to the complexity of ground conditions, usually, 2D modelling is adopted (Potts and Zdravkovic 2001). However, some assumptions have to be made in order to account for the 3D effects. Several approaches are available in the literature for 2D analyses. For the TT10 tunnel case study, tunnel construction was modelled using the convergence-confinement method (Panet and Guenot, 1982). This approach takes into account the important feature of installing the tunnel lining support with a time

delay behind the excavation face, allowing then a certain amount of deformation in the ground. The latter deformation strongly depends on the assumed degree of ground stress relief at the time of tunnel lining installation. This method implies a gradual reduction of ground pressure at the periphery of the tunnel lining to allow movement into the tunnel.

Initially, the internal pressure in the tunnel opening is equivalent to the external earth pressure (Figure 6.5a). The tunnel is then excavated by removing the soil elements inside the opening and by applying the equivalent soil forces at the tunnel boundary (Figure 6.5.b). The internal pressure is then decreased with a reduction factor of 0.7, corresponding to the 70% stress relief before installing the lining, which is bearing the further 30% of pressure (Figure 6.5c).

(a)   (b)

(c)
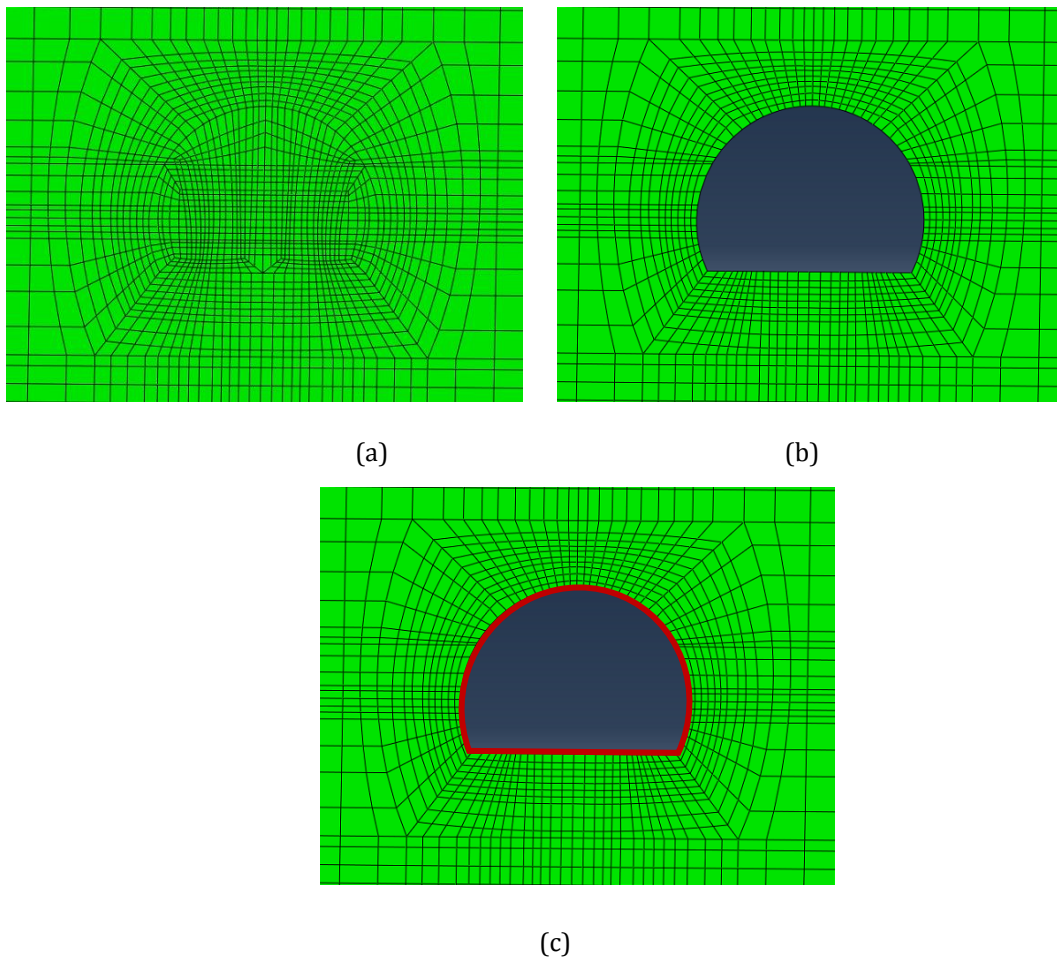
Figure 6.5. Modelling scheme adopted: (a) tunnel before the excavation phase; (b) tunnel excavation phase and (c) activation of tunnel lining.

The construction stages in the proposed model were assumed to be undrained conditions, as the excavation process is considered to be completed within a period of 24 hours.

6.3.4 Tunnel lining model

A continuous concrete tunnel lining was considered for the numerical simulations, by adopting an isotropic, homogeneous and linear-elastic material, with the Young's modulus initially of 20 GPa and the Poisson's ratio of 0.25. The tunnel lining was modelled by adopting beam elements. Both tunnel lining and the soil are sharing the same nodes at the interface of the tunnel boundary, assuming that there is no slippage between the tunnel and the ground. Additionally, the tunnel lining was simply activated when the desired unloading stress has been obtained, as described previously for the tunnel excavation methodology.

6.4 Long-term tunnel lining response

6.4.1 Introduction

The long-term performance of circular tunnels and cross-passage construction in stiff London Clay was investigated by previous works (Wongsaroj 2005; Laver 2010; Li 2014).

This section aims to provide the results of a numerical investigation into the effect of groundwater flow regime change on the long-term tunnel lining performance of a concrete-lined tunnel. Observational data results from both conventional and advanced monitoring technologies have shown a similar mechanism of tunnel lining deformation. Some compression and tension developments were observed at the tunnel crown and tunnel spring lines respectively, indicating that the tunnel lining may deform with a vertical elongation mode (Figure 6.6).
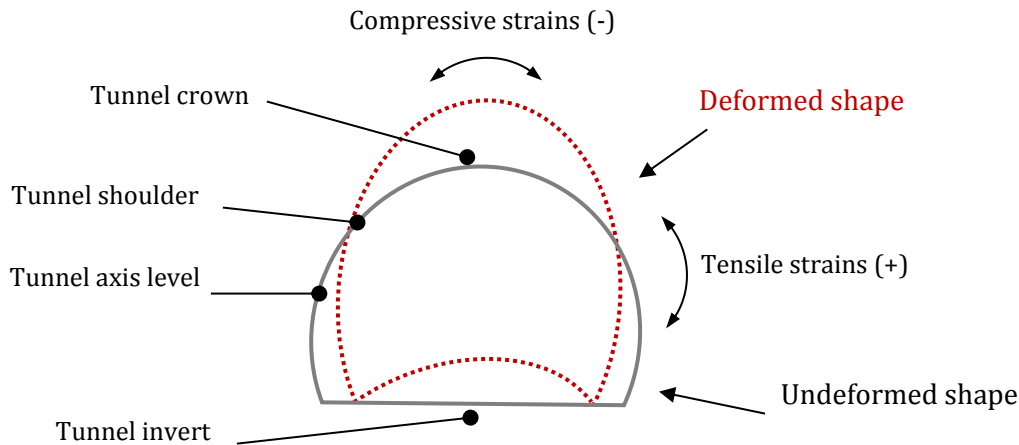
Figure 6.6. Tunnel lining mechanism of deformation: an undeformed and deformed shape with compression and tension development at tunnel crown and tunnel axis respectively.

The following main hypotheses have been adhered to in the performed numerical analyses:

- Shortly after the construction period, for sprayed concrete linings, concrete properties (i.e. stiffness, strength) may change considerably with time due to long-term effects, such as shrinkage and creep (BTS, 2004). This would cause damage behaviour and, therefore, initiate the development of cracks in the tunnel lining. For this reason, a reduction of the elasticity modulus E of the sprayed concrete tunnel lining was implemented.

- Many years after tunnel construction, the tunnel lining was subjected to an external water pressure acting on the tunnel lining due to a change in the groundwater condition. This caused a pore pressure build-up in the formation around the tunnel.

In the next section, the calculation phases are presented, and the computed tunnel lining behaviour is described for different scenarios on one representative tunnel cross-section case, which is considered to be the most critical and is located at a tunnel depth of 38.7 m from the ground surface.

6.4.2 Long-term consolidation and modelling of external water pressure on the tunnel lining

A fully coupled soil-fluid analysis was performed to simulate the long-term behaviour of the TT10 tunnel induced by tunnel construction in the short-term and ground consolidation in the long-term thereafter. Due to the unloading of the bedrock and consequent reduction in the initial stresses, the short-term conditions were replicated. The long-term ground consolidation considers the dissipation of the excess pore pressures generated during tunnel construction with time.

After defining a geostatic stress state, the tunnel construction stage was modelled by removing excavated soil elements and reducing the nodal forces at the tunnel boundary of a certain percentage. The tunnel lining was then put in place by activating the beam elements. The consolidation stage was allowed in the following step. Since the TT10 tunnel is provided with water drainage pipes, a fully permeable lining was assumed during this stage, which represents from the year 1972 to the year 2013.

As mentioned in Chapter 3, extreme weather conditions with heavy rainfall event in addition to the calcification deposits may have reduced the tunnel drainage system's capacity, resulting in the build-up of pore pressure behind tunnel lining, as shown in Figure 6.7. The accumulated external water pressure acting on the lining was simulated by enforcing the equivalent hydrostatic load on the tunnel lining at the considered tunnel depth (Figure 6.8). In fully drained conditions, the groundwater collected by the drainage pipes located at both sides of tunnel invert would be conveyed into the main drainage system. However, as the tunnel drainage starts to get clogged, the water pressure on the lining gradually rises and accumulates with time. The current water table is assumed at the ground surface. However, as the water table level might be drawn down towards the tunnel with time due to a change in the groundwater conditions, the magnitude of the hydrostatic load was evaluated by fitting the field data available for the monitoring period that goes from 2013 to 2017. Therefore, this additional phase of water pressure build-up was modelled for a period of four years (from 2013 to 2017).
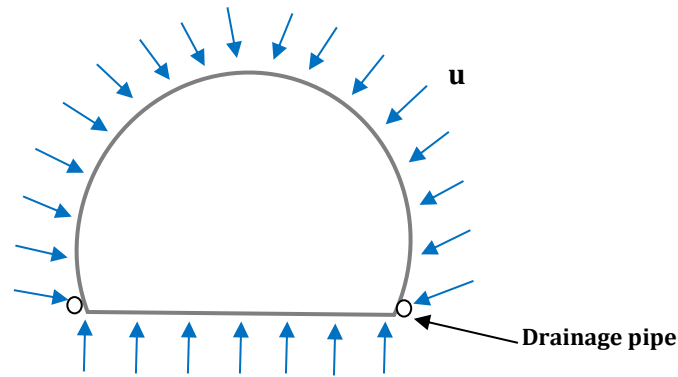
Figure 6.7. Application of the external water pressure on the outer edge of the tunnel lining.
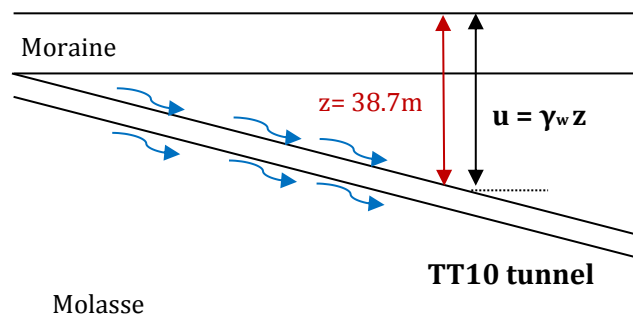
Figure 6.8. Longitudinal section of TT10 tunnel.

To summarize, the tunnel construction stages assumed in the FE analysis are shown in Table 6.1.

Table 6.1. General construction stages adopted for the FE model.

Calculation stage	Description of each stage
1. **Geostatic stage**	Equilibrium of soil
2. **Tunnel excavation**	Soil elements removal and application of nodal forces (undrained conditions)
3. **Unload 1**	Nodal forces reduction of 70 % for ground stress relief
4. **Unload 2**	Nodal forces reduction of 30 % and activation of tunnel lining
5. **Consolidation 1**	Long-term consolidation (drained conditions)
6. **Consolidation 2**	Application of water pressure behind tunnel lining

6.5 Tunnel lining response

In this section, the post-construction tunnel lining structural behaviour will be analysed.

To evaluate the tunnel lining performance after tunnel construction and with the intent of validating the field measurement data, different scenarios were investigated for the most critical tunnel cross-section, located at tunnel depth z = 38.7 m. Figure 6.9 shows the soil profile defined for the considered tunnel cross-section, which presents an alternate sequence of horizontal layers of medium marl, sandstones, very weak marl and sandy marl, as shown previously in Figure 6.1. A zoom in on the soil surrounding the tunnel is also shown in Figure 6.9, with the tunnel crown located in the very weak marl layer of a thickness of 4.4 m (defined with a red colour), whereas the tunnel invert is located in the medium-weak marl, characterized by a depth of 2.8 m (defined with a yellow layer).

The tunnel lining deformations in terms of change in tunnel diameter as well as the tunnel lining stresses (i.e. axial forces, bending moments) are analysed and the results for different scenarios are discussed.

Figure 6.9. Soil profile for tunnel cross-section at 38.7 m from the ground surface.

6.5.1 Scenario 1: tunnel lining stiffness reduction

The first scenario involves a reduction of the elasticity modulus E of the beam elements, with a consequent decrease of both axial and be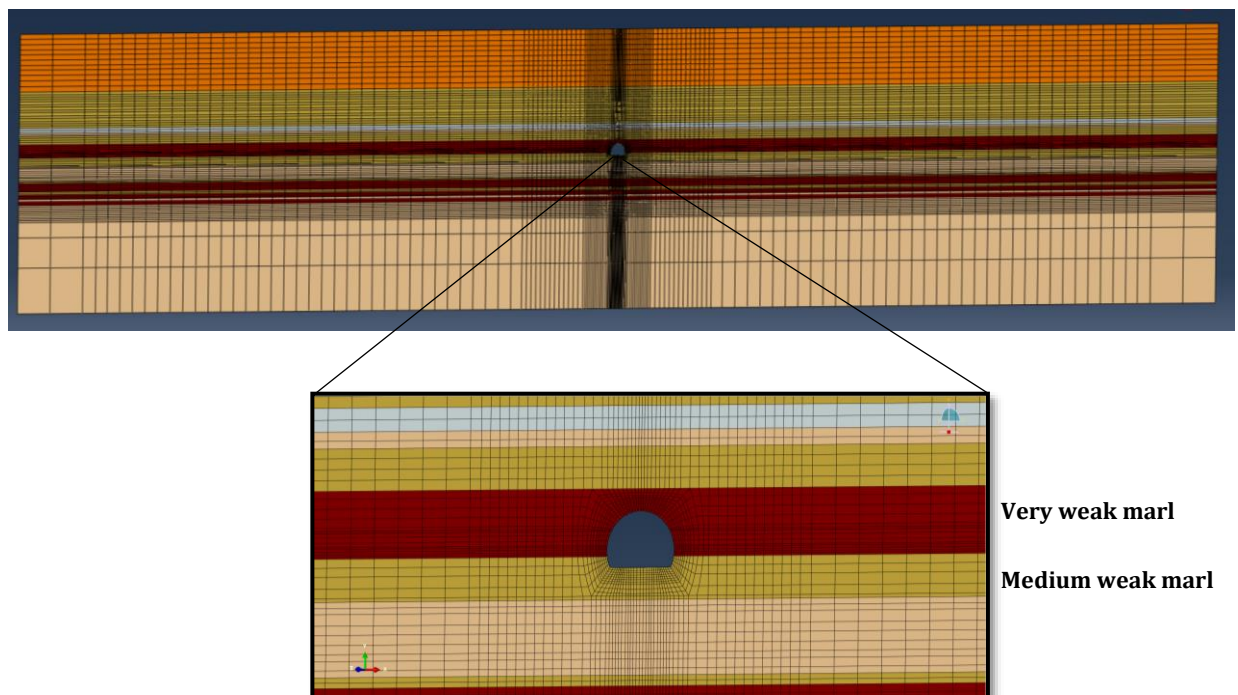nding stiffness, EA and EI respectively. The stiffness reduction was applied uniformly along the tunnel lining and the calculation phases considered for scenario 1 are shown in Table 6.2.

After tunnel construction, the tunnel lining is fully drained and the pore pressures are considered to be zero at the tunnel boundary (Figure 6.10). Also, within the first year after tunnel excavation, the stiffness of the concrete lining was initially assumed to be 20 GPa. Due to the tunnel lining cracking observed around 1-2 years after the construction, the lining stiffness modulus E was then reduced to 15 GPa, whereas the tunnel lining drainage condition was kept to be fully permeable. However, due to the clogging of the tunnel drainage system occurred in 2013 (after around 41 years after tunnel construction), the groundwater pressure increased behind the lining, acting as a hydrostatic load. It should be noted that as a first attempt, the external pore pressure was applied instantaneously on the tunnel lining, at the beginning of the stage (i.e. instantaneous clogging of tunnel drainage pipes). Also, as water infiltration was initially observed at the interface of the TT10 tunnel with the moraine layer, the hydrostatic load was considered by assuming the water table located at 19 m from ground surface. However, due to numerical convergence issues associated with the instantaneous imposition of the pressure load, a pore pressure of 160 kPa was applied instead for this scenario for a period of 1 year (2013 - 2014), after which the tunnel drainage system was assumed to be cleaned, and the pore pressure was brought back to the initial drained condition (u= 0 kPa) for a period of four years, as shown in Figure 6.10. During the last stage, the tunnel lining stiffness was reduced from a value of 15 GPa to 5 GPa, to account for the cracks experienced by the tunnel lining.

Table 6.2. Calculation phases for scenario 1.

Calculation stage	Time Period	Young's modulus E [GPa]	Pore pressure at tunnel lining u [kPa]
Consolidation 1	1 year	E = 20 GPa	u= 0 kPa
Consolidation 2	40 years	E reduced to 15 GPa	u= 0 kPa
Consolidation 3	1 year	E = 15 GPa	u= 160 kPa
Consolidation 4	4 years	E reduced to 5 GPa	u= 0 kPa
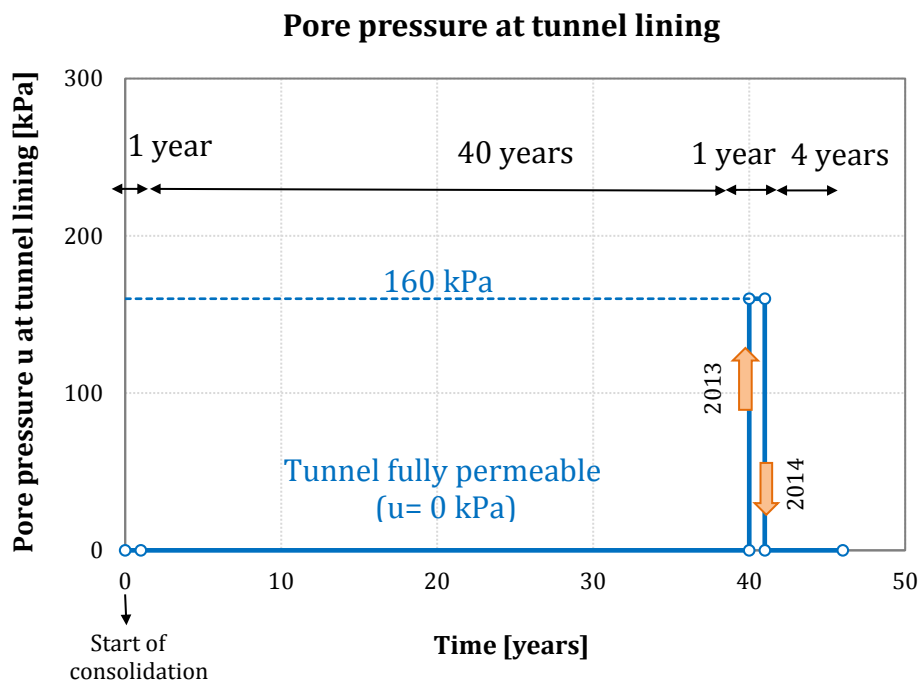
Figure 6.10. Development of pore pressure at tunnel lining boundary with time.

Tunnel deformation

Figure 6.11a and Figure 6.11b show the change in tunnel diameter with time after tunnel construction for the chosen cross-section. During the first year of consolidation, a value of 20 GPa was assumed for the tunnel lining stiffness E. In the subsequent forty years of consolidation, a stiffness reduction factor was adopted, by reducing the tunnel lining stiffness from 20 GPa to 15 GPa, for encountering of concrete cracking opening developed after the construction, as concrete proprieties might change due to long-term effects (i.e. shrinkage) (BTS, 2004).

The change in the vertical diameter decreased by 0.24 mm, whereas at the tunnel axis the horizontal diameter increased by 0.03 mm as the soil consolidates (Figure 6.11a), meaning that the tunnel is squatting.

The squatting deformation has been also observed for tunnels in London Clay, which is likely to continue years after tunnel construction (Ward & Thomas, 1965). Additionally, a tunnel with permeable lining is observed to squat more in the long-term compared with an impermeable lining (Wongsaroj, 2005). For a fully permeable tunnel lining, pore pressure becomes zero at the tunnel boundary and the effective stress of the soil near the tunnel increases as the soil consolidates, until a new steady state condition is reached. For the impermeable tunnel lining, the tunnel boundary acts as a watertight tunnel, sustaining more lining load than a permeable lining due to the recovery of pore pressure in the long-term (Shin et al. 2002).

(a)

(b)
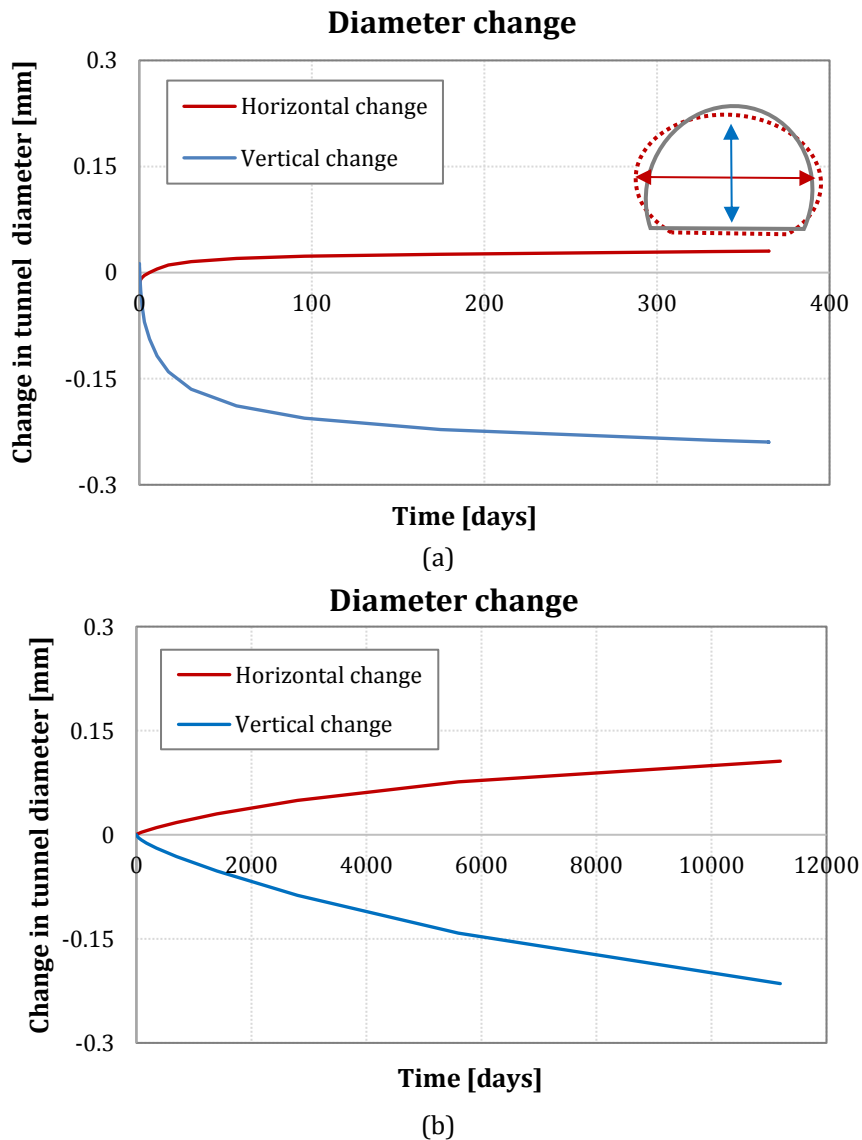
Figure 6.11. Change in tunnel diameter during consolidation phases: (a) Consolidation stage 1 and (b) Consolidation stage 2.

Figure 6.12a presents the change in tunnel diameter while applying a water pressure of u= 160 kPa instantaneously, simulating a sudden blockage of the drainage. The change in the vertical diameter is 0.14 mm whereas the change in the horizontal diameter is 0.15 mm. Both vertical and horizontal changes build up in the first 50 days and then remain constant until the end of the stage. The application of the external water pressure behind the tunnel lining induced a vertical tunnel ovalisation, as the distance of the lateral sides is decreasing, and the crown seems to experience some compression (Figure 6.12a). This behaviour is consistent with the observational data. However, the change in tunnel diameter develops quickly (i.e. within 50 days) and the magnitude is very small (0.2 mm) compared to that detected from conventional measurements.

The further reduction of the tunnel lining stiffness as well as the assumption of the tunnel lining being fully permeable induced an inwards convergence of the lining, as a reduction of both vertical and horizontal distances is observed, with a greater vertical convergence compared to the horizontal one (Figure 6.12b).

(a)

(b)
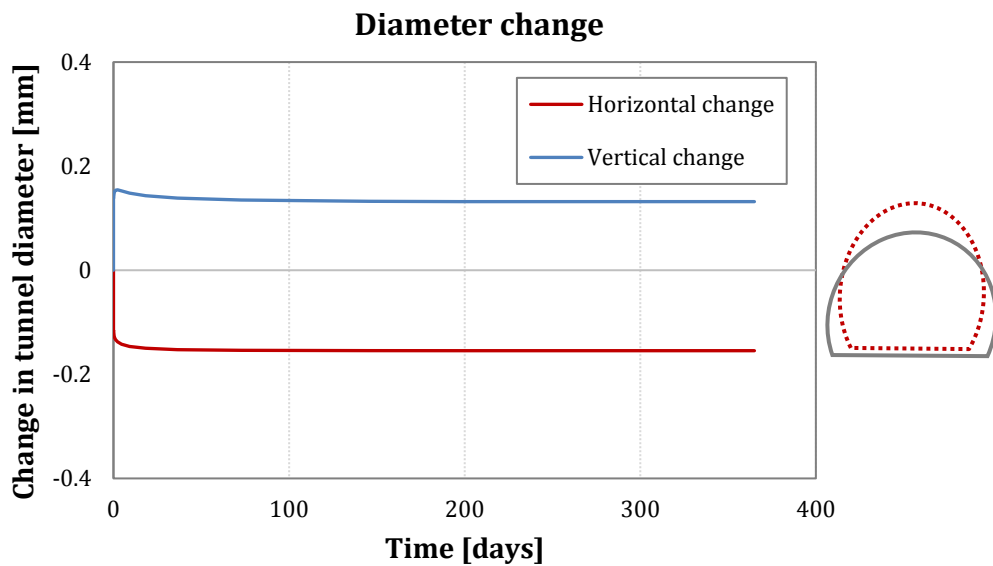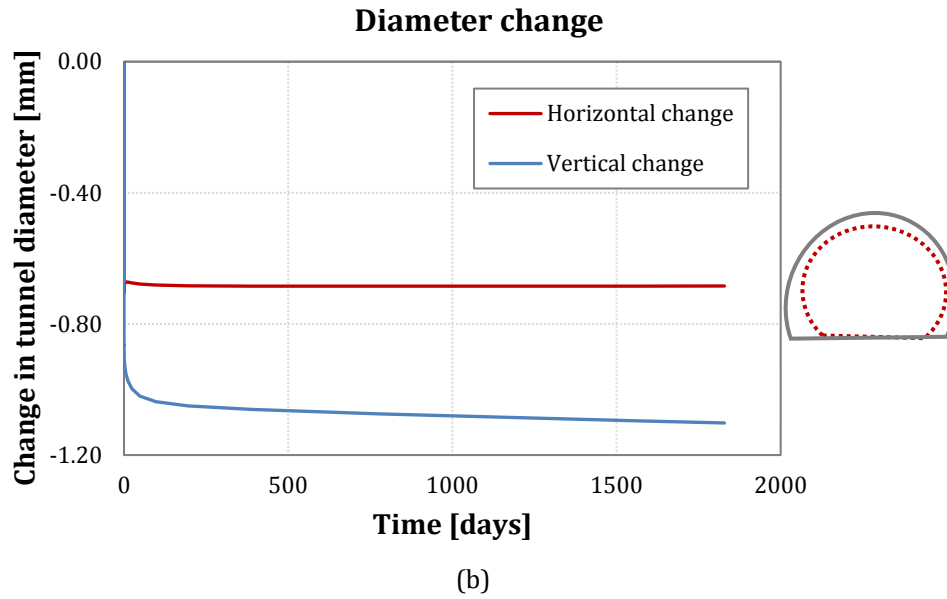
Figure 6.12. Change in tunnel diameter during (a) the application of the external pore pressure behind tunnel lining (u= 160 kPa) and (b) reduction of tunnel lining stiffness from 15 GPa to 5 GPa.

Tunnel lining stress

From the computed FE results, both bending moments and hoop thrusts along the tunnel lining are analysed.

In order to validate the computed results with the FO strain profile, the adopted method is based on calculating the total strains at the intrados of the lining, resulting in a sum of axial strains ε_a and bending strains ε_b (Eq. 6.1):

$$\varepsilon_{total} = \varepsilon_{axial} + \varepsilon_{bending} \tag{6.1}$$

The axial strains ε_a can be calculated from the axial forces, directly extracted from ABAQUS for each beam element along the lining. However, obtaining the bending strains from the FE environment is troublesome, as the results show a zig-zag pattern. This might be due to the relatively small magnitudes of computed bending strains. Therefore, the bending strains are evaluated from the theoretical relation between the bending moment and the curvature on the basis of the beam theory, as expressed in Equation 6.2. To compare with the actual measurement, the resulted bending strains on the tunnel intrados are then equal to the distance from neutral axis times the curvature (Eq. 6.3).

$$M = EI \cdot \chi \tag{6.2}$$

$$\varepsilon_{bending} = \frac{M}{E \cdot I} y = \chi \cdot \frac{d}{2} \qquad (6.3)$$

where:

- M is the bending moment in the beam;

- E is the elastic modulus of the beam material;

- I is the second moment of inertia of the beam;

- χ is the beam element curvature;

- y is the distance from the neutral axis of the beam;

- d is the lining thickness.

To measure the bending strains experienced by the lining, the procedure implies the calculation of the radius of curvature (ROC) along the lining, as the ROC is equal to the inverse of the beam curvature (ROC = 1/ χ). The adopted method is commonly used by design practice (Wilcock, 2017). The ROC can be determined by fitting a circle between three consecutive data points (i.e. beam nodes), by finding the centre of the fitted circle which, hence, enables the calculation of the ROC (Figure 6.13) (Wilcock, 2017; Alhaddad, 2017). By knowing the coordinates of three points connected through a chord (Figure 6.13), the centre of a circle can be obtained by intersecting perpendicularly the two halved distances between data points along lines a and b (Wilcock, 2017). Therefore, the curvature was evaluated for the various calculation phases by considering the horizontal and vertical displacements (u_1 and u_2) performed for the lining nodes with time, with a total of 56 tunnel lining nodes along the tunnel boundary (from the left invert side to the right invert, without considering the tunnel floor).
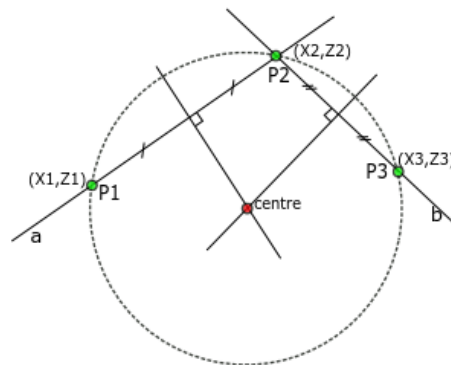

Figure 6.13. ROC (radius of curvature) calculation (Wilcock, 2017).

It is important to clarify that this approach for evaluating the bending strains experienced by the tunnel lining is based on various assumptions. Firstly, the lining was modelled by using 3-node beam elements, which are sharing nodes with the surrounding ground. Secondly, to improve the performed magnitudes of bending strains, the distance *y* (Eq. 6.3) was considered as the sum of the distance from the central axis (d/2) plus the thickness of secondary lining, leading to larger bending strains along the tunnel lining intrados (Figure 6.14b). Lastly, the computed total strains were compared with the strains experienced by the optical fibre, which was attached to the lining through discrete drilled hooks (Figure 6.14a), leading to the evaluation of a strain within the gauge-length. Hence, the computed results obtained from the mentioned method may not be very accurate for assessing the bending moments at the tunnel lining, albeit it was the only approach to adopt within the framework of FE environment. Additionally, such endeavour of comparing the strain development through FE modelling and the strain profile obtained from DFOS sensors was not encountered in previous works that involved the monitoring of tunnels using DFOS technologies (Mohamad, 2008; Gue et al., 2015).

Therefore, further investigations in the evaluation of bending strains along the lining may be addressed in future research for more accurate prediction of the magnitudes of bending moments.
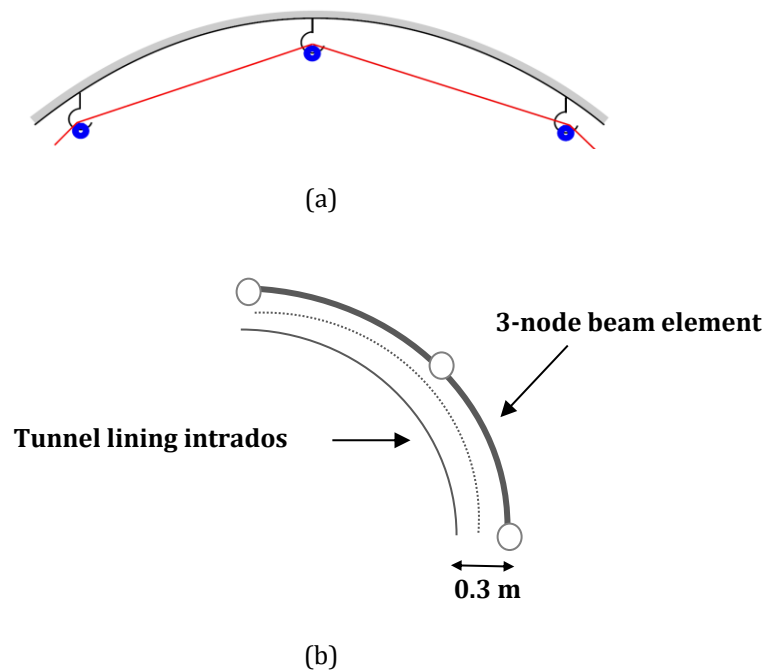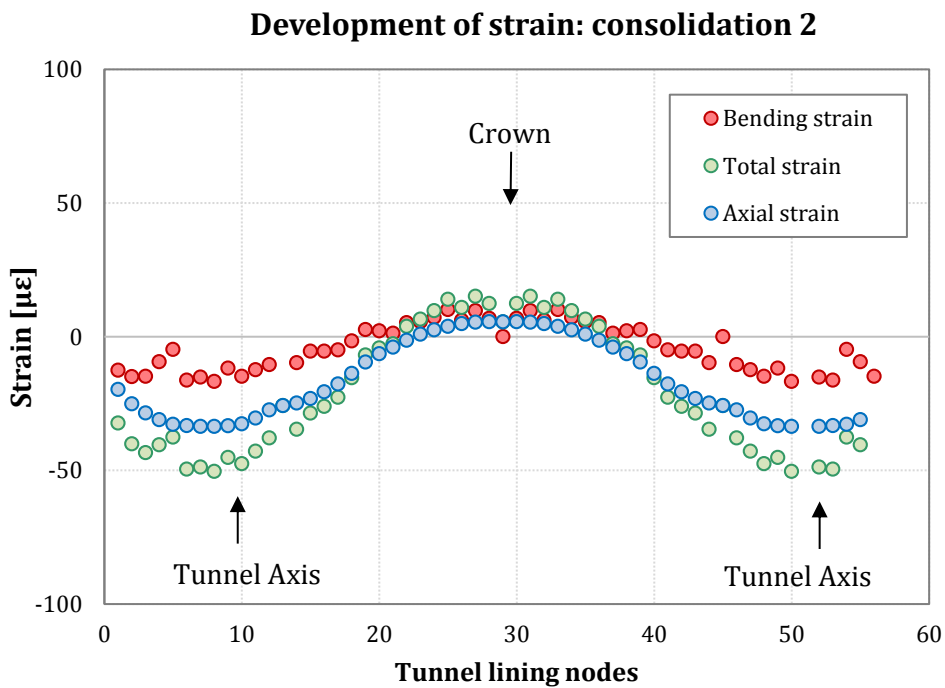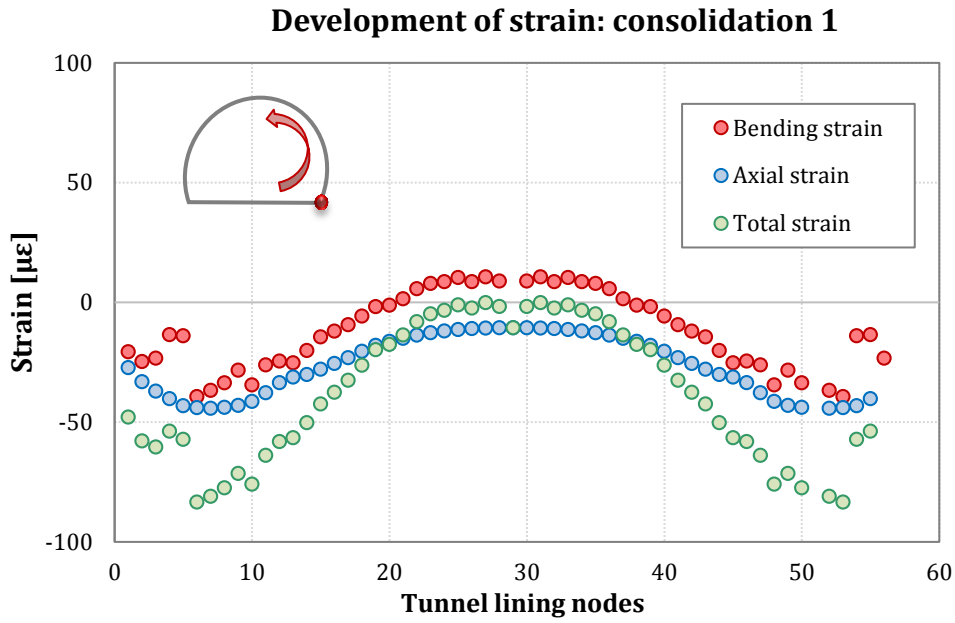

(a)

(b)

Figure 6.14. (a) Schematic of the method of attaching the optical fibre to the tunnel lining through discrete hooks (Di Murro et al., 2016) and (b) modelling of tunnel lining.

The development of strains around the tunnel lining is plotted against the tunnel lining nodes at various calculation stages. Figure 6.15 shows the bending, axial and total strains along the tunnel lining, where the horizontal axis corresponds to the nodes around the tunnel lining starting from the right bottom invert in the anticlockwise direction. Therefore, the two ends of the x-axis refer to the two invert sides of the cross-section, whereas the middle section refers to the tunnel crown.

As the soil consolidates after tunnel construction, the axial strains are larger than the bending strains. The bending strains are negative values at both tunnel spring lines and positive values at the tunnel crown (i.e. tunnel squatting) as shown in Figure 6.15a. Some anomalous fluctuation in the data is observed at both sides of tunnel invert.

The total strains are 80 µε and 2 µε at the tunnel axis and the tunnel crown respectively during the first year of consolidation (Figure 6.15a), whilst values of 50 µε and 12 µε are recorded when the tunnel lining stiffness is reduced to 15 GPa for the further 40 years of consolidation, with both axial and bending strains exhibiting negative strains at the tunnel axis level and positive strains at the tunnel crown, indicating a squatting tunnel lining deformation mode (Figure 6.15b). As the external water pressure of 160 kPa is applied to model the drainage blockage, the tunnel lining deforms with a vertical elongation shape. Positive total strains of 12 µε and negative total strains of 25 µε are recorded at both the tunnel sides and at the tunnel crown respectively, with the development of larger axial strains compared with the bending strains along tunnel lining, as shown in Figure 6.15c. Moreover, the reduction of the tunnel lining stiffness from 15 GPa to 5 GPa caused the development of small bending moments and large compressive axial loads, resulting in inwards tunnel lining convergence, as shown in Figure 6.15d.

Development of strain: consolidation 1

(a)

Development of strain: consolidation 2

(b)

Development of strain: pore pressure application

(c)

Development of strain: E reduction

(d)
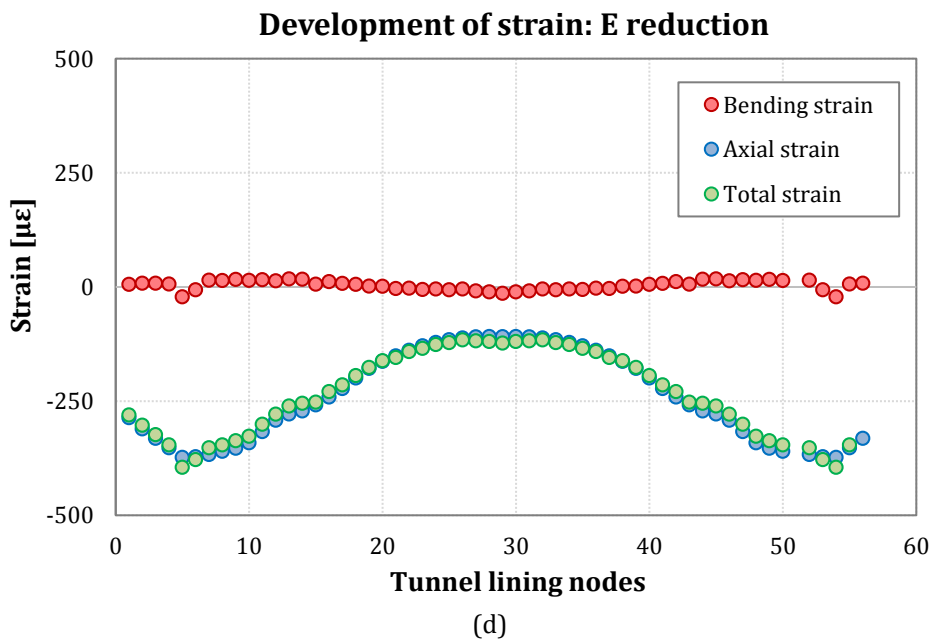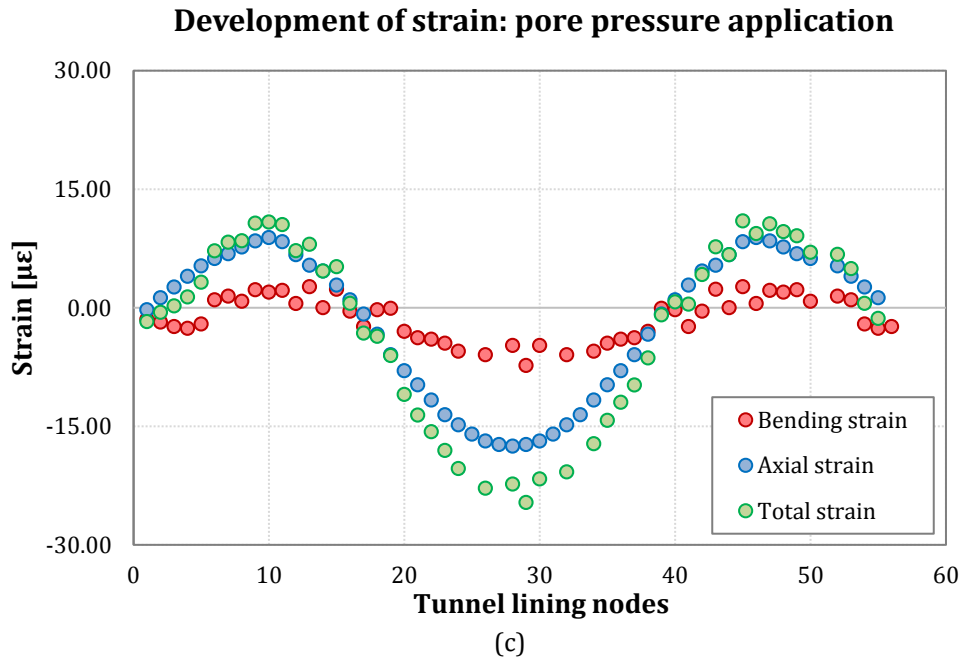
Figure 6.15. Development of strains at tunnel lining during (a) Consolidation 1 (one year after construction), (b) Consolidation 2 (40 years after construction), (c) Consolidation 3 with the application of pore pressure u= 160 kPa and (d) Consolidation 4 with the tunnel lining stiffness E reduction from 15 GPa to 5 GPa and tunnel lining fully permeable.

6.5.2 Scenario 2: tunnel lining thickness d reduction

This section describes the computed lining performance by changing the lining geometry. Therefore, the influence of bending stiffness (EI) of the lining was investigated by keeping the elastic modulus E constant and by reducing the thickness

d of the beam section, since concrete structural elements may resist axial load but not bending when subjected to cracks. For a rectangular beam section of base *b* and height *d* (lining thickness), the reduction of the Moment of inertia about the x-axis I_x ($bd^3/12$) would be larger than the reduction of the cross-sectional area A (b·d). Therefore, three calculation phases were defined, by assuming a constant value of E = 20 GPa and a reduced lining thickness (d= 0.12 m) in the last stage, as shown in Table 6.3.

Table 6.3. Calculation phases for scenario 2.

| Calculation stage	Time period	Young's modulus E [GPa]	Pore pressure at tunnel lining u [kPa]	Thickness at tunnel lining d [m]
Consolidation 1	41 years	E=20 GPa	u=0 kPa	d=0.3 m
Consolidation 2	1 year	E=20 GPa	u= 160 kPa	d=0.3 m
Consolidation 3	4 years	E=20 GPa	u=0 kPa	d=0.12 m

The change in the tunnel diameter for scenario 2 is shown in Figure 6.16. During the consolidation after tunnel construction (Figure 6.16a), the change in the vertical diameter decreases with time, reaching around 1 mm at the end of the consolidation time, whereas the horizontal diameter increases to 0.23 mm (Figure 6.16a). The application of the external pore pressure of 160 kPa caused a small change in tunnel diameter in both horizontal and vertical directions (Figure 6.16b), whereas the reduction of lining thickness to 0.12 m induced a convergence inwards movement of lining, with large negative horizontal and vertical diameter changes (i.e. -1.4 mm and -3.85 mm respectively), as shown in Figure 6.16c.

However, the change of lining cross-sectional properties (i.e. reduction of thickness) simultaneously to the change of lining permeability (i.e. fully permeable) resulted in a compressive tunnel lining deformation mode not compatible with that observed in the field, which showed a bending mode.

The development of strain along the tunnel lining at various calculation phases confirmed the deformation mechanism described above, as shown in Figure 6.17. Negative axial and bending strains develop at the tunnel axis level during the first year of consolidation, with the axial strains being more significant than the bending ones (almost doubled in magnitude), whereas positive bending strains develop at

the tunnel crown (i.e. around 13 µε) compared to the negative axial strains (around -14 µε), as shown in Figure 6.17a.

When the external pore pressure of 160 kPa is applied on the lining, comparable magnitudes of positive axial and bending strains develop at tunnel axis level (around 5 µε), whereas slightly larger axial strains (around 17 µε) are observed at the tunnel crown compared to the bending strains (approximately 10 µε), as shown in Figure 6.17b. The tunnel lining undergoes high strains when its thickness is reduced (Figure 6.17c). Yet, the development of negative compressive strains is computed, indicating that the tunnel may converge inwards in both vertical and horizontal directions (Figure 6.17c).
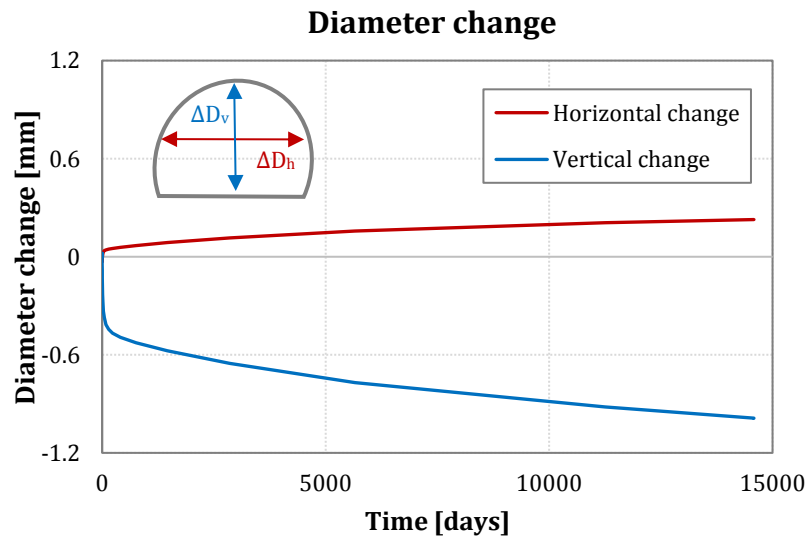
(a)
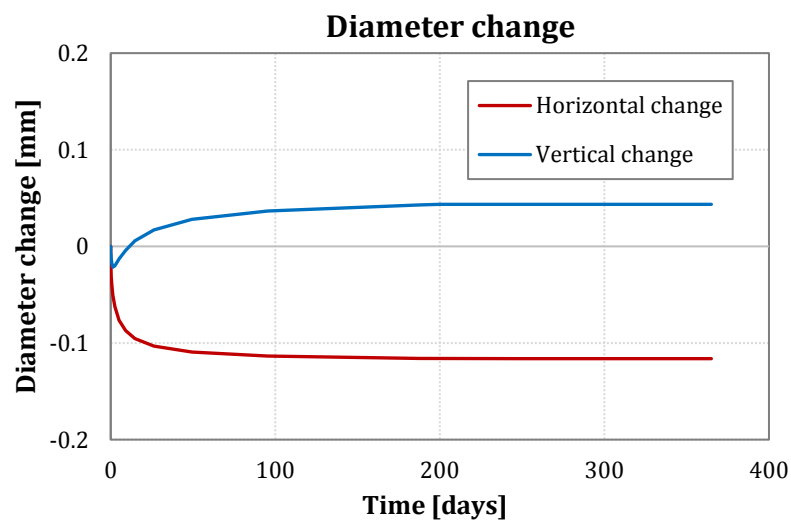
(b)
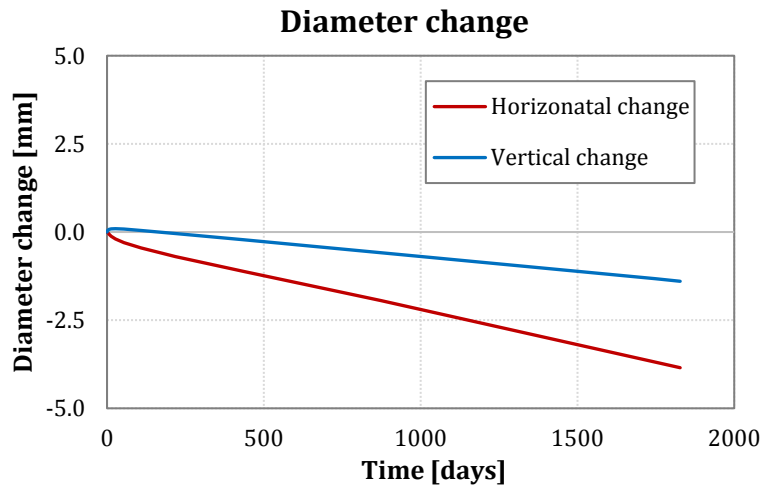
(c)

Figure 6.16. Change in tunnel diameter during (a) Consolidation 1 stage, (b) Consolidation 2 with the application of pore pressure u= 160 kPa at tunnel lining and (c) Consolidation 3 with the tunnel lining thickness reduction.
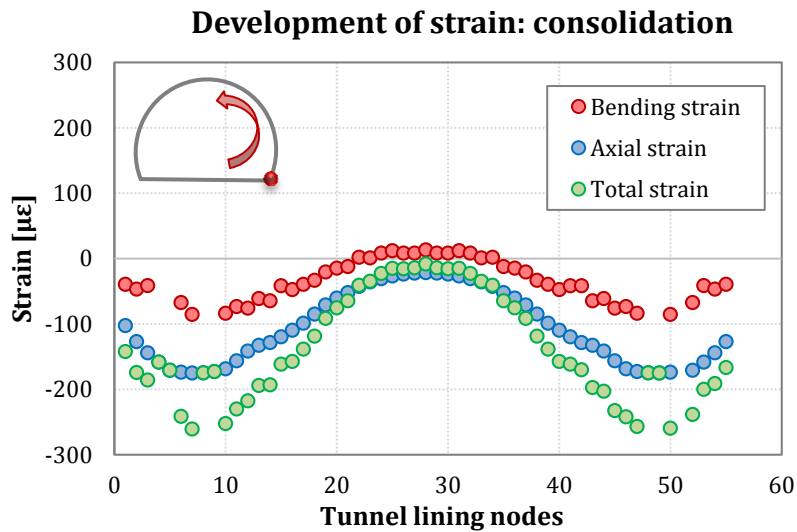
(a)
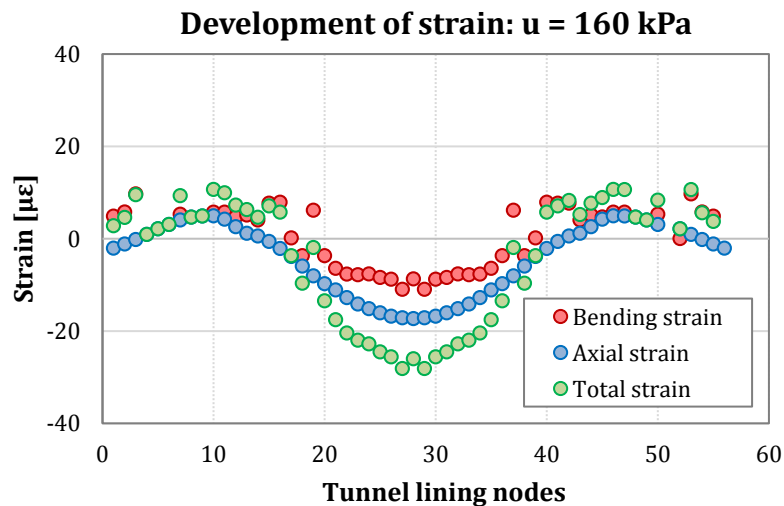
(b)
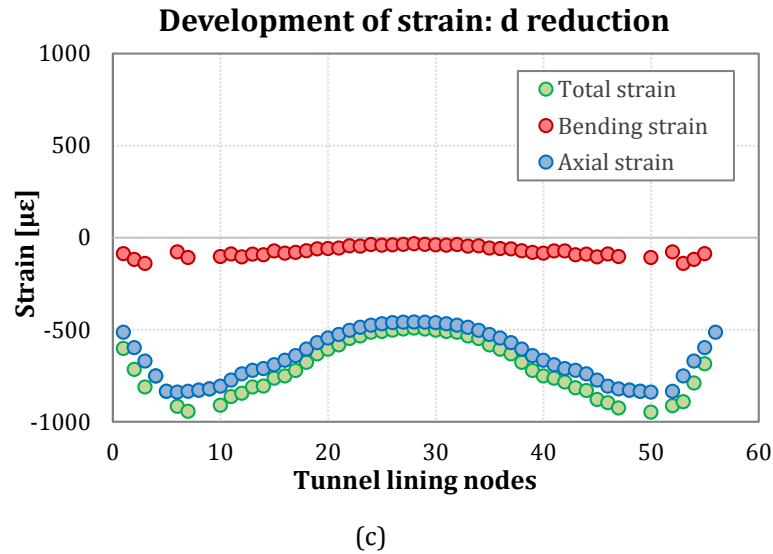
Figure 6.17. Development of strain at tunnel lining during (a) Consolidation 1 (u= 0 kPa), (b) Consolidation 2 with the application of pore pressure u= 160 kPa at tunnel lining and (c) Consolidation 3 with the tunnel lining thickness reduction and tunnel lining fully permeable.

6.5.3 Discussion

The different outcomes obtained from the two simulations with the reduced lining stiffness (*scenario 1*) and a reduced tunnel lining thickness (*scenario 2*) were examined in order to get the best match with the field measurement data. The discussion made can be explained as follows.

After simulating the blockage of the tunnel drainage system, both scenarios involved the modelling of a calculation phase where the pore pressure at the tunnel boundary is brought back to the initial condition (i.e. zero kPa), particularly during the consolidation 4 stage and the consolidation 3 stage for *scenario 1* and *scenario 2* respectively. This assumption led to the development of compressive strains along the lining as a mechanism of deformation, which is not in agreement with the bending deformation mode observed on site.

Also, the assumption of applying a water pressure of u= 160 KPa on the tunnel lining to simulate a sudden blockage of the drainage system may not be appropriate, as no records of pumping the drainage water were found, and therefore the water pressure may be gradually building up. The shape of the total strain profile computed when the external water pressure is applied (i.e. compressive strain at the tunnel crown and tensile strain at the tunnel axis level) seems to be compatible with field measurements. However, the computed magnitudes (e.g. 10 με at the tunnel axis

level and 28 με at the tunnel crown) are much smaller compared to those recorded by the instrumented tunnel targets.

The hypothesis of a reduced lining thickness in the last step of *scenario 2* produced the development of larger displacements and, therefore, more significant strains were computed along the lining. Nevertheless, the simultaneous intake drainage condition in this step (pore pressures equal to 0 kPa at the tunnel perimeter) lead to a tunnel lining mechanism of deformation not in agreement with the field data.

The main findings from these series of simulations suggest that the computed magnitudes of strains and displacements were improved by reducing the lining thickness, whereas the application of the water pressure on the outer edge of the tunnel lining produced a tunnel deformation shape profile similar to that observed in the field.

6.5.4 Scenario 3

According to the findings aforementioned, the following assumptions have been made in order to assess the tunnel behaviour during ground consolidation and long-term lining conditions:

i)   A reduced and a constant value of elasticity modulus E of the tunnel lining was assumed throughout the FE simulation. Due to lack of tunnel as-built properties and considering that during tunnel construction concrete properties might change due to long-term effects for sprayed concrete linings (BTS, 2004), the assumption of reducing the lining stiffness E seems to be appropriate.

ii)   The short and long-term loading conditions for the final concrete lining involved a reduction of the thickness of lining (d= 0.12 m), as a reduced value led to smaller bending stiffness values EI of tunnel beam elements due to the reduction of the Moment of Inertia I, which is equal to $bd^3/12$ for a rectangular beam section, resulting then in the development of higher bending strains of beam elements, as shown previously in the Eq. 6.3. The imposed hydrostatic water pressure on the concrete lining simulated the long-term build-up external pressure due to the reduced capacity of the drains (i.e. clogging of drains).

Each simulation assumed the water table located at ground surface, acting hydrostatic with depth. Additionally, the water pressure around the tunnel lining increased gradually in order to simulate the gradual clogging of the drainage system.

The effectiveness on how a tunnel acts as a drain depends on the permeability of the tunnel lining and the immediately surrounding soil. In the Jubilee Extension Line (JLE), data showed that most of the tunnels were visibly wet to varying degrees, supporting that tunnels in London Clay act as a drain (Harris 2002). Furthermore, Mair (2008) also observed that the pore pressures were almost zero around tunnels in London Clay. Further studies highlighted the importance of relative permeability between the tunnel lining and the surrounding ground by proposing a coefficient RP for determining the tunnel lining drainage condition (Wongsaroj 2005; Laver 2010).

However, the manifestation of extreme weather circumstances may lead to the deterioration of the tunnel drainage system, such as clogging of drain pipes, causing a build-up water pressure on the lining acting as an external water load around the tunnel. As the drainage system reduces its capacity with time, the numerical investigation will consider a gradual increase of water pressure behind tunnel lining with time (instead of imposing it instantaneously at the beginning of the phase as implemented for scenario 1 and scenario 2). The magnitude of the mentioned pore pressure was investigated by fitting the field data measurements taken for a monitoring period of four years (2013-2017). Three different hydraulic pore pressures were investigated: (a) u= 197 kPa (i.e. water table at the interface with the moraine layer), (b) u= 230 kPa and (c) u=250 kPa. The mentioned pore pressures were gradually increased with time, by reaching the desired magnitudes (i.e. 197 kPa, 230 kPa and 250 kPa) within four years (2013 – 2017), as shown in Figure 6.18. A summary of the defined calculation phases is shown in Table 6.4.

Table 6.4. Calculation phases for scenario 3.

Calculation stage	Time period	Young's modulus E [GPa]	Pore pressure at tunnel lining u [kPa]	Thickness at tunnel lining d [m]
Consolidation 1	40 years	E=10÷5 GPa	u=0 kPa	d=0.12 m
Consolidation 2	4 years	E=10÷5 GPa	u= 197 kPa	d=0.12 m
Consolidation 3	5 years	E= 5 GPa	u= 387 kPa	d=0.12 m

It should be noted that the maximum hydrostatic load at the considered tunnel depth would be equal to 387 kPa, with the water table located at ground surface (u= $\gamma_w \cdot$ z = 10·38.7= 387 kPa), making the tunnel drainage fully clogged and impermeable. Therefore, in order to predict the tunnel lining deformation in case of occurrence of the maximum hydrostatic load behind the tunnel lining (i.e. u= 387 kPa), an additional phase was modelled. By assuming a linear interpolation of the computed data, if the hydrostatic load falls within the range of water pressures of magnitudes 197 kPa, 230 kPa and 250 kPa, then the maximum pressure load of 387 kPa would be reached within four years (i.e. year 2021), three years (2020) and two years (2019) respectively, as shown in Figure 6.18. Therefore, the uncertainties related to the prediction of the lining deformation would fall within the range of pore pressure 197÷ 250 kPa.
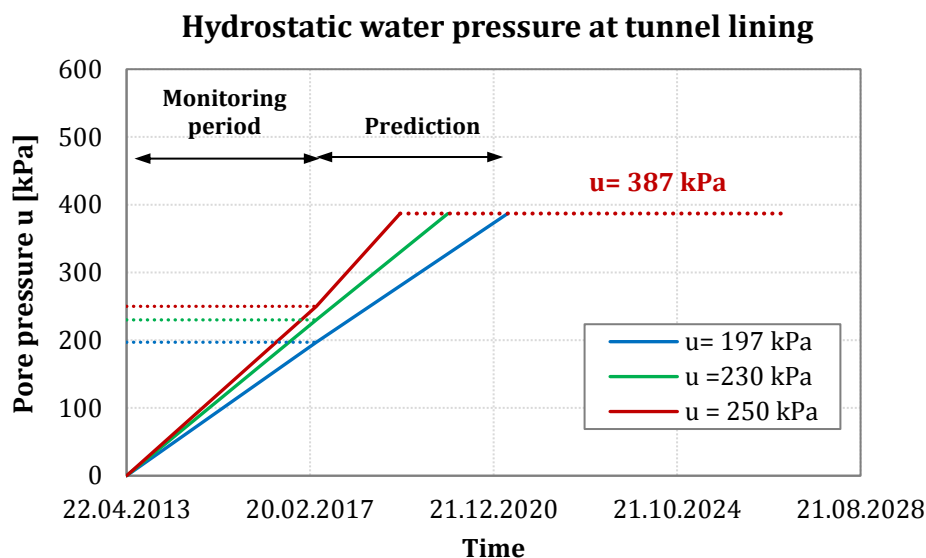
Figure 6.18. Hydrostatic water pressure behind tunnel lining.

The comparison between the computed changes in tunnel distances and field data is shown in Figure 6.19. It is noteworthy that the magnitudes of vertical and horizontal diameter changes are close to those measured in the field by total stations, albeit under a small range of hydrostatic pressures. Particularly, by applying a water pressure of 197 kPa behind the lining, the FE results match quite well both the change in the horizontal diameter at the tunnel axis level (Figure 6.19b) and the change in vertical distances (Figure 6.19a), but they underestimate the change in the horizontal distances at the tunnel shoulder location (Figure 6.19c). However, as the water pressure increases to 230 kPa and 250 kPa, the changes of horizontal and vertical tunnel diameter are overestimated. For this reason, the assumption of a hydrostatic pore pressure load on the lining to be as 197 kPa at the end of the monitoring period appears to best fit the observed data.

Further modelling of tunnel lining response under the maximum hydrostatic load of 387 kPa are shown in Figure 6.20. The lining at the tunnel axis level exhibits the largest horizontal diameter change, increasing of approximately one order of magnitude, reaching a value of -2.26 mm for the assumed pressures 197 kPa, 230 kPa and 250 kPa within 4 years, 3 years and 2 years respectively, as shown in Figure 6.20b. A similar increase has been predicted for the diameter change at the tunnel shoulder (Figure 6.20c), whereas the vertical diameter change has simply risen of 0.3 mm when subjected to u= 387 kPa (Figure 6.20a).

(a)

Change in horizontal distance: tunnel axis

(b)

Change in horizontal distance: tunnel shoulder
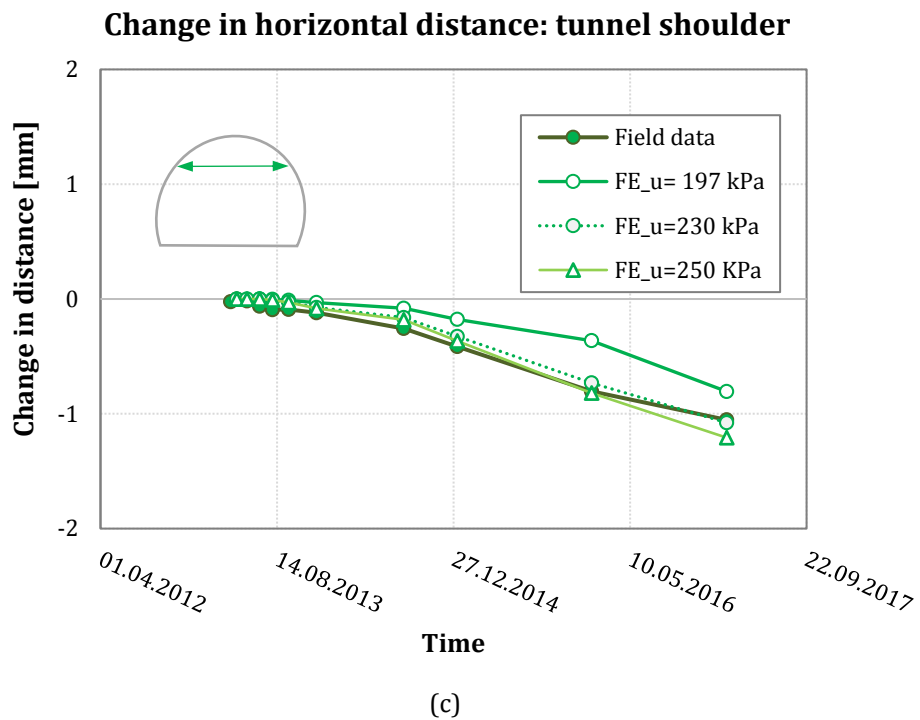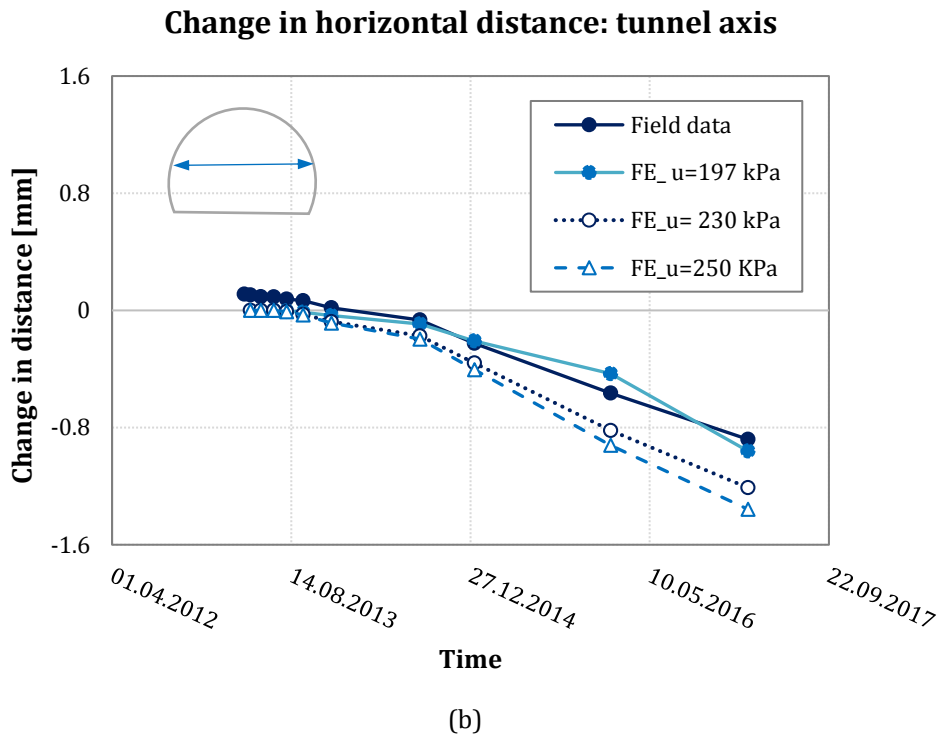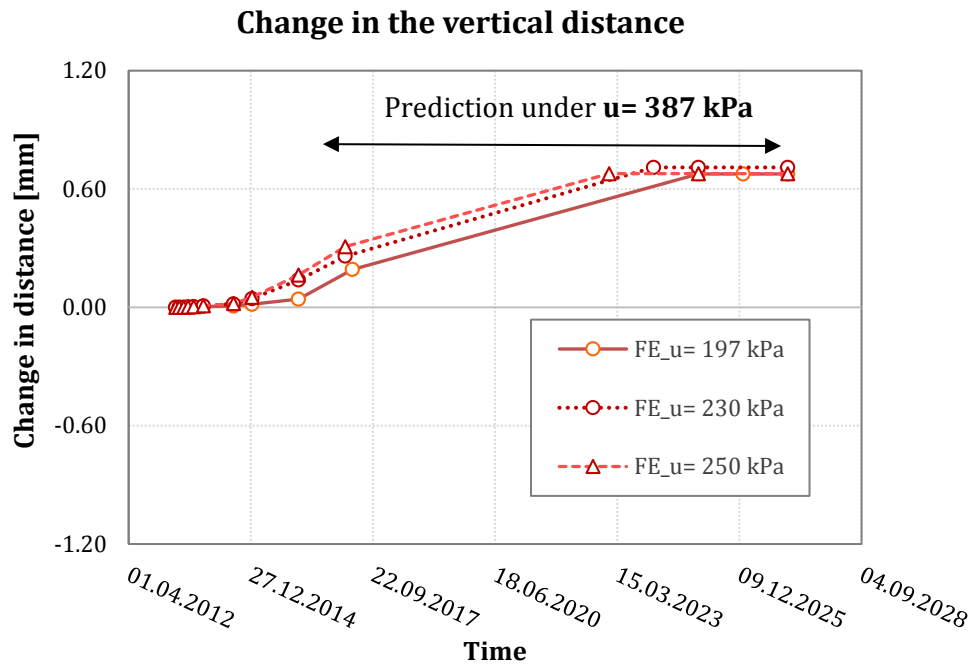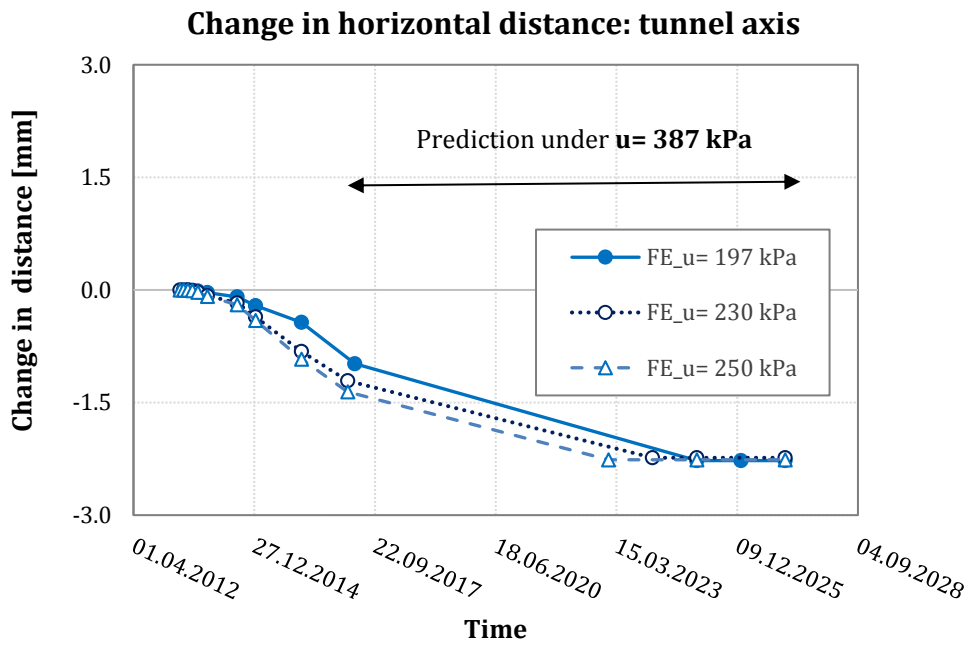

(c)
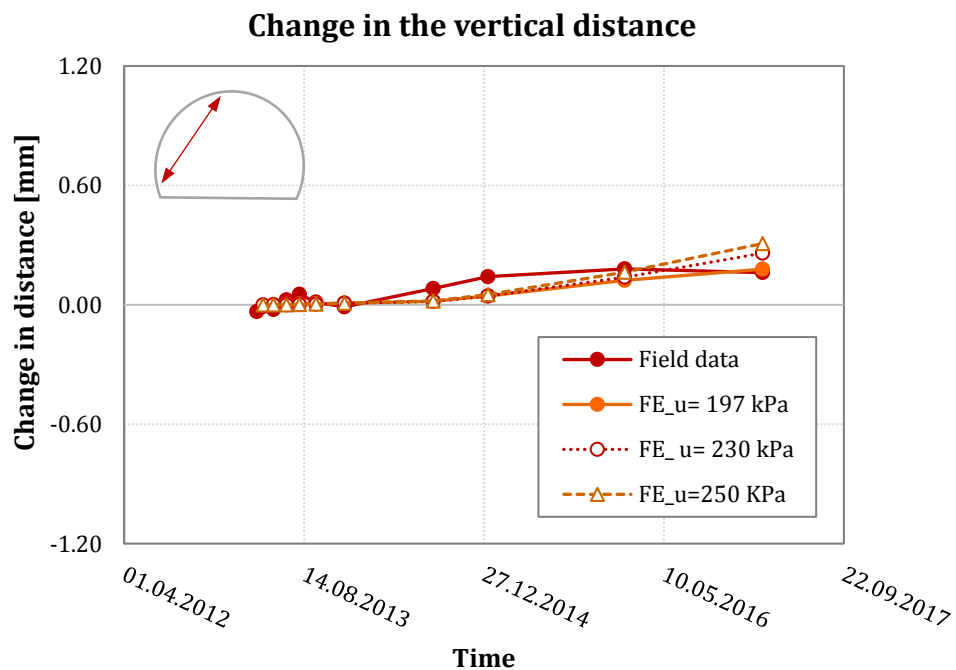
Figure 6.19. Evaluation of the hydrostatic water pressure at tunnel lining by fitting the field data: (a) change in vertical tunnel distances, (b) change in the horizontal distances at tunnel axis level and (c) change in the horizontal distances at tunnel shoulder level.

Change in the vertical distance

(a)

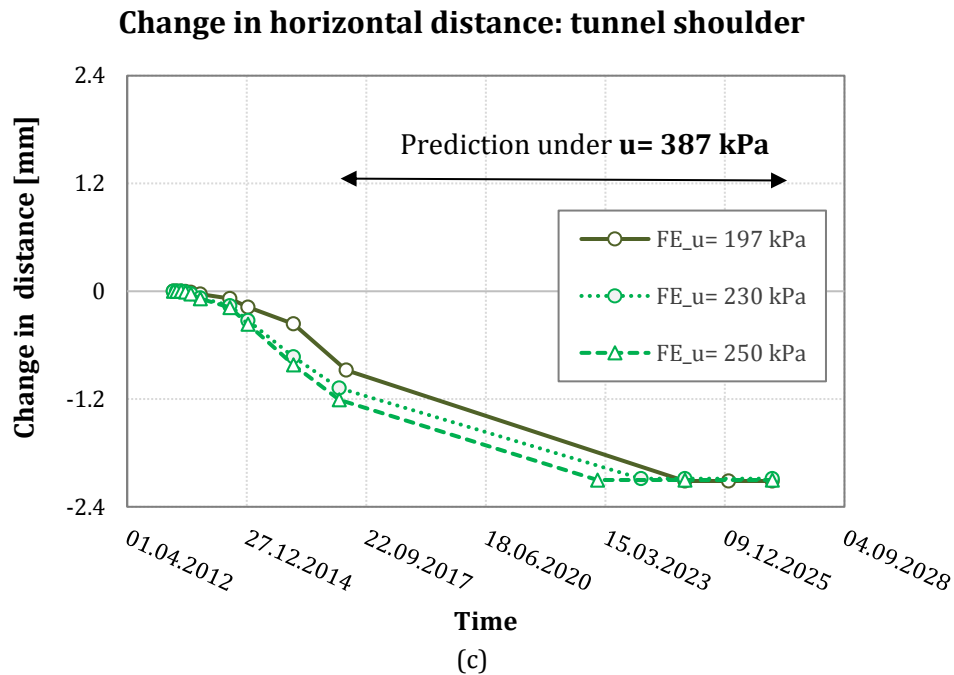**Change in horizontal distance: tunnel axis**

(b)

Figure 6.20. Predicted tunnel lining diametric change when the maximum hydrostatic water pressure of 387 kPa occurs: (a) vertical diameter change, (b) horizontal diameter change at tunnel shoulder level and (c) horizontal change at tunnel axis level.

A broad and accurate prediction of the tunnel lining response should also include the assessment of excess pore pressure generation during tunnel excavation and, hence, their dissipation with time.

When the tunnel lining is fully permeable, the pore water pressure would flow towards the tunnel causing the pore pressure around the tunnel to reduce. This reduction in pore water pressure causes an increase in ground effective stress with consequent soil consolidation. Hence, further surface settlement is expected in the long-term until a steady-state flow condition is reached.

The computed pore pressures around the tunnel are shown in Figure 6.21. The figure indicates that the FE model seems to compute negative pore pressures at the tunnel crown during tunnel construction (i.e. at the end of unloading stage I and stage II), as shown in Figure 6.21a and Figure 6.21b.

A fully permeable tunnel lining drainage condition (u= 0 kPa) is then performed during the consolidation stage (Figure 6.21c). Within a time of around 200 days, the ground consolidation seems to be completed, as no pore pressure changes are detected afterwards, which is related to the very stiff rock of the molasse region (Di Murro et al. 2018) (Figure 6.21d and Figure 6.21e). As a matter of fact, survey records

carried out in 1976 have shown that the bulk of the tunnel lining movements occurred soon after tunnel construction (CERN Survey, 1976). Parkin et al. (2002) also assessed that during the excavation of the USA15 cavern in the frame of the LHC project, convergence measurements and deformations were observed up to three years after construction.

Due to the change of flow regime around the tunnel (i.e. gradual blockage of the drainage), the water pressure on the tunnel lining was gradually imposed, reaching the predicted pore pressure of 197 kPa within 4 years (Figure 6.21i). It should also be noted that the pore pressures dissipation is noticeably influenced by the layering model within the molasse region, as it is characterized by different permeabilities, ranging from more permeable moraine layer going to the more impermeable marls and sandstones (Figure 6.21f).
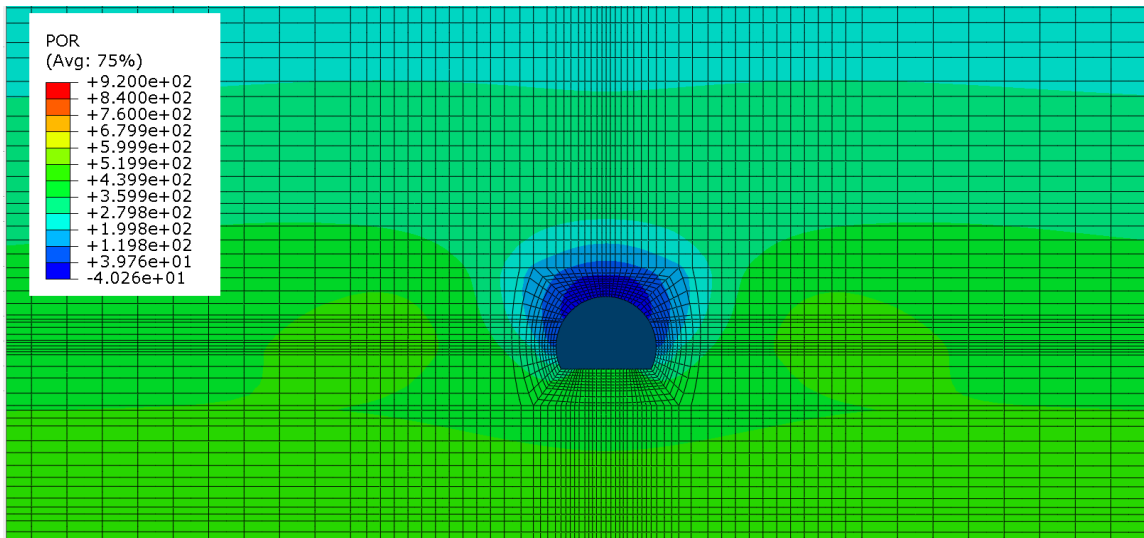
(a) end of unloading stage I (1 day)
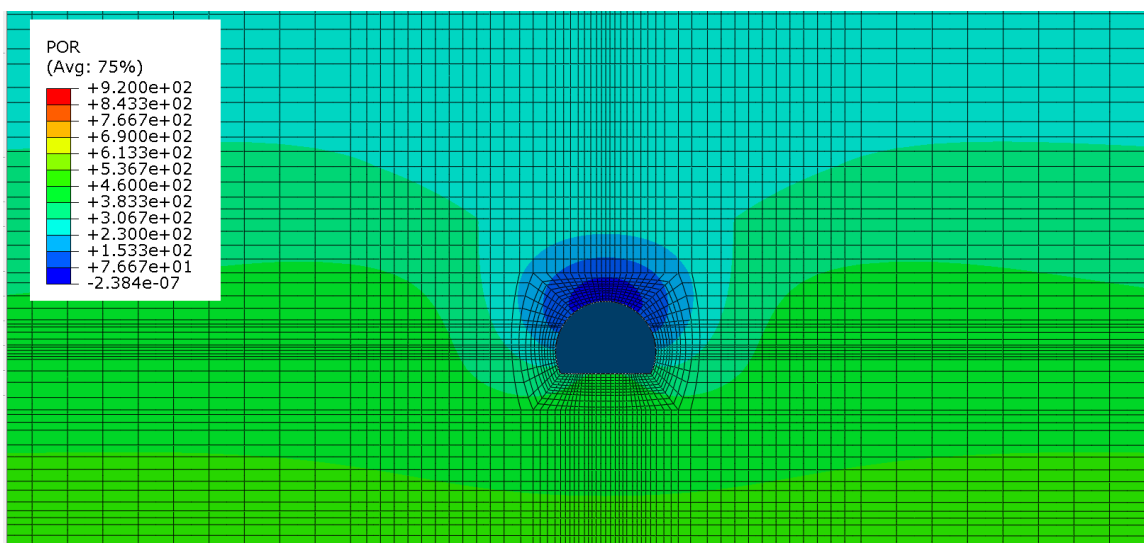
(b) end of unloading stage II (1 day)
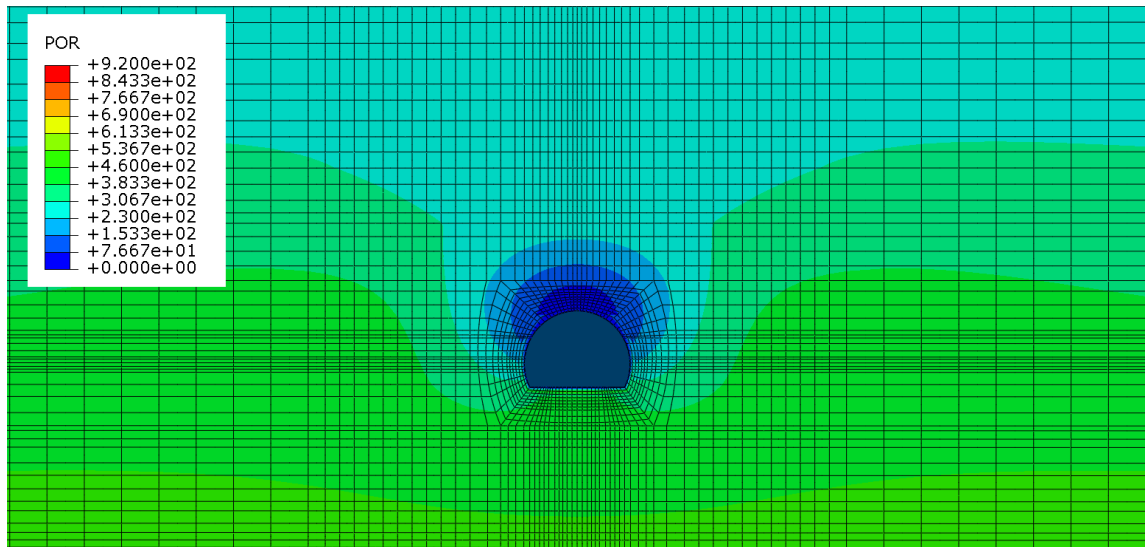
(c) t = 0 start of consolidation
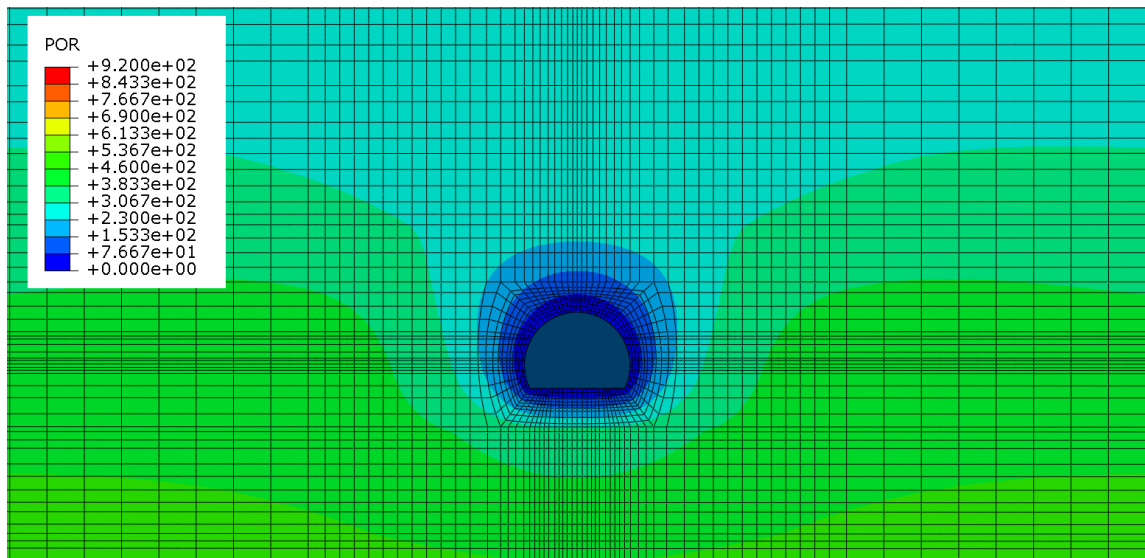
(d) 1 day of consolidation
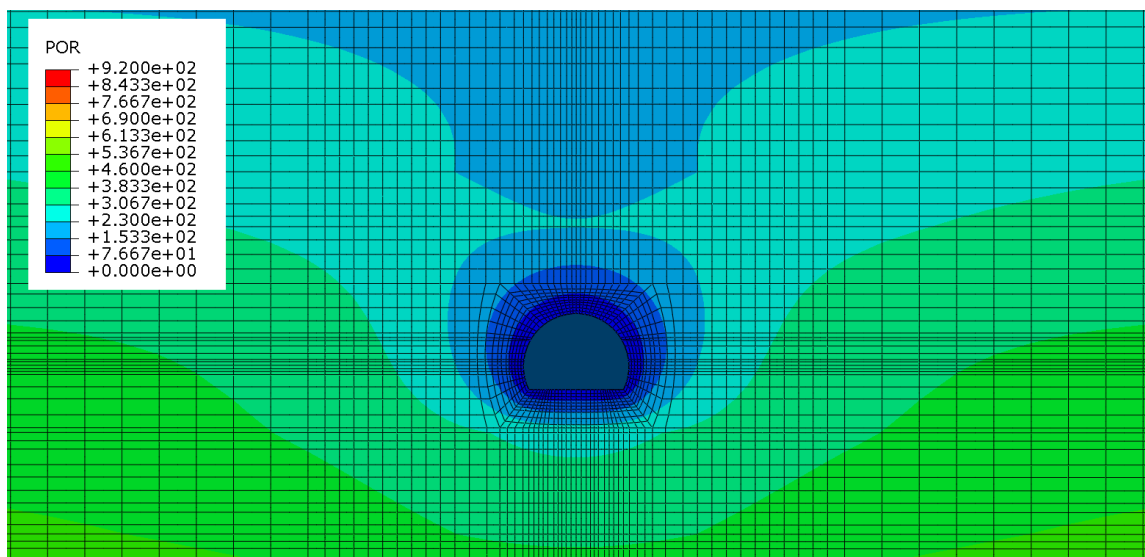
(e) 10 days of consolidation
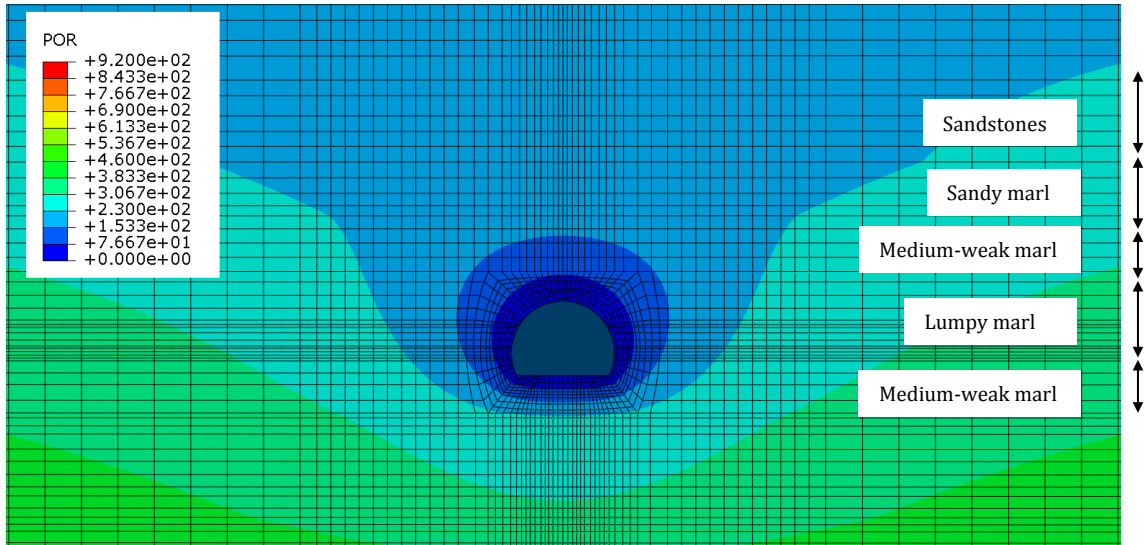
(f) 200 days of consolidation
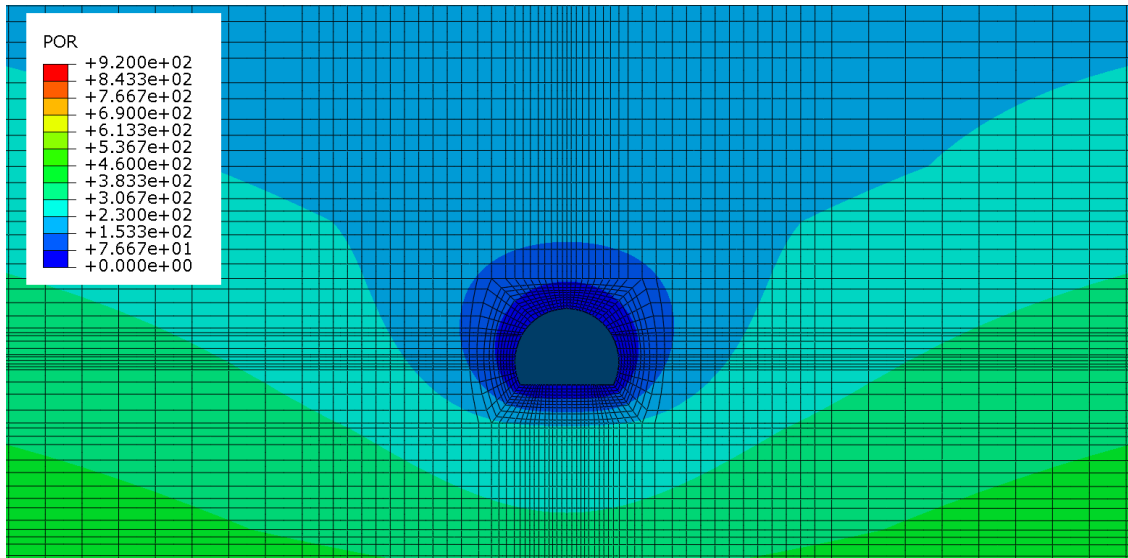
(g) 1000 days of consolidation
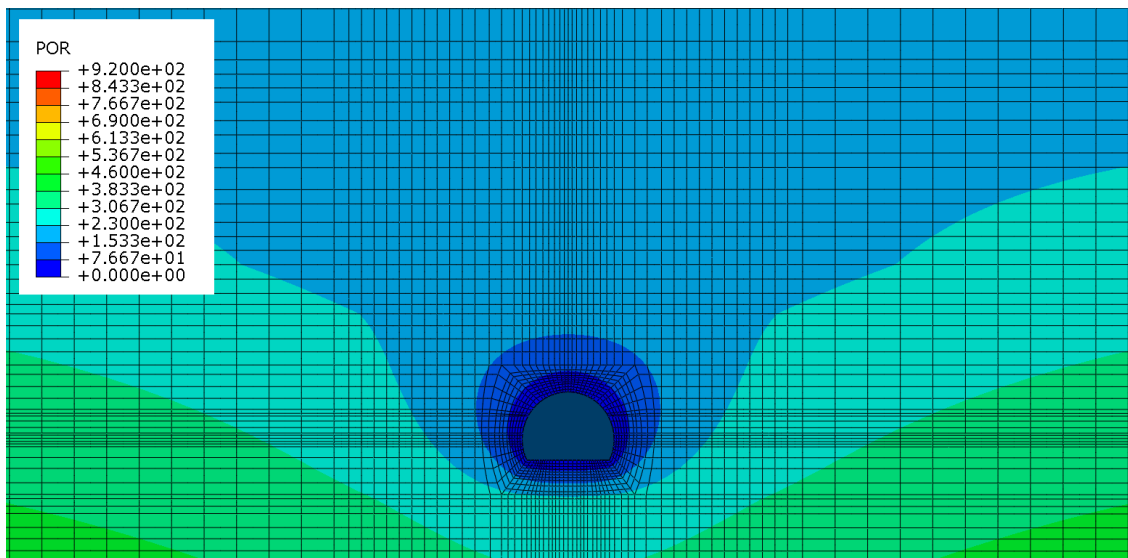
(h) 100 days after the application of u= 197 kPa
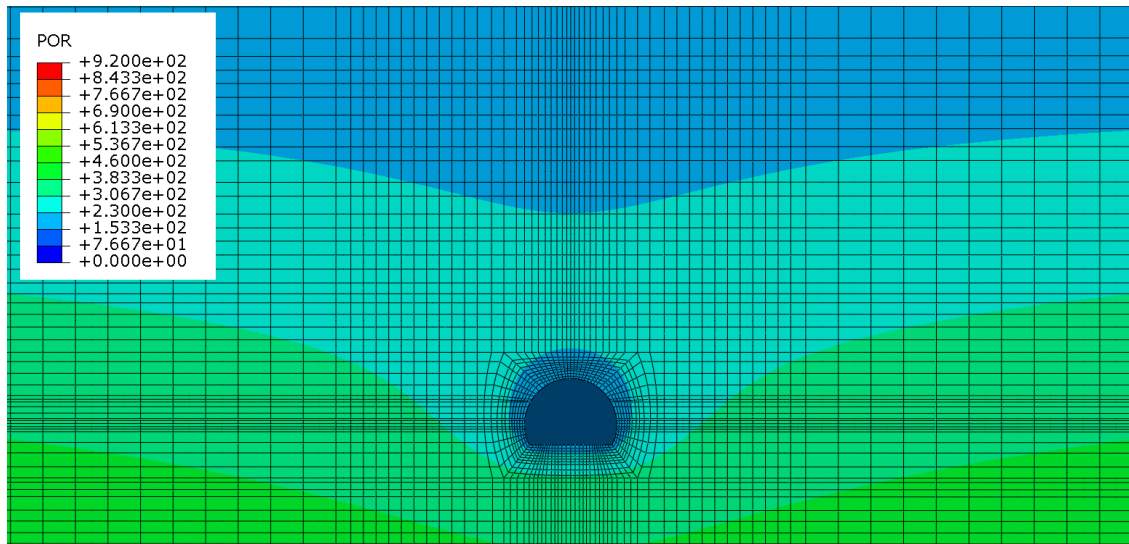
(i) 4 years (u= 197 kPa)

Figure 6.21. Pore pressure dissipation during: (a) unloading <u>stage I</u> of nodal forces, (b) unloading <u>stage II</u> of nodal forces, (c) ground consolidation at t= 0 (u= 0 kPa at tunnel lining), (d) consolidation at t= 1 day, (e) t= 10 days, (f) t= 200 days and (g) t= 1000 days and during the imposition of the hydrostatic water pressure u= 197 kPa at tunnel lining: (h) after 100 days and (i) after 4 years.

Figure 6.22a and Figure 6.22b show the change in tunnel diameter during the initial 40-year consolidation stage and during the imposition of the water pressure of 197 kPa on the outer edge of the lining (i.e. the end of the monitoring period), respectively. It can be noted that the vertical diameter change decreases with a rapid rate during the 40-year consolidation stage, reaching a maximum value of 5 mm, while the horizontal diameter increases of 0.76 mm, indicating a squatting deformation mode (Figure 6.22a). Also, when the pore pressure behind the lining builds up with time, both the vertical and horizontal diameter change linearly with a vertical tunnel elongation mechanism of deformation, as shown in Figure 6.22b. The horizontal diameter change increases gradually with time and a magnitude of - 0.63 mm is reached after one year, whilst the vertical change increases of 0.05 mm.

As mentioned before, the hydrostatic load of 197 kPa corresponds to the equivalent hydraulic pressure at tunnel depth z= 38.7 m if the water table is located at the interface with the moraine layer. However, the maximum hydrostatic load at tunnel occurs when the water table reaches the ground surface (u= 387 kPa). Therefore, after the application of u= 197 kPa, the water pressure at the tunnel lining boundary was increased up to the maximum value of 387 kPa, in order to predict the tunnel

lining behaviour under this condition as a possible future worst case scenario. Figure 6.22c shows the horizontal and vertical diameter change under this scenario.

The horizontal diameter change at tunnel axis level and shoulder increased by about 40%, reaching a value of around -1.3 mm compared to that computed in the previous phase (-0.93 mm), whereas the magnitude of vertical diameter change increased from a magnitude of 0.18 mm to 0.48 mm, as shown in Figure 6.22c.

(a)

(b)

(c)
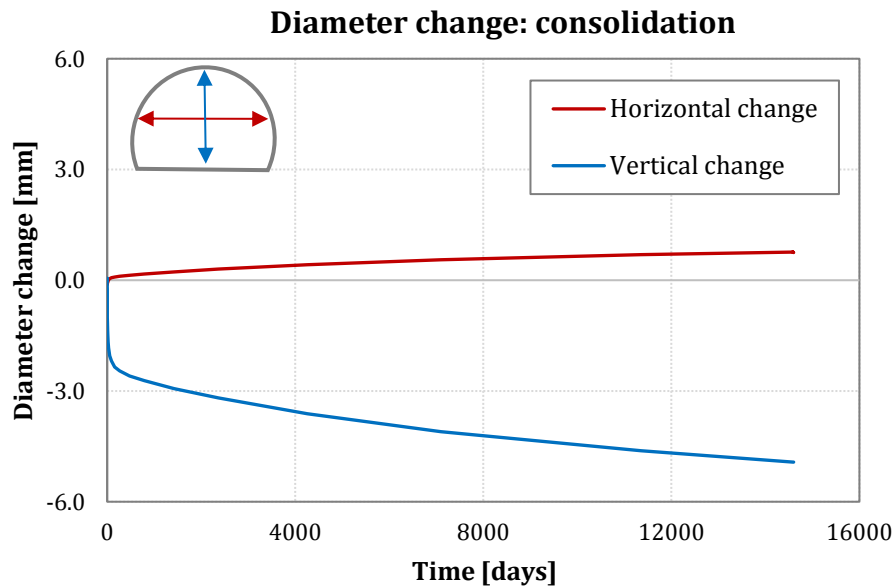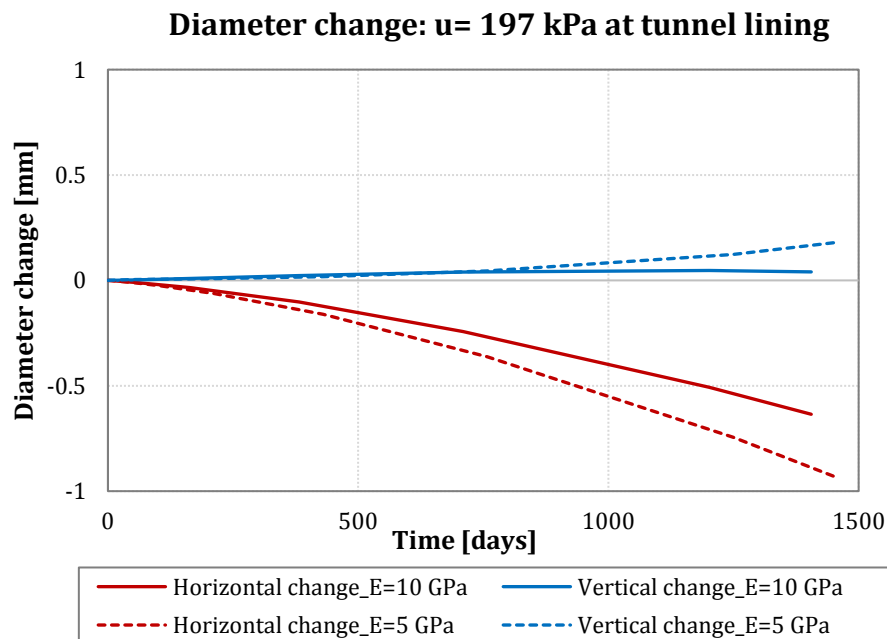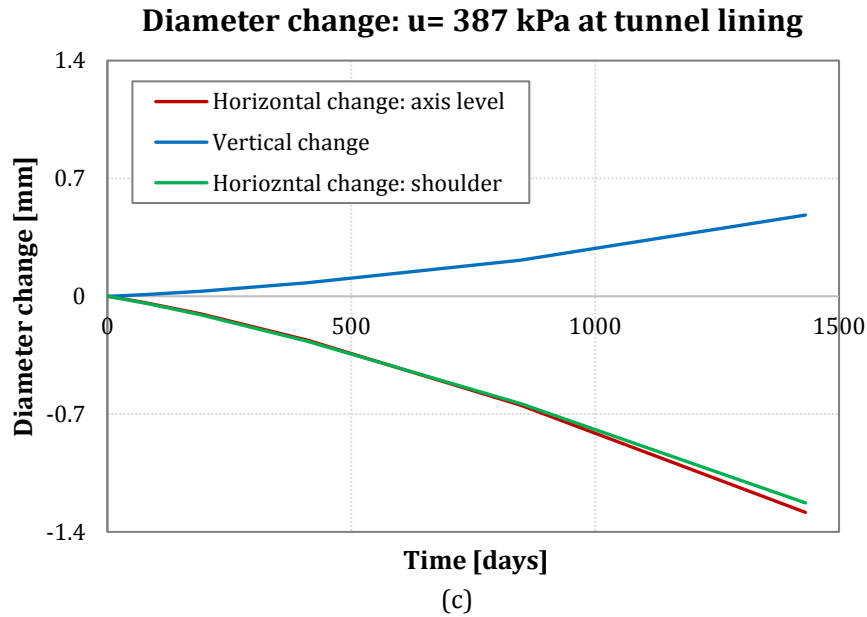
Figure 6.22. Change in tunnel diameter during (a) Consolidation 1, (b) Application of the external pore pressure u= 197 kPa and (c) long-term behaviour under u= 387 kPa at the tunnel lining (maximum hydrostatic load).

The development of bending and axial strains along the tunnel lining is presented in Figure 6.23. Figure 6.23a shows the strains computed at tunnel lining during ground consolidation. Compressive and tensile bending strains are observed at the tunnel axis level and the tunnel crown respectively, whereas larger axial strains developed along tunnel lining, by recording around -1000 με at tunnel axis and almost -200 με at the tunnel crown (Figure 6.23a). Large total strains were computed at the tunnel crown and tunnel axis when the lining is subjected to an external pore pressure of 197 kPa (Figure 6.23b). Comparison between total strains obtained by assuming the tunnel lining elasticity modulus E equals to 10 GPa and 5 GPa is presented in Figure 6.23b and Figure 6.23c respectively. The plots show a minor increase in total strains at the tunnel axis level by assuming E= 5 GPa, whereas substantial strains are recorded at the tunnel crown (i.e. 50 % increase) by assuming E= 5 GPa compared to the stiffer tunnel lining case (E= 10 GPa). Therefore, the assumption of a reduced stiffness value improved the computation of strains at the tunnel crown, which is located in the very weak lumpy marl, while the strains developed at the tunnel axis seem to experience only a small increase. This behaviour may be due to the fact that the tunnel at the crown is entirely placed in the lumpy marl layer, whereas the tunnel lining at axis level may be influenced by the stiffer medium weak marl layer surrounding the tunnel invert, characterized by a stiffness

modulus E' much larger than that of the very weak marl (almost 5 times larger), which may prevent the tunnel lining to deform.

Despite considering a smaller stiffness value for modelling the lining (Figure 6.23c), the computed total strains for the considered tunnel depth remain slightly smaller than those measured in the field. DFOS has measured noteworthy peak strains of magnitudes of around 580 με and 500 με at the tunnel crown and the tunnel axis respectively for tunnel circumferential loop 2-5, plotted in Chapter 4. However, the shape of the computed strain pattern of tensile and compressive strains at the tunnel axis and the tunnel crown respectively seems to be in agreement with the one observed with the FO sensors, suggesting the same tunnel lining mechanism of deformation (i.e. tunnel vertical elongation). It should also be noted that the computed horizontal and vertical changes in tunnel diameter match quite well with the observational data recorded by the total station measurements of Profile 4 shown in Chapter 3. In fact, by assuming a tunnel lining stiffness of 5 GPa, the vertical and horizontal diameter changes of -0.93 mm and +0.18 mm are computed respectively, compared to the magnitudes of -0.9 mm and +0.18 mm measured with the conventional monitoring tunnel bolts.

The discrepancy between the tunnel strains performed with the FE model and observational data may be caused by uncertainties of many factors, such as i) ground permeability anisotropy, as the assumption of $k_h/k_v \neq 1$ ratio (horizontal and vertical permeability ratio) showed larger squatting deformation during ground consolidation (Wongsaroj 2005), ii) the tunnel lining permeability, as the assumption of fully permeable or fully impermeable lining may not provide an accurate tunnel lining response due to localised seepage into the tunnel through cracks and tunnel joints, in addition to iii) the approach adopted for assessing the bending strains, as discussed before, which may provide less conservative values. The mechanical FO strain results do not account for any temperature change inside the tunnel, as no temperature FO cable was installed due to the quite stable environment. However, a potential change in the temperature of $\Delta T = 5$ °C would generate a strain change of approximately 100 με. Also, the change in groundwater regime due to heavy rainfall periods may induce some seasonal fluctuation in the data.

Development of strain: consolidation

(a)

Development of strain: u= 197 kPa

(b)

(c)
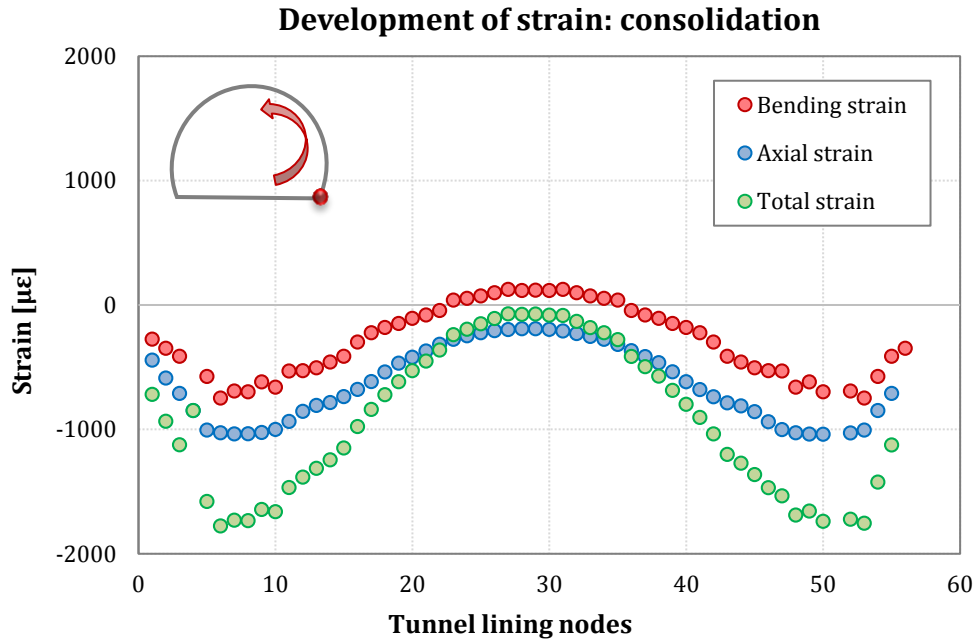
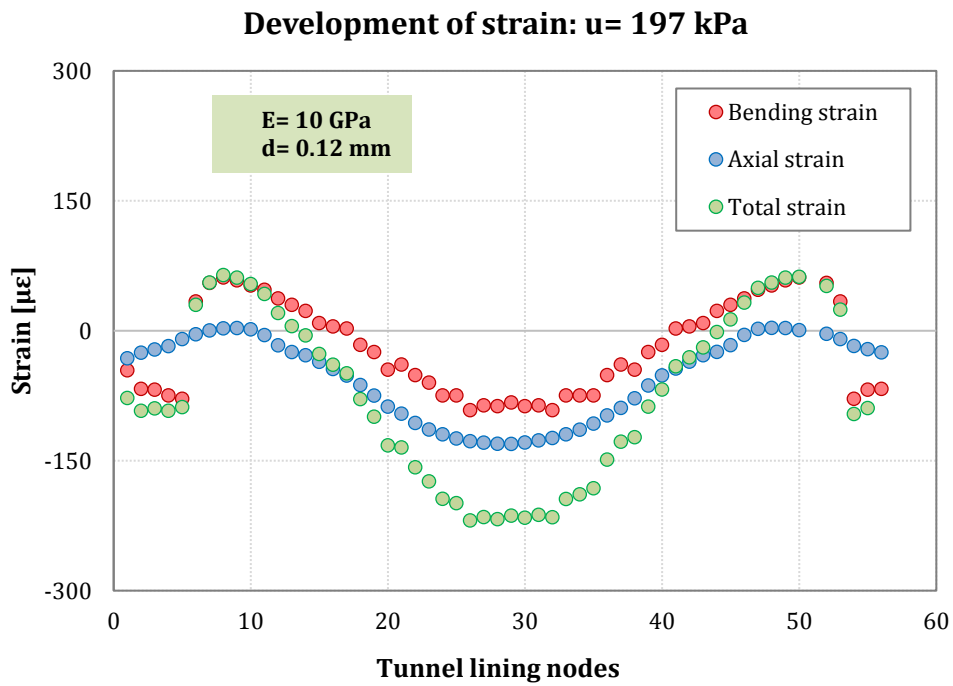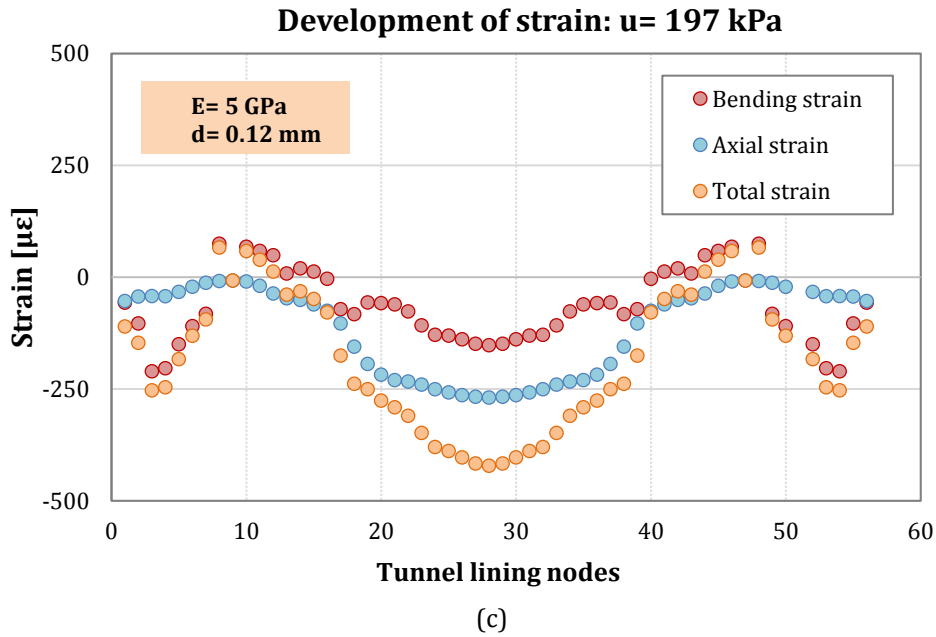**Figure 6.23**. Development of strain at tunnel lining during (a) Consolidation, (b) application of pore pressure u= 197 kPa (E tunnel lining of 10 GPa), (c) application of pore pressure u= 197 kPa (E tunnel lining of 5 GPa).

Figure 6.24a illustrates the computed lining hoop thrust forces at the tunnel axis level, the tunnel crown and the tunnel invert during the short term (start of consolidation stage) and the long-term (after 40-year consolidation). After tunnel construction (short-term), greater hoop thrust force is computed at the tunnel axis level compared to that at the tunnel crown and tunnel invert. The larger hoop force at the tunnel axis than that at the tunnel crown is due to the anisotropic load leading to distortion of the lining (Wongsaroj, 2005). During the 40-year consolidation stage, the hoop thrust at the tunnel axis level builds up with time, reaching a value of 1017 kN/m at the end of consolidation (i.e. 47.10 % full overburden) compared to the hoop thrust of 527 kN/m at the tunnel crown (24.4 % full overburden). The very small decrease in the hoop load at the tunnel crown during ground consolidation was also observed by Wongsaroj (2005) for a tunnel in London Clay, however, this behaviour might be unrealistic since no evidence was found in the literature.

When the tunnel lining drainage condition changes (i.e. water pressure of 197 kPa and 387 kPa behind the lining), the hoop thrust of the tunnel crown increases with a faster rate compared to the hoop thrust at the tunnel axis level, as shown in Figure 6.24. Considerably lower hoop thrust was instead computed at the tunnel invert, expected for non-circular tunnel shapes (Yoon et al., 2014). Particularly, due to the flat geometry of the tunnel invert, the vertical lining displacement u_2 at the centre of

tunnel floor increases when the lining is subjected to an external water pressure of 197 kPa and 387 kPa, as shown in Figure 6.24b. In particular, under the maximum hydrostatic load, the vertical movement at the tunnel floor almost doubled (i.e. around 3 mm), compared to that computed when a pore pressure of u= 197 kPa is applied (1.6 mm).

Hoop force at tunnel lining

(a)

Vertical movements u_2 at tunnel floor
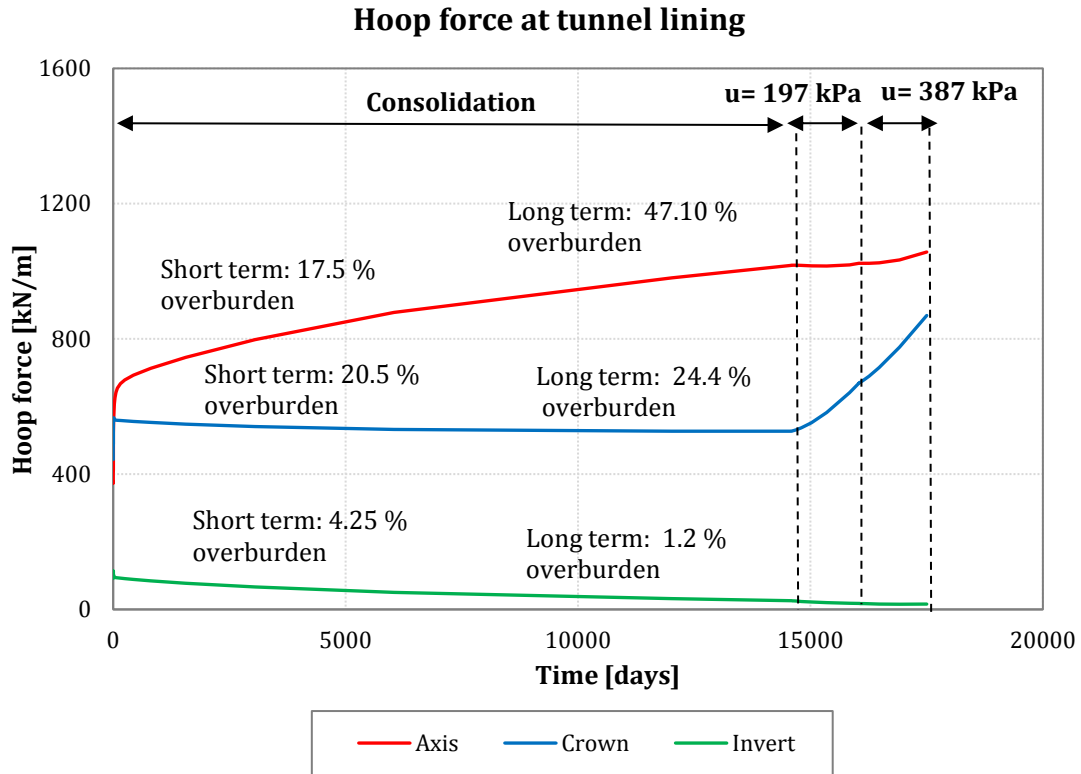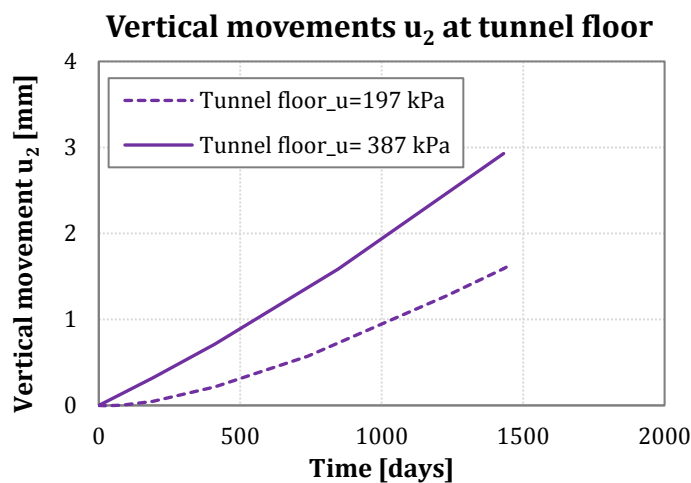
(b)

Figure 6.24. (a) Hoop thrust force at tunnel lining: crown, axis and invert (E tunnel lining = 5 GPa) and (b) Vertical movement u_2 at tunnel floor (middle point) when the external pressure u=197 kPa is applied and prediction of vertical movements u_2 under the maximum hydrostatic load u=387 kPa.

Coefficient of earth pressure at rest K_0

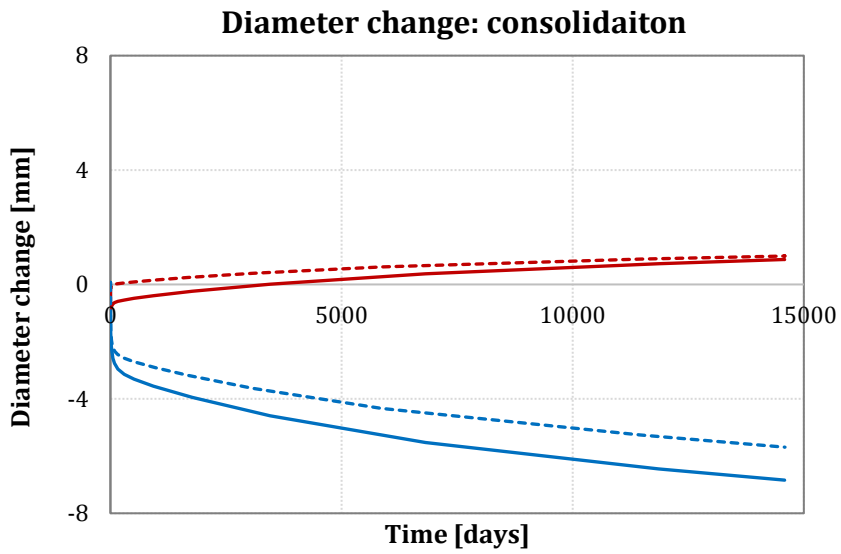The influence of the coefficient of earth pressure K_0 of the *very weak* marl layer on the tunnel lining response was investigated during the 40-year consolidation stage and the subsequent lining drainage condition change. In particular, the K_0 coefficient was increased to look at the influence of the anisotropic load on the tunnel lining response, by taking into account the range of K_0 values stated by GADZ (2016a, 2016b) for Point 1 (ATLAS), where a maximum value of $K_0 = 2$ was reported. The computed change in tunnel diameter and the development of strains along the lining are presented in Figure 6.25. With a higher value of K_0 (equals to 2), a slightly smaller change in the horizontal tunnel diameter was computed compared to a value of $K_0 = 1.2$, resulting in larger squatting for lower K_0 conditions during the 40-year consolidation stage, as shown in Figure 6.25a, indicating that lower K_0 values result in lower horizontal ground pressure on the lining and therefore more squatting is observed. When the tunnel lining is subjected to the external water pressure of 197 kPa, greater horizontal diameter change was performed for higher K_0 values, as shown in Figure 6.25b. The tunnel crown shows more significant total strains with higher K_0 magnitudes, due to the larger horizontal ground load of the very weak marl layer acting on the lining (Figure 6.25d).

The increase of the coefficient of earth pressure at rest K_0 of the very weak marl layer from a value of 1.2 to a value of 2 provides more significant strains at the tunnel crown (20 % increase) and comparable strains at the tunnel axis level for both K_0 values during the application of the external pore pressure of 197 kPa. Therefore, compared to the influence of the tunnel lining stiffness reduction (from 10 GPa to 5 GPa) on the tunnel lining response, which gave more significant strains only at the tunnel crown (i.e. double magnitudes of total strain, from around 213 $\mu\varepsilon$ to 420 $\mu\varepsilon$), the effect of K_0 on tunnel lining response seems not to be large.

Diameter change: consolidaiton

(a)

Diameter change: u= 197 kPa

(b)

Development of strain: consolidation

(c)

Development of strain : u= 197 kPa

(d)
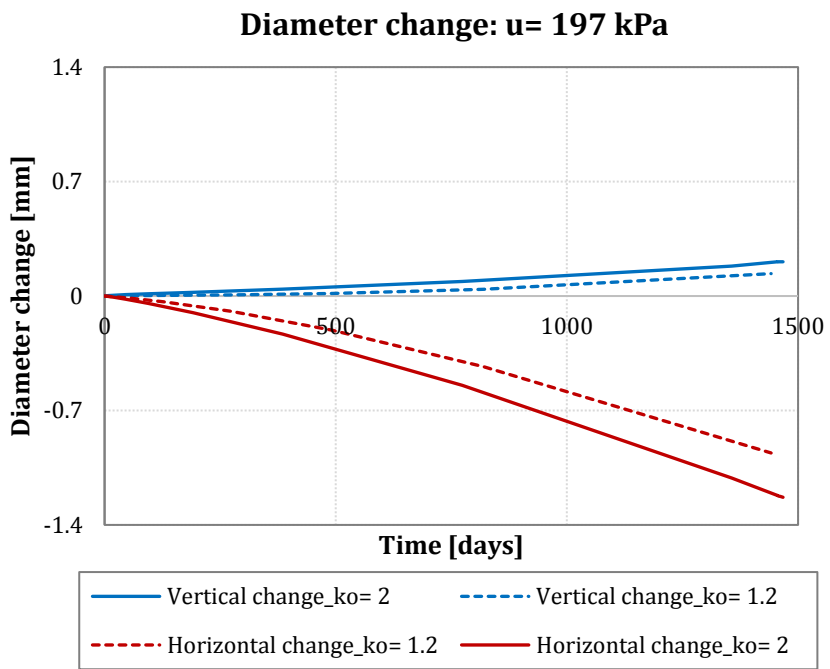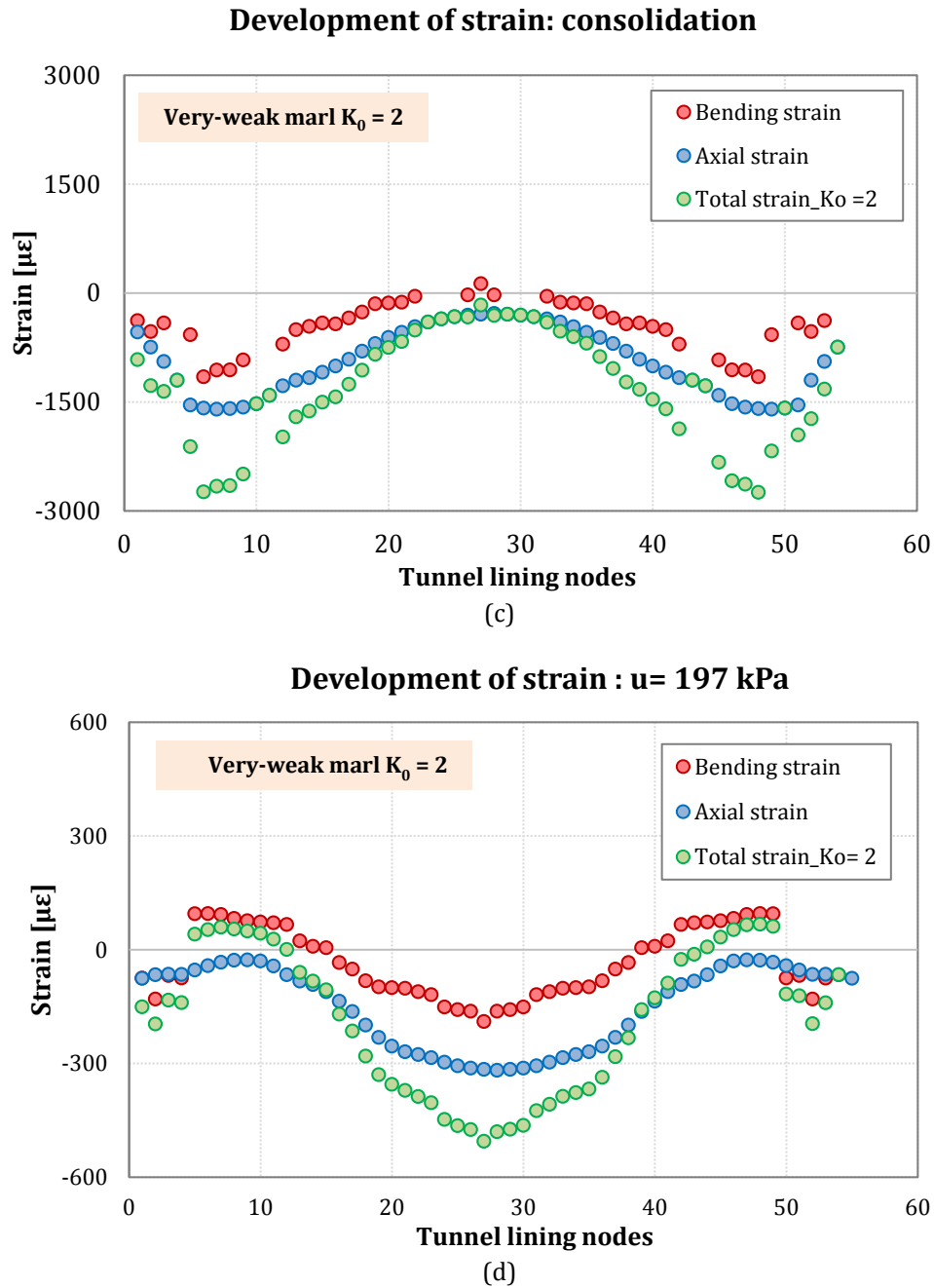
Figure 6.25. Influence of earth pressure coefficient K_0 of the very weak marl unit on tunnel lining response: (a) change in tunnel diameter during consolidation, (b) change in tunnel diameter during the application of pore pressure on the lining, (c) development of strain along the lining during consolidation and (d) development of strain along the lining during the application of u=197 kPa.

Influence of stiffness of medium weak marl unit

Since at the considered tunnel depth the tunnel is located partially in the _very weak marl_ unit (at the tunnel crown and the tunnel axis level) and in the _medium weak_ marl layer (at the tunnel invert), further modelling involved the investigation of the properties of the latter rock unit. As discussed before, in order to improve the

magnitudes of strains at the tunnel axis level to better match the observational data, the influence of the medium weak marl layer on the development of the tunnel lining response was investigated.

Figure 6.26a and 6.26b show the computed strains along the lining by assuming a reduced value of effective stiffness modulus E' of the *medium-weak marl* layer (half the initial value was considered). Therefore, a *weak marl* rock unit was considered instead. Particularly, comparable total strains were computed at the tunnel crown during the progress of pore pressure upon the tunnel lining (i.e. around 510 με), with no improvement in the magnitude of the strains at the tunnel axis level, as shown in Figure 6.26b. This implies that the attempt of considering a softer marl layer around the tunnel invert hasn't resulted in larger tensile strains at the tunnel axis level, suggesting that the elasticity property of the marl has no effect on the tunnel lining response.

(a)

Development of strain : u= 197 kPa

(b)
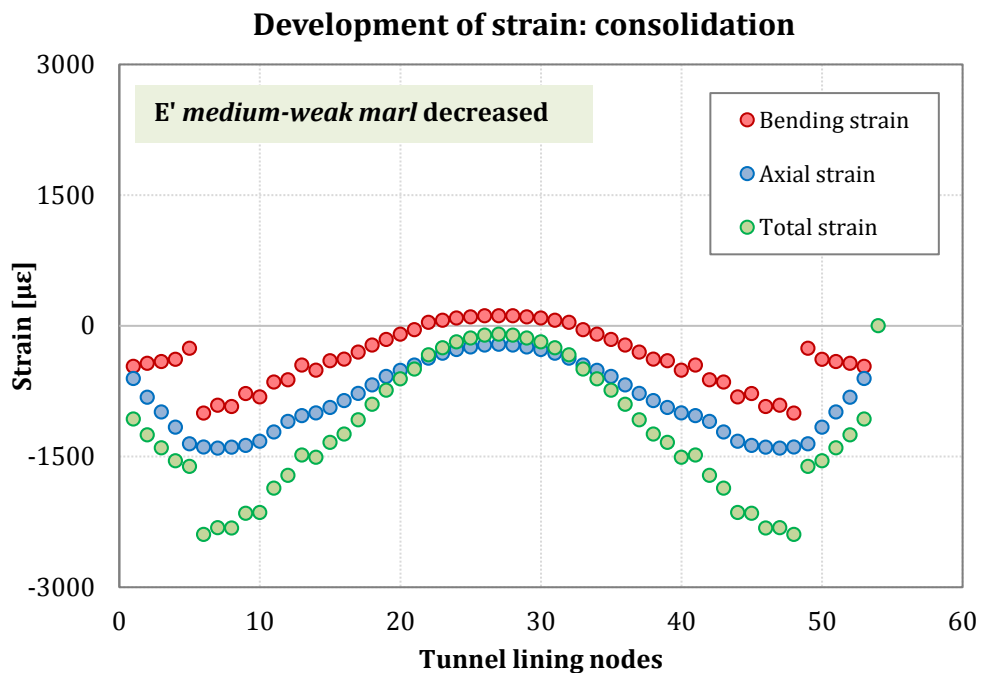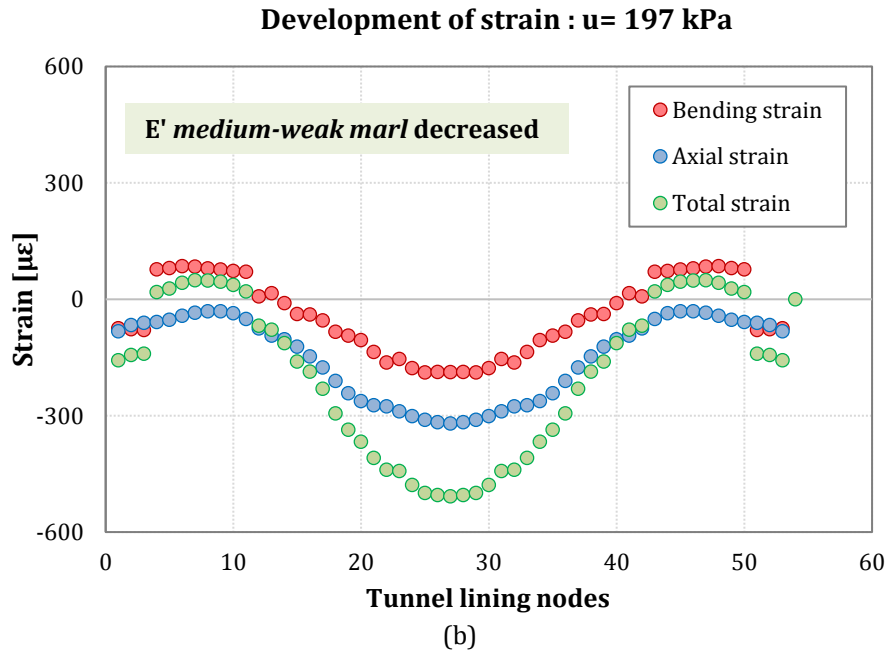
Figure 6.26. Influence of effective stiffness E' of the medium weak marl unit on tunnel lining response: (a) development of strain along the lining during consolidation and (b) development of strain along the lining during the application of u=197 kPa.

Linear elasto-plastic Mohr-Coulomb model

To investigate the distribution of load in the tunnel lining, a selection of appropriate constitutive laws for describing the ground behaviour can be important. To this end, this section presents the results of simulations obtained by adopting (a) the linear-elastic perfectly plastic model (Mohr-Coulomb) and (b) the advanced critical state model. As discussed in Chapter 5, the results of triaxial compression tests of the marls and sandstones formations enabled the evaluation of their mechanical behaviour. In particular, for the very weak marl layer, which showed a soil-like behaviour, a shear failure was observed, whereas a tension failure was observed for the other rock units. Therefore, the advanced critical state model was used only to model the very weak marl (lumpy marl), whereas the other layers (i.e. medium marl, medium sandstones etc.) were modelled by adopting a linear-elastic behaviour. The elasto-plastic Mohr-Coulomb model was also implemented for modelling the very weak marl unit, in order to compare the tunnel lining response by using the two constitutive models.

Figure 6.27 shows the change in tunnel diameter with time by using Mohr-Coulomb model, and the prediction was performed with the input mechanical parameters (E', ν', φ', c', ψ') listed in Table 5.3 of Chapter 5. It can be seen that the

bulk of diameter change in both vertical and horizontal direction occurs within the first year of consolidation, reaching the steady state condition very soon. Furthermore, the lining experiences a decrease in the vertical diameter (i.e. -0.91 mm) and an increase in the horizontal diameter, meaning that the tunnel deforms with a squatting deformation mode (Figure 6.27a). During the application of the external water pressure on the lining of 197 kPa, the predicted vertical diameter change behaves elastically within 750 days, after which it becomes plastic, reaching a value of 0.13 mm (Figure 6.27b). However, the plot of the computed change in tunnel diameter in Figure 6.27b confirms the deformation mode of the tunnel lining previously described (i.e. the tunnel deforms with vertical elliptical mode). Overall, smaller magnitudes of diameter changes were recorded for the Mohr-Coulomb model compared to the advanced critical state model, during both the consolidation stage and the application of the pore pressure u=197 kPa, as shown in Figure 6.27a and Figure 6.27b.

(a)

Diameter change: u= 197 kPa at tunnel lining

(b)
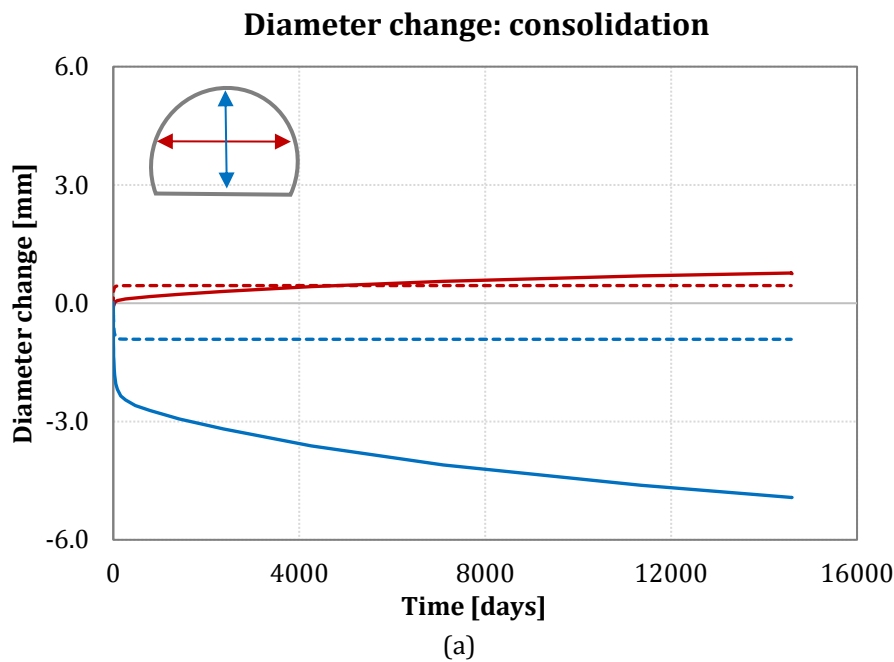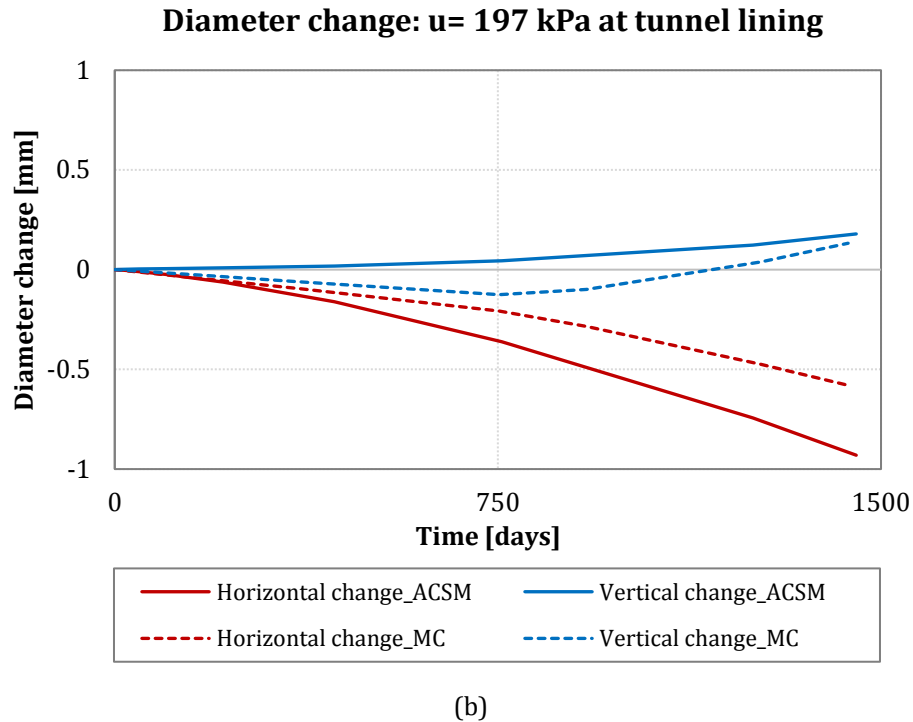
Figure 6.27. Change in tunnel diameter: vertical and horizontal change during (a) Consolidation stage and (b) Application of pore pressure (u=197 kPa) at tunnel lining.

Further modelling that included the development of total strain along the lining is shown in Figure 6.28. Comparable bending and axial strains were computed during the ground consolidation stage, resulting in negative tensile strain at the tunnel crown and positive tensile strains at the tunnel axis level, with the former being smaller than the latter (i.e. tunnel squatting) (Figure 6.28a).

A vertical tunnel elongation mechanism is instead observed when a change of flow regime around the tunnel occurs (Figure 6.28b), which seems to be in line with the one observed from the advanced critical state model.

Comparison between the lining deformations computed from the advanced critical state model and the elastic-perfectly plastic Mohr-Coulomb model presented in Figure 6.28c shows that the latter model predicts smaller magnitudes of both tensile and compressive strain. The advanced critical state model provides a bigger change in the tunnel diameter, compared to that computed by the Mohr-Coulomb model. Peak total strains of approximately -238 $\mu\varepsilon$ and 422 $\mu\varepsilon$ were recorded at the tunnel crown for the MC model and the advanced critical state model respectively, whereas at the tunnel axis level less significant strains were obtained, as shown in Figure 6.28c. Overall, smaller strain values were computed with the Mohr-Coulomb model

compared to the advanced critical state model at both the tunnel crown and the tunnel axis level.

Development of strain: consolidation

(a)

Development of strain: u= 197 kPa

(b)

Development of strain: u= 197 kPa
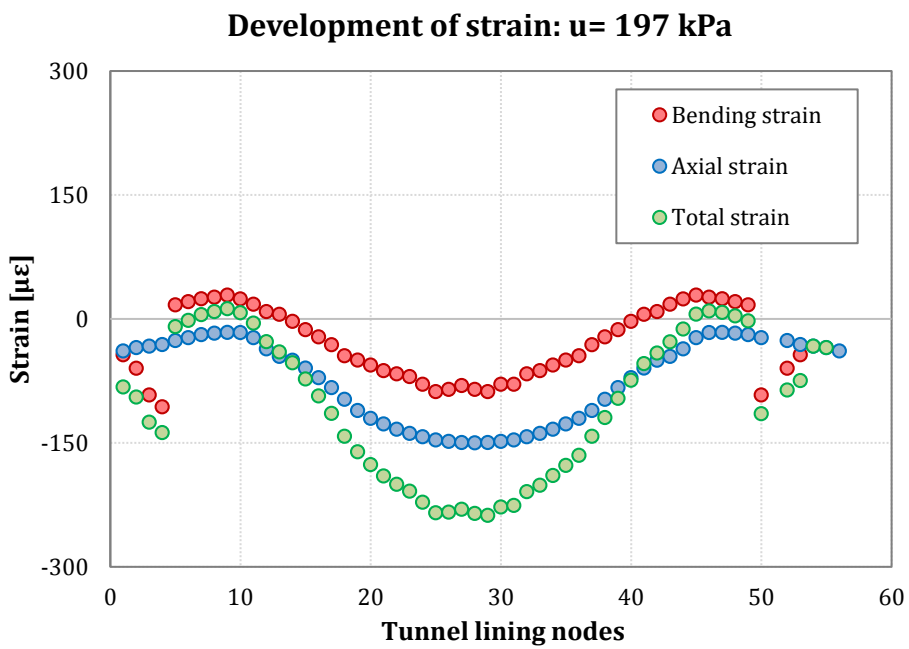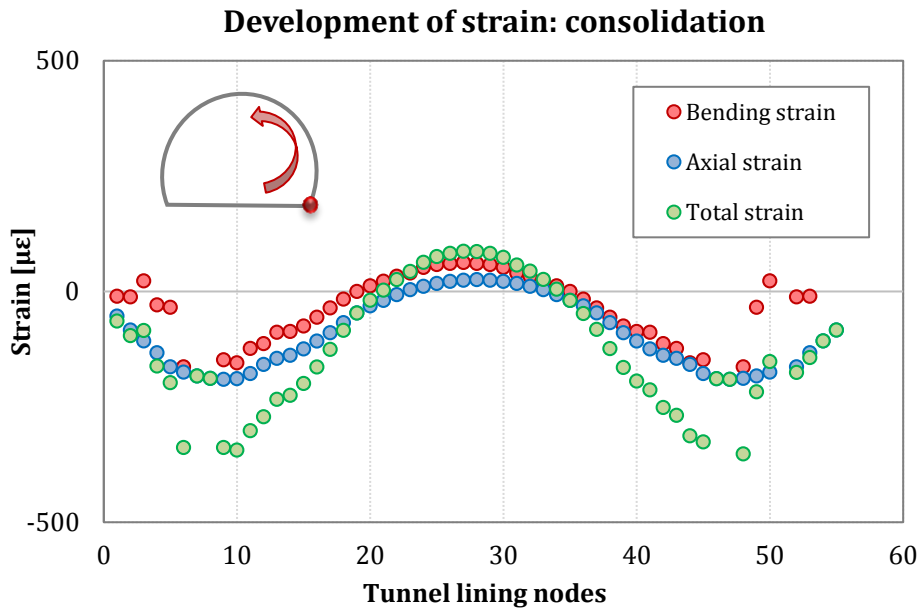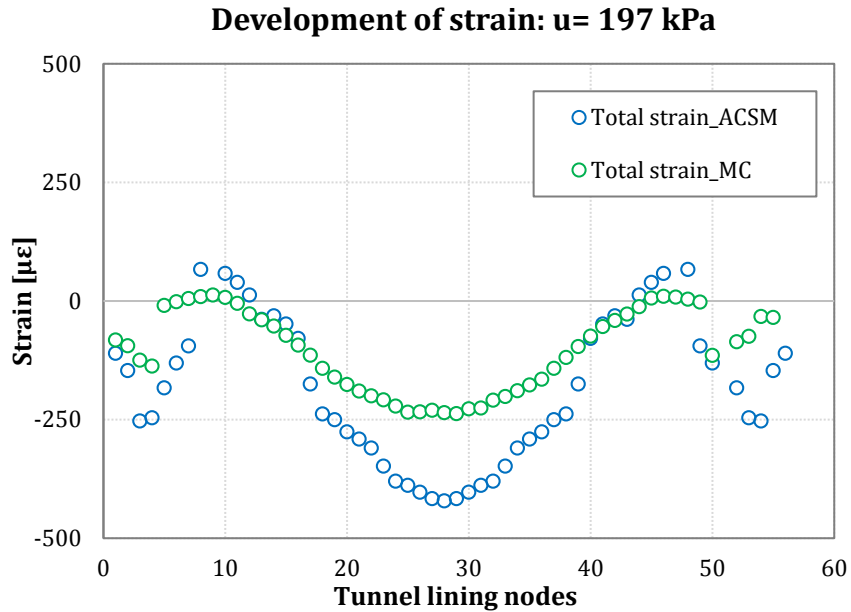
(c)

Figure 6.28. Strain development along tunnel lining by adopting the Mohr-Coulomb model: (a) Consolidation stage, (b) Pore pressure rise at tunnel lining (u=197 kPa) and, (c) Comparison between the advanced critical state model and the Mohr-Coulomb model when u=197 kPa is applied.

Figure 6.29 shows the development of plastic strains performed around tunnel lining by assuming the Mohr-Coulomb model at the end of the unloading stage II (Figure 6.29a), ground consolidation stage (Figure 6.29b) and at the end of the pore pressure rising at tunnel lining (Figure 6.29c). The figures show the development of some more important plastic strains at the tunnel shoulder and at the tunnel crown within the very-weak lumpy marl layer, propagating towards the upper boundary, at the interface with the medium-weak marl layer. Additionally, at both tunnel invert lateral sides and at the interface between the very-weak and the medium-weak marl layers, ground elements reached the plasticity condition.

The volumetric plastic strains developed around the tunnel are also plotted for the soil elements modelled with the advanced critical state model, as shown in Figure 6.30. In particular, the plastic strains are displayed only for the very weak marl layer. Small plastic strains develop around the tunnel at the end of the unloading stage II (when the tunnel lining is put in place), in particular at the tunnel shoulder level and at the interface between the two different marl layers (Figure 6.30a).

Figure 6.30b shows that at the end of the 40-year consolidation stage large plastic strains develop at the tunnel shoulder level, spreading towards the upper marl layer

and towards the lower boundary between the very weak and medium weak marl units. Similar behaviour was observed with the Mohr-Coulomb model, albeit the latter model computes larger magnitudes of soil plastic strains. The plastic strains of the soil around the tunnel shoulder level increased at the end of the application of a pore pressure u= 197 kPa on the lining, as shown in Figure 6.30c.
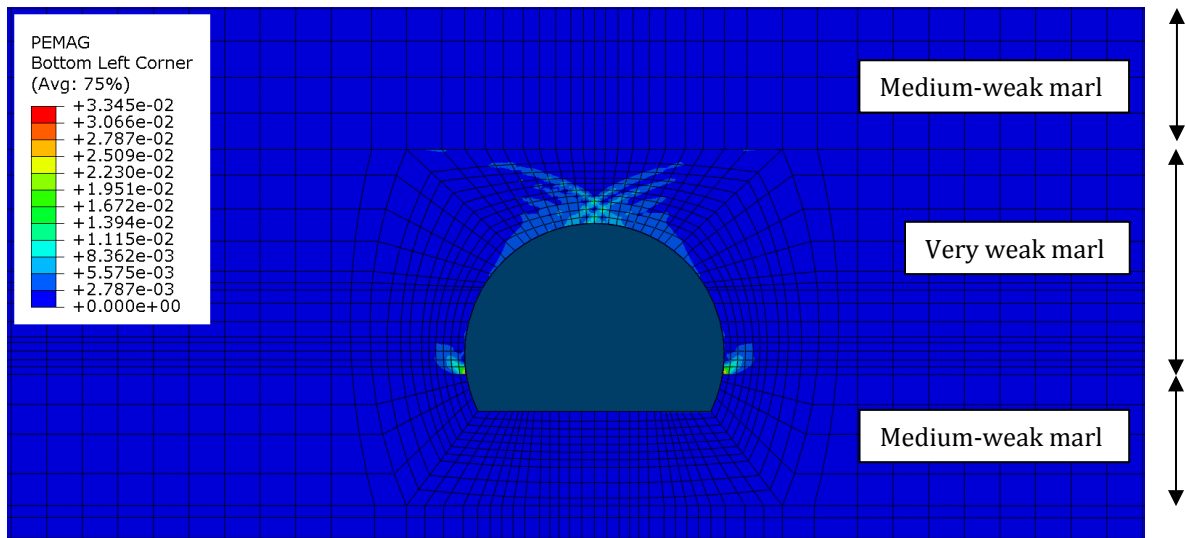
(a) End of unloading stage II
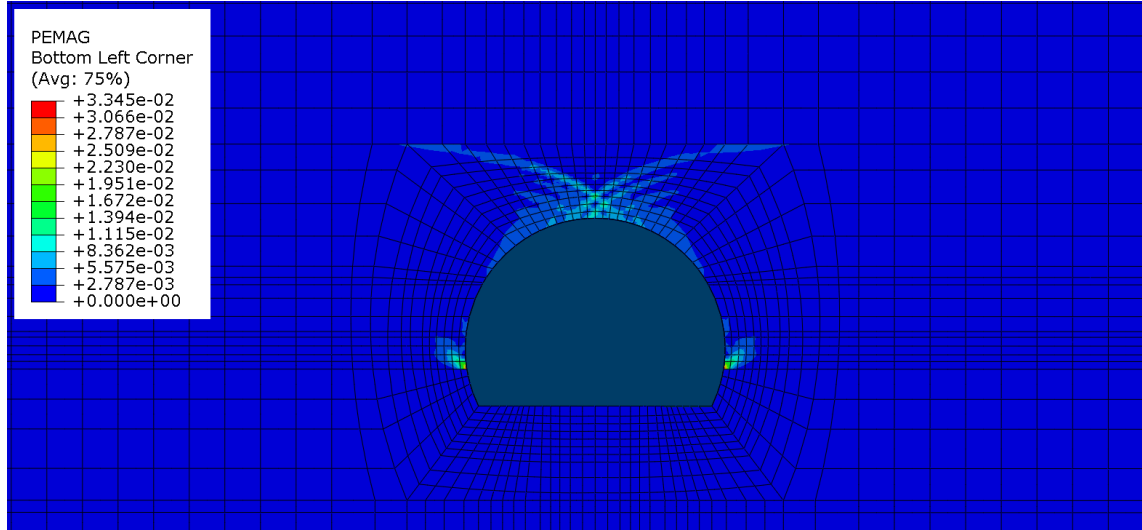
(b) End of 40-year consolidation
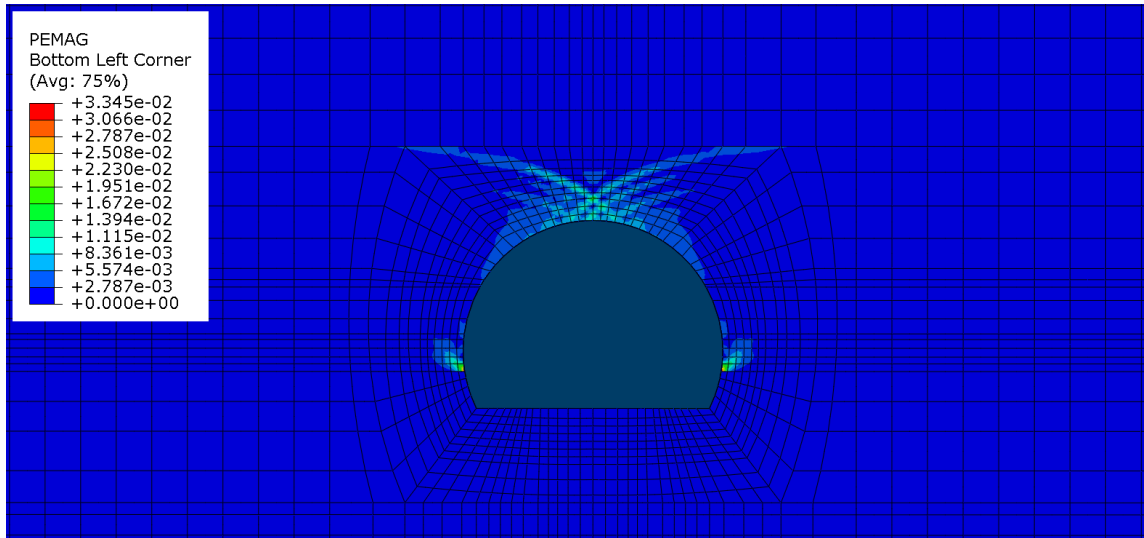
(c) End of pore pressure rise

Figure 6.29. Plastic strains around the tunnel lining by assuming the Mohr-Coulomb model: (a) End of unloading stage II, (b) End of consolidation stage and (c) End of the application of pore pressure u= 197 kPa at tunnel lining.

(a) End of unloading stage II
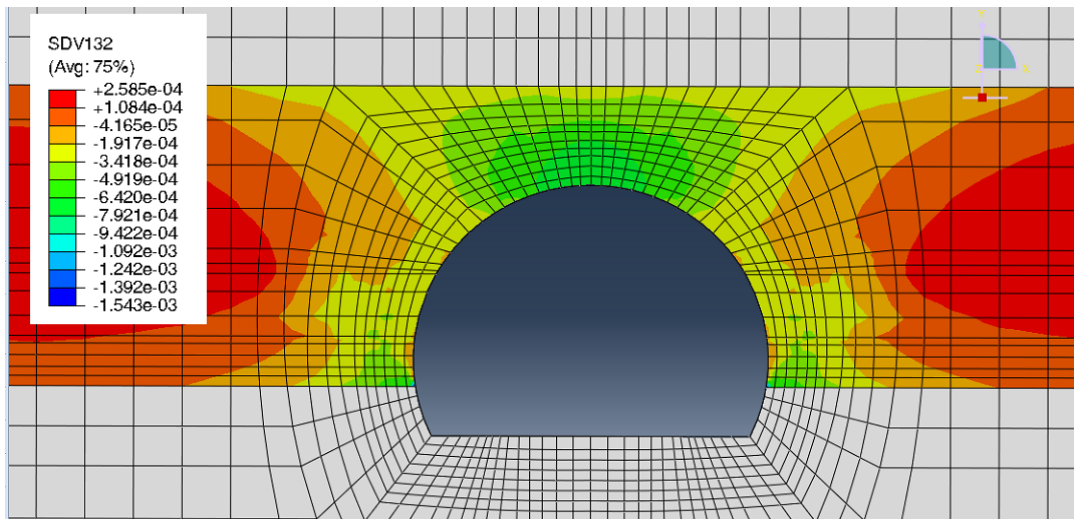
(b) End of 40-year consolidation stage
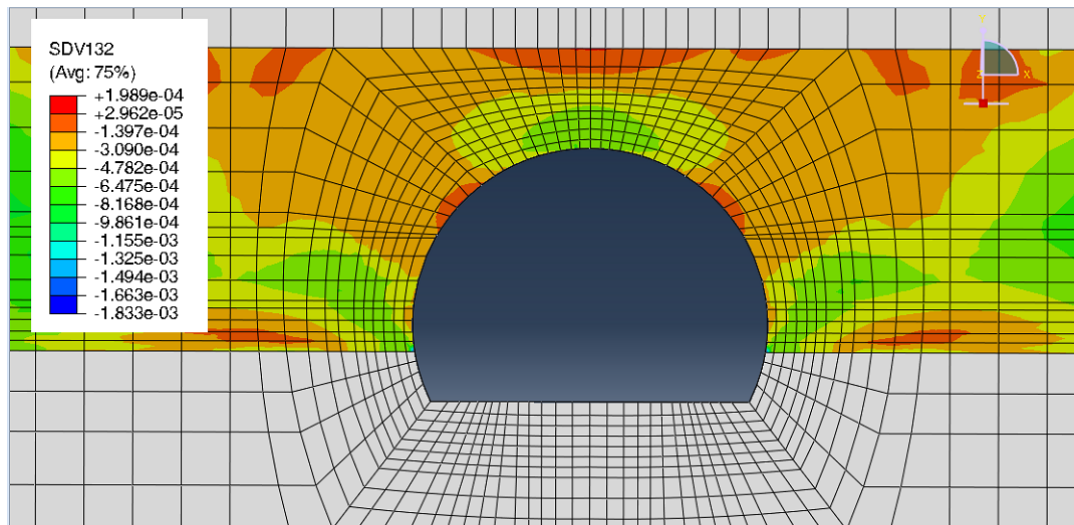
(c) End of pore pressure rise
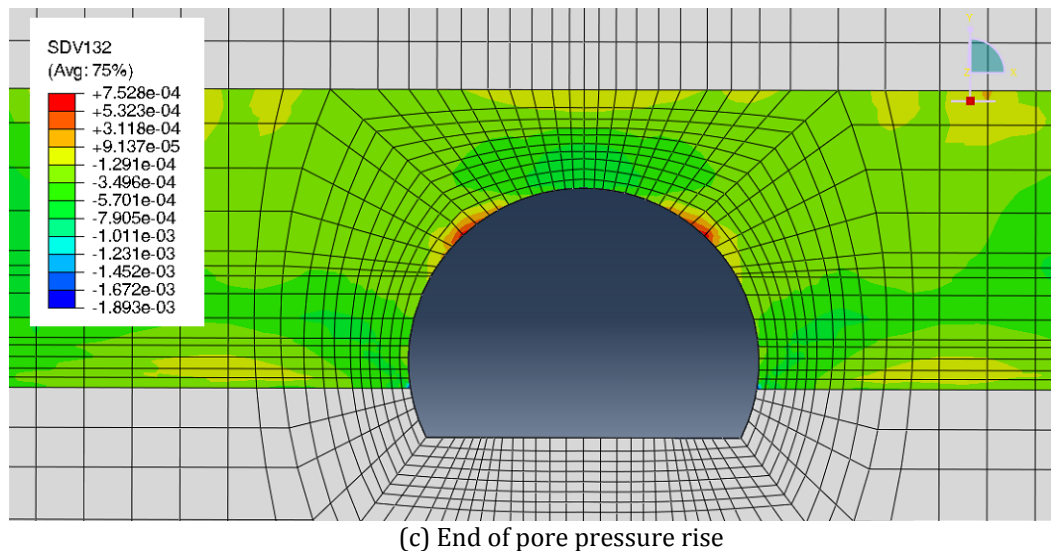
Figure 6.30. Plastic strains in the very weak marl layer by assuming the ACSM model: (a) End of unloading phase II, (b) End of consolidation stage and (c) End of the application of pore pressure u= 197 kPa at tunnel lining.

Stress paths around tunnel lining

The stress paths around the tunnel for both constitutive models are plotted in Figure 6.31 in the *s'–t* plane. The results are taken from elements taken at different locations as shown in Figure 6.31a, with both elements located in the weak lumpy marl, at the tunnel axis level and at the tunnel crown.

During the tunnel construction (i.e. *stage I: unloading phase I*) the ground at the tunnel crown underwent higher change in deviatoric stress (*t*), as shown in Figure 6.31b, reaching the Critical state line (CSL) during the final *unloading phase II.*

Yet, during ground consolidation (*stage III*), the mean effective stress s' increases as the excess pore pressures dissipate with time, whereas during the application of the external water pressure on the lining (*stage IV*) the s' decreases as the pore pressure increases. Additionally, Figure 6.31b and Figure 6.31c indicate that whilst at the tunnel crown the plasticity condition is reached during the *unloading phase II* and the simultaneous installation of the lining, at the tunnel axis level the ground does not reach the peak state. This behaviour seems to be compatible with the development of some plastic strains at the tunnel crown, shown previously in Figure 6.29.

The stress paths computed with the advanced critical state model in Figure 6.31d and Figure 6.31e, show that at the tunnel crown during the unloading *stage I* the predicted shearing stresses are similar to those computed by the MC model.
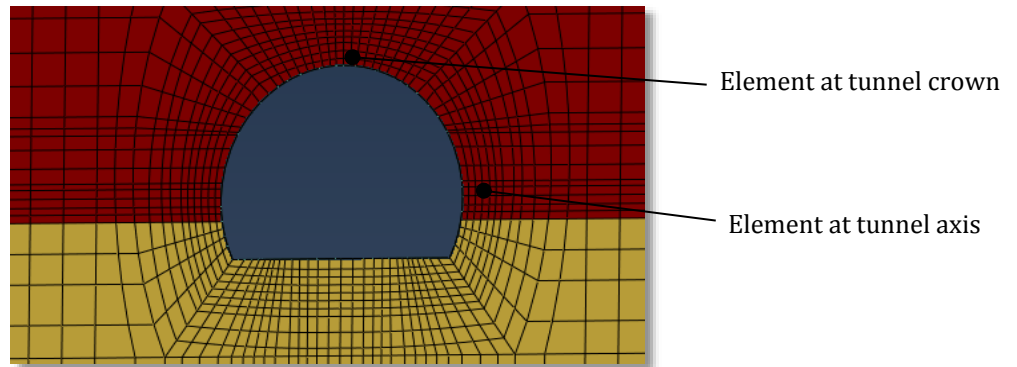
(a)
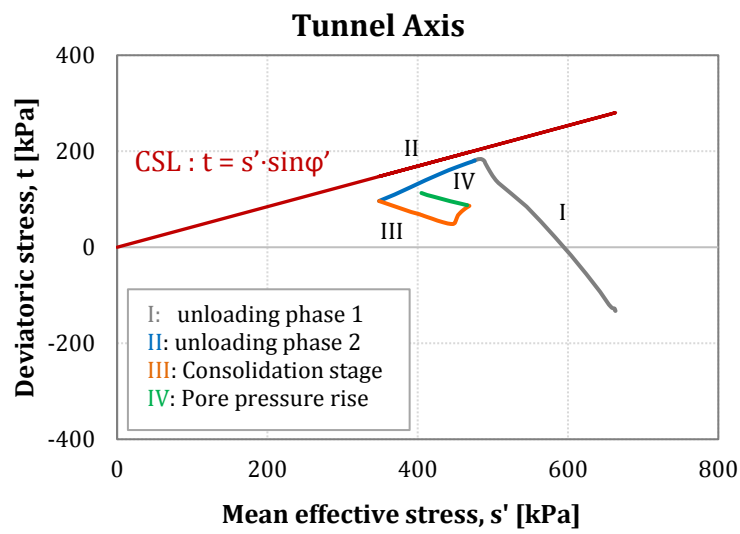
(b)
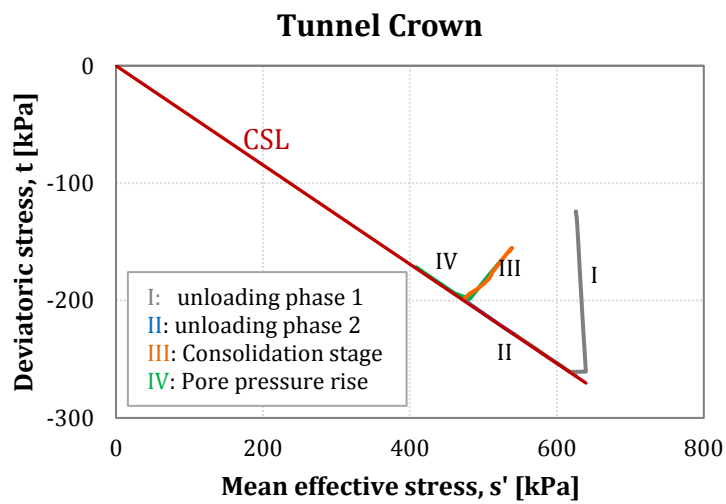
(c)
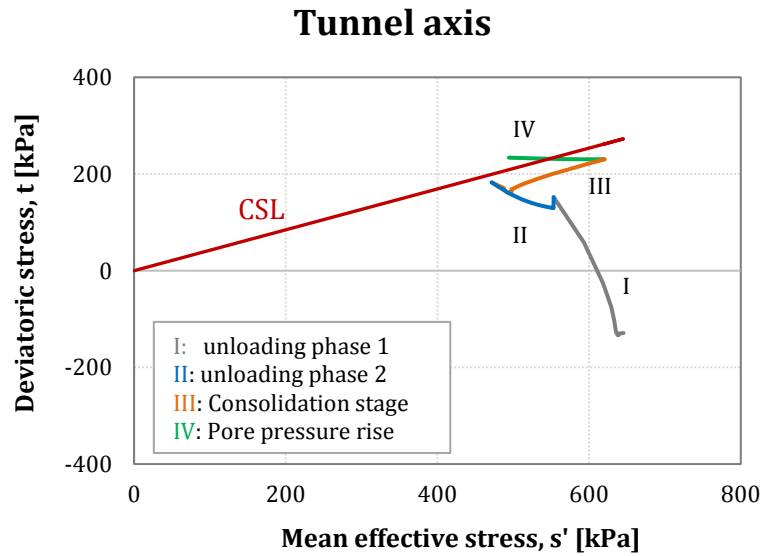
(d)
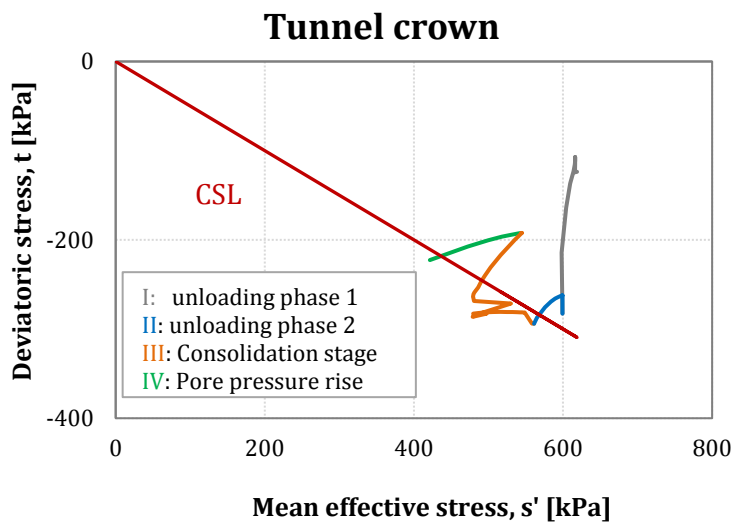
(e)

Figure 6.31. Computed stress path for soil elements at tunnel crown and tunnel axis: (a) Location of elements in the mesh around the tunnel, (b) Soil element at tunnel axis (MC), (c) Soil element at tunnel crown (MC), (d) Soil element at tunnel axis (ACSM), and (e) Soil element at tunnel crown (ACSM).

6.5.4.1 *Parametric study*

In this section, a parametric study was performed to investigate the effect of the layering formations on the long-term tunnel lining performance, with particular interest on the water pressure rise stage (i.e. u= 197 kPa at tunnel lining).

The examined tunnel cross-section is located between two layers: the tunnel crown and the tunnel axis level are located in the very weak marl unit, whereas the tunnel invert is located in the medium weak marl unit.

The computed shape of the strain profile seems to match well the tunnel deformation mode obtained with the field data, with compressive and tensile strains at the tunnel crown and the tunnel axis level respectively. Also, the computed change in tunnel diameter is in agreement with the observational measurements, suggesting the same tunnel lining mechanism of deformation. Further modelling has been conducted to improve the understanding of the tunnel lining behaviour by comparing two different cases: (a) the tunnel is entirely located in one homogeneous rock unit (i.e. very weak marl) and (b) the tunnel is located in two different rock formations (i.e. the tunnel crown in very weak marl layer and the tunnel invert in the medium weak marl).

The lining response was investigated assuming the tunnel entirely located in the very weak marl layer. Both constitutive models were adopted (i.e. advanced critical state model (ACSM) and Mohr-Coulomb (MC) model).

Figure 6.32 shows the computed axial, bending and total strains along the lining by using the ACSM model and the MC model, as shown in Figure 6.32a and Figure 6.32c respectively, whereas Figures 6.32b and 6.32d present the comparison between the total strains computed for the homogeneous case (a) and for the layered case (b), by adopting the ACSM and the MC model respectively.

When assuming the ACSM model, larger axial strains are observed along the lining compared to the bending strains, when the external water pressure of 197 kPa is applied on the tunnel lining, resulting in the development of negative total strains at both the tunnel crown and the tunnel axis level, as shown in Figure 6.32a. By comparing the results obtained from the (a) homogeneous case and (b) the layered case, it can be seen that the tunnel lining response is influenced by the layering divisions within the molasse region surrounding the tunnel, when its drainage condition changes, as shown in Figure 6.32b. While the homogenous model shows the development of negative total strains at both the tunnel axis and the tunnel crown, the layered model performs negative and positive strains at the tunnel crown and axis level respectively, suggesting a tunnel ovalisation as tunnel lining deformation mode.

When modelling the very weak marl layer by using the MC model, slightly larger magnitudes of total strains are computed along the tunnel lining compared to the ACSM model, as shown in Figure 6.32c. However, both constitutive models have

shown a consistent tunnel lining strain pattern, characterized by the development of uniform compressive strains along the lining.

This behaviour suggests that the tunnel lining exhibits the development of tensile and compressive strains at the tunnel axis and the tunnel crown respectively (i.e. tunnel vertical elongation) when the layered model is considered, whereas the homogeneous ground model displays a uniform development of compressive strains.

This implies that in the layered formation the different mechanical behaviour of the two rock units surrounding the tunnel (very weak marl and medium weak marl) contributes to the development of bending moments in the tunnel lining and, hence, to tunnel lining distortions. Conversely, when the whole tunnel cross-section is surrounded by a homogeneous rock formation (very weak marl layer), the tunnel lining deforms through the development of compressive strains at both the tunnel crown and the tunnel axis. This distribution of strains (i.e. tunnel vertical ovalisation) along the tunnel boundary was found to be dependent on the relative stiffness of the layered formations. Zhang et al. (2015) also observed significant differences on the tunnel lining response of a shield tunnel for a homogeneous soil model and multi-layered formation depending on the relative layers' thickness and stiffness.
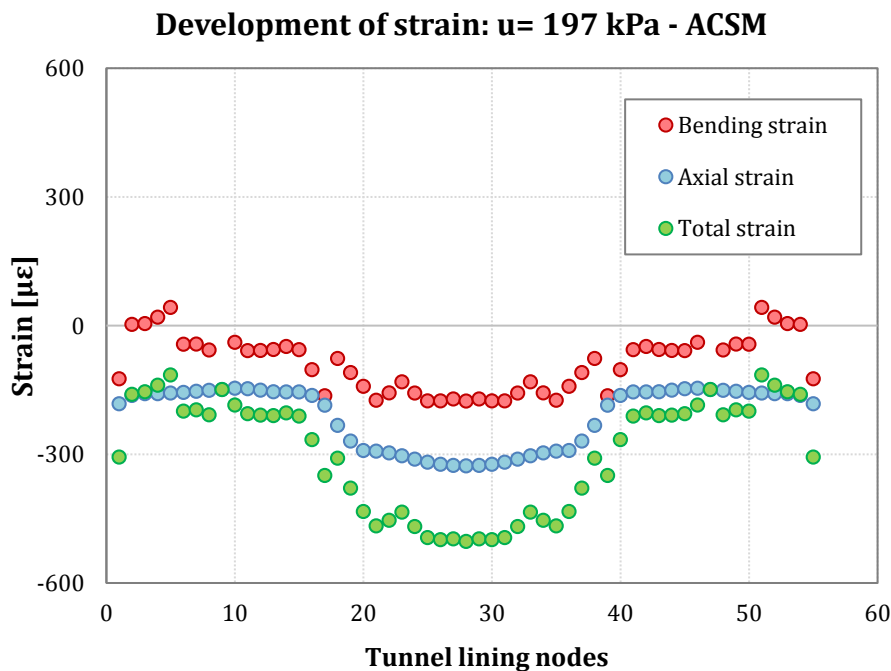
(a)

Comparison layered/homogeneous: ACSM

(b)

Development of strain u= 197 kPa: MC

(c)

Comparison layered/homogeneous: MC

(d)
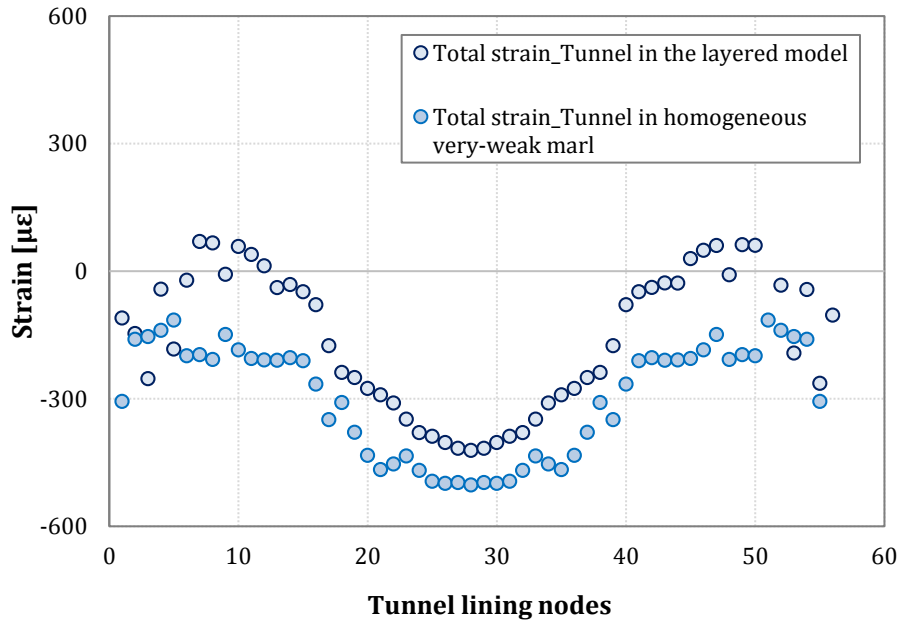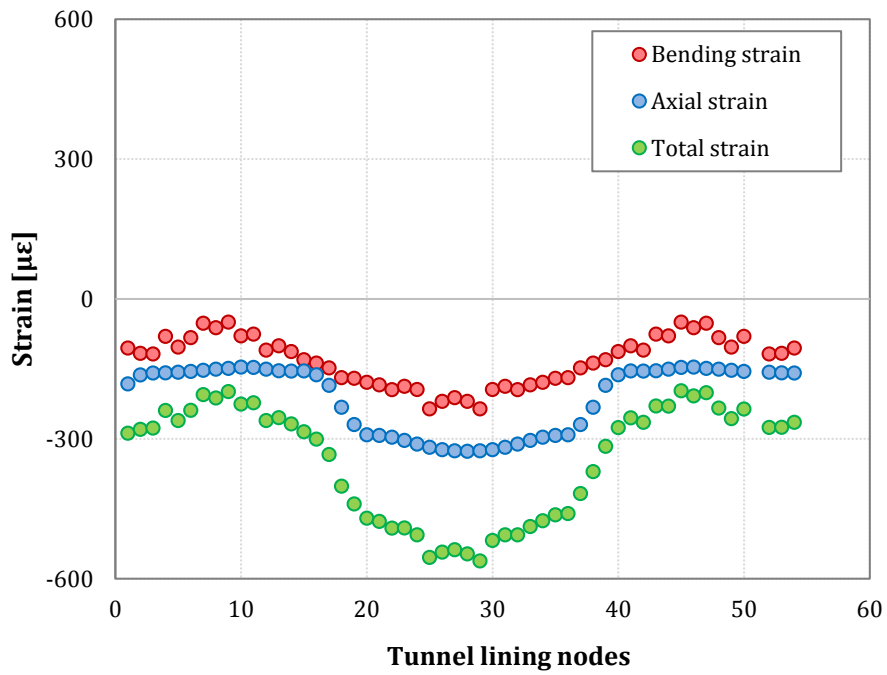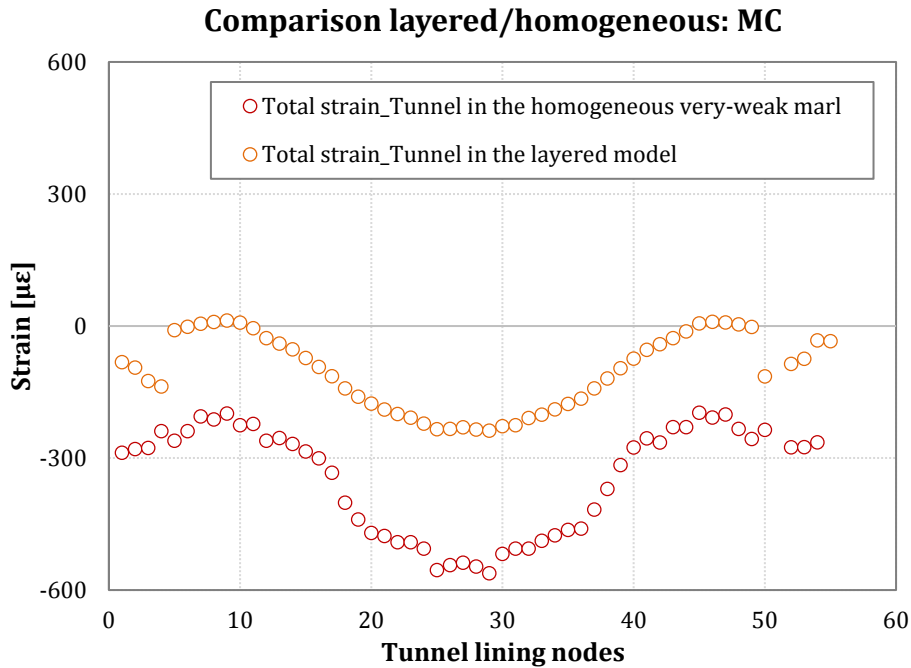
Figure 6.32. Development of strain at tunnel lining during the application of pore pressure u=197 kPa: (a) Homogeneous case (ACSM), (b) Comparison between the homogeneous and the layered model by using the ACSM, (c) Homogeneous case (MC) and (d) Comparison between the homogeneous and the layered model by using the MC model.

Figure 6.33 presents the change in tunnel diameter when the tunnel lining is experiencing an external pore pressure of 197 kPa, by assuming both the advanced critical state model and the Mohr-Coulomb model. The prediction of tunnel diameter change when the maximum hydrostatic load of 387 kPa occurs is also shown in the figure. Both the horizontal and vertical changes in tunnel diameter decrease with time, reaching similar magnitudes of around -1.25 mm when assuming the ACSM, suggesting that the tunnel lining is converging inwards when the pore pressure load of 197 kPa builds-up on the lining, as shown in Figure 6.33a. A bigger difference between the vertical and horizontal diameter change was computed by the Mohr-Coulomb model at the end of the 4-year period of water pressure rise on the tunnel lining (Figure 6.33a).

Also, the magnitudes of diameter change seem to increase under the maximum water pressure acting on the tunnel lining for both constitutive models, as shown in Figure 6.33b. Overall, larger changes in tunnel diameter were computed when assuming the Mohr-Coulomb constitutive model.

Diameter change: u= 197 kPa

(a)
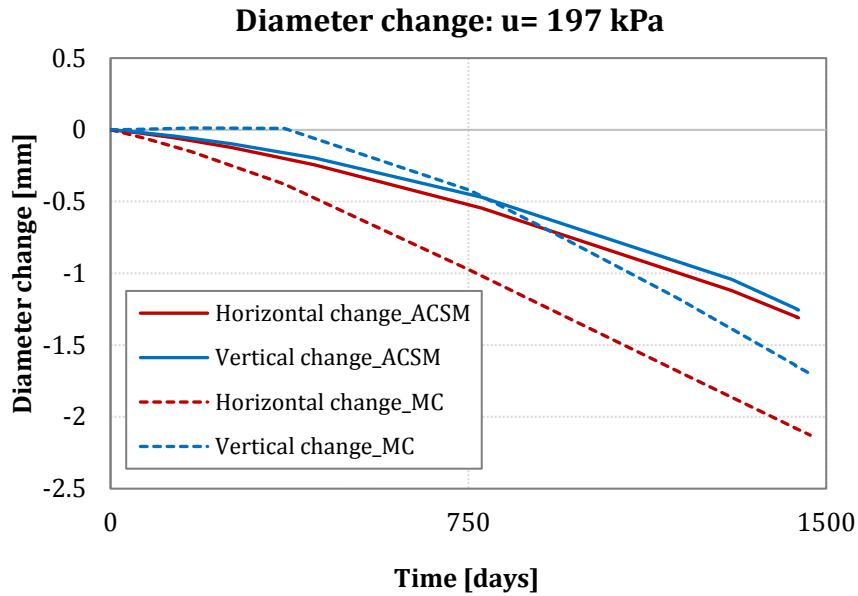
Diameter change: u= 387 kPa
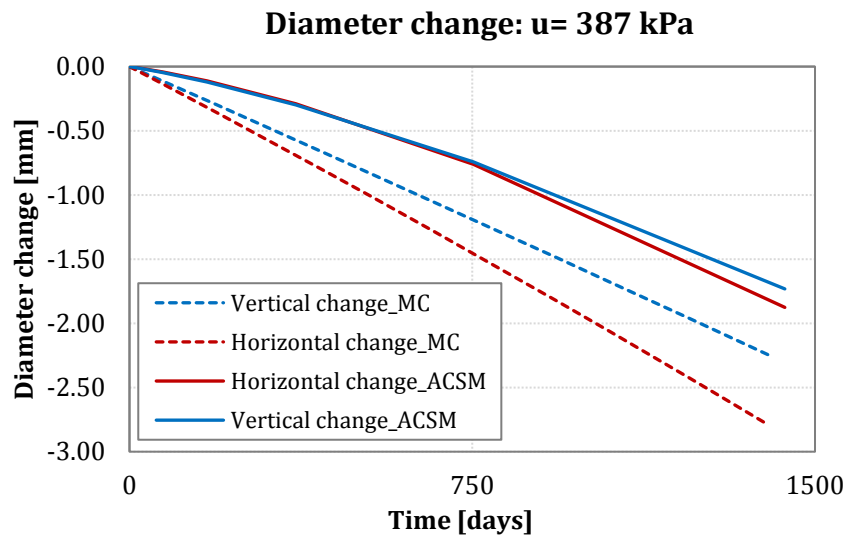
(b)

Figure 6.33. Change in tunnel diameter during (a) the application of the external pore pressure of 197 kPa and (b) under the maximum hydrostatic load of 387 kPa.

The stress paths of ground elements around the tunnel computed with the advanced critical state model are analysed and plotted in Figure 6.34 in the s'–t plane, for soil elements located in different locations: above the tunnel crown, at the tunnel axis level, at the tunnel invert (side) and below the tunnel invert, as shown in Figure 6.34a, with all the elements placed within the very weak lumpy marl formation. The soil elements at both the tunnel crown and the tunnel axis level exhibit the same stress paths shown for the layering model (Figure 6.34), since both elements are located in the very weak marl layer as well as the previous case. For the soil element

at the bottom of tunnel invert, during the tunnel construction (i.e. *unloading phase I and II*) the ground underwent a change in deviatoric stress (*t*) as shown in Figure 6.34c, followed by the ground consolidation (*stage III*) and the application of the external water pressure on the lining (*stage IV*), where the mean effective stress s' decreases as the pore pressure increases. The ground at the bottom of the tunnel invert does not reach the failure envelope, as well as the rock unit placed at the side of the tunnel invert (Figure 6.34d).

Additionally, Figure 6.35 displays the contours of the plastic strains developed in the very weak marl unit surrounding the tunnel. At the end of the tunnel construction, the soil surrounding the tunnel axis level and tunnel shoulder underwent some plastic strains, slightly larger than those at the tunnel crown and the tunnel invert, as shown in Figure 6.35a. Similarly to the layered model, larger plastic strains develop at the tunnel shoulder level and at the lower interface with the medium weak marl layer at the end of the 40-year consolidation phase, as shown in Figure 6.35b. When the tunnel drainage condition changes (i.e. an external pore pressure of 197 kPa is applied on the tunnel lining), further plastic strains develop around the tunnel shoulder and the tunnel axis level, as shown in Figure 6.35c.

Figure 6.36 and Figure 6.37 show the stress path and the plastic strains of the ground surrounding the tunnel when the Mohr-Coulomb model is assumed. It can be seen that the failure envelope is only reached for the soil element located at the tunnel crown and at the tunnel invert (bottom) during the unloading stage II, as shown in Figure 6.36a and 6.36b. Moreover, Figure 6.37 illustrates the development of plastic strains at the tunnel crown and the tunnel invert, which extends towards the upper and lower soil boundary respectively, at the end of the tunnel construction stage, consolidation stage and the water pressure rise stage.

Tunnel crown

Tunnel axis

Tunnel invert side

Tunnel invert bottom

(a)

(b)

(c)

(d)
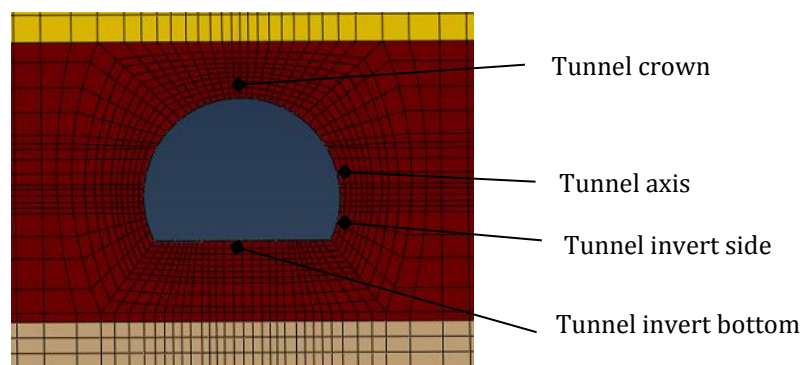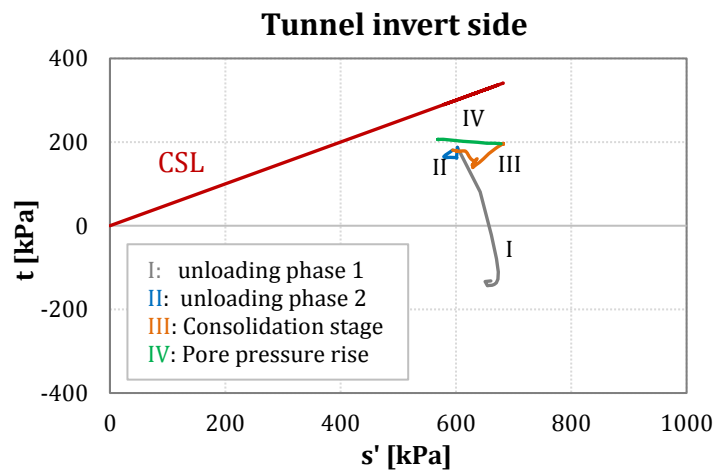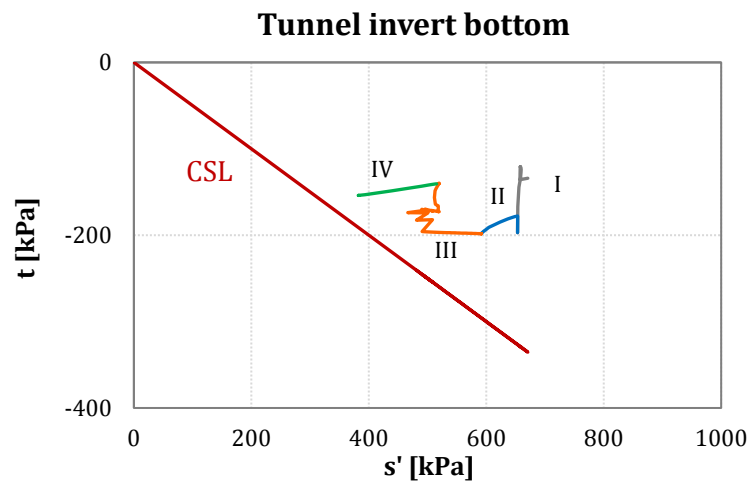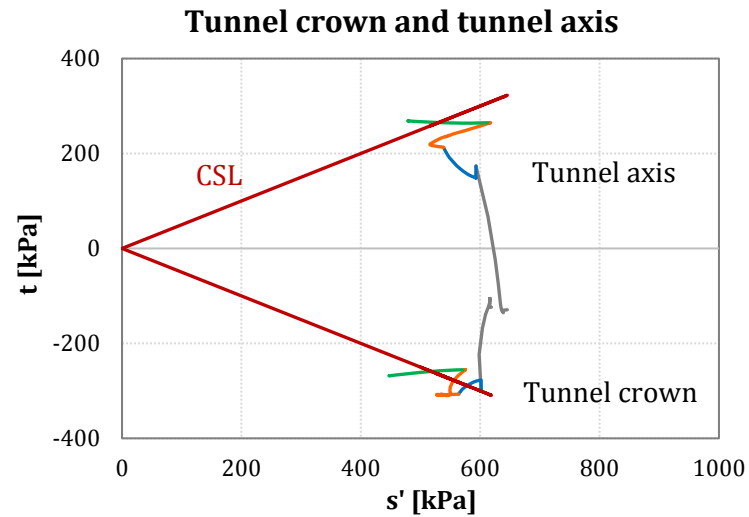
Figure 6.34. Computed stress paths for soil elements around the tunnel lining boundary by assuming the ACSM: (a) Location of the soil elements, (b) stress path for soil elements at the tunnel crown and the tunnel axis, (c) at the tunnel invert bottom and (d) at the tunnel invert side.
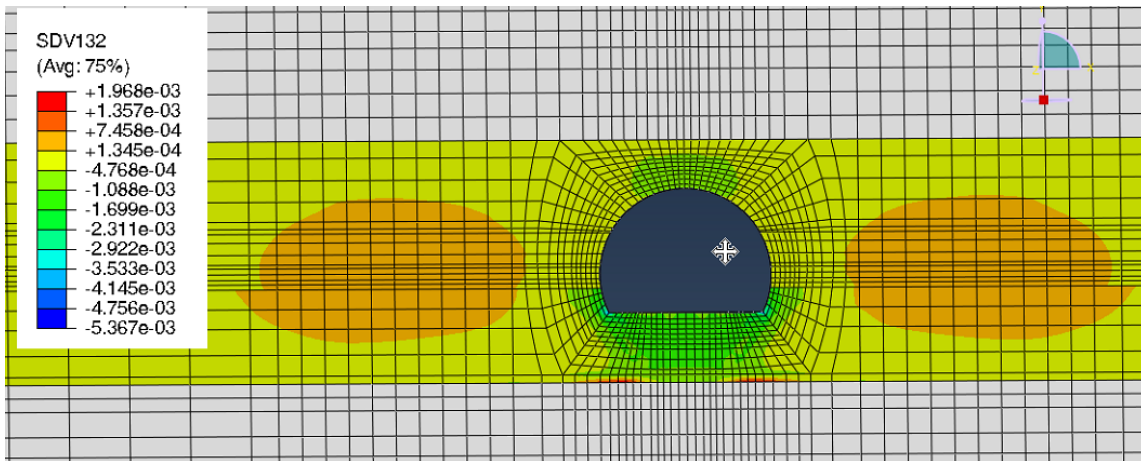
(a) End of unloading stage II
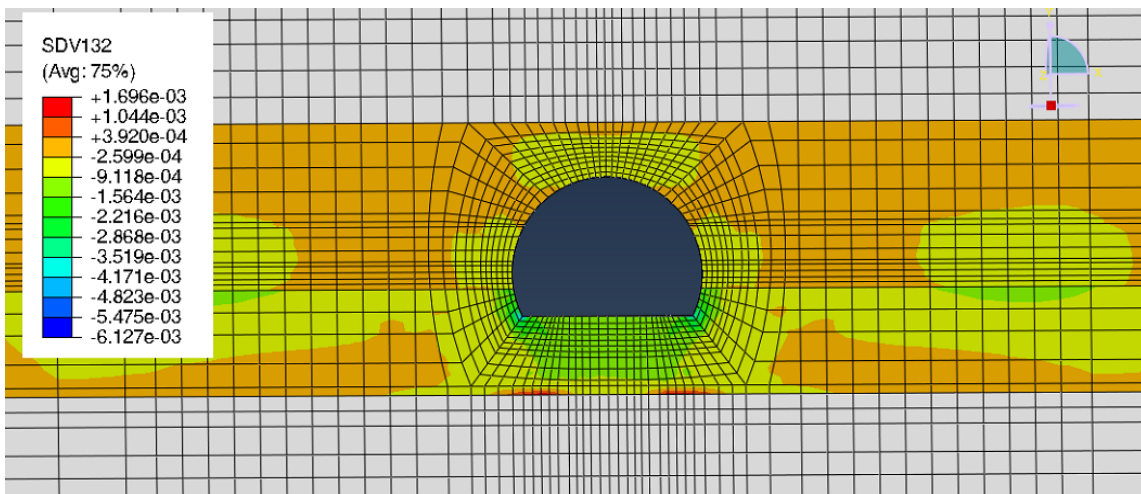
(b) End of consolidation stage
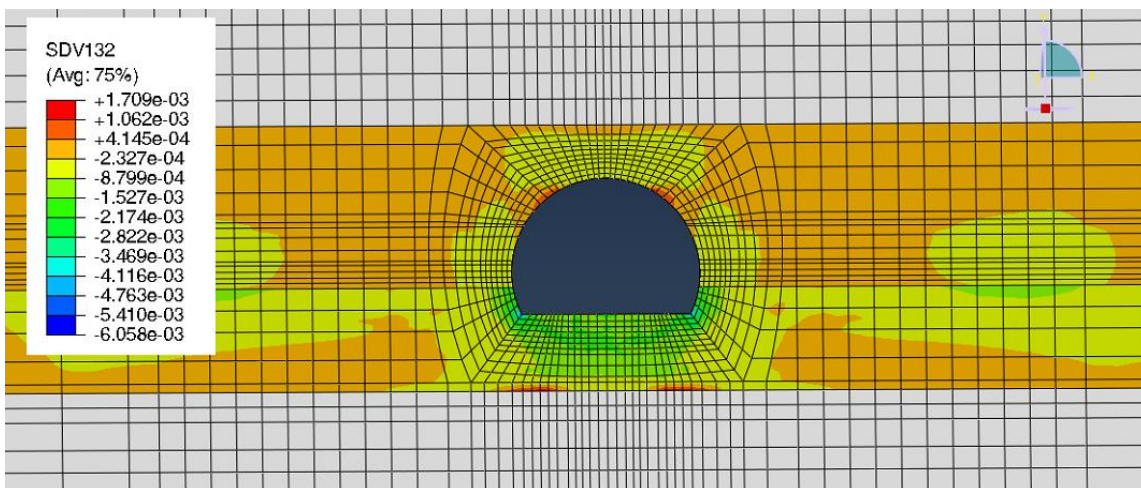
(c) End of pore pressure rise

Figure 6.35. Plastic strains development in the very weak marl layer by using the ACSM model: (a) end of unloading II stage, (b) end of 40-year consolidation stage and (c) end of application of the external pore pressure u=197 kPa on the tunnel lining.

Tunnel crown and tunnel axis

(a)

Tunnel invert bottom

I: unloading phase 1
II: unloading phase 2
III: Consolidation stage
IV: Pore pressure rise

(b)

Tunnel invert side

I: unloading phase 1
II: unloading phase 2
III: Consolidation stage
IV: Pore pressure rise

(c)
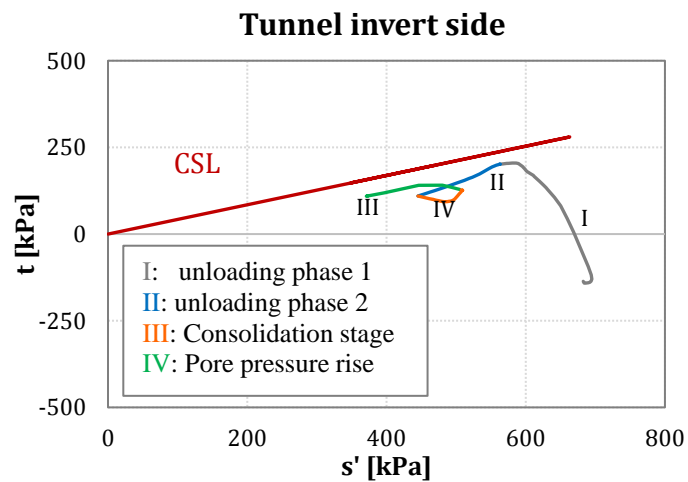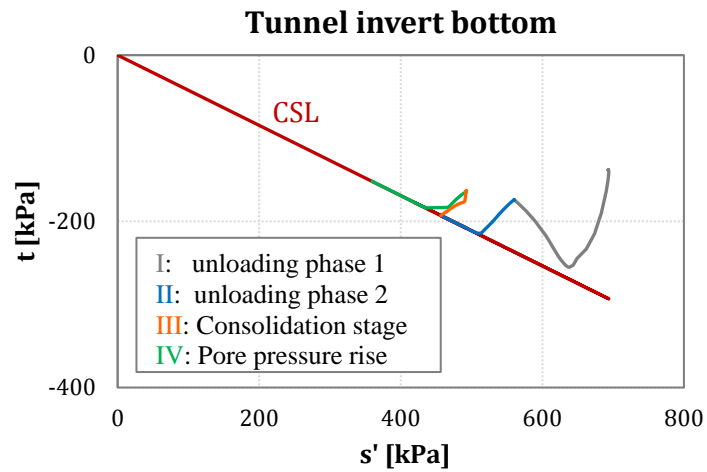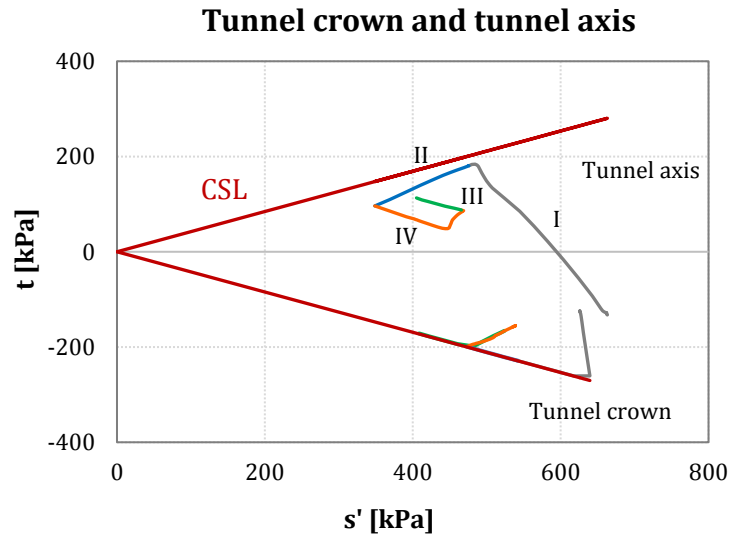
Figure 6.36. Computed stress paths for soil elements around the tunnel lining boundary by assuming the MC model for ground elements at: (a) the tunnel crown and the tunnel axis level, (b) the tunnel invert bottom and (c) the tunnel invert side.
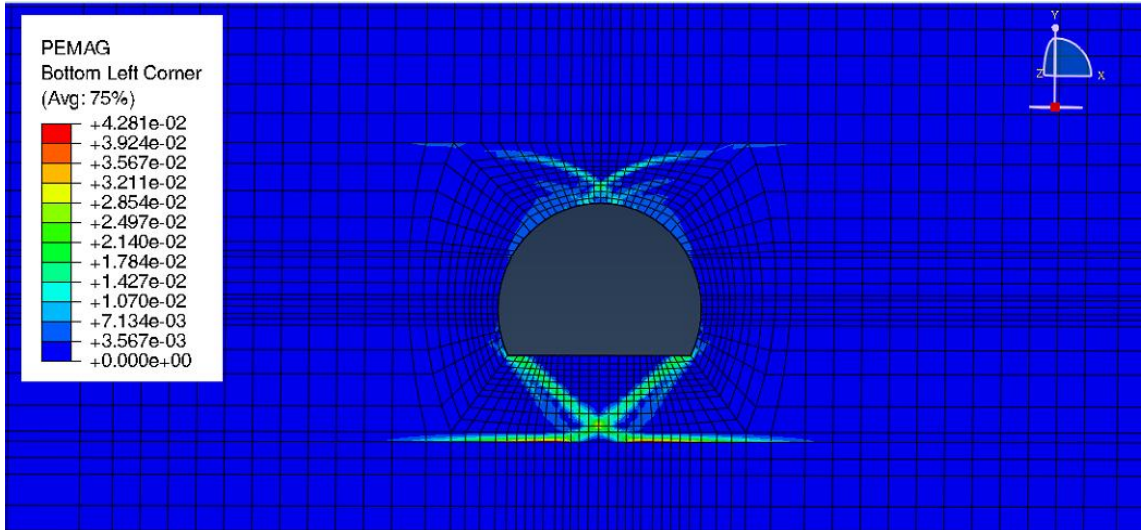
(a) End of unloading stage II
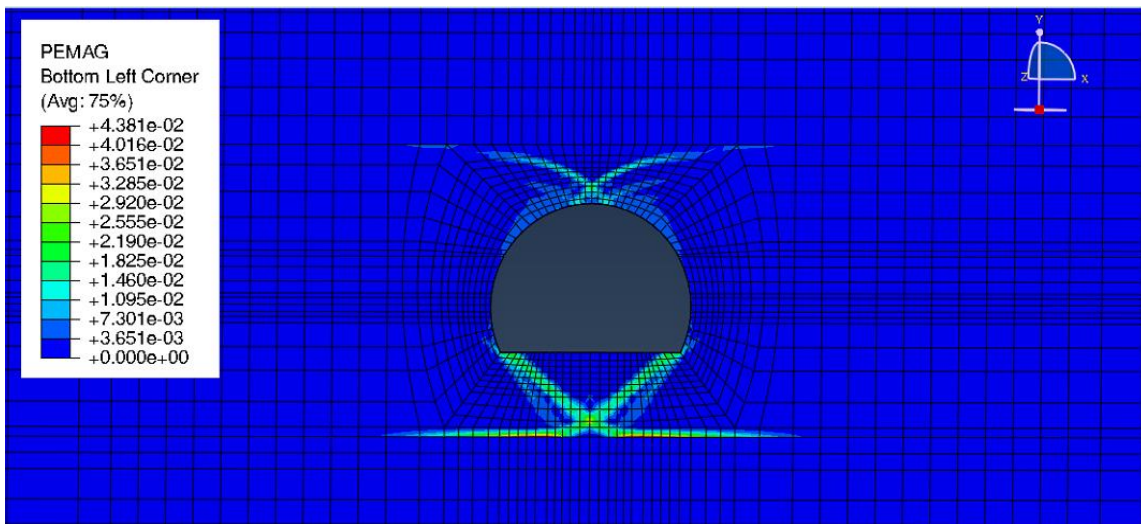
(b) End of 40-year consolidation stage
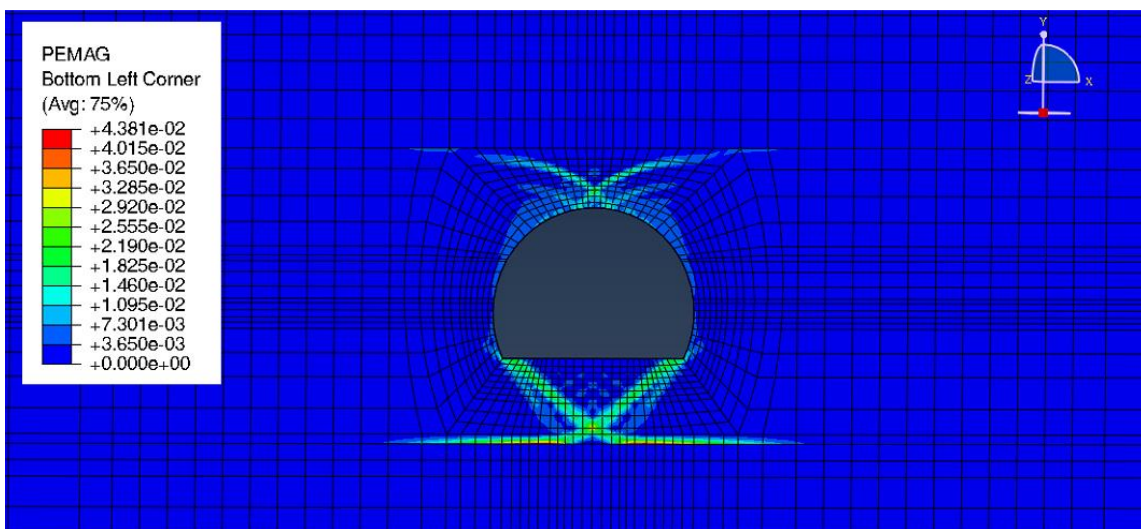
(c) End of pore pressure rise u= 197 kPa

Figure 6.37. Plastic strains development in the very weak marl layer by using the MC model: (a) end of unloading stage II, (b) end of 40-year consolidation stage and (c) end of application of the external pore pressure u=197 kPa.

The observed behaviour puts forward the importance to examine the range of layers within the rock mass in order to predict appropriately the tunnel lining mechanism of deformation.

6.6 Summary of key findings

A series of two-dimensional finite element analyses was performed to investigate the long-term behaviour of CERN tunnel lining. The numerical model is validated against field monitoring data (i.e. total station data and DFOS data) by analysing the lining response when the hydraulic regime in the ground changes. The simulated FE model considers the in-situ features of a concrete-lined tunnel in the CERN underground network, simulating both short-term and long-term behaviours for one representative tunnel cross-section, considered to be the most critical one. Particularly, the model improved the understanding of lining behaviour when its permeability condition changes from fully permeable conditions (after tunnel construction) to impermeable conditions, as a result of a reduced capacity of the drainage system with time, leading to the generation of water pressure acting on the tunnel lining. This may have caused significant lining distress with time, resulting in a tunnel ovalisation as a deformation mode.

The computed results highlighted the importance of the groundwater regime and, therefore, a change in the lining permeability on the lining performance. The main findings derived from the numerical study are summarized below:

- The model shows that the reduction of tunnel lining stiffness with time at each calculation phase produces the development of both total strain and change in tunnel diameter along the lining, but relatively small magnitudes were recorded. Thus, without as-built tunnel lining properties, and by considering that in sprayed concrete linings the concrete may change its properties due to long-term effects (i.e. shrinkage, creep), the assessment of lining stiffness being a reduced value soon after tunnel construction seems to be appropriate.

- The modelling of a reduced tunnel lining thickness improved the tunnel deformation response much closer to the field data. This is due to the reduction of the Moment of Inertia I of the tunnel lining section, which for a

rectangular beam cross-section is greatly influenced by the height of the beam (i.e. thickness d, with I= $bd^3/12$). Therefore, the assumption of a reduced value of tunnel lining thickness will produce both larger bending and axial strains, which are indirectly proportional to the bending and axial stiffness of beam elements respectively (EI and EA).

- The FE model shows that the tunnel lining deforms with a vertical tunnel elongation mechanism, resulting in a compression behaviour at the tunnel crown and tension at the tunnel axis level, in line with the DFOS data.

- By assuming the deterioration of the tunnel drainage pipes and, hence, a reduced capacity of the drainage system, the resulting magnitude of water pressure acting behind the outer edge of lining was back-calculated by fitting the result to the field data. The model has shown very good match of the change in tunnel diameter (i.e. horizontal and vertical) with the instrumented tunnel bolts data when a water pressure of u = 197 kPa (i.e. water table located at the interface with the moraine layer) is applied on the tunnel lining. Additionally, by comparing the computed total strains along the lining with the FO results of the loop 2-5, the tunnel lining at the crown seems to experience comparable magnitudes of total strains, whereas less significant values were seen at the tunnel axis level compared to those observed in the field. This behaviour may be due to the effect of the very stiff medium weak marl layer located at tunnel invert level on the development of tensile strains at tunnel springline. Moreover, the FE model considers the water pressure applied uniformly on the tunnel lining (fully impermeable tunnel lining), which may not be realistic due to localized seepage through the cracks.

    Overall, the FE models underestimated the strains obtained on site. This discrepancy may be associated with the attempt made for comparing the strain measured from the optical fibre attached to the lining through different hooks with the bending and axial strains computed from the FE results. Particularly, the adopted approach for assessing the bending strains was based on the calculation of the beam elements curvature along the tunnel lining, which may not provide accurate magnitudes of strains. Therefore, further investigations should be carried out for a more precise assessment of tunnel lining bending moments.

- A parametric study has been carried out in order to understand the effect of the layering formations surrounding the tunnel on the tunnel lining response during the application of the external pore pressure. Two different cases were examined: (a) the tunnel entirely located in a homogeneous layer of very weak marl, and (b) the tunnel located in the very weak marl unit at the tunnel crown and in the medium weak marl at the tunnel invert (layered model). The computed results show that the layering within the molasse region affects the tunnel lining deformation mode in the long-term. The distinct strain pattern along the tunnel lining of tensile and compressive strains at the tunnel axis level and the tunnel crown level respectively is observed when the layered model (b) is considered, whereas a compressive strain profile is computed for the tunnel located in the homogeneous formation, whose change of both horizontal and vertical diameter decreased with time. This behaviour suggests that the distribution of strains along the tunnel boundary is dependent on the ground formation's properties, as the layered formations contribute to the development of tunnel lining distortions (i.e. tunnel vertical ovalisation), whilst the homogeneous case exhibits a uniform compressive behaviour. This implies that the relative stiffness of the layered formations plays an important role when evaluating the tunnel lining response, due to the stiffer behaviour of the medium weak marl layer compared to the very weak marl.

- The increase in the coefficient of earth pressure K_0 of the *very weak marl* layer (i.e. $K_0 = 2$) leads to higher development of strains along the lining when the lining is subjected to the external water pressure, particularly at the tunnel crown, due to larger compressive axial strains computed at the tunnel crown. However, the effect of the change of the coefficient of earth pressure on tunnel lining response seems to be relatively small compared to the effect of the tunnel lining stiffness reduction.

- The influence of the properties of the *medium weak marl* layer on tunnel lining response was also investigated by reducing its stiffness and, therefore, considering a *weak marl* layer. Yet, this assumption has not improved the magnitudes of the computed total strains, especially at the tunnel axis level.

- Simulations with the advanced critical state soil model have predicted more realistic changes in the vertical and horizontal tunnel diameter, which are in agreement with the observational data.

- Within the model, the tunnel lining may exhibit further development of movements with time under the application of the maximum water pore pressure load at the considered tunnel depth (u=387 kPa). The computed FE results predict an increase in the horizontal and vertical diameter change for the potential future worst scenario. Particularly, the magnitude of vertical diameter change reached a value of 0.48 mm, whereas the horizontal diameter change increased to approximately -1.3 mm.

References

ABAQUS 2014. User's Manual, Version 6.14. SIMULIA. www.simulia.com

Alhaddad, M. (2017). Photogrammetric Monitoring of Cast-Iron Tunnels and applicability of empirical methods for damage. PhD thesis, University of Cambridge.

BTS (2004). Tunnel Lining Design Guide. Thomas Telford Publishing, London.

Di Murro, V., Li, Z., Soga, K., Scibile, L., (2018). Long-Term Behavior of CERN Tunnel in the Molasse Region. In *Proceedings of GeoShanghai 2018 International Conference: Fundamentals of Soil Behaviours*, 671–78. Springer Singapore.

Fern, E.J., Di Murro, V., Soga, K., Li, Z., Scibile, L., and Osborne, J.A. (2018). Geotechnical Characterisation of a Weak Sedimentary Rock Mass at CERN, Geneva. *Tunnelling and Underground Space Technology* 77 (July): 249–60.

Franzius, J.N., and Potts, D. M. (2005). Influence of Mesh Geometry on Three-Dimensional Finite-Element Analysis of Tunnel Excavation. 5 (3): 256–66.

Gue, C.Y., Wilcock, M., Alhaddad, M.M., Elshafie, M.Z.E.B., Soga, K. and Mair, R.J., (2015). The monitoring of an existing cast iron tunnel with distributed fibre optic sensing (DFOS). Journal of Civil Structural Health Monitoring, 5(5), pp.573-586.

Harris, D. (2002). Long-Term Settlement Following Tunnelling in Overconsolidated London Clay. *Geotechnical Aspects of Underground Construction in Soft Ground*, 393–98.

Laver, R. (2010). Long-Term Behaviour of Twin Tunnels in London Clay. PhD thesis, University of Cambridge.

Li, Z. (2014). Long-term behaviour of cast-iron tunnel cross passage in London clay. PhD thesis, University of Cambridge, UK.

Mair, R. J. (2008). Tunnelling and Geotechnics : New Horizons. Geotechnique. Vol. 58. No. 9: 695–736.

Mohamad, H. (2008). Distributed Optical Fibre Strain Sensing of Geotechnical Structures. PhD thesis, Department of Engineering, Cambridge University, UK.

Panet, M., and Guenot. A. (1982). Analysis of convergence behind the face of a tunnel. *Tunnelling '82*, London, pp. 197–204.

Parkin, R.J.H, Varley, P.M. and Laigle, F. (2002). The CERN LHC Project – Design and

Construction of large caverns in tight spaces. *Geotechnical Aspects of Underground Construction in Soft Ground*, Lyon.

Potts, D.M., and Zdravkovic, L. (1999). *Finite element analysis in geotechnical engineering: Theory*. Thomas Telford, London.

Potts, D.M., and Zdravkovic, L. (2001). *Finite element analysis in geotechnical engineering: application*. Thomas Telford, London, pp. 38-73.

Wang, K., Jansen, D.C., Shah, S. P., and Karr, A.F. (1997). Permeability Study of Cracked Concrete. Cement and Concrete Research, Vol. 27 (3): 381–93, USA.

Wilcock, M.J. (2017). The Behaviour of Existing Segmental Cast Iron Tunnel Linings Subject to Ground Movement from New Tunnelling. PhD thesis, University of Cambridge.

Wongsaroj, J. (2005). Three-dimensional finite element analysis of short-term and long-term ground response to open-face tunnelling in stiff clay. PhD thesis, University of Cambridge.

Yoon, J., Han, J., Joo, E., and Shin, J. (2014). Effects of Tunnel Shapes in Structural and Hydraulic Interaction. KSCE Journal of Civil Engineering, 18 (3): 735-741.

Zhang, D., Huang, H.W., Hu, Q.F., Jiang, F. (2015). Influence of multi-layered soil formation on shield tunnel lining behaviour.

Chapter 7

7 Effect of formation layering on tunnel lining response

7.1 Introduction

As described in Chapter 6, the long-term tunnel lining response in the molasse depends on the drainage conditions of the tunnel lining and the ground profile. This chapter aims to provide a more detailed picture of the concrete-lined tunnel behaviour through further 2D modelling. A parametric study is conducted to examine the formation layering effect within the molasse on the tunnel lining response, by considering the tunnel located at different depths from the ground surface. The computed change in tunnel diameter and the total strains along the lining are analysed and compared against field measurement data.

7.2 Finite element modelling

As described in Chapter 3, the divisions within the molasse were identified through a detailed geotechnical investigation based on the face-loggings recorded during tunnel excavation. Results from the previous Chapter highlighted the importance of simulating the range of different layers within the molasse in order to examine an appropriate tunnel lining mechanism of deformation that can match well to the observational data when the tunnel is subjected to a hydrostatic load. In particular, the changes in tunnel drainage conditions proved to greatly influence the lining deformation mode. To this end, further FE simulations are conducted in this study assuming the tunnel located at:

- Tunnel depth z_1 = 35 m from ground surface;

- Tunnel depth z_2 = 25.7 m from ground surface.

For each simulation, the bending and axial strains are obtained when the change of flow regime around the tunnel is made, enforcing a water pressure upon the lining. Moreover, the results computed during the ground consolidation stage are also analysed.

7.2.1 Case 1: tunnel depth z_1

This section describes the results obtained considering the horseshoe-shaped tunnel placed at 35 m from ground surface, with the tunnel crown located in the medium weak marl layer and the tunnel invert in the swelling-potential weak marl layer, as shown in Figure 7.1. The same ground properties adopted for the simulation documented in Chapter 6 are used in this study.
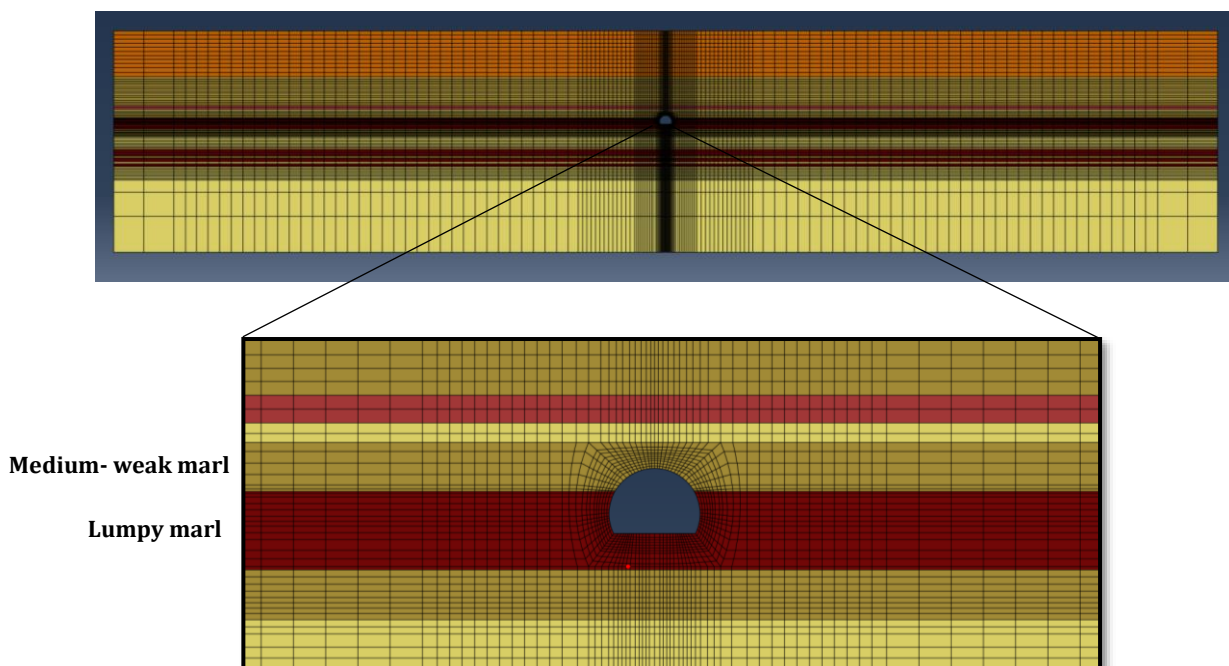
Figure 7.1. Ground profile at tunnel depth z_1 = 35 m from ground surface.

7.2.2 Case 2: tunnel depth z_2

This section presents the computed results obtained for investigating the tunnel lining response with the tunnel entirely located in the medium marl layer, at 25.7 m from ground surface (Figure 7.2).
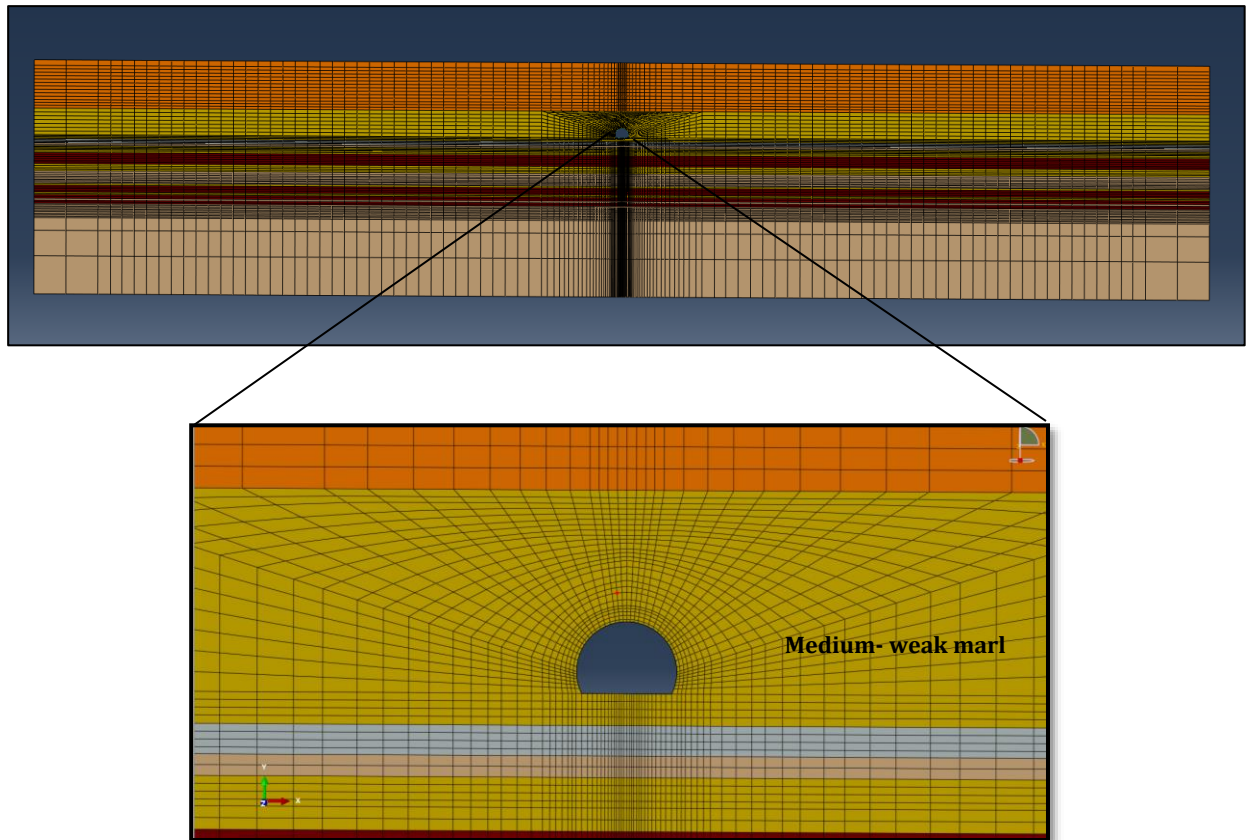
Figure 7.2. Ground profile at tunnel depth z_2= 25.7 m from ground surface.

7.2.3 Model assumptions

Based on the study carried out for the representative tunnel depth described in Chapter 6, the following assumptions are considered when analysing Case 1 and Case 2:

- The tunnel lining is modelled as a linear homogenous material, assuming a reduced value for Young's modulus and a reduced lining thickness (i.e. E = 5 GPa and d= 0.1 m respectively). Considering no as-built tunnel properties are known, the concrete of the SCL lining may change its properties due to long-term effects during tunnel construction (BTS, 2004). It is assumed that a reduced E value to be suitable.

- It is assumed that the tunnel drainage system reduced its capacity with time, causing a change in the flow regime around the tunnel and, hence, enforcing a water pressure to build on the lining. The water table level is therefore considered to be placed at the interface between the tunnel and the moraine layer (i.e. 19 m from surface). This implies that the hydrostatic

load behind the lining is 160 kPa for Case 1 and 67 kPa for Case 2 during a period of four years.

- The mechanical behaviour of the very weak marl layer is modelled by adopting both the advanced critical state soil model (ACSM) and the elasto-plastic Mohr-Coulomb model (MC), whereas that of the medium weak marl layer is modelled assuming the linear elastic behaviour.

As done in the previous chapter, the computed results for both tunnel depths are presented for the following three calculation stages: (a) the tunnel construction and initial consolidation stage (40 years), (b) water pressure rising stage and (c) a future scenario stage by simulating the worst tunnel drainage condition (i.e. the maximum pore pressure load).

7.3 Construction and initial consolidation stage

This section presents the results computed during the ground consolidation stage for both tunnel depths z_1 and z_2. Figure 7.3 indicates the changes in the tunnel diameter from the end of construction to the steady-state long-term consolidation (tunnel lining fully permeable) for the two cases, as shown in Figure 7.3a and Figure 7.3b. It can be seen that the steady state condition is reached very soon for both cases (Figure 7.3a and Figure 7.3b), as the pore pressures dissipate rapidly due to the very stiff soil surrounding the tunnel.

In Case 1, when the tunnel is located between the very weak and the medium weak marl layers (z_1) (Figure 7.3a), the change in the horizontal tunnel diameter increases of around 0.4 mm and 0.5 mm for the ACSM and MC models, respectively. At the tunnel crown the lining is converging inwards, reaching values of -2.9 mm with the ACSM and -1.2 mm with the MC model. This behaviour corresponds to a squatting deformation of the tunnel lining in the long-term, as shown in Figure 7.3a.

In Case 2, when the tunnel is located entirely in the medium marl layer (Figure 7.3b), both the vertical and the horizontal tunnel diameters are decreasing, reaching values of -0.2 mm and -0.08 mm respectively. Therefore, the tunnel lining is converging inwards in both vertical and horizontal directions, with the former showing a larger convergence. Yet, small values of displacements are recorded because the tunnel is constructed in a stiff elastic model.

Diameter change: consolidation - z_1

(a)

Diameter change: consolidation - z_2

(b)
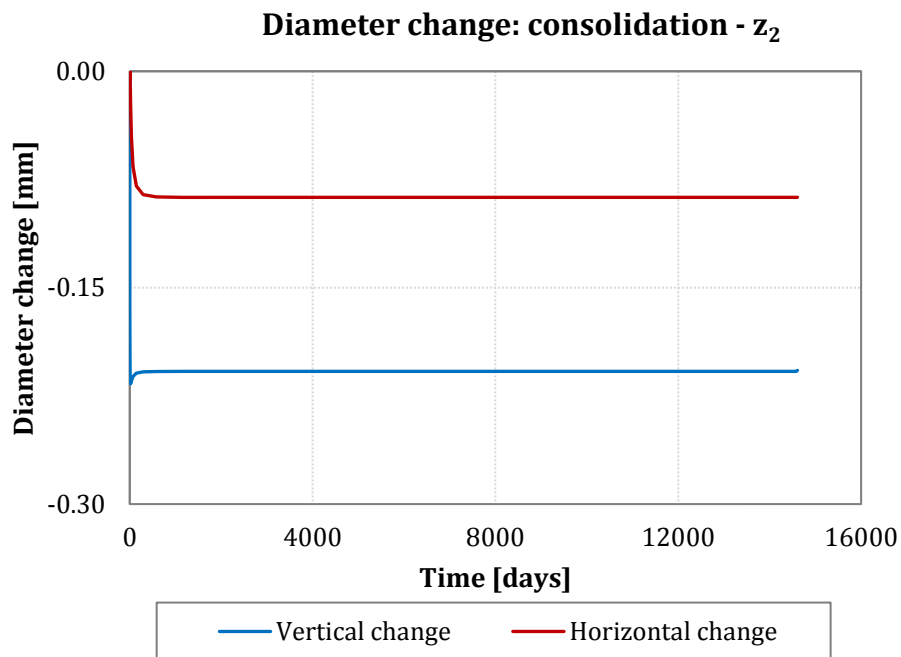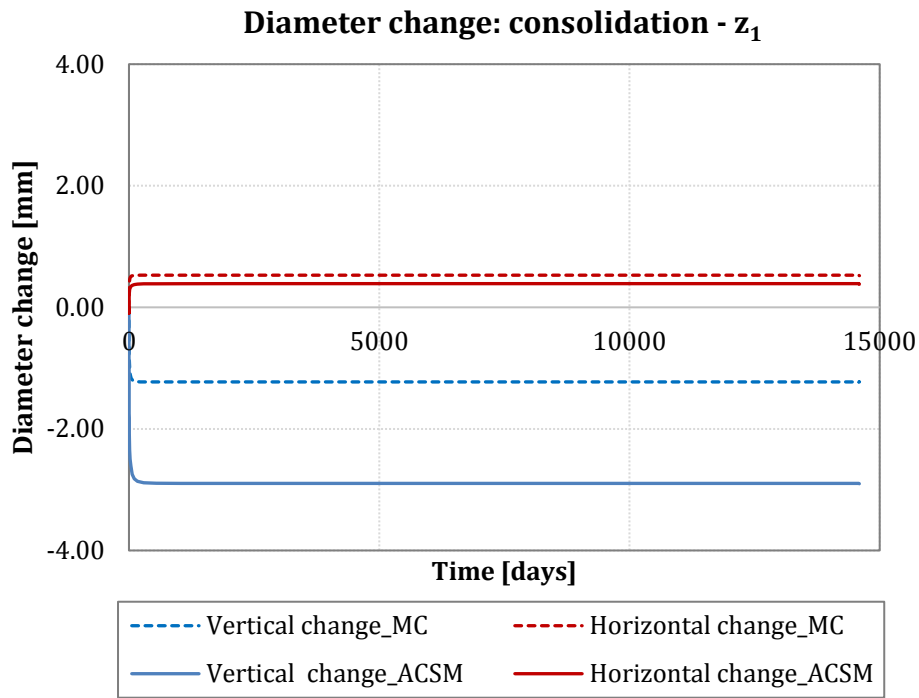
Figure 7.3. Change in tunnel diameter during the consolidation stage: (a) Tunnel depth z_1 =35 m and (b) Tunnel depth z_2 =25.7 m.

The computed results of axial, bending and total strains along the tunnel lining are plotted in Figure 7.4 for the two cases. In Case 1, larger total strains are computed at the tunnel axis level compared to that at the tunnel crown by adopting the ACSM. Positive total strains (i.e. tensile) develop at the tunnel crown, whereas negative strains (i.e. compressive) develop at the tunnel axis level (Figure 7.4a). The development of strains performed by using the MC constitutive model is shown in Figure 7.4b. Smaller magnitudes of total strains are computed at both the tunnel crown and the tunnel axis level compared to the ACSM (Figure 7.4b). However, both constitutive models show a similar trend of strain development along the lining, with tensile strains at the tunnel crown and compressive strains at the tunnel axis level, indicating a squatting deformation mode of the tunnel lining during the consolidation stage.

Figure 7.4c shows the computed strains in Case 2. Very small positive bending strains develop at the tunnel crown (i.e. around 1.5 $\mu\varepsilon$), whereas negative bending strains develop at tunnel sides. Negative axial strains develop along the lining, resulting in compressive total strains at both the tunnel axis and at the tunnel crown, as shown in Figure 7.4c.

(a)

(b)

(c)
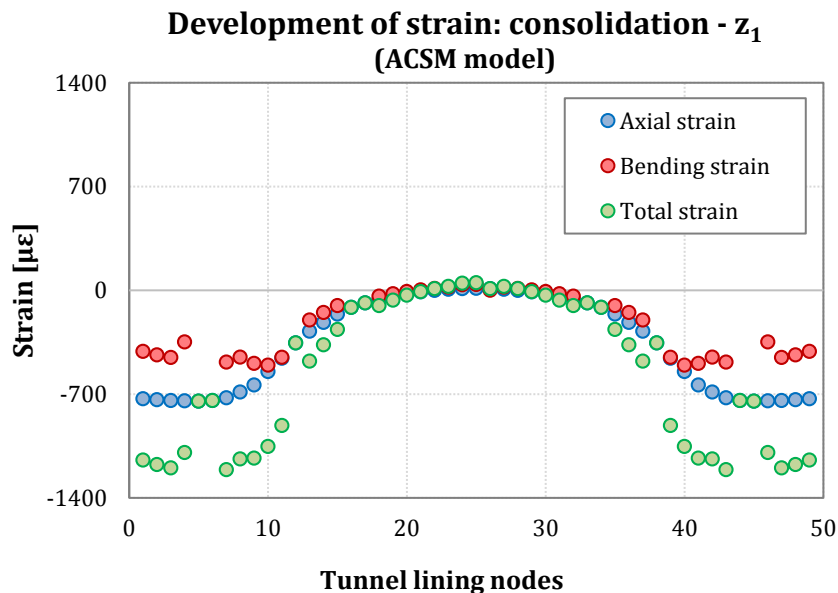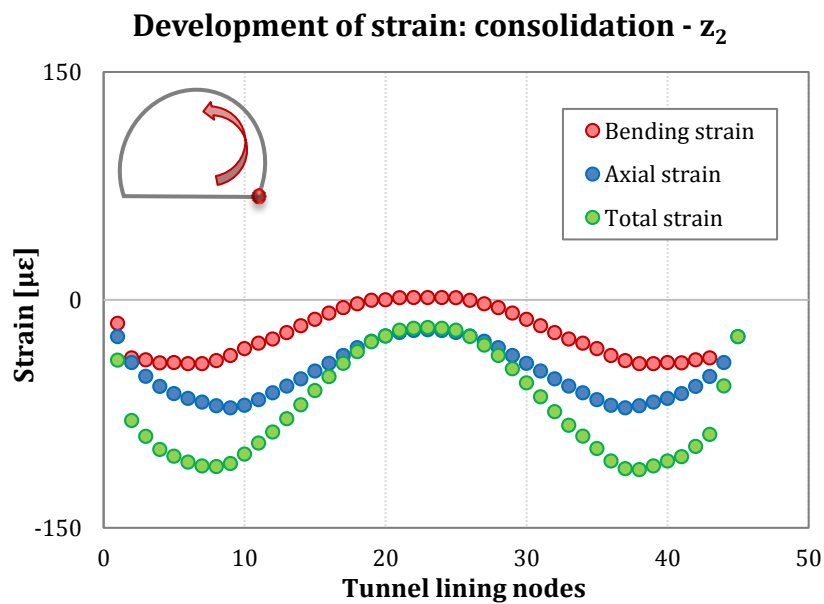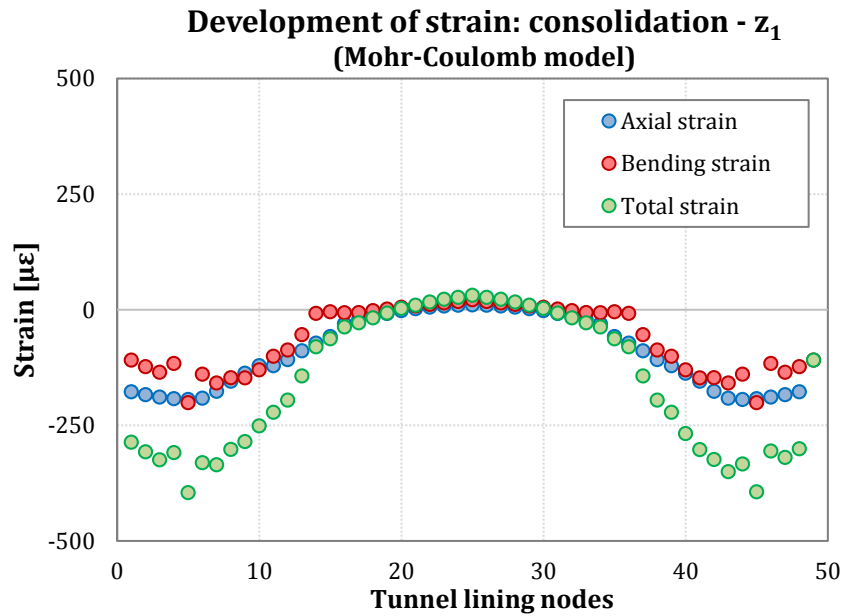
Figure 7.4. Development of strain along the lining during the consolidation stage: (a) Case 1 (ACSM), (b) Case 1 (MC), and (c) Case 2 using the linear elastic model.

Pore pressure

In Case 1, the pattern of pore pressure dissipation in the ground surrounding the tunnel during the 40-year consolidation stage is shown in Figure 7.5. After tunnel construction, negative excess pore pressure develops around the tunnel. The tunnel is fully drained (i.e. pore pressure equals to zero at the tunnel boundary) and the

ground consolidates due to pore pressure around the tunnel decreasing by seepage into the tunnel, until a new steady-state condition is reached. In particular, Figure 7.5 shows the dissipation of pore pressure after 1 day of ground consolidation (Figure 7.5a), after 10 days (Figure 7.5b), after 100 days (Figure 7.5c) and after 500 days (Figure 7.5d), when the consolidation stage is finished due to the very stiff rock units encountered. In fact, the bulk of tunnel diameter change shown previously in Figure 7.3 occurs within 200 days during the consolidation stage, after which the tunnel lining does not experience further movements.

The pattern of pore pressure around the tunnel is influenced by the layering formations within the molasse, which are characterized by different permeabilities, ranging from more permeable moraine layer going to the more impermeable marls.

Figure 7.5 (e)-(h) show the pore pressure dissipations for Case 2. Analogously to Case 1, the steady-state condition is reached after 500 days of ground consolidation (Figure 7.5h). But, due to the homogeneity of the soil surrounding the tunnel of Case 2, which is located in one layer of medium weak marl of 12 m depth, more uniform pore pressure contours are observed compared to the layered formations of Case 1.
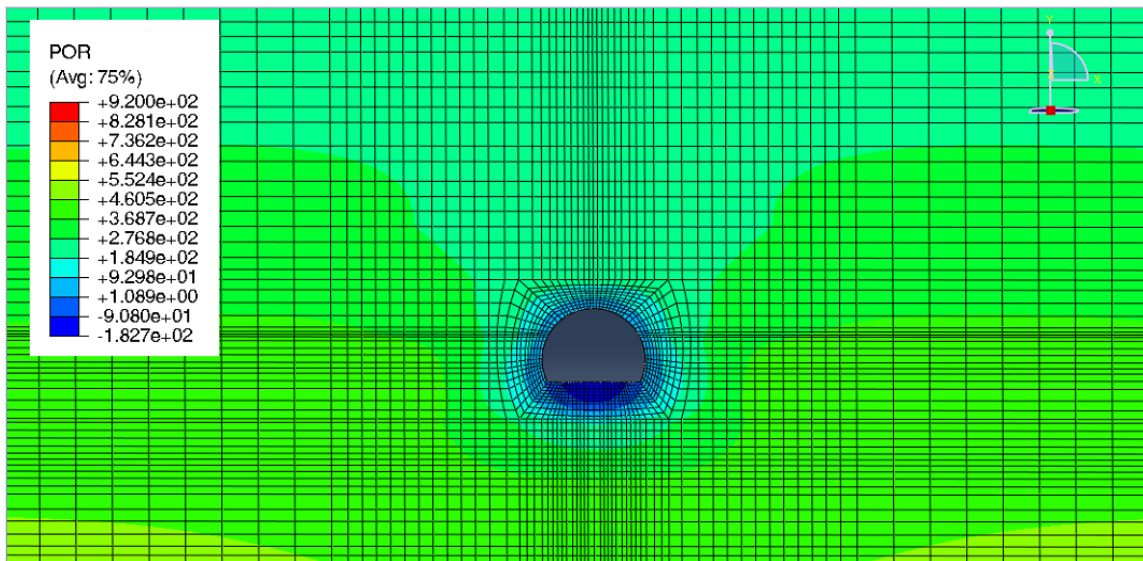
(a) after 1 day – Case 1
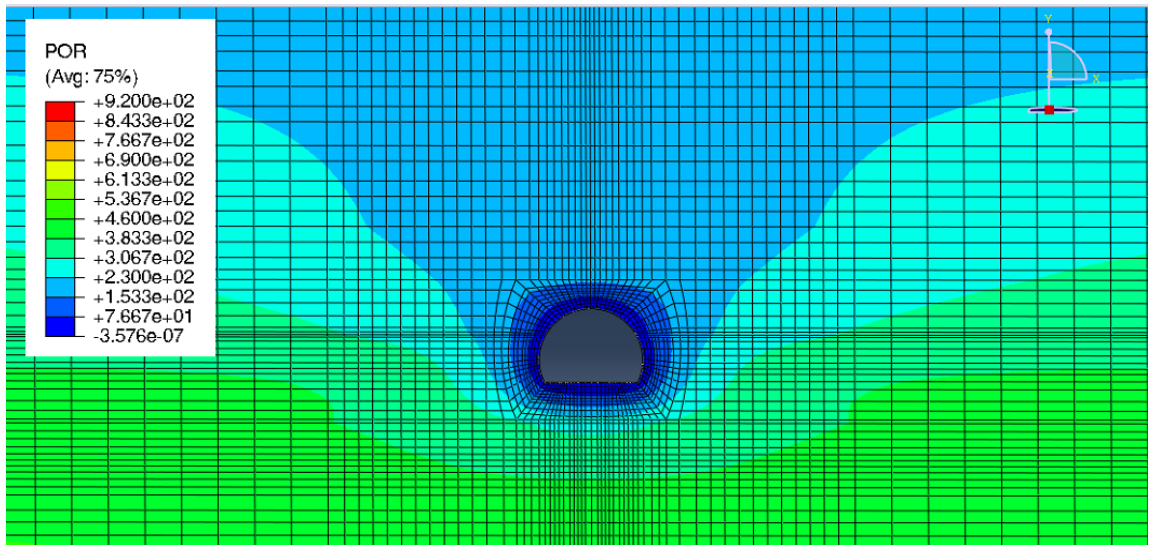
(b) after 10 days – Case 1
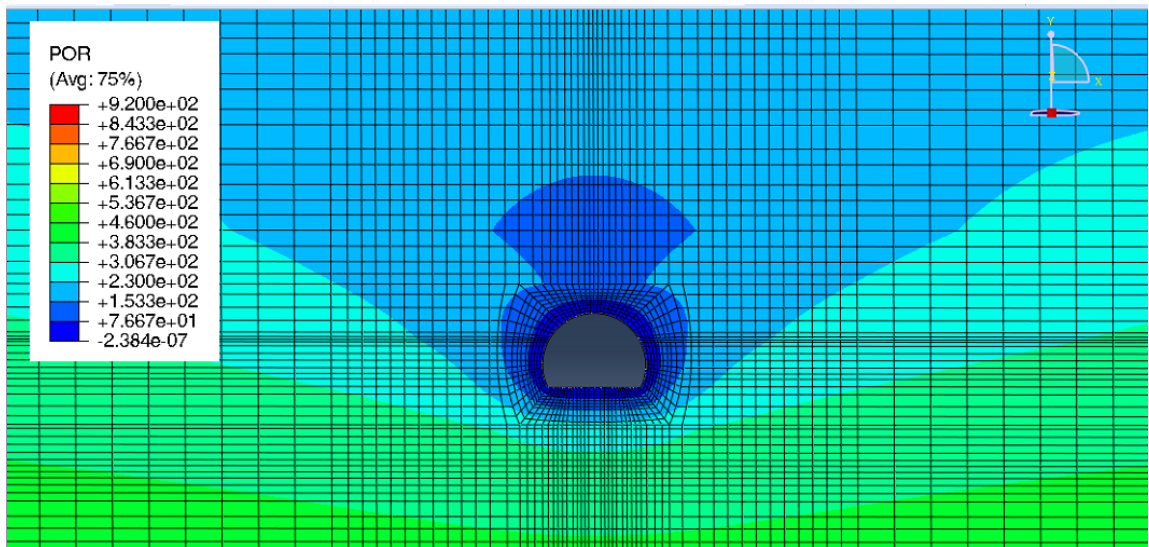
(c) after 100 days – Case 1
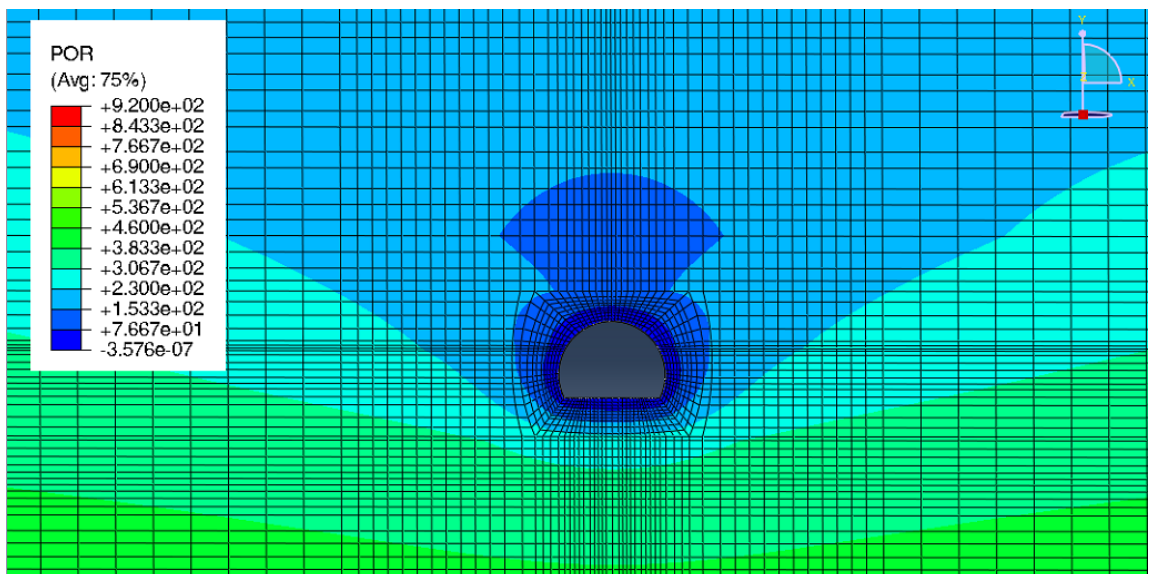
(d) after around 500 days – Case 1
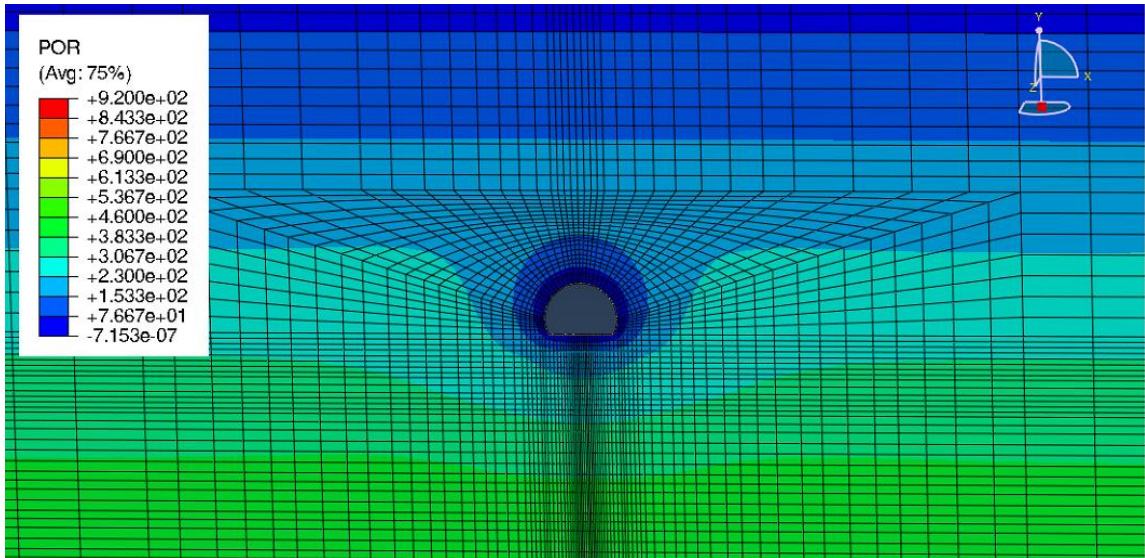
(e) after 1 day – Case 2
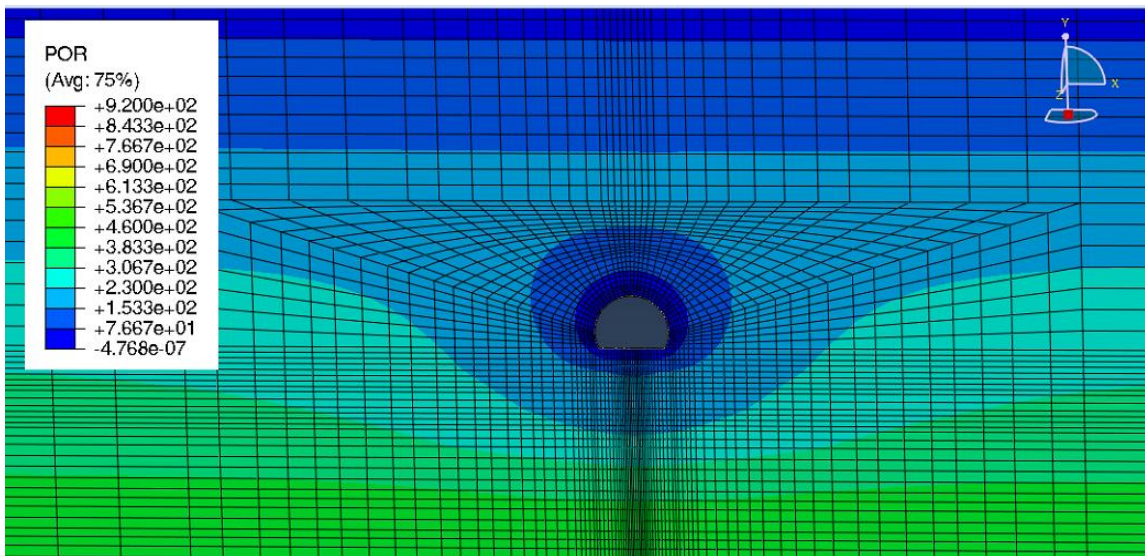
(f) after 10 days – Case 2
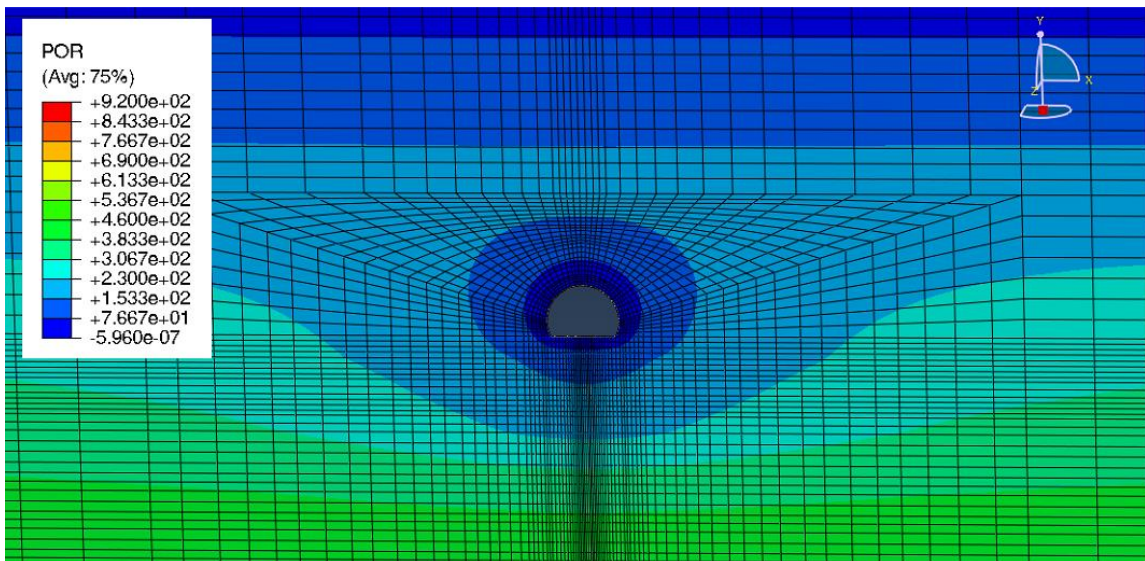
(g) after 100 days – Case 2
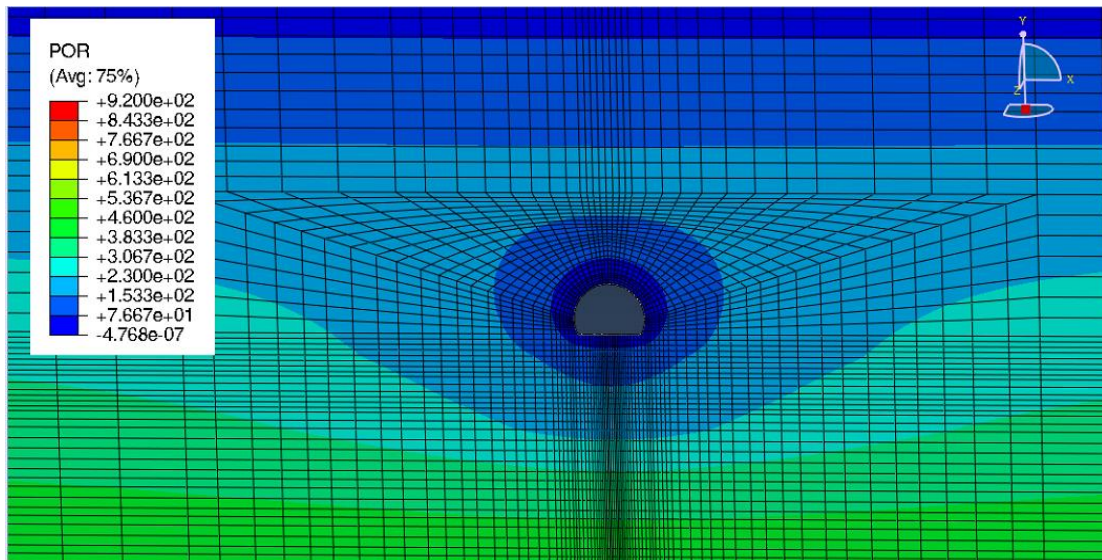
(h) after 500 days – Case 2

Figure 7.5. Dissipation of pore pressure during the consolidation stage for Case 1 and Case 2: (a) after 1 day – Case 1, (b) after 10 days – Case 1, (c) after 100 days – Case 1, (d) after 500 days – Case 1; (e) after 1 day – Case 2, (f) after 10 days- Case 2, (g) after 100 days – Case 2, (h) after 500 days - Case 2.

Stress paths of ground elements around tunnel lining

The computed stress paths in the $s' – t$ space of ground elements located right above the tunnel crown and beside the tunnel axis level during tunnel construction (unloading phase I and unloading phase II), ground consolidation and during the change in tunnel lining drainage condition are shown in Figure 7.6. Figures 7.6a and 7.6b refer to Case 1 by using the advanced critical state model (ACSM), whereas Figures 7.6c and 7.6d refer to Case 1 by using the Mohr-Coulomb model. The Figure 7.6e presents the stress paths of Case 2, where the Linear elastic model is adopted for modelling the homogeneous medium weak marl unit.

Figure 7.6b illustrates the stress paths for a very-weak lumpy marl element located beside the tunnel axis level by adopting the anisotropic model, whereas in Figure 7.6d the linear elastic perfectly plastic Mohr-Coulomb model was adopted. It can be seen that at tunnel axis the failure envelope is reached during the unloading phase II (Figure 7.6d). During ground consolidation (*stage III*), the mean effective stress s' increases as the excess pore pressures dissipate with time. When the lining undergoes a pore pressure increase on the tunnel lining (*stage IV*), the mean effective stress s' decreases as the pore pressure increases. Both constitutive models show that significant shearing does occur during tunnel excavation (stage I). However,

while the stresses do not reach the failure envelope at tunnel axis when using the ACSM (Figure 7.6b), the soil behaviour simulated with the MC model shows that during the stage II (unloading phase II with the installation of the tunnel lining) the soil reaches the maximum shearing stress condition (Figure 7.6d).

The stress paths of the ground located in the medium weak marl right above the tunnel crown of Case 1 are plotted in Figure 7.6a and 7.6c. Since the medium-weak marl rock unit was simulated with the linear elastic model, the failure condition is not reached for the mentioned ground elements.

The stress paths experienced by the ground at the crown and axis levels, located in the homogenous layer of medium weak marl of Case 2, are plotted in Figure 7.6e. The ground above the tunnel crown and adjacent the tunnel axis experiences similar shearing stresses during tunnel excavation.

(a)

(b)

(c)

(d)

Tunnel crown and tunnel axis -z_2
(in medium weak marl)

(e)
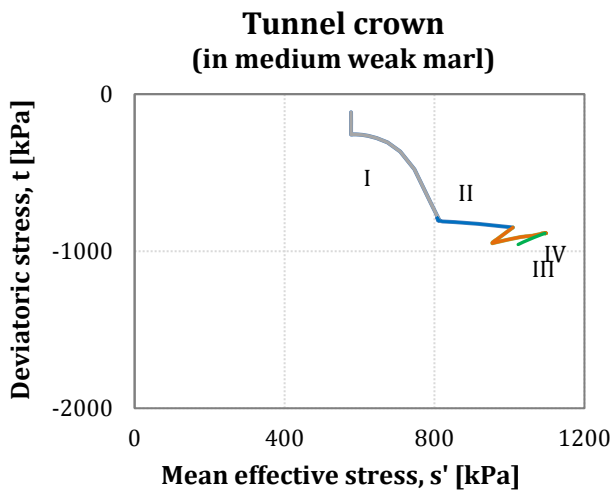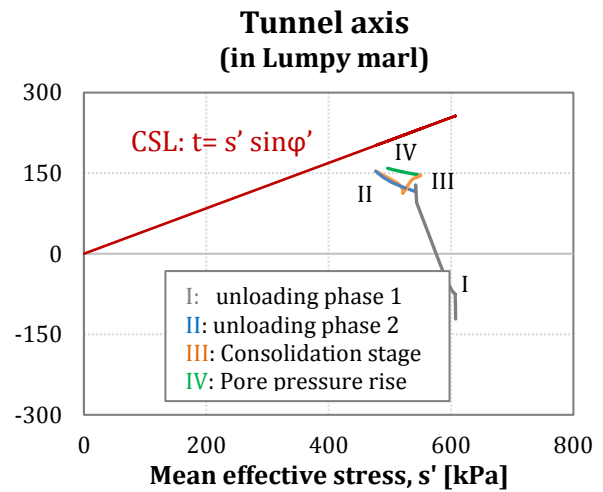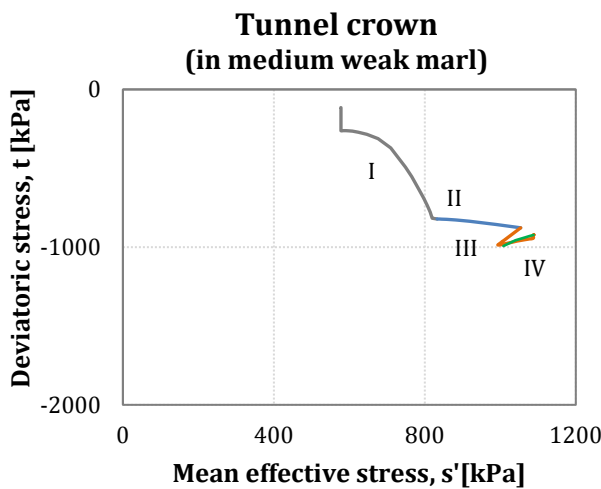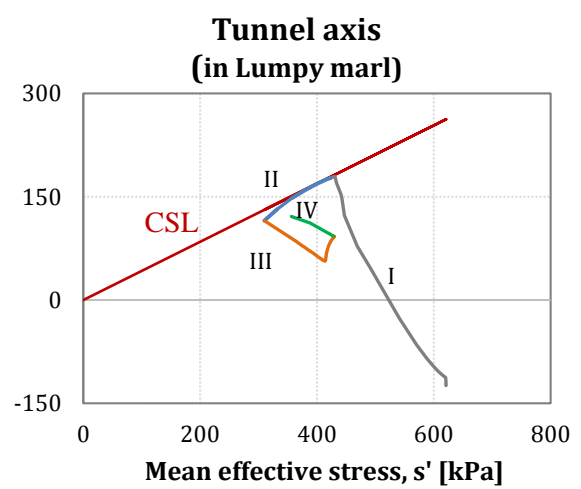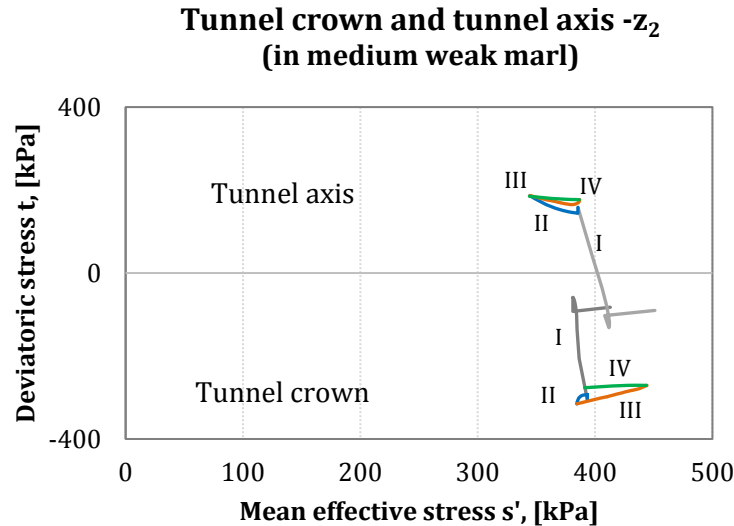
where the mean effective stress *s'* and the deviatoric stress *t* are evaluated from the effective vertical and horizontal stresses (σ'_v and σ'_h respectively):

$$s' = (\sigma'_v + \sigma'_h)/2 \qquad t = (\sigma'_v - \sigma'_h)/2$$

Figure 7.6. Stress paths for Case 1 and Case 2: (a) Tunnel crown with ACSM (Case 1), (b) Tunnel axis with the ACSM (Case 1), (c) Tunnel crown with MC model (Case 1), (d) Tunnel axis with the MC model (Case 1), (e) Tunnel crown and tunnel axis for Case 2.

Figure 7.7 shows the locations of plastic strains developed in the ground surrounding the tunnel in Case 1, by using the Mohr-Coulomb model (Figure 7.7a) and by using the advanced critical state model (Figure 7.7b). In Case 1, some plastic strains develop at the boundary between the medium weak marl layer (at the top) and the very weak marl unit (at tunnel bottom), for both the MC model and the ACSM model at the end of the consolidation stage. The pattern of shearing observed when adopting the MC model develops at both the tunnel invert corners, moving diagonally towards the lower interface with the medium weak marl layer, as shown in Figure 7.7a.

The ground around the tunnel crown does not exhibit any plastic strains, as it was modelled with the linear elastic model, while at the tunnel floor the ground experiences larger plastic strains compared to those around the tunnel axis when assuming the ACSM (Figure 7.7a). In fact, the vertical diameter change computed during the consolidation stage is more significant than the horizontal diameter change when using the ACSM, as shown previously in Figure 7.3a for Case 1.

Case 2 was modelled using the linear elastic model and, hence, there are no plastic strains.

However, the input parameters describing the soil behaviour for the ACSM, in particular the coefficients used to control the amount of plastic strains within the yield surface (u and m defined in Table 5.4 of Chapter 5), were assumed from Wongsaroj (2005) and defined for London Clay. Therefore, further investigations should be carried out on the molasse rock in order to calibrate more accurately the model.
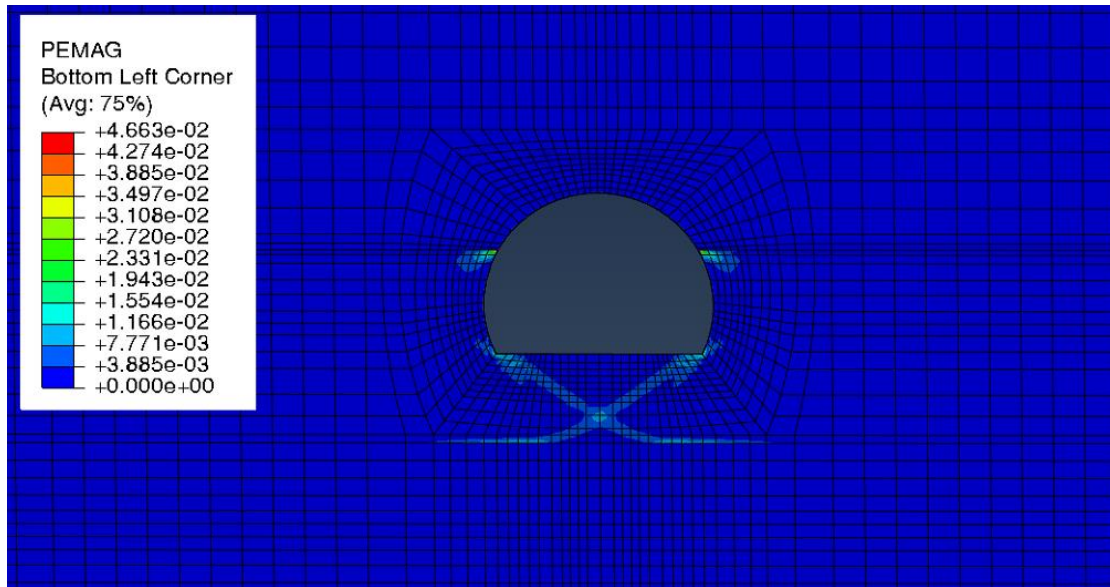
(a) MC model
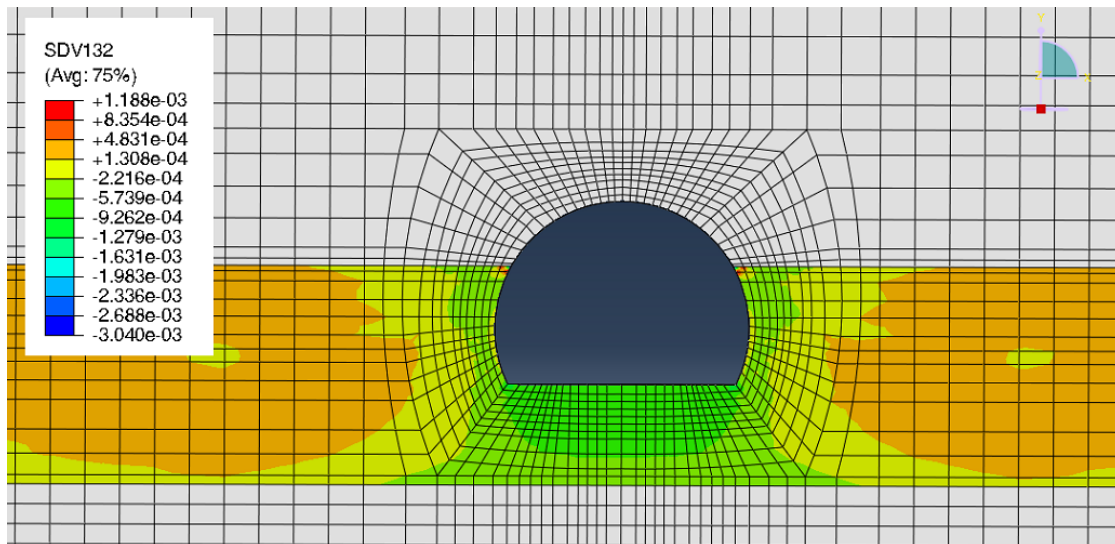
(b) ACSM model

Figure 7.7. Development of plastic strains around the tunnel lining at the end of the consolidation stage in Case 1 by using: (a) the Mohr-Coulomb model and (b) the advanced critical state model.

7.4 Water pressure rising stage

The changes in the tunnel drainage condition due to the clogging of the drainage system are simulated by applying a water pressure load on the tunnel lining. According to the results computed for the tunnel cross-section located at 38.7 m presented in Chapter 6, the hydrostatic load acting on the lining was evaluated by considering the water table at the interface with the moraine layer (19 m from ground surface). This condition was applied in both Case 1 and Case 2.

Figure 7.8 shows a comparison between the computed change in tunnel diameter and the conventional field measurements for Case 1 when the lining is subjected to an external water pressure of 160 kPa during the monitoring period (2013-2017). The tunnel lining experiences a gradual decrease in the horizontal tunnel diameter at both the tunnel axis level and shoulder and an increase in the vertical tunnel diameter. The FE model gives smaller magnitudes of the change in the horizontal diameter at the tunnel shoulder throughout the monitoring period when the ACSM model is assumed, compared to those observed in the field, as shown in Figure 7.8b. Similar behaviour is computed by the Mohr-Coulomb model, as shown in Figure 7.8. The vertical change in tunnel distances also shows slightly smaller values when assuming the ACSM compared to the field data, whereas the MC model provides slightly larger values, as shown in Figure 7.8c. The change in the horizontal tunnel diameter at the tunnel axis level shows a slow development of displacements with time, reaching approximately -1 mm against -0.81 mm observed on site when assuming the ACSM, as shown in Figure 7.8a. The horizontal distances computed with the MC model, instead, match well the field data during the first year (2013-2014), reaching a smaller magnitude at the end of the monitoring period (Figure 7.8a).

Overall, the computed FE results seem to underpredict the horizontal tunnel distances (at the tunnel shoulder level) and the vertical tunnel distances, compared to the slightly larger value computed at the tunnel axis level with the ACSM model. This discrepancy may be related to the assumption of considering the water table at 19 m from the ground surface, which was made for the representative cross-section of Chapter 6, as it produced a good fit with field data. This implies the generation of a uniform external pore pressure of 160 kPa on the lining for Case 1, which may not represent the reality due to the seasonal variability in the water table depth

following extreme rainfall events. However, the difference between the computed change in tunnel distances and the observational data is relatively small considering the uncertainty in the model parameters adopted in this study.

Additionally, the change in tunnel diameter indicates that the tunnel lining is experiencing a decrease in the horizontal tunnel distance (at both the tunnel shoulder and the tunnel axis level) and an increase in the vertical tunnel distance. This behaviour suggests a vertical tunnel elongation as a mechanism of deformation when the tunnel lining is subjected to a water pressure rise due to the drainage blockage.

(a)

(b)

Change in vertical distance

(c)
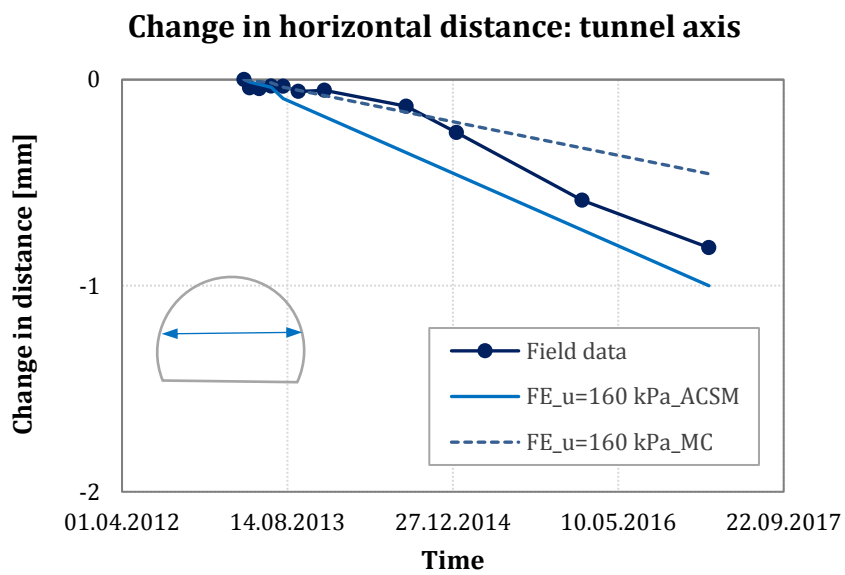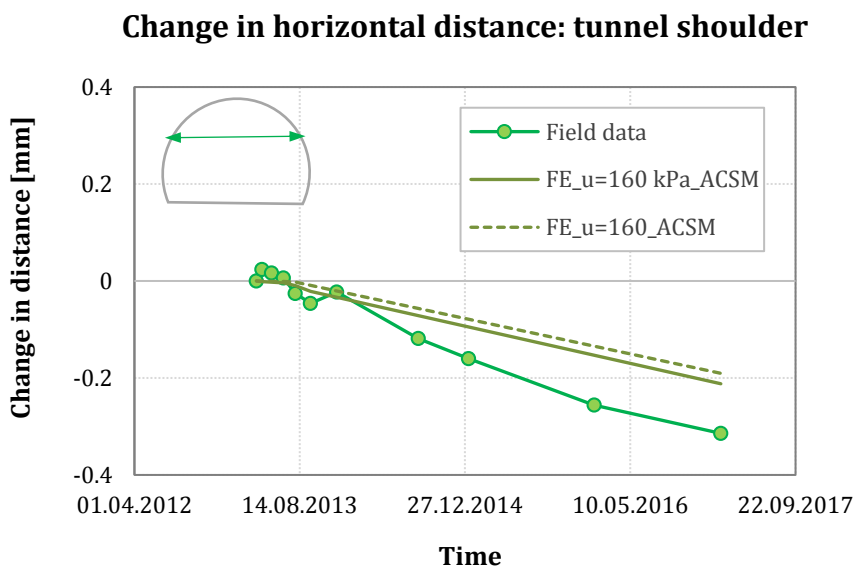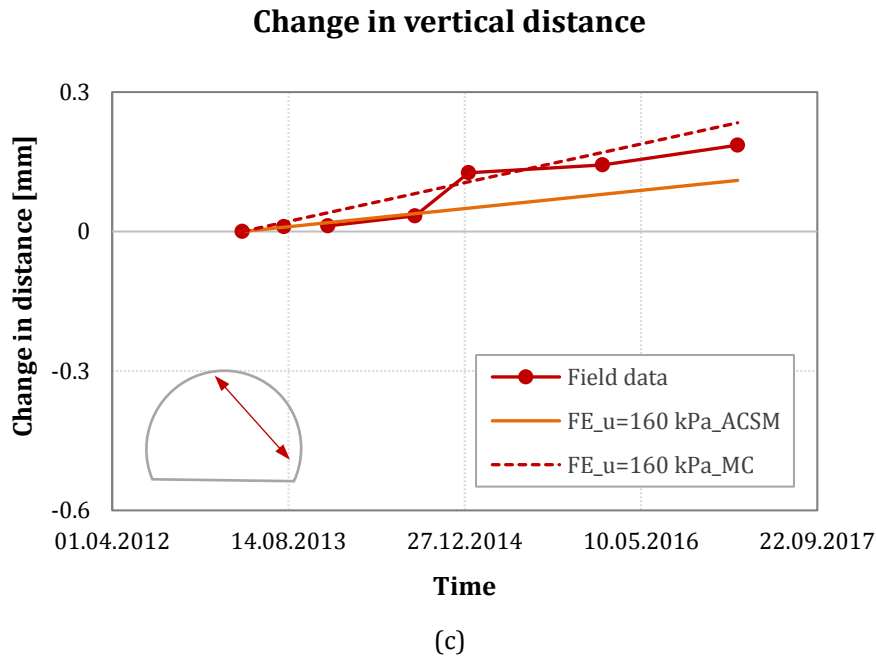
Figure 7.8. Computed change in tunnel distances and field data measurements for tunnel depth z_1: (a) horizontal distance at tunnel axis level, (b) horizontal distance at tunnel shoulder and (c) vertical distance.

As shown in Figure 7.9a for Case 1, a linear increase in vertical diameter is observed with time, whereas the horizontal diameter is decreasing. The magnitudes of the change in the vertical and horizontal tunnel diameter computed by ACSM are 0.83 mm and -0.95 mm respectively. When the Mohr-Coulomb model is used, the changes in diameter are around 0.24 mm and -0.46 mm. The observed behaviour for the layered model of Case 1 suggests that, when the lining is subjected to an external pore pressure of 160 kPa, the horizontal tunnel diameter decreases while the vertical one increases. This behaviour indicates a vertical tunnel lining elongation as a mechanism of deformation. The ACSM provides larger values of change in tunnel diameter compared to the MC model when simulating the tunnel drainage blockage. Also, the comparison with the field data has shown that the ACSM slightly underestimated the change in tunnel distances compared to the MC model but gives values closer to the observational data. The reasons may be related to the fact that compared to the MC model, the advanced critical state model takes into account the elastic anisotropic stiffness (i.e. the ratio G_{hh}/G_{vh} = 1.5 was used in this study and it is adopted from Wongsaroj, 2005), the plastic deformation within the yield surface and small strain stiffness and its non-linearity with strain response. Wongsaroj (2005) stated that for accurate prediction of pore pressure response and ground settlements, stiffness anisotropy must be incorporated in the elasto-plastic soil

model. Also, Wongsaroj (2005) noted that the Mohr-Coulomb failure criterion does not achieve a good agreement with the observed failure conditions for London Clay, compared to the Matsuoka and Nakai's failure criterion, which is considered in the ACSM. However, due to the lack of in situ and laboratory measurements, the model comprises some soil parameters evaluated for London Clay. Therefore, further investigations should be carried out in order to adopt more realistic ground parameters (i.e. stiffness values), which could reproduce the behaviour of the molasse region.

In Case 2, an external water pressure of 67 kPa (i.e. u= (25.7-19) *10= 67 kPa) is applied on the lining. Figure 7.9b shows the change in tunnel diameter computed for the homogeneous elastic model of Case 2. Both horizontal and vertical tunnel diameters increase with time, and very small values are computed due to the high stiffness modulus of the marl unit surrounding the tunnel (i.e. 0.018 mm and 0.04 mm respectively). The observed behaviour indicates that when the tunnel is located in a homogenous competent formation (medium weak marl) and the water pressure increases on the tunnel boundary, the tunnel diameter increases in both directions, with the vertical tunnel diameter exhibiting a slightly larger value than the horizontal one.

The behaviour in such mode results in a different tunnel lining mechanism of deformation compared to the layered model of Case 1 (i.e. vertical elongation). Similar behaviour was observed when analysing the layering effect on the tunnel lining response in Chapter 6, with the tunnel entirely located in the very weak lumpy marl (Section 6.5.4.1). However, in the latter case, the tunnel exhibited a decrease in both horizontal and vertical diameter when subjected to the external pore pressure, resulting in a tunnel convergence. Conversely, the results for Case 1 (tunnel entirely in the medium-weak marl) show a very small increase of tunnel diameter, suggesting that the lining is deforming outwards (i.e. expansion) when the water pressure builds up behind the lining.

Overall, the tunnel lining mechanism of deformation as a vertical tunnel elongation is computed only when the external pore pressure is applied on the lining, with the tunnel located in a layered formation (tunnel depth 38.7m and tunnel depth 35m). Conversely, when the tunnel is surrounded by a homogeneous layer (either very-weak or medium-weak marl) and the pore pressure increases along the lining, the lining converges inwards (for the soft marl layer) or deforms outwards (tunnel in

the stiff marl layer). This suggests that not only the tunnel lining drainage condition matters on the evaluation of tunnel lining response but also the layering formation surrounding the tunnel and the lining stiffness relative to the surrounding soil influence the lining mechanism of deformation. The different tunnel lining mechanisms of deformation will be compared and discussed in more detail in Section 7.6.
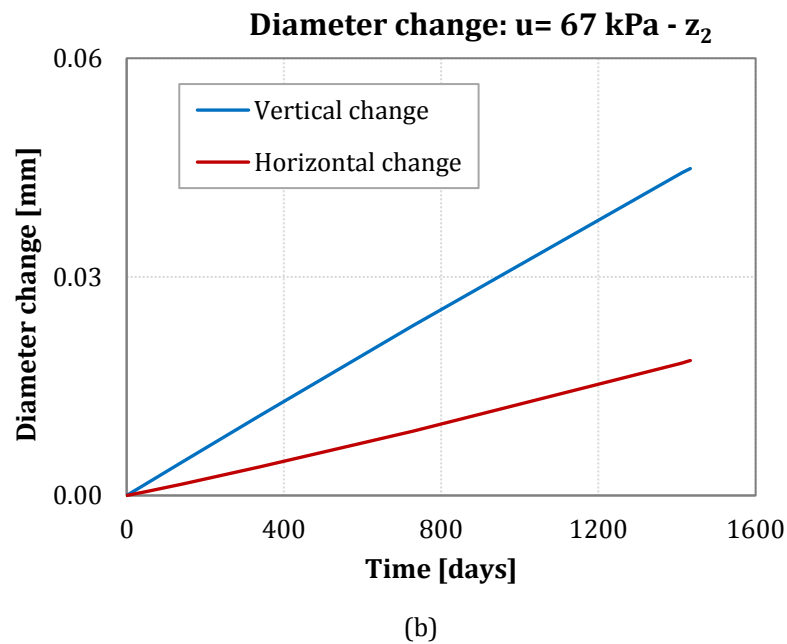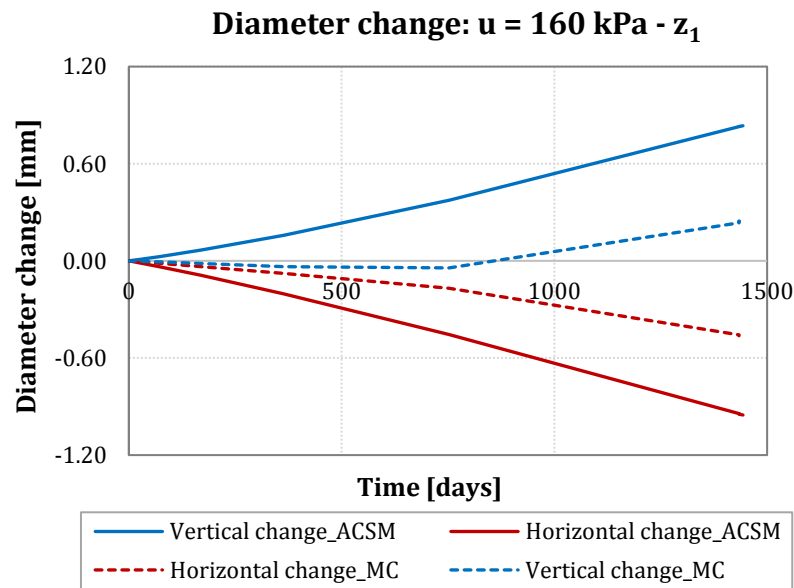

(a)

(b)

Figure 7.9. Change in tunnel diameter during the water pressure rise stage: (a) Case 1 and (b) Case 2.

In Case 1, as the tunnel drainage system deteriorates with time causing the accumulation of the water pressure behind the lining, positive bending strains develop at the tunnel axis level, whereas negative bending strains were performed at the tunnel crown, as shown in Figure 7.10a. Peak total strains values of around -55 με and 80 με are computed at the tunnel crown and the tunnel axis, respectively, when ACSM is used. When the Mohr-Coulomb model is used, peak total strains of around +12 με and 37 με are computed, which are smaller than those for the ACSM case.

Although the FE results suggest a tunnel lining mechanism of deformation in agreement with the one observed on the field from the DFOS, smaller values of total strains are computed when they are compared to the FO strain data obtained from the circumferential loop 2-4 of _CERN 2_ installation (peak strain values of 150 με at the tunnel axis and 120 με and the tunnel crown, See Figure 4.16d in Chapter 4). As discussed in the previous chapter, the discrepancy between the FE results and the observational data may be due to the assumptions in estimating strains detected by the optical fibre and the strains computed through the FEA. In particular, the total strains developed at tunnel lining are considered as a sum of axial and bending strains, with the latter being computed by calculating the beam element's curvature along the lining from the FE result. Conversely, the strain profile obtained from the FO data refers to the strain developed along the optical fibre that is attached to the tunnel lining intrados through discrete hooks, and not uniformly. Therefore, the attempt of comparing the strains obtained from the FEA and the FO circumferential loops may not be realistic. Future investigations should consider different approaches when comparing the FE results with the FO strain data.

Figure 7.10c shows the axial, bending and total strains developed at tunnel lining in Case 2, as the tunnel drainage condition changes (i.e. pore pressure of 67 kPa applied on the lining). Small negative bending strains are observed at the tunnel crown (approximately -1.2 με), whereas small positive bending strains develop at the tunnel axis level (around 9 με). However, the changes in axial strains in tension are computed along the lining due to the swelling of the surrounding soil. The computed strains refer to the accumulated strain response evaluated during the water pressure rise stage.

The strains computed from the FE model underestimate the results from field measurements. In particular, the FO axial strains of the loop 1-7 are around 150 με

at both the tunnel axis and the tunnel crown. However, due to the more competent rock unit surrounding the tunnel, the magnitudes of strain in Case 1 are smaller than Case 2.

The layered formation around the tunnel boundary seems to have a great influence on the tunnel lining response. In fact, the mechanism of tunnel lining deformation observed for both layered models of tunnel depth 38.7 m (from the previous chapter) and tunnel depth of 35 m (Case 1) indicates the development of tensile and compressive strains at the tunnel axis and the tunnel crown respectively, resulting in tunnel lining elongation as a deformation mode. This was not observed for the homogenous soil model of Case 2. Figure 7.10c illustrates the development of axial and bending strains for Case 2, where the tunnel is entirely located in the homogeneous medium-weak marl layer and it's subjected to the external pore pressure of 67 kPa. Small compressive bending strains are computed at the tunnel crown (i.e. around -1 με), while positive tensile strains are observed at the tunnel axis level (i.e. around 10 με). However, positive axial strains develop along the lining at both the tunnel crown and the tunnel axis of magnitudes of around 3 με and 15 με respectively. This resulted in the development of tensile total strains along the tunnel lining, albeit the small magnitudes computed. The observed behaviour indicates that the tunnel seems to experience relatively small tensile strains at both the tunnel crown and the tunnel axis when surrounded by a homogeneous medium weak marl layer and subjected to the external water pressure accumulated due to drainage blockage (Figure 7.10c).

Also, the change in the position of the marl and very weak marl layers around the tunnel led to different distributions of total strains along the lining. Larger strains (bending and axial) are computed at the tunnel crown compared to the tunnel axis level when the very weak marl layer is located in the top ground layer (i.e. tunnel depth 38.7 m of Chapter 6), whereas more significant strains are observed at the tunnel axis level when the very weak marl unit is placed at tunnel invert (Case 1 with the tunnel crown in the medium weak marl and the tunnel axis and invert in the very weak marl), as shown in Figure 7.10a. Therefore, the distribution of the strains along the tunnel lining seems to be influenced by the position of the very weak marl unit in the layered formation surrounding the tunnel. The mechanism of deformation of the layered formation will be discussed in more detail in Section 7.6.

(a)

(b)

Development of strain: u = 67 kPa - z$_2$
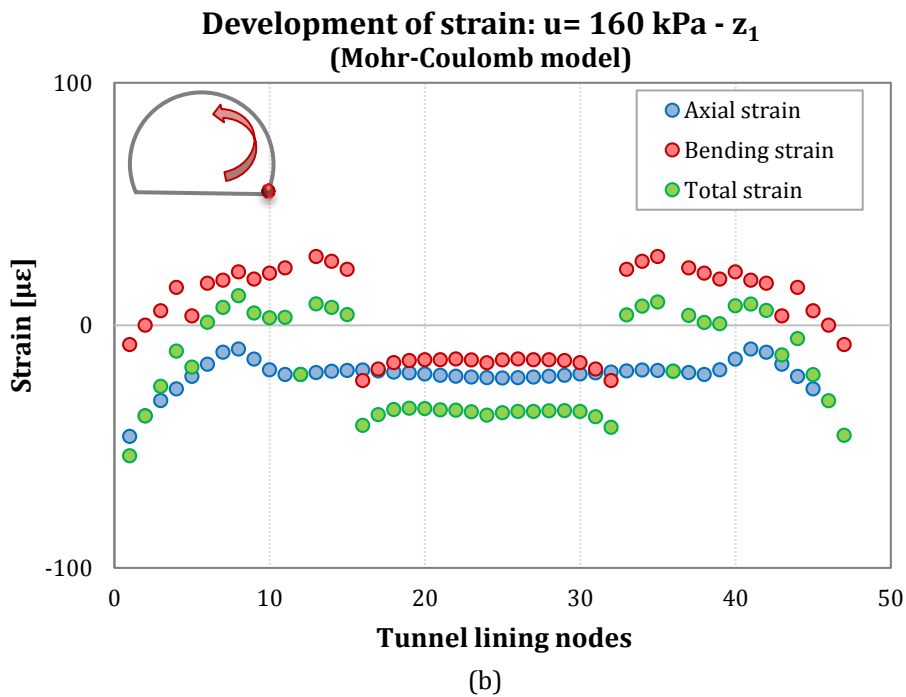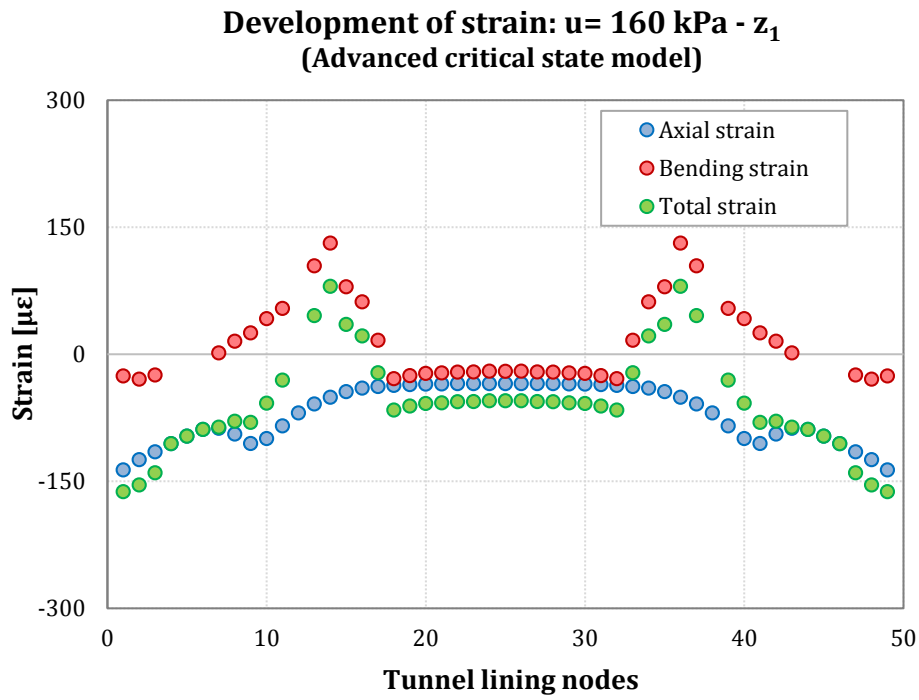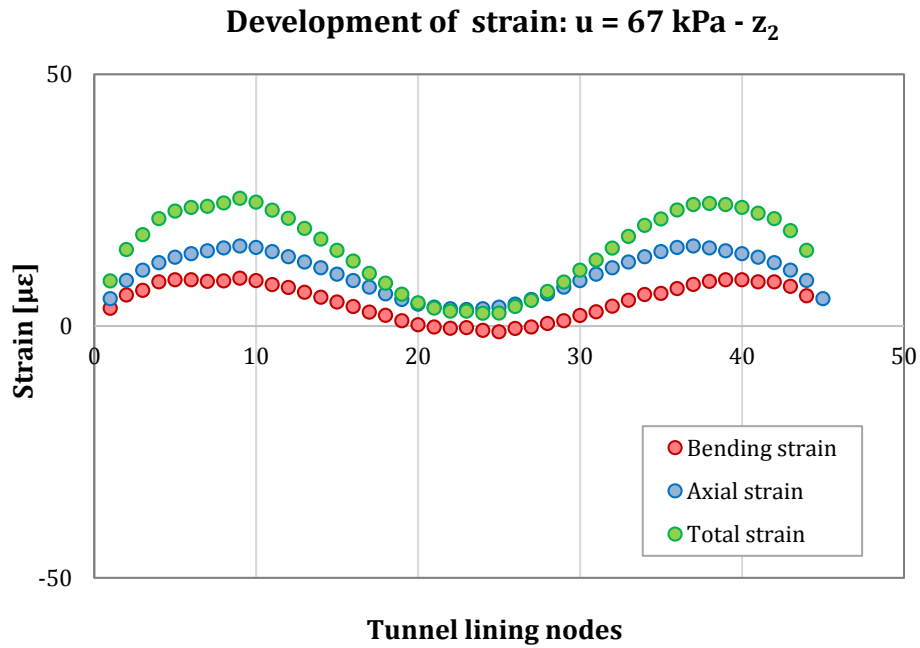
(c)

Figure 7.10. Development of strain along the lining during the application of the external pore pressure on the lining: (a) Case 1 (ACSM), (b) Case 1 (MC) and (c) Case 2 (Linear elastic model).

Figure 7.11 shows the pore pressure distribution during the application of the water pressure on the tunnel lining for Case 1 and Case 2 at the end of the 4-year stage. The change in pore pressure around the tunnel gave contours that seem to spread vertically in Case 1, whereas those computed in Case 2 spread more uniformly in the horizontal direction, as shown in Figure 7.11a and 7.11b respectively.
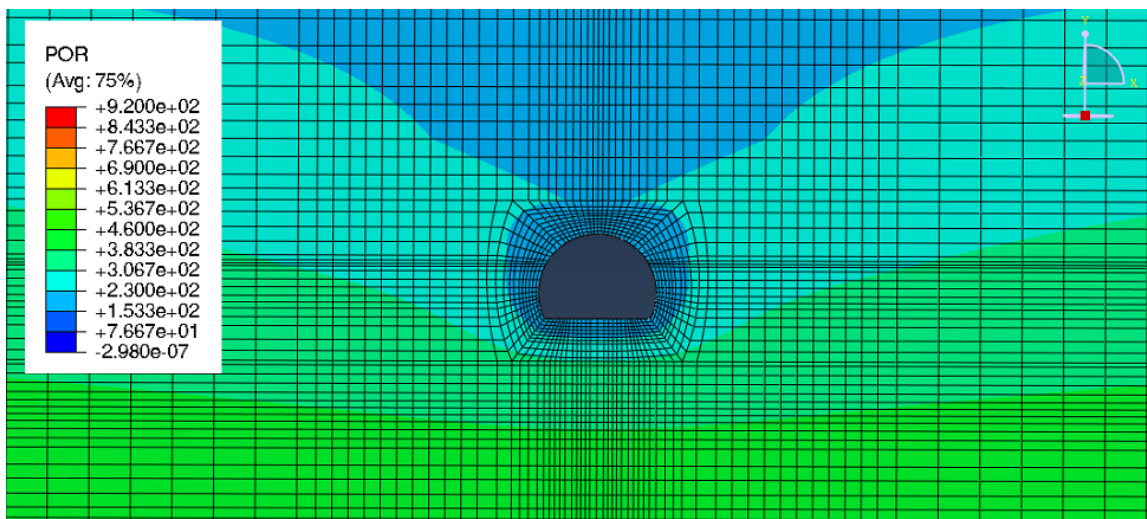
(a) Case 1 – end of pore pressure rise stage
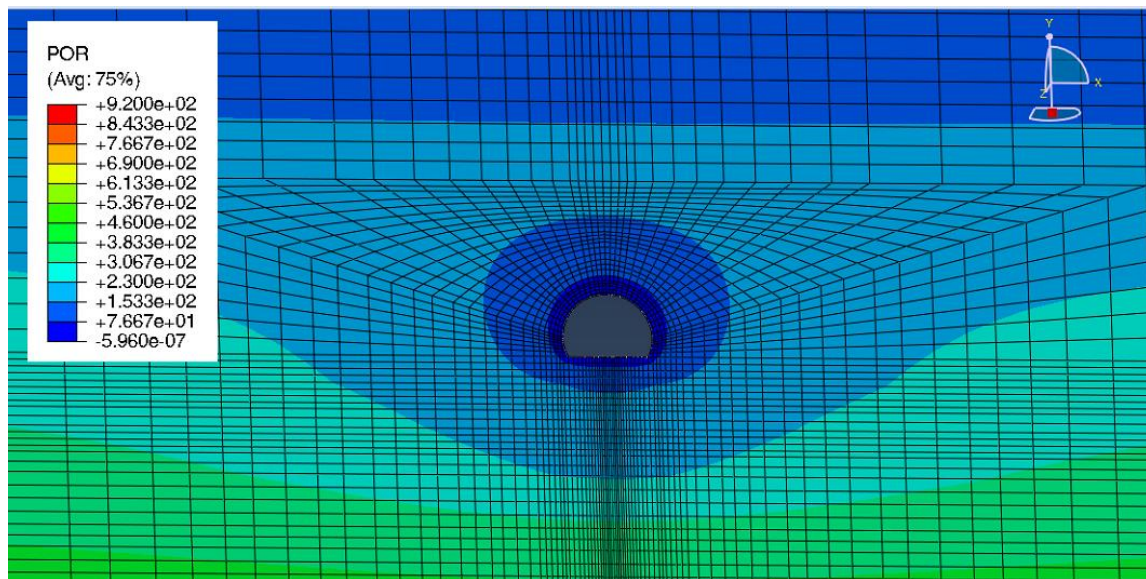
(b) Case 2– end of pore pressure rise stage

Figure 7.11. Pore pressure distribution during the water pressure rise on tunnel lining at the end of the stage (4 years): (a) Case 1 and (b) Case 2.

The development of the plastic strains in the ground surrounding the tunnel is shown in Figure 7.12 for Case 1, by using the Mohr-Coulomb model (7.12a) and the advanced critical state model (7.12b). During the water pressure rising stage, plastic strains develop not only at the interface between the two different marl layers (i.e. tunnel shoulder level) but also at the tunnel axis level, extending towards the tunnel invert and propagating diagonally to the lower boundary ground interface, by adopting the MC model (Figure 7.12a). Similar behaviour is computed around the tunnel perimeter when using the advanced critical state model, but slightly smaller magnitudes of plastic strains are computed. This indicates that the change in the tunnel lining drainage condition with the application of the external water pressure would cause further tunnel deformation around the tunnel boundary, developing plastic strains when the very weak marl layers are encountered.
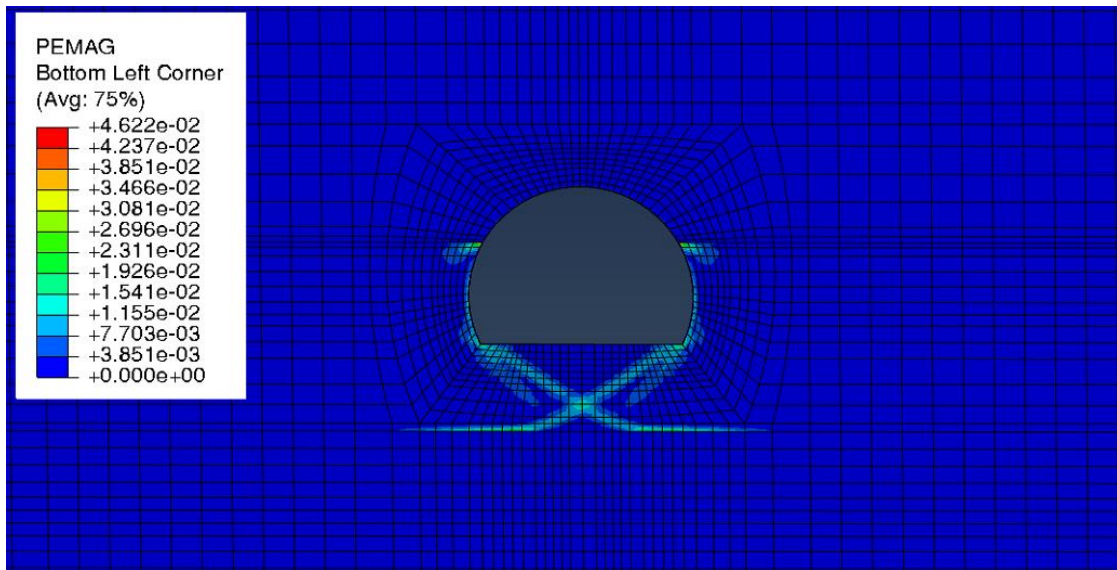
(a) MC model
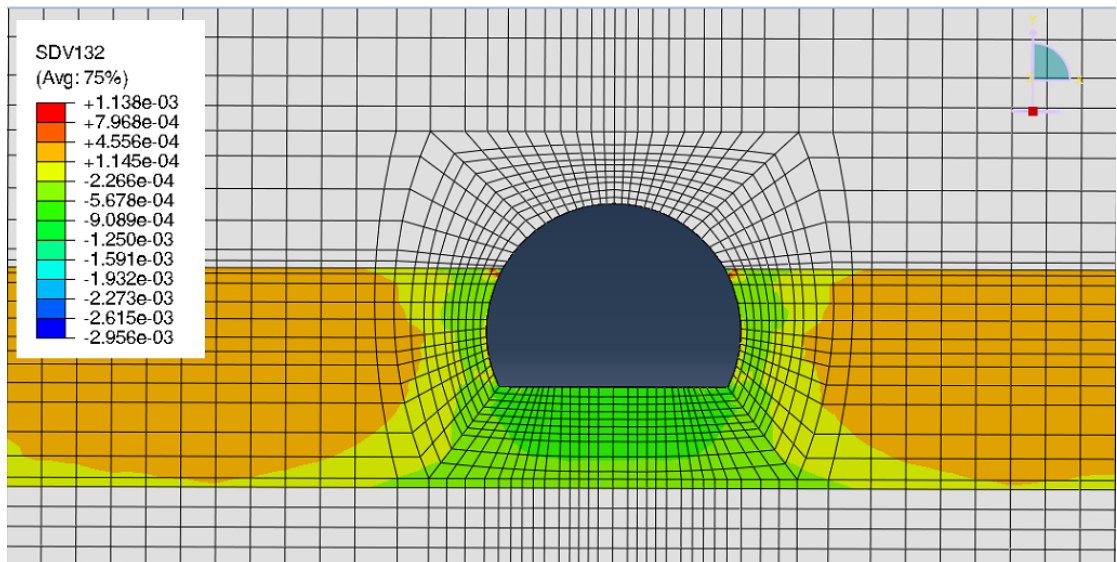
(b) ACSM model

Figure 7.12. Development of plastic strains around the tunnel lining at the end of the application of water pressure rising stage at tunnel lining for tunnel depth z_1 by using: (a) the Mohr-Coulomb model and (b) the advanced critical state model.

7.5 Future scenario stage

This section presents the computed results for the worst scenario case when the tunnel lining experiences the maximum hydrostatic water pressure (i.e. the water table reaches the ground surface). The tunnel lining response in terms of change in tunnel diameter was investigated for both Case 1 and Case 2.

The maximum water pressure load applied on the tunnel boundary is 350 kPa in Case 1 and 257 kPa in Case 2.

Figure 7.13 shows the computed change in tunnel diameter when the maximum hydrostatic load occurs at tunnel depth 35 m (i.e. u= 350 kPa) and by assuming a linear interpolation of the performed data, as discussed in Chapter 6. Therefore, if the tunnel lining is subjected to a water pressure of 160 kPa within a period of four years (2013-2017), the maximum load of 350 kPa would be reached within further 5 years (i.e. 2022).

For Case 1, Figure 7.13a shows the changes in tunnel distance at the tunnel axis level when the ACSM model is adopted, reaching a value of -2.28 mm under the maximum load of 350 kPa, whereas the MC model predicts a value of around -1.2 mm. A magnitude of –0.52 mm is computed at the tunnel shoulder level with the ACSM, against a value of -0.28 mm predicted by the MC model, as shown in Figure 7.13b. Also, Figure 7.13c shows that the tunnel lining experiences an increase in the vertical tunnel distances (distance between the tunnel crown and the tunnel invert side) of 0.52 mm when subjected to the maximum water pressure load by using the ACSM, whereas a final value of 0.44 mm is computed by the MC model. Overall, the tunnel lining exhibits an increase in the vertical distances and a decrease in the horizontal distances when the maximum water pressure is applied on the outer edge of tunnel lining, implying that the tunnel lining deformation pattern can be associated with a vertical elongation, as observed for the previous stage (i.e. water pressure rise).

Change in horizontal distance: tunnel axis

(a)

Change in horizontal distance: tunnel shoulder

(b)

(c)
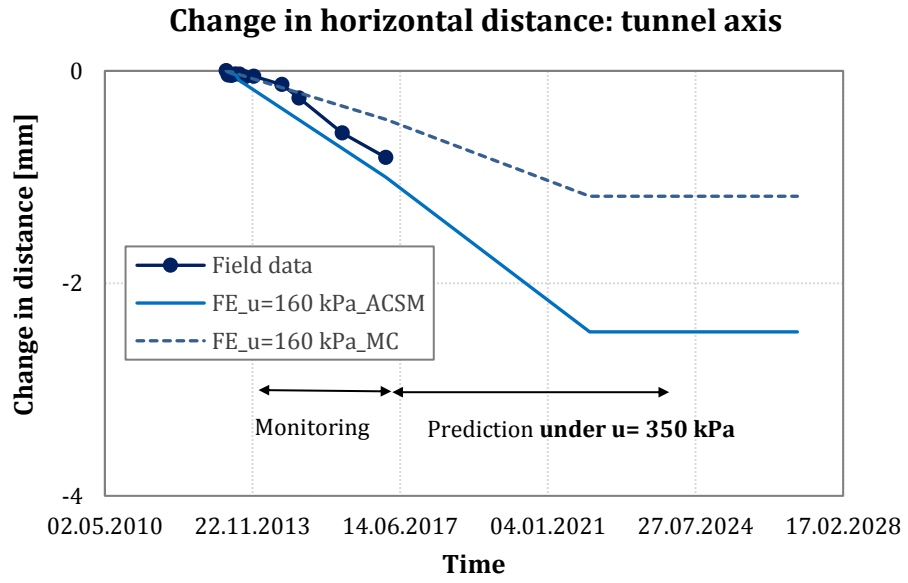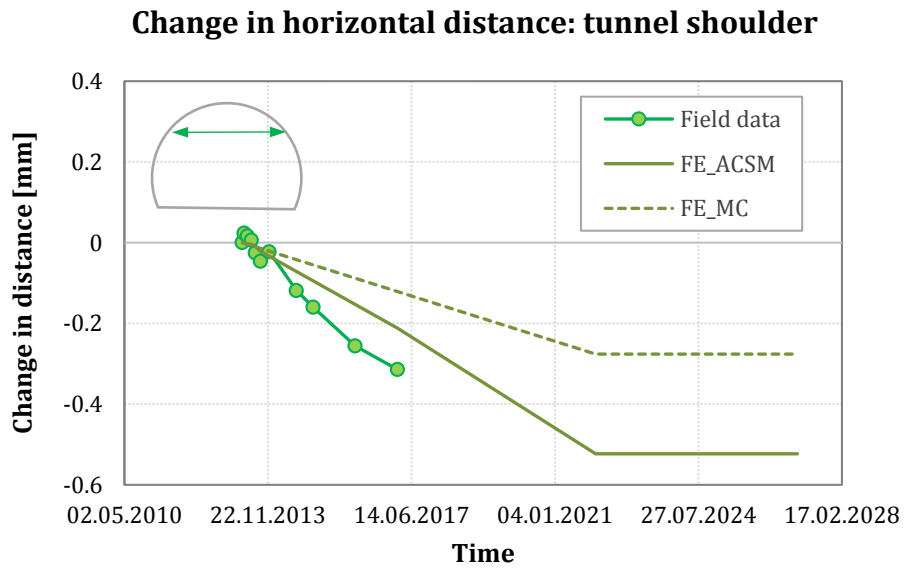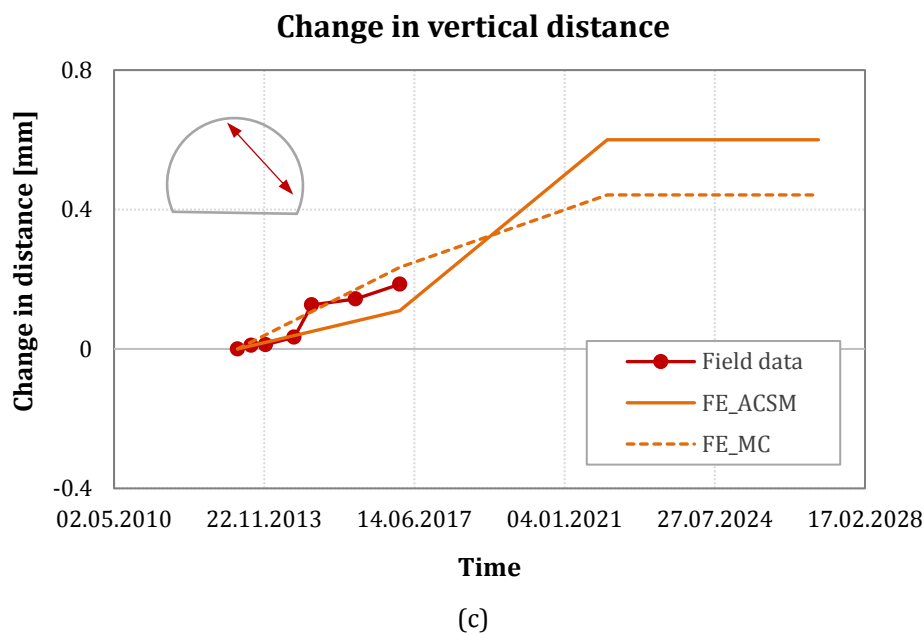
Figure 7.13. Prediction of change in tunnel distances under the maximum hydrostatic pressure load: (a) horizontal distance at tunnel axis level, (b) horizontal distance at tunnel shoulder and (c) vertical tunnel distance.

Figure 7.14 (a) and (b) show the performed changes in tunnel diameter when the maximum hydrostatic load is applied behind the tunnel lining in Case 1 and Case 2, respectively. In Case 1, the change of horizontal tunnel diameter (at the tunnel axis level) decreases to 1.3 mm, whereas the vertical tunnel diameter (tunnel crown – tunnel floor) increases of around -1.2 mm, by using the advanced critical state model. Slightly smaller magnitudes are computed with the MC model, recording a vertical diameter change of 1.18 mm and a horizontal diameter change of -0.87 mm. The observed behaviour suggests that the tunnel lining, when subjected to the maximum pressure load, exhibits an increase of the vertical diameter and a decrease in the horizontal, resulting in a vertical elongation as a deformation mode.

Figure 7.14b shows the change in tunnel diameter in Case 2 when the lining is subjected to the maximum hydrostatic load of 257 kPa. The tunnel lining experiences slightly larger vertical diameter change compared to the horizontal tunnel change, reaching approximately 0.1 mm and 0.07 mm within 10 years, respectively. This implies that the tunnel lining deforms with an increase of both tunnel diameter (vertical and horizontal) when the tunnel is subjected to a maximum water pressure load and is surrounded by a homogeneous formation. This deformation pattern suggests that the layering formation surrounding the tunnel in Case 1 allows the

tunnel lining to experience bending moments (i.e. tunnel lining distortions), whereas the tunnel lining placed in the homogeneous formation encountered in Case 2 is uniformly deforming by increasing the tunnel diameter at both the tunnel crown and the tunnel axis level (i.e. tunnel lining moving outwards).

(a)

(b)
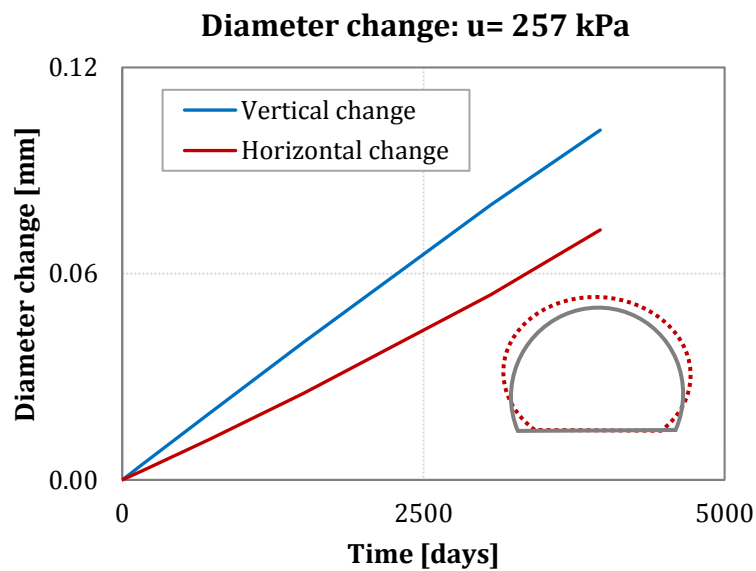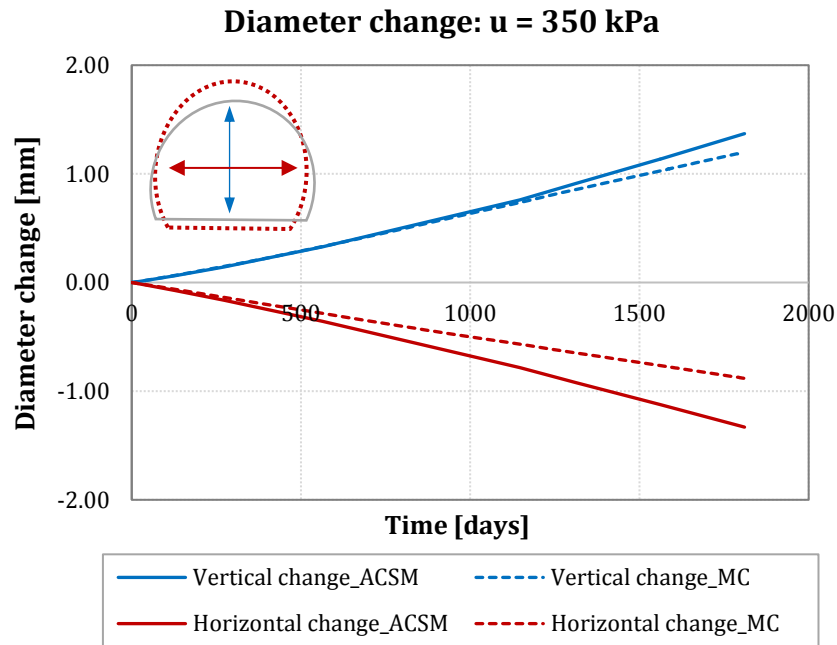
Figure 7.14. Change in tunnel diameter during the application of the maximum hydrostatic load on tunnel lining: (a) Case 1 and (b) Case 2.

Figure 7.15 shows the strain profile along the tunnel boundary in the future scenario case. Larger total strains develop when the lining is subjected to the maximum water pressure load compared to the previous water pressure rise stage for both tunnel depths. In Case 1, peak tensile strains of 117 µε and compressive strains of -66 µε are computed at the tunnel axis and the tunnel crown, respectively (Figure 7.15a). Positive total strains are computed at both the tunnel crown and the tunnel axis in Case 2 when the tunnel is surrounded by a homogeneous formation.

The FE results suggest that the structural behaviour of the tunnel lining is influenced by the patterns of layering formation surrounding the tunnel. Particularly, the tunnel lining deforms with a vertical tunnel elongation when the tunnel cross-section is placed in a layered formation (i.e. two layers). The tunnel lining behaviour is sensitive to the variation of soil properties (i.e. stiffness), as the medium weak marl unit exhibits a stiffer behaviour compared to the very weak marl. Further research should be carried out in order to gain a better understanding of layering formations on tunnel lining response.

(a)

Development of strain: u = 257 kPa- z_2

(b)
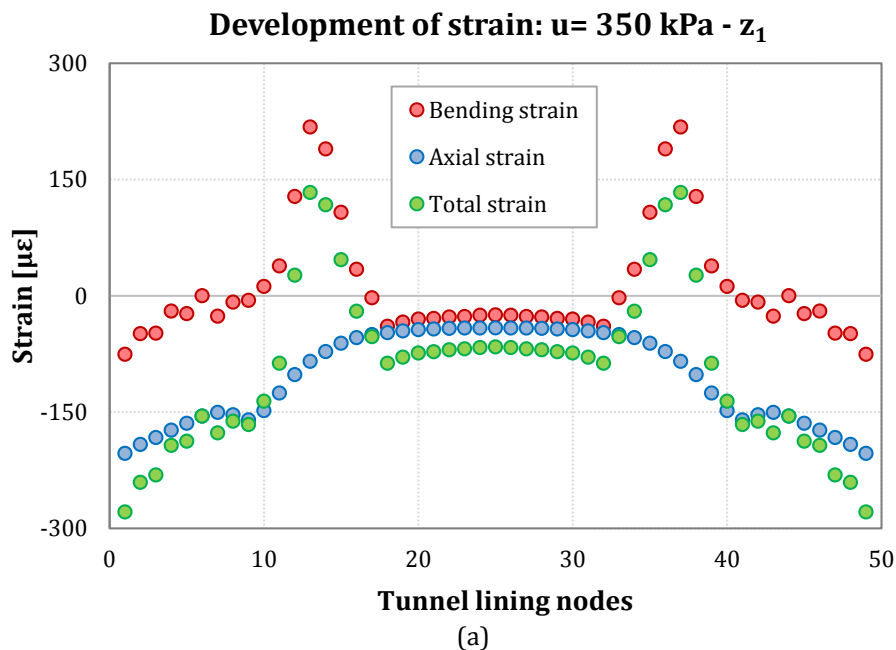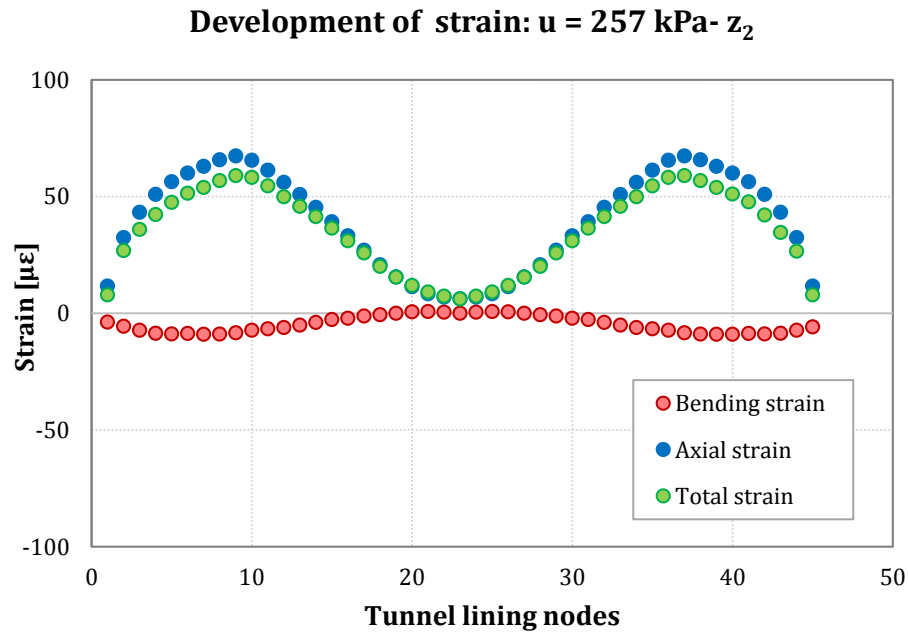
Figure 7.15. Development of strain along the tunnel lining when the maximum water pressure load is applied: (a) Tunnel depth z_1 and (b) Tunnel depth z_2.

7.6 Summary

The influence of the layering divisions on the TT10 tunnel lining response has been investigated through a series of FE analyses. Two different tunnel depths were analysed: tunnel depth z_1 and z_2 located at 35 m and 25.7 m from ground surface respectively. The tunnel lining performance of both tunnel depths was investigated during three different stages: (a) ground consolidation, (b) water pressure rise on the tunnel lining for simulating the tunnel drainage blockage and (c) a future scenario stage, which predicts the lining response under the worst water pressure load that might occur if the water table reaches ground surface.

As observed in the previous chapter, the progress of the deterioration of the tunnel drainage system and, hence, the application of the external pore pressure behind the lining resulted in a vertical tunnel elongation as a mechanism of deformation when the tunnel is placed in the layered formation, highlighting the importance of groundwater surrounding the tunnel on its long-term response. Also, for the layered soil configuration, it was found that the change in tunnel diameter and the distribution of the total strains are affected by the presence of the soil layering conditions, which led to the development of a different structural behaviour at the

tunnel axis and the tunnel crown, as shown in Figure 7.16a and Figure 7.16b for the layered formation.

Figure 7.16a shows that the tunnel is located between a very stiff marl layer around tunnel invert and a very weak marl unit around the tunnel crown (i.e. tunnel depth 38.7 m, examined in Chapter 6). This soil configuration suggests that the lining at tunnel axis level is influenced by the presence of the lower stiff layer, when subjected to the external water pressure, implying that the tunnel lining response at the tunnel axis is sensitive to the different behaviour of the two layers encountered. The lining surrounded by the very weak marl unit is prevented from deforming inwards (i.e. decrease in the horizontal diameter) and from developing large strains when subjected to the water pressure rise, due to the stiff response of the medium weak marl layer at the interface (Figure 7.16a). Such influence is not seen at the tunnel crown, where the lining is surrounded by a very weak homogeneous marl unit. The lining at the crown exhibits larger vertical movements than the tunnel floor and larger strains compared to those at the tunnel axis level, resulting in a vertical ovalisation.

Analogous lining behaviour is observed for the layered formation of tunnel depth 35 m of Case 1 shown in Figure 7.16b, which presents the opposite layering pattern, as the very weak marl layer is placed at the tunnel invert and the stiff marl layer around the tunnel crown. In this soil configuration, the lining at the tunnel crown does not experience large movements because of the competent rock unit encountered, while the tunnel at both axis level and invert is placed in the weaker swelling marl and experiences larger strains, resulting in a tunnel vertical elongation when subjected to the water pressure rise (increase in vertical tunnel diameter and a decrease in the horizontal diameter).

The tunnel lining deformation modes shown in Figure 7.16a and 7.16b become very critical for the tunnel lining performance due to the development of lining distortions, which can lead to damage of the tunnel lining such as cracking. This implies that the change in the groundwater condition around the tunnel many years after the tunnel construction as well as the layering formation surrounding the tunnel boundary play a crucial role in the tunnel lining response.

A different tunnel lining mechanism of deformation is observed for the homogeneous ground models shown in Figure 7.16c and Figure 7.16d. Figure 7.16c illustrates the FE model with the tunnel entirely located in the very weak marl layer,

examined in Section 6.5.4.1 of Chapter 6. This rock unit was modelled by assuming the advanced critical state model (Wongsaroj, 2005). When the tunnel is subjected to an increase of water pressure around the lining due to the tunnel drainage blockage, the ground surrounding the tunnel experiences a decrease in the effective stresses, becoming then a softer ground due to pressure dependent elastic model. Due to a reduction in soil stiffness around the tunnel, the lining converges inwards at both the tunnel crown and tunnel axis level as a mechanism of deformation (i.e. both horizontal and vertical tunnel diameter decrease), as shown in Figure 7.16c. Conversely, when the tunnel is located in the homogeneous stiff marl layer (Case 2), the application of water pressure on the outer edge of the lining led to the tunnel lining expansion, as shown in Figure 7.16d.

The reason behind the different tunnel lining mechanism of deformation for the two homogeneous models may depend on the different response of the ground surrounding the tunnel. The very weak marl unit is modelled by using the ACSM, whose non-linear elastic components (i.e. bulk modulus K' and the shear stiffness G) are related to the mean effective pressure p' (pressure dependent). Therefore, when the pore pressure behind the lining rises, the homogenous weak marl around the lining becomes softer and the arching around the tunnel reduces. This, in turn, results in a uniform tunnel lining convergence (Figure 7.16c). The stiffer marl unit is modelled using the linear elastic model, defined by the two parameters E' and v', which do not depend on the mean effective pressure p', leading the tunnel lining to expand outwards when the external water pressure is applied behind the lining (Figure 7.16d).

(a) Layering model- Tunnel depth 38.7m (Chapter 6)

(b) Layering model-Tunnel depth 35m (Case 1)

(c) Homogeneous – very weak marl (Chapter 6)

(d) Homogeneous – Medium weak marl (Case 2)
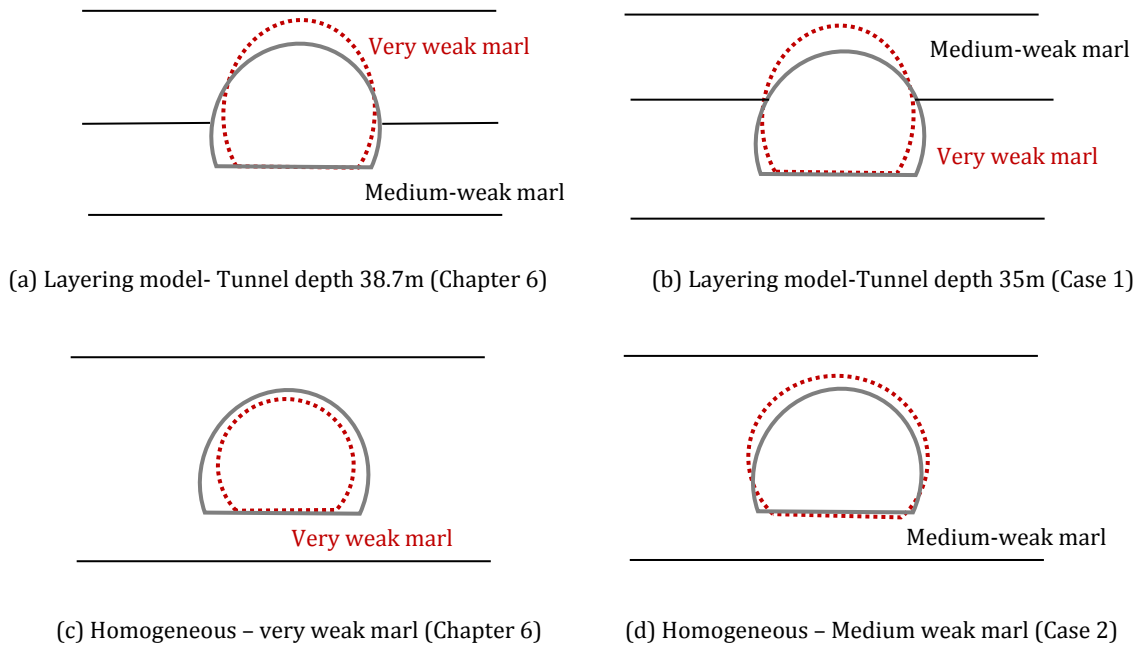
Figure 7.16. Mechanism of deformation of tunnel lining for different layering scenarios during the pore pressure rise stage: (a) Layering model for tunnel depth 38.7 m, (b) Layering model for tunnel depth 35 m (Case 1), (c) Homogeneous model – very weak marl layer, (d) Homogeneous model – medium weak marl layer (Case 2).

Furthermore, due to the flat geometry of the tunnel invert, the vertical tunnel displacement at the centre of tunnel floor increases more when the tunnel invert is located in the very weak marl layer (Case 1) compared to the stiff marl unit surrounding the tunnel invert of tunnel depth 38.7 m, when the tunnel is subjected to an external water pressure, as shown in Figure 7.17
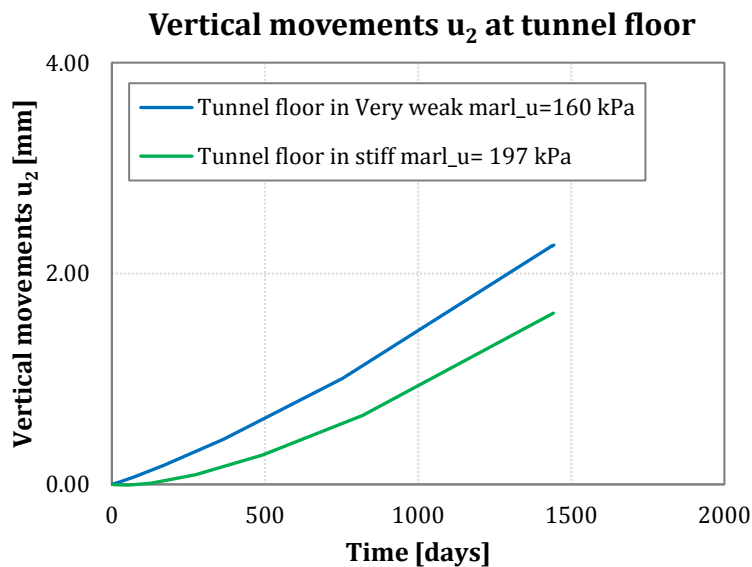
Figure 7.17. Vertical movement at tunnel floor (middle point) when the tunnel lining is subjected to the external water pressure invert is located in the very weak and stiff marl.

Overall, the computed results have shown that the presence of *very weak marl* layers surrounding the tunnel axis and the tunnel invert (i.e. for tunnel depth z_1) gave greater magnitudes of total strains at tunnel lining. Conversely, when the tunnel is surrounded by more competent rock layers, such as *medium weak marl*, less important tunnel lining displacements were computed.

For both cases, the discrepancy between the field measurement data and the results computed with the FEA suggests that more research is required to gain a better understanding of tunnel lining response. In particular, the attempt of comparing the computed strains from the FE modelling with the FO strain data may not provide accurate values. Therefore, different approaches may be assumed in the future for a more realistic evaluation of the strain distribution along the lining.

Chapter 8

8 Conclusions and recommendations for future research

This research thesis was conducted to improve the understanding of the long-term performance of an existing horseshoe-shaped concrete-lined tunnel, housed within the underground facilities at CERN, the European Centre of Nuclear Research, based in Geneva.

Due to ageing of the tunnel, tunnel lining structural damage has appeared, enhancing groundwater infiltration, leakage and further development of tunnel lining deterioration with time. Previous research highlighted the importance of tunnel lining permeability relative to the surrounding soil on the long-term ground response due to tunnelling in London Clay (Wongsaroj 2005; Laver 2010). In fully drained conditions, no pore water pressure develops behind the tunnel lining. The long-term operation of a tunnel may cause the deterioration of the tunnel drainage system, such as the clogging of the drain pipes, resulting in the generation of an external water pressure on the lining. This effect may occur over a long period, and thus may be difficult to measure on site.

In this study, the effect of a change in tunnel lining drainage condition on the lining response was investigated for a site at CERN in which the long-term performance was expected to be critical. To address the mentioned effect, a monitoring scheme was implemented for the TT10 tunnel in the *red molasse* region, where evidence of ongoing movement has triggered the need for an accurate study. The instrumentation comprised distributed fibre optic strain sensors (DFOS) and total station surveys to evaluate the tunnel lining mechanism of deformation and to measure tunnel lining convergence. The data were presented in Chapter 3 and Chapter 4.

A series of finite element analyses was performed to study the long-term tunnel lining response into the finite element software ABAQUS 6.14-1. The results were

compared against the field data. Further numerical modelling was conducted into the effect of layering divisions within the rock mass on the tunnel lining response. The main conclusions are detailed in the following sections.

8.1 Main findings

8.1.1 Field investigation and monitoring

An extensive suite of site investigations and monitoring instrumentation undertaken in this research has contributed to the identification of tunnel lining deformation modes and, therefore, have improved the understanding of lining response under certain circumstances. Particularly, the deterioration of the tunnel drainage system may have caused the clogging of drain pipes, leading to the build-up of water pressure on the outer edge of the lining with time. Additionally, the analysis of the geological face-logs and geotechnical boreholes surrounding the tunnel highlighted the presence of *very weak* marl units, which have influenced the tunnel lining behaviour many years after construction. Some tunnel cross-sections were found to be more damaged than others due to the geology encountered. Further, the horseshoe tunnel geometry in addition to a flat unreinforced slab seem not to provide appropriate resistance to the potential swelling pressure of the *very weak* marl, resulting in tunnel invert heave.

Long-term deformation mechanisms

This study has enabled the identification of two main tunnel lining deformation mechanisms, implying that the tunnel lining undergoes compressive failure at the tunnel crown and tension cracks at the tunnel shoulder, whereas the tunnel floor exhibits heaving.

The observational monitoring data presented in this thesis provide evidence that the tunnel lining deforms through a vertical elongation. Conventional geodetic measurements show that the change in tunnel diameter exhibits a slow decrease horizontally, accompanied by an increase in the vertical direction throughout the monitoring period.

This research has implemented a novel monitoring technique to observe the tunnel lining performance under certain circumstances. Distributed fibre optic sensors have successfully measured the circumferential strain profile of several sections, providing remote and continuous strain data over a monitoring period of three years (2014 – 2017). The monitoring instruments have proved to be suitable in the CERN radioactive tunnel environment for future installations during operational experiments, providing reliable supplementary data for assessing the performance of CERN infrastructure. Also, this would allow to overcome the limitations of electronic devices, which would provide limited monitoring data also for a much shorter lifetime.

The fibre optic strain data has given key insights into the behaviour of the concrete tunnel lining and has suggested the development of compressive and tensile strains at the tunnel crown and the tunnel axis level respectively, implying a tunnel lining vertical elongation as a mechanism of deformation.

Effect of Weak Marl

More severe strain values were recorded for certain tunnel cross-sections where the *very weak* and swelling-potential marl unit is encountered. The *very weak* rock units in addition to the change in the groundwater condition around the tunnel may have worsened tunnel lining stability, with the development of further cracks and, therefore, caused the development of strains with time. Distinct peaks and troughs strain values were noticed in the tension and compression development for certain months of the year, indicating that there might be a seasonal effect on the FO data.

The study conducted on the laboratory data results and field tests collected in the past years at CERN has shown that the weak sedimentary rock comprises a sequence of marls and sandstones, forming 6 rock sub-units with different mechanical properties. Due to the complexity associated with the rapid transition between the horizontally bedded rock units, a clear distinction of different layers can be often difficult from a single borehole. From the strength-stiffness relationship of the molasse, the marls have shown to be significantly more ductile than the sandstones. One particular marl layer identified as *very weak* marl was found to have soil-like properties, with high plasticity clay minerals and swelling potential when in contact with water.

8.1.2 Tunnel lining response: numerical modelling

To improve the understanding of an existing concrete tunnel lining behaviour when subjected to change in the drainage condition, a series of FE analyses has been implemented in this research, for one representative tunnel cross-section, whose the tunnel crown is located in the *very weak* lumpy marl whereas the tunnel invert is located in the more competent *medium* marl. The computed data was validated against field measurements.

The data collected from the total station system was used to derive the hydrostatic pore pressure load to be applied upon the tunnel lining. The assumption of considering the phreatic water table placed at the interface between the more permeable moraine deposits and the molasse region (i.e. 19 m from ground surface) seems to perform a pore pressure magnitude that provides a good match between computed and field results in terms of tunnel diameter change.

Effect of drainage conditions and water pressure around the tunnel

The numerical simulations undertaken show the importance of groundwater condition around the tunnel on the long-term lining response. The model has shown some noteworthy observations. A change in tunnel lining permeability due to a reduced capacity of the drainage system several years after construction simulated by the imposition of a pore pressure behind the lining has provided a distinct tunnel lining mechanism of deformation, which involves compressive (i.e. negative) and tensile (positive) strains at the tunnel crown and the tunnel axis respectively. This behaviour would suggest a vertical elongation of the tunnel as a deformation mode, which is critical for tunnel stability as it results in tunnel lining distortions and, therefore, the development of cracks.

Furthermore, tunnel lining thickness and stiffness have shown to have an impact on the computation of displacements and strains magnitudes along the lining.

However, while the computed change in tunnel diameter result seems to match quite well with field data measurements, the magnitude of total strains performed for the beam elements at the tunnel lining has been consistently underestimated.

A likely explanation behind the discrepancy between predicted and observed strains along the lining may be associated with the adopted approach for evaluating the bending strains from the beam elements curvature. Particularly, the strains obtained

from the FO measurements referred to the strain experienced by the optical fibre attached to the tunnel lining only at discrete locations, whereas the evaluation of the strains performed in the FE environment comprises the calculation of the curvature of the beam elements adopted to model the tunnel lining and, consequently, the bending strains developed along the lining. When comparing against observational FO profiles, the results have suggested that the implemented assessment procedure may not be appropriate for predicting the magnitudes of bending strains experienced by the tunnel lining. This indicates that more research is required to compute more accurately the strains along the tunnel lining.

Effect of soil layering

Further modelling into the influence of layering divisions within the red molasse region on the tunnel lining response have been also carried out. The results have shown that the sequence of various marl units with different mechanical properties has the potential to influence the tunnel lining mechanism of deformation. The numerical results of the layered ground conditions have indicated that the structural behaviour of the tunnel lining is affected by the layering formations surrounding the tunnel. The change in tunnel diameter and the distribution of the compressive and tensile strains along the lining boundary seem to depend on the presence of layered soil conditions (i.e. medium weak marl and very weak marl unit). In fact, the tunnel lining visibly deforms with a vertical tunnel elongation when the tunnel cross-section is placed in a layered formation, indicating that the tunnel lining behaviour appears to be sensitive to the variation of soil properties (i.e. stiffness). Moreover, the change of the position of the marl layers around the tunnel has led to the development of different magnitudes of strains along the lining. Larger strain values were observed at the tunnel crown when the very weak ground unit was located in the top ground layer (i.e. around the tunnel crown), whilst more important strains were computed at the tunnel axis level when the very weak marl layer is placed at the tunnel invert level. A different tunnel lining behaviour was observed when the tunnel is entirely located in a homogenous soil model (i.e. tunnel in the very weak marl layer or in medium weak marl layer). This behaviour suggests that the change in the groundwater condition around the tunnel boundary many years after construction as well as the ground formation surrounding the tunnel (layered or homogeneous) play a crucial role in the long-term tunnel lining response.

8.2 Recommendations for future work

This research has implemented novel and conventional monitoring techniques for assessing the tunnel lining behaviour of an existing tunnel that underwent some displacements and damage with time.

The monitoring through the deployment of DFOS sensors has shown the potential of using a remote and innovative technology, providing useful data. The FO results have enabled the collection of a 3-year monitoring data set, suggesting a tunnel lining deformation mode in agreement with that observed by conventional systems. However, the instrumentation involved the installation of only a strain FO cable, due to the stable thermal environment in the deep CERN tunnels. It would be beneficial to consider the deployment of a temperature cable in future installations, to enhance the temperature compensation on the final assessment of the mechanical strain and, hence, provide more accurate circumferential strain profiles. This should also include the installation of some slack circumferential loops (i.e. zero mechanical strain loops) beside the pre-tensioned instrumented cross-sections, not only to provide further fibre optic cable in the case of fibre breakage, but also to have a better understanding of the influence of the method of attachment of the optical fibre to the structure on the observed tunnel cross-section strain profiles.

Supplementary installation of thermistors would also confirm the stable environment.

The conducted numerical simulations have been shown to quantify accurately the change in the tunnel diameter that appears to agree well with observational data. However, further investigation is required to predict more precisely the magnitudes of bending strains along the tunnel lining, which would involve a more detailed tunnel lining modelling. Moreover, the FE simulations that have been conducted in this thesis have implemented the advanced critical state model developed by Wongsaroj (2005) for stiff London Clay only to model the *very weak* marl units. Particularly, the anisotropy stiffness values calibrated for London Clay have been used for the soil-like very weak marl layer. Further work should be carried out to assess more realistic parameters for modelling the molasse rock.

Further research in the long-term investigation of tunnels should include localised seepage into the tunnel and, hence, considering non-uniform tunnel lining permeability. Also, a parametric study on the assumption of the reduction in

percentage of nodal forces along the tunnel lining when adopting the convergence-confinement method should be carried out when simulating the tunnel lining construction in the FE environment.